# EFFECT OF SODIUM CHANNEL SNVS ASSOCIATED TO ARRHYTHMOGENIC DISEASES. MODULATORY ROLE OF THE GENETIC BACKGROUND

**Rebecca Martinez Moreno**

Per citar o enllaçar aquest document:
Para citar o enlazar este documento:
Use this url to cite or link to this publication:

**ADVERTIMENT**. L'accés als continguts d'aquesta tesi doctoral i la seva utilització ha de respectar els drets de la persona autora. Pot ser utilitzada per a consulta o estudi personal, així com en activitats o materials d'investigació i docència en els termes establerts a l'art. 32 del Text Refós de la Llei de Propietat Intel·lectual (RDL 1/1996). Per altres utilitzacions es requereix l'autorització prèvia i expressa de la persona autora. En qualsevol cas, en la utilització dels seus continguts caldrà indicar de forma clara el nom i cognoms de la persona autora i el títol de la tesi doctoral. No s'autoritza la seva reproducció o altres formes d'explotació efectuades amb finalitats de lucre ni la seva comunicació pública des d'un lloc aliè al servei TDX. Tampoc s'autoritza la presentació del seu contingut en una finestra o marc aliè a TDX (framing). Aquesta reserva de drets afecta tant als continguts de la tesi com als seus resums i índexs.

**ADVERTENCIA.** El acceso a los contenidos de esta tesis doctoral y su utilización debe respetar los derechos de la persona autora. Puede ser utilizada para consulta o estudio personal, así como en actividades o materiales de investigación y docencia en los términos establecidos en el art. 32 del Texto Refundido de la Ley de Propiedad Intelectual (RDL 1/1996). Para otros usos se requiere la autorización previa y expresa de la persona autora. En cualquier caso, en la utilización de sus contenidos se deberá indicar de forma clara el nombre y apellidos de la persona autora y el título de la tesis doctoral. No se autoriza su reproducción u otras formas de explotación efectuadas con fines lucrativos ni su comunicación pública desde un sitio ajeno al servicio TDR. Tampoco se autoriza la presentación de su contenido en una ventana o marco ajeno a TDR (framing). Esta reserva de derechos afecta tanto al contenido de la tesis como a sus resúmenes e índices.

**WARNING**. Access to the contents of this doctoral thesis and its use must respect the rights of the author. It can be used for reference or private study, as well as research and learning activities or materials in the terms established by the 32nd article of the Spanish Consolidated Copyright Act (RDL 1/1996). Express and previous authorization of the author is required for any other uses. In any case, when using its content, full name of the author and title of the thesis must be clearly indicated. Reproduction or other forms of for profit use or public communication from outside TDX service is not allowed. Presentation of its content in a window or frame external to TDX (framing) is not authorized either. These rights affect both the content of the thesis and its abstracts and indexes.

DOCTORAL THESIS

# Effect of sodium channel SNVs associated to arrhythmogenic diseases. Modulatory role of the genetic background.

Rebecca Martinez Moreno

2021

DOCTORAL THESIS

# Effect of sodium channel SNVs associated to arrhythmogenic diseases. Modulatory role of the genetic background.

Rebecca Martinez Moreno

2021

Doctorat en Biologia Molecular, Biomedicina i Salut

Dirigida per:

Dra. Fabiana Silvia Scornik Gerzenstein i Dra. Elisabet Selga Coma

Tutora: Dra. Fabiana Silvia Scornik Gerzenstein

Memòria presentada per optar al títol de doctora per la Universitat de Girona

1 Annex

La **Dra. Fabiana Scornik,** professora de la Facultat de Medicina de la Universitat de Girona i codirectora de la unitat d'electrofisiologia del Centre de Genètica Cardiovascular de l'Institut d'Investigació Biomèdica de Girona i de la Universitat de Girona.

La **Dra. Elisabet Selga Coma,** professora de la Facultat de Medicina de la Universitat de Vic – Universitat central de Catalunya.

DECLAREM:

Que el treball titulat "**Effect of sodium channel SNVs associated to arrhythmogenic diseases. Modulatory role of the genetic background**", que presenta **Rebecca Martinez Moreno** per a l'obtenció del títol de doctor/a, ha estat realitzat sota la nostra direcció i que compleix els requisits per poder optar a Menció Internacional.

I, perquè així consti i tingui els efectes oportuns, signem aquest document.

Girona, 26 de Març del 2021

# Acknowledgements

Después de todo lo pasado redactando esta Tesis, ha llegado **por fin** el momento de escribir los agradecimientos. Veréis una mezcla de idiomas, pero quien me conoce ya sabe que es lo que hago normalmente cuando hablo.

Como no podía ser de otra manera, en primer lugar, quiero agradecer a mis directoras de tesis todo lo que han hecho por mí. Fabi, gracias por confiar des del principio en mí para tirar adelante este maravilloso proyecto. Has conseguido que una persona que no sabía prácticamente nada de electrofisiología, la acabara apreciando hasta el punto de querer dedicar mi futuro profesional a este ámbito. Lo de entenderla del todo ya es otro tema, pero, como tú siempre dices, es algo que conlleva muchos años. Eli, gràcies per haver-me ensenyat tot el que saps de cultius cel·lulars, que no és poc! Sense tu, a hores d'ara no sabria ni canviar-li el medi a un flascó de HEKs. També per tota la teva saviesa en l'àmbit molecular en general. Muchas gracias a las dos por haberme enseñado tantísimas cosas y por vuestra paciencia. Por darme la posibilidad de ir a los mejores congresos en USA, y al curso de Plymouth. Por corregirme minuciosamente cada *abstract*, aplicaciones para becas y el artículo entre otras muchas cosas. Y, sobre todo, por vuestras correcciones en la redacción de esta tesis, que es tanto mía como vuestra. Nunca os lo podré agradecer lo suficiente.

Más allá del ámbito educativo, os agradezco muchísimo vuestra cercanía. Me habéis ayudado muchísimo en mis peores momentos. Habéis confiado en mí cuando ni yo misma lo hacía, y me habéis hecho tirar hacia adelante siempre. Sois unas personas maravillosas, y soy extremadamente afortunada de haberos tenido ahí durante todos estos años.

Gracias también a Guille, el revisor por excelencia. Por tus ánimos y todos tus consejos, aunque no te gustaran los rombos de mis posters. También me siento muy afortunada de haber tenido a mi lado una persona como tú.

Vull agrair també a en Ramon per haver-me deixat formar part de Gencardio, i també per donar-me la oportunitat d'implicar-me en el projecte de l'Alexandra. Això em porta a l'Alexandra, una de les persones que també m'ha ajudat moltíssim en aquesta tesis. Gràcies per tot: pels teus consells, les xerrades (tant sobre ciència com d'altres temes) i per ser com ets amb mi. També per mimar-me tant portant-me xuxes i dolços varis. Gràcies també als altres membres de LDG: Mònica, Ferran, Marta P, Laura i Nuria; i a l'Anna I i a en Carles.

Gràcies a la Mireia, la Sara i en Marcel per tota la vostra ajuda. També als ex-predocs: Mel·lina, Bernat, Txús i Èric; i als predocs actuals: David, Marta V, Anna F i Yajaira. A l'Adrià, que és quasi tant friki com jo i hem pogut parlar de temes de vital importància com són els videojocs.

A en David li vull dedicar algunes paraules més. Gràcies per totes les hores interminables de cultius (que donen per parlar de moltes coses) i d'experiments junts. Per aguantar el meu mal caràcter (encara que sé que el trobaries a faltar) i tots els meus drames. Gràcies per ajudar-me tant, i per la custòdia compartida de les nostres *cells* els caps de setmana i festius. Sense tu hauria acabat boja (ja, ja ho sé, més de lo que estic de naixement). Ja ho diu la Bet sempre que fem un bon equip.

Bet, la meva mutada preferida, què hauria sigut de mi sense tu? Gràcies per tots els moments a cultius i per la teva ajuda, ets una font de saviesa sense límits. També pels teus concerts amb coreografia incorporada. Gràcies també a la Sara de l'ICO, la Bet i tu sou un duo meravellós.

Thank you to my bitchy cluster (sorry for the bad word, that's who we are) from the Microelectrodes course at Plymouth: Oscar, Marta, Sarah, Laura, Marcella and Mario. I had the best time there thanks to you guys. I hope that in the future we can reunite to *ballenying* more together.

I would like to thank too all the people at Brown University, who made me feel so comfortable in their lab. Specially to Dr. Koren for giving me the opportunity of learning so much in his research group, and Anatoli for your patience and all the funny moments with you.

Ahora pasemos a la lista de amigos y familia. Mis nenas bonicas: Maria, Sara y Sílvia. Gracias por absolutamente todo lo que habéis hecho por mí, son demasiadas cosas como para resumirlas aquí. Llevamos muchísimos años juntas y espero que sean muchísimos años más. Sois las mejores amigas que una persona podría desear, y aunque sé que no lo demuestro mucho os quiero con todo mi *kokoro*.

A las que han seguido ahí tras acabar la uni: Clara y las dos Irenes. Gracias por los maravillosos años de uni con vosotras y los que han venido después. Por todo lo que hemos vivido juntas. Marc, gracias también a ti por todo tu apoyo durante todos estos años. Ya sabes que siempre te

he deseado lo mejor ya sea en Bilbao, Dinamarca o donde quiera que vayas a continuación, ¡pero te echo mucho de menos!
Gracias por el apoyo y los ánimos a mis compañeros de frikadas en general: Sabo y Esteve.

A mi hermana, Maggie. Pese a los miles de Km que nos separan, has sido y eres un pilar fundamental en mi vida. Gracias por todo tu apoyo, tus consejos, y por compartir conmigo todas las frikadas que tanto nos gustan. Gracias por acogerme en tu casa durante mi estancia en Brown (and thanks to Matt too!), y por todas las experiencias vividas juntas. Te quiero.
A mi padre, gracias por todo el cariño que me diste y por ser la persona más bondadosa que he conocido en toda mi vida. Te echo y te echaré siempre de menos, pero sé que estarías muy orgulloso de mi. He sido muy afortunada al tener un padre como tú.
A mis gatos, Odin y Kylo, que también forman parte de mi pequeña familia porque son como hijos para mí. Todos sabéis que soy la definición de diccionario de loca de los gatos, así que este agradecimiento no podía faltar. Gracias por hacerme tantísima compañía y por vuestro amor incondicional.
Gracias a Maria Gracia y Cristina por haber pasado a formar parte de mi familia. Por vuestro apoyo, y por lo muchísimo que me cuidáis. También a Pepa, por ser la perrita más amorosa del mundo.

Finalmente, a Joan. Gracias por cuidarme y por apoyarme, tanto en lo bueno como en lo malo. Por animarme a seguir cuando ya no podía más, y por escuchar todos mis problemas. Por hacerme sentir tan querida, pese a que soy una persona muy complicada. Aún nos queda mucho por vivir juntos, te quiero.

“And blood-black nothingness began to spin.
A system of cells interlinked within
Cells interlinked within cells interlinked
Within one stem. And dreadfully distinct
Against the dark, a tall white fountain played.”
Vladimir Nabokov, Pale Fire

# Scientific publications derived from this Thesis

Rebecca Martinez-Moreno, Helena Riuró, Elisabet Selga, Michael F. Wangler, Ramn Brugada, Guillermo J. Pérez, Fabiana S. Scornik. An *SCN1B* Variant Found in a Child Diagnosed with Epilepsy and Brugada Syndrome Modifies Brain-Type (Na$_V$1.1) and Cardiac-Type (Na$_V$1.5) Sodium Currents. *Biophysical Journal*. **3**, 490a (2018).

Rebecca Martinez-Moreno, Elisabet Selga, Georgia Sarquella-Brugada, Ramon Brugada, Guillermo J. Pérez, Fabiana S. Scornik. Cardiac Sodium Current is Severely Impaired in Induced Pluripotent Stem Cell-Derived Cardiomyocytes from Brugada Syndrome Patients. *Biophysical Journal*. **3**, 390a-391a (2019).

Rebecca Martinez-Moreno, David Carreras, Elisabet Selga, Georgia Sarquella-Brugada, Ramon Brugada, Guillermo J. Pérez, Fabiana S. Scornik. Comparative Study of the Effects of an *SCN5A* Mutation within a Family Diagnosed with Brugada Syndrome using iPS-CM. *Biophysical Journal*. **3**, 500a (2020).

Rebecca Martinez-Moreno, Elisabet Selga, Helena Riuró, David Carreras, Mered Parnes, Chandra Srinivasan, Michael F. Wangler, Guillermo J. Pérez, Fabiana S. Scornik, Ramon Brugada. An *SCN1B* Variant Affects Both Cardiac-Type (Na$_V$1.5) and Brain-Type (Na$_V$1.1) Sodium Currents and Contributes to Complex Concomitant Brain and Cardiac Disorders. *Frontiers in Cell and Developmental Biology*. **8**, 1-17 (2020).

# Abbreviations

| | |
|---|---|
| **A** | Absorbance |
| **AC** | Arrhythmogenic cardiomyopathy |
| **AF** | Atrial fibrillation |
| **Amp** | Ampicillin |
| **AP** | Action potential |
| **AVN** | Atrioventricular node |
| **BrS** | Brugada Syndrome |
| **BSA** | Bovine serum albumin |
| **C** | Coulombs |
| **CAM** | Cell adhesion molecules |
| **cDNA** | Complementary DNA |
| **CPVT** | Catecholaminergic polymorphic ventricular tachycardia |
| **Dex** | Dexamethasone |
| **DMEM** | Dulbecco’s Modified Eagle’s Medium |
| **DMSO** | Dimethyl sulfoxide |
| **DN** | Dominant negative |
| **DNA** | Deoxyribonucleic acid |
| **dNTPs** | Deoxynucleotides |
| **DS** | Dravet Syndrome |
| **E-C** | Excitation-contraction |
| **ECG** | Electrocardiogram |
| **EDTA** | Ethylenediaminetetraacetic acid |
| **$E_m$** | Membrane potential |
| **ES** | Embryonic stem |
| **FBS** | Fetal bovine serum |
| **FCS** | Fetal calf serum |
| **FW** | Forward |

| | |
|---|---|
| **GEFS+** | Generalized epilepsy with febrile seizures plus |
| **HEK-293T** | Human embryonic kidney-293 tsA201 |
| **Ig** | Immunoglobulin |
| **$I_{Na}$** | Sodium current |
| **iPSc** | Induced pluripotent stem cells |
| **iPS-CM** | iPSc-derived cardiomyocytes |
| **I-V** | Current-voltage |
| **KOSR** | Knock out serum replacement |
| **LQT** | Long QT |
| **mV** | Millivolts |
| **O/D** | Overday |
| **O/N** | Overnight |
| **PBS** | Phosphate-buffered saline |
| **PCR** | Polymerase chain reaction |
| **PD** | Pore domain |
| **Pen-Strep** | Penicillin-Streptomycin |
| **qPCR** | Quantitative PCR |
| **RNA** | Ribonucleic acid |
| **ROCKi** | Y-27632 2HCl ROCK1 inhibitor |
| **Rq** | Relative quantification |
| **SERCA** | Sarcoplasmic reticulum calcium transport ATPase |
| **SR** | Sarcoplasmic reticulum |
| **RT** | Room temperature |
| **RV** | Reverse |
| **RVOT** | Right ventricular outflow tract |
| **SAN** | Sinoatrial node |
| **SCD** | Sudden cardiac death |
| **SIDS** | Sudden infant death syndrome |
| **SNV** | Single nucleotide variant |
| **SQT** | Short QT |
| **SUDEP** | Sudden unexpected death in epilepsy |

| | |
|---|---|
| **T3** | 3,3′,5-Triiodo-L-thyronine |
| **TeSR** | Stem cell selection media |
| **VF** | Ventricular fibrillation |
| **VGSC** | Voltage-gated sodium channels |
| **VSD** | Voltage-sensing domain |
| **WT** | Wild type |

# Contents

# Figures

# Tables

# Summary

Inherited arrhythmogenic diseases, also known as channelopathies, are mostly due to pathogenic mutations located in ion channels. These channelopathies affect a wide variety of organs, such as the brain and the heart. The type of mutations that are more frequently identified in patients suffering such diseases are changes of a single nucleotide (single nucleotide variants, SNVs).

Genetic analysis has been a useful tool to identify mutations in ion channels as the cause for various arrhythmogenic diseases, such as epilepsy and neurodevelopmental disorders in the brain; and Brugada Syndrome (BrS), long and short QT syndromes and catecholaminergic polymorphic ventricular tachycardia in the heart.

However, it is known that many mutations inherited within a family display incomplete penetrance and variable expressivity. The advent of the next generation sequencing techniques has allowed researchers to obtain information on the patient-specific genetic background. Later on, the possibility of generating individual-specific induced pluripotent stem cell-derived cardiomyocytes (iPS-CM), brought the advantage of studying a given mutation in a patient-specific cellular model.

With all this in mind, we proposed the central hypothesis of this thesis, which is that **the effect of sodium channel SNVs associated to inherited arrhythmogenic diseases is modulated by the individual's specific genetic background.** To assess this hypothesis, we studied two SNVs linked to inherited arrhythmogenic diseases that presented incomplete penetrance and/or variable expressivity in the families where they were identified.

The first SNV that we studied is located in the *SCN1B* gene (*SCN1B*_c.308A>T), in a region shared by the encoded β1 and β1b subunits. This SNV was identified in heterozygosis in a whole-exome sequencing study of an 8-year-old male (proband), and was inherited from his father. Although both parents are asymptomatic, the clinical picture of the proband includes cardiac and neurological impairment. Furthermore, the proband's sister, who also carried the SNV, died from multi-organ failure.

Thus, we hypothesized that the SNV would alter the regulatory properties of both β1 and β1b subunits over the cardiac and neuronal sodium channels ($Na_V1.5$ and $Na_V1.1$, respectively). To

address this point, we transiently transfected the SNV in HEK-293T cells, and studied the sodium current properties using the whole-cell patch clamp technique.

Both mutant β1 and β1b subunits caused a loss of function of Na$_V$1.5, possibly explaining the cardiac disorders observed in the proband. Our results showed that the mutant β1b subunit caused a gain of function of Na$_V$1.1, while the mutant β1 produced a loss of function of the channel. β1b is predominant in the brain during development and early life. During adulthood, the predominant isoform is β1. Thus, both mutant isoforms could contribute to the arrhythmogenic brain activity at different stages of development. Additionally, the proband and her sister also carry two mutations in the gene *POLR1C*, inherited one from each of their progenitors. Therefore, we surmise that these mutations in *POLR1C* might be aggravating the brain condition of the proband, and could have contributed to the clinical phenotype of her sister.

The second SNV studied in this Thesis is located in the *SCN5A* gene (*SCN5A*_c.4573G>A). This SNV was identified in several carriers of a family, and had been previously identified in a BrS patient. The SNV was found in a subject (proband) diagnosed with atrial fibrillation, who displayed the typical BrS electrocardiogram (ECG) pattern when treated with flecainide. His daughter inherited the SNV, although she remains asymptomatic to date. The SNV was inherited by the proband's grandchildren, a girl and a boy. When tested for flecainide, the boy's ECG displayed the typical BrS phenotype but his sister's did not. Both children remain asymptomatic to date. However, since BrS symptoms occur typically in the adulthood, these patients could still develop symptoms in the future.

We hypothesized that the *SCN5A* SNV would modify the sodium current properties of Na$_V$1.5. To assess this, we studied the effects of the SNV using the whole-cell patch clamp technique in two cellular models: HEK-293T cells transiently transfected with the SNV, and iPS-CM derived from a family unit of four members, three of which are carriers of the SNV: the mother (daughter of the proband), her children (grandchildren of the proband) and their father (non-carrier of the SNV).

The SNV caused a loss of function of Na$_V$1.5 when it was heterologously expressed in HEK-293T cells. The study of the iPS-CM derived from the children also showed a loss of function of the sodium channel, but the magnitude of the effect was greater in this cellular model. This loss of sodium current function effect was not observed in the iPS-CM derived from the mother. Thus, our results support the second hypothesis of this study where we proposed that the effect would be different in the three carrier individuals.

In our third hypothesis, we proposed that effect of the SNV on the $Na_V1.5$ current in the iPS-CM derived from carrier individuals of the same family would be different to the effect observed in HEK-293T cells heterologously expressing the SNV. Our results support this hypothesis. We interpret that these differences are due to the cardiac tissue specificity that iPS-CM provide. This means that other molecules interacting with the α subunit can modify the effect of the SNV in this cellular context. Furthermore, the loss of function greater than 50% that we observed in the iPS-CM derived from the children can be explained by a dominant negative effect of the mutant α over the wild type α subunit.

We observed huge differences in sodium current properties between the mother's and the children's derived iPS-CM. As stated in our fourth hypothesis, patient-specific variants, other than the studied one, could influence both the cellular phenotypical effect of the SNV and the individual clinical features. To investigate this possibility, we performed a genetic panel customized for genes related to cardiac arrhythmias. We identified a common polymorphism carried only by the mother (leading to $Na_V1.5$_p.H558R), which had been reported as a protective factor for other sodium channel mutations. Thus, it could explain the lack of the deleterious effect of the SNV in the mother. Other variants identified in the panel could give light to the differences observed in the flecainide test in both children. The boy has variants in the genes *MYBPC3*, *MYH6*, *MYH7* and *TNNI3,* which could be compromising the heart conductivity or the junction between cardiomyocytes, thus affecting the observed response to flecainide. The girl is a carrier of an SNV in *CACNB2*, which could be suppressing the BrS ECG.

Overall, the evidence presented in the two studies of this Thesis supports that incomplete penetrance and variable expressivity, observed within families carrying a disease-causing mutation, are highly subject to modulation by patient-specific variants. Therefore, the pathogenicity of a mutation in a family should be addressed by assessing the presence of other variants that could modulate its phenotypical expression.

# Resum

Les malalties aritmogèniques hereditàries, també conegudes com a canalopaties, es donen principalment per mutacions patogèniques situades als canals iònics. Aquestes canalopaties afecten a diversos òrgans, com per exemple el cervell i el cor. El tipus de mutació identificat més freqüentment en pacients que pateixen aquestes malalties són els canvis en un sol nucleòtid (SNV, de l'anglès *single nucleotide variant*).

L'anàlisi genètic ha sigut una eina molt útil per identificar mutacions a canals iònics com a causa de vàries malalties aritmogèniques, com els trastorns del neurodesenvolupament i l'epilèpsia al cervell; i la Síndrome de Brugada (BrS), els síndrome de QT llarg i curt, i la taquicàrdia ventricular polimòrfica catecolaminèrgica al cor.

No obstant, moltes de les mutacions familiars presenten penetrància incompleta i expressivitat variable. L'advent de tècniques de seqüenciació de nova generació ha permès als investigadors obtenir informació del *background* genètic específic del pacient. A més, la possibilitat de generar cardiomiòcits derivats de cèl·lules mare induïdes pluripotents específiques d'un individu (iPS-CM, de l'anglès *induced pluripotent stem cell-derived cardiomyocytes*), ha proporcionat l'avantatge d'estudiar una mutació en un model cel·lular específic del pacient.

Amb tot això en ment, vam proposar la hipòtesi central d'aquesta Tesi, que **l'efecte d'una SNV al canal de sodi associada a una malaltia aritmogènica hereditària és modulada pel *background* genètic específic del pacient**. Per avaluar aquesta hipòtesi, vam estudiar dues SNV relacionades amb malalties aritmogèniques hereditàries que presentaven penetrancia incompleta i/o expressivitat variable en les famílies on van ser identificades.

La primera SNV que vam estudiar està localitzada al gen *SCN1B* (*SCN1B*_c.308A>T), en una regió comuna entre les subunitats β1 i β1b codificades per aquest gen. Aquesta SNV va ser identificada en heterozigosi en un estudi de seqüenciació d'exoma complet en un nen de 8 anys (proband), i l'havia heretada del seu pare. Encara que els seus dos progenitors son asimptomàtics, la imatge clínica del proband inclou deteriorament cardíac i neuronal. A més, la germana del proband, que també era portadora de la SNV, va morir d'una fallada multi-orgànica.

Així doncs, vam hipotetitzar que la SNV alteraria les propietats reguladores de les subunitats β1 i β1b sobre els canals de sodi cardíac i neuronal (Na$_V$1.5 i Na$_V$1.1, respectivament). Per avaluar-ho, vam transfectar transitòriament el gen *SCN1B* amb la SNV en cèl·lules HEK-293T, i vam estudiar les propietats del canal de sodi mitjançant la tècnica *whole-cell patch clamp*.

Ambdues subunitats β1 i β1b mutades van causar una pèrdua de funció de Na$_V$1.5, el qual podria explicar els trastorns cardíacs observats en el proband. Els nostres resultats mostren que la subunitat β1b mutada va causar un guany de funció de Na$_V$1.1, mentre que la β1 mutant va produir una pèrdua de funció del canal. La subunitat β1b és predominant al cervell durant el seu desenvolupament i als primers anys de vida. A l'edat adulta, la isoforma predominant és β1. Així doncs, ambdues isoformes mutants podrien contribuir a l'activitat aritmogènica del cervell a diferents etapes del desenvolupament. Addicionalment, el proband i la seva germana també eren portadors de dues mutacions al gen *POLR1C*, heretades una de cadascun dels seus progenitors. Per tant, proposem que aquestes mutacions a *POLR1C* poden estar agreujant el trastorn al cervell del proband, i podrien haver contribuït al fenotip clínic de la seva germana.

La segona SNV estudiada en aquesta Tesi està localitzada al gen *SCN5A* (*SCN5A*_c.4573G>A). Aquesta SNV va ser identificada en varis membres d'una família, i havia sigut prèviament descrita en un pacient de BrS. La SNV va ser trobada en un individu (proband) diagnosticat amb fibril·lació auricular, que mostrava el patró comú de BrS a l'electrocardiograma (ECG) quan era tractat amb flecainida. La seva filla va heretar la SNV, però fins a data d'avui és asimptomàtica. La SNV va ser heretada pels nets del proband, una noia i un noi. Ambdós nens fins a data d'avui són asimptomàtics. De totes maneres, donat que els símptomes de la BrS ocorren sobretot en l'edat adulta, aquests pacients encara podrien desenvolupar símptomes en un futur.

Vam hipotetitzar que la SNV a *SCN5A* modificaria les propietats de la corrent de sodi de Na$_V$1.5. Per avaluar-ho, vam estudiar els efectes de la SNV mitjançant la tècnica *whole-cell patch clamp* en dos models cel·lulars: cèl·lules HEK-293T transfectades transitòriament amb el gen *SCN1B* mutat, i en iPS-CM derivats de la unitat familiar formada per quatre membres, tres dels quals són portadors de la SNV: la mare (filla del proband), els seus dos fills (nets del proband) i el seu pare (no portador de la SNV).

La SNV va causar una pèrdua de funció de Na$_V$1.5 quan es trobava expressada heteròlogament en les cèl·lules HEK-293T. L'estudi dels iPS-CM derivats dels nens també va mostrar aquesta pèrdua de funció del canal de sodi, però la magnitud de l'efecte va resultar major en aquest model cel·lular. Aquesta pèrdua de funció del canal de sodi no es va observar en els iPS-CM derivats de la mare. Així doncs, els nostres resultats recolzen la segona hipòtesi d'aquest estudi, on vam proposar que l'efecte seria diferent en els tres individus portadors.

A la nostra tercera hipòtesi, vam proposar que l'efecte de la SNV a la corrent de $Na_V1.5$ en els iPS-CM derivats dels portadors de la mateixa família seria diferent a l'efecte observat a les cèl·lules HEK-293T expressant la SNV heteròlogament. Els nostres resultats recolzen aquesta hipòtesi. Interpretem que aquestes diferències són causades per l'especificitat de teixit cardíac que proporcionen els iPS-CM. Això significa que altres molècules que interactuen amb la subunitat α poden modificar l'efecte de la SNV en aquest context cel·lular. A més, la pèrdua de funció major a 50% observada en els iPS-CM derivats dels nens es pot explicar per un efecte dominant negatiu de la α mutada sobre la subunitat α *wild type* del canal.

Vam observar grans diferències en les propietats de la corrent de sodi entre els iPS-CM derivats de la mare i dels seus fills. Tal i com proposa la nostre quarta hipòtesi, variants específiques de pacient, diferents a l'estudiada, podrien influenciar tant l'efecte fenotípic de la SNV com les propietats clíniques de l'individu. Per investigar aquesta possibilitat, vam realitzar un panell genètic perquè incloïa gens relacionats amb arítmies cardíaques. Vam identificar un polimorfisme comú del qual només la mare n'era portadora (i que dóna lloc a la proteïna $Na_V1.5$_p.H558R), el qual ha estat reportat com un factor protector per altres mutacions al canal de sodi. Així doncs, podria explicar la falta de l'efecte perjudicial de la SNV a la mare. Altres variants identificades amb el panell poden donar llum a les diferències observades en el test de flecainida dels dos nens. El noi és portador de variants als gens *MYBPC3*, *MYH6*, *MYH7* i *TNNI3*, que podrien comprometre la conductivitat cardíaca o la unió entre els cardiomiòcits, afectant així la resposta observada a la flecainida. La noia és portadora d'una SNV al gen *CACNB2*, que podria suprimir l'ECG de BrS.

En general, la evidència presentada en els dos estudis d'aquesta Tesi recolza que la penetrància incompleta i l'expressivitat variable, observades en famílies portadores d'una mutació causant d'una malaltia, es troben influenciades pels efectes moduladors de variants específiques de pacient. Per tant, la patogenicitat d'una mutació en una família hauria de ser abordada avaluant la presència d'altres variants que podrien modular la seva expressió fenotípica.

# Resumen

Las enfermedades arritmogénicas hereditarias, también conocidas como canalopatías, se deben principalmente a mutaciones patogénicas situadas en los canales iónicos. Estas canalopatías afectan a diferentes órganos, como por ejemplo el cerebro y el corazón. El tipo de mutación identificado más frecuentemente en pacientes que sufren estas enfermedades son los cambios en un solo nucleótido (SNV, del inglés *single nucleotide variant*).

El análisis genético es una herramienta muy útil para identificar la asociación de las mutaciones en canales iónicos como causa de un gran número de enfermedades arritmogénicas (e.g: epilepsia y trastornos del neurodesarrollo en el cerebro; Síndrome de Brugada (BrS), síndromes de QT largo y corto, y taquicardia ventricular polimórfica catecolaminérgica en el corazón).

No obstante, muchas de las mutaciones familiares presentan penetrancia incompleta y expresividad variable. El advenimiento de técnicas de secuenciación masiva de nueva generación ha permitido a los investigadores obtener información del acervo genético específico del paciente. Además, la posibilidad de generar cardiomiocitos derivados de células pluripotentes inducidas específicas de un individuo (iPS-CM, del inglés *induced pluripotent stem cell-derived cardiomyocytes*), ha proporcionado la ventaja de estudiar los efectos de una mutación dada en un modelo celular especifico del paciente.

En base a esto, propusimos la hipótesis central de esta Tesis: **el efecto de una SNV en el canal de sodio asociada a una enfermedad arritmogénica hereditaria se encuentra modulada por el acervo genético específico del paciente**. Para evaluar esta hipótesis, estudiamos dos SNV relacionadas con enfermedades arritmogénicas hereditarias que presentaban penetrancia incompleta y/o expresividad variable en las familias donde fueron identificadas.

La primera SNV que estudiamos se encuentra localizada en el gen *SCN1B* (*SCN1B*_c.308A>T), en una región común entre las subunidades β1 y β1b codificadas por este gen. Esta SNV se encuentra en heterocigosis y fue identificada en un estudio de secuenciación de exoma completo en un niño de 8 años (probando), quien la había heredado de su padre. Mientras que los padres son asintomáticos, la imagen clínica del probando incluye un deterioro cardíaco y

neuronal. Además, la hermana del probando, también portadora de la SNV, murió de un fallo multiorgánico.

Así pues, hipotetizamos que la SNV altera las propiedades reguladoras de las subunidades β1 y β1b sobre los canales de sodio cardíaco y neuronal (Na$_V$1.5 y Na$_V$1.1, respectivamente). Para evaluarlo, transfectamos transitoriamente la SNV en células HEK-293T, y estudiamos las propiedades del canal de sodio usando la técnica *whole-cell patch clamp*.

Ambas subunidades β1 y β1b mutadas causaron una pérdida de función del canal Na$_V$1.5, posiblemente explicando los trastornos cardíacos observados en el probando. Nuestros resultados muestran que la subunidad β1b mutada causó una ganancia de función del canal Na$_V$1.1, mientras que la subunidad β1 mutada produjo una pérdida de función de este canal. La subunidad β1b es predominante en el cerebro durante su desarrollo y en los primeros años de vida. En la edad adulta, la isoforma predominante es la β1. Así pues, ambas isoformas mutadas podrían contribuir a la actividad arritmogénica del cerebro en diferentes etapas de su desarrollo.

Adicionalmente, el probando y su hermana también eran portadores de dos mutaciones en el gen *POLR1C*, heredadas de cada uno de sus progenitores. Por lo tanto, proponemos que estas mutaciones en *POLR1C* podrían estar agravando el trastorno en el cerebro del probando, y podrían haber contribuido en el fenotipo clínico de su hermana.

La segunda SNV estudiada en esta Tesis está localizada en el gen *SCN5A* (*SCN5A*_c.4573G>A). Esta SNV fue identificada en varios miembros de una familia, y había sido previamente identificada en un paciente de BrS no relacionado con esta familia. La SNV se encontró en un individuo (probando) diagnosticado con fibrilación auricular, que mostraba un patrón común de BrS en el electrocardiograma (ECG) cuando fue tratado con flecainida. Su hija heredó la SNV, aunque a día de hoy es asintomática. La SNV fue heredada por los nietos del probando, una chica y un chico. Ambos niños hasta ahora son asintomáticos. No obstante, dado que los síntomas del BrS ocurren sobre todo en la edad adulta, estos pacientes podrían aún desarrollar síntomas en un futuro.

Nuestra hipótesis era que la SNV en *SCN5A* modificaría las propiedades de la corriente de sodio del canal Na$_V$1.5. Para evaluar esto, estudiamos los efectos de la SNV mediante la técnica *whole-cell patch clamp* en dos modelos celulares: células HEK-293T transfectadas transitoriamente con la SNV, y en iPS-CM derivados de cuatro miembros de la familia, tres de los cuales son portadores de la SNV: la madre (hija del probando), sus dos hijos (nietos del probando) y su padre (no portador de la SNV).

La SNV causó una pérdida de función del canal Na$_V$1.5 en el modelo de expresión heteróloga en las células HEK-293T. El estudio de los iPS-CM derivados de los niños también mostró esta pérdida de función del canal de sodio, pero la magnitud del efecto fue mayor en este modelo celular. Esta pérdida de función del canal de sodio no se observó en los iPS-CM derivados de la madre. Así pues, nuestros resultados apoyan la segunda hipótesis de este estudio, en la cual propusimos que el efecto de la SNV sería diferente en los tres individuos portadores.

En nuestra tercera hipótesis, propusimos que el efecto de la SNV en la corriente de Na$_V$1.5 en los iPS-CM derivados de los portadores de la misma familia sería diferente al efecto observado en las células HEK-293T que expresaban la SNV heterólogamente. Nuestros resultados apoyan esta hipótesis. Interpretamos que estas diferencias vienen dadas por la especificidad de tejido cardíaco que dan los iPS-CM. Esto significa que otras moléculas que interactúan con la subunidad α del canal pueden modificar el efecto de la SNV en este ambiente celular. Además, la pérdida de función mayor que 50% observada en los iPS-CM derivados de los niños podría ser explicada por un efecto dominante negativo de la α mutada sobre la subunidad α *wild type* del canal.

Observamos grandes diferencias entre las propiedades de la corriente de sodio entre los iPS-CM derivados de la madre y los niños. Tal y como se propone en la cuarta hipótesis, algunas variantes específicas de los pacientes, diferentes a la estudiada, podrían influir tanto en el efecto fenotípico de la SNV como en el cuadro clínico del individuo. Para investigar esta posibilidad, realizamos un panel genético diseñado para genes relacionados con arritmias cardíacas. Identificamos un polimorfismo común del cual solo la madre es portadora (Na$_V$1.5_p.H558R). Este polimorfismo ha sido reportado como un factor protector en otras mutaciones en el canal de sodio cardíaco. Así pues, podría explicar la ausencia del efecto perjudicial de la SNV en la madre. Otras variantes identificadas en el panel pueden dar luz a las diferencias observadas en el test de flecainida de los dos niños. El niño es portador de variantes en los genes *MYBPC3*, *MYH6*, *MYH7* y *TNNI3*, que podrían comprometer la conducción eléctrica en el corazón o la unión entre los cardiomiocitos, afectando así la respuesta observada en el test de flecainida. La niña es portadora de una SNV en el gen *CACNB2*, que podría contrarrestar el efecto de la mutación en el canal de sodio e influir en la ausencia del patrón de BrS en el ECG.

En conjunto, la evidencia presentada en los dos estudios de esta Tesis apoya que la penetrancia incompleta y la expresividad variable, observadas en familias portadoras de una mutación causante de una enfermedad arritmogénica hereditaria, se encuentran influenciadas por la modulación de variantes específicas del paciente. Por lo tanto, la patogenicidad de una mutación en una familia debe ser evaluada teniendo en cuenta la presencia de otras variantes que podrían modular su expresión fenotípica.

# I. Introduction

## 1. Inherited arrhythmogenic diseases or channelopathies

Ion channels are transmembrane proteins located across the lipid bilayer of cell membranes, where they form a pore to facilitate the inflow or outflow of specific ions. The passage of these ions through the pore is controlled by either the membrane potential (voltage-gated channels), extracellular ligand molecules (ligand-gated channels), or different mechanisms (such as second messengers, temperature, mechanical stimuli, or light).[1,2]

Arrhythmogenic diseases occur when the normal rhythm of either neuronal or cardiac cells is disrupted. Inherited arrhythmogenic diseases (from now on channelopathies), are developed by alterations in ion channels activity, either due to pathogenic mutations in genes that encode the proteins that form the ion channels or by acquired factors.[1] Pathogenic mutations are the most common cause, and these mutations lead to alterations in the protein structure, function, localization and/or modulation. They can be located in the pore-forming α subunits, the β subunits and/or other regulatory proteins.[1,3]

The type of mutations that are more frequently identified in patients suffering a channelopathy are changes of a single nucleotide (single nucleotide variant, SNV), which can result in either a different aminoacid (missense SNV) or a stop codon (nonsense SNV). Other types of variants can be identified in a lower proportion of cases. These include deletions or insertions of one or more bases (known as indels) and copy number variants, in which a DNA segment of 1kb or bigger is present in a different number of copies with respect to the reference genome. These two latter types of mutations can shift the way the sequence is read (frameshift).

Once the mutation has been identified, it can be classified, based on its frequency in the population, as: new, rare (present in <1% of the population) or as polymorphisms (>1% of the population). To determine whether the mutation can be pathogenic and thus can be the cause of the channelopathy in the patient, the following criteria points are assessed:[4]

- Cosegregation of the variant and the phenotype in a family diagnosed with a disease.
- Absence or extreme rarity of the variant in control cohorts and exome/genome datasets.
- The variant is nonsense, frameshift or insertion/deletion that leads to a truncated protein.
- The variant is missense and is located in highly conserved aminoacids or key functional domains.

- Evidence of a perturbed ion channel function through functional studies.
- In silico prediction of pathogenicity with bioinformatic tools.

Depending on how many items of the pathogenicity criteria a mutation fulfills, it can be classified as:[5,6]

- Possibly pathogenic: can lead to a phenotypic change.
- Possibly benign or neutral: the mutation might not cause the channelopathy.
- Variant of uncertain significance: there is not enough evidence to catalogue the mutation.

Pathogenic mutations in ion channels are recognized causes of disease in a wide variety of tissues. Besides brain and heart, they have been reported in skeletal muscle, and in the respiratory, endocrine, urinary and immune systems.[1,7,8] Furthermore, some mutations have been reported to have a concomitant effect in more than one tissue, mostly involving the brain and the heart. Evidence from animal models and human case studies suggests that genetic variants associated with cardiac arrhythmias may contribute to some cases of sudden unexpected death in epilepsy (SUDEP). It has been reported that *KCNH2* mutations can increase the risk of both long QT syndrome (LQT) and epilepsy, and are found more frequently among SUDEP patients.[9–11] Additionally, Tiron *et al*. suggested that a SNV in *KCNQ1* could be causing both LQT syndrome and epilepsy.[12] Haugaa *et al*. reported that 72% of their cohort of patients carrying a LQT-associated mutation displayed electroencephalogram abnormalities.[13] Andersen-Tawil syndrome, also known as LQT7, is a rare channelopathy with a wide variety of symptoms, including episodic muscle weakness, cardiac arrhythmias and dysmorphic features.[14] Additionally, a SNV in the *SCN5A* gene was reported to cause both Brugada Syndrome (BrS) and epilepsy.[15]

In this Thesis, we studied two SNVs affecting the sodium current. One of these mutations was identified in a patient with concomitant brain and heart diseases. The other SNV is related to BrS, a cardiac channelopathy. Although the main focus of this Thesis was on cardiac diseases, brain-associated channelopathies will be briefly explained in the following section. Channelopathies affecting the heart will be further discussed in **section 5.3**.

## 1.1. Neurological channelopathies

Ion channels are fundamental in the neuronal signaling processes, and different types of ion channels have been identified in neuron's membranes. The voltage-gated sodium channels predominantly expressed in brain are Na$_V$1.1, Na$_V$1.2 and Na$_V$1.6 (encoded by the *SCN1A*, *SCN2A* and *SCN8A* genes, respectively). Other identified channels in neurons include potassium channels (voltage-gated and calcium-activated, among others), calcium channels (high- and low-voltage activated) and voltage-gated channels permeable to potassium and sodium ions (*HCN* channels). Other channels located in neuron's cell membrane are ion pumps and ligand-gated channels.[2]

Neurological channelopathies can compromise neurons, thus affecting the generation and spread of the action potential (AP) or suppressing it. The membrane excitability impairment may lead to a diversity of symptoms, including seizures, paralysis, ataxia or extreme pain.[1,2,16] Neurological channelopathies have been described to be caused by mutations in the genes encoding for the previously mentioned ion channels and the sodium channel regulatory β1 subunit (*SCN1B*).[2,17,26,18–25]

The more prevalent channelopathies include several types of epilepsy, neurodevelopmental and psychiatric disorders, and hemiplegic migraine among others.[1,20,21,23,26] Mutations in *SCN1A* have been principally linked to Dravet Syndrome (DS), a severe type of epilepsy, and to generalized epilepsy with febrile seizures plus (GEFS+).[27] These mutations mostly cause a loss of function of the channel, but a few cases present either a gain of function or a mixed modulation.[28–30] A few mutations linked to DS and GEFS+ have been found in *SCN1B*, and have been described to cause a loss of function of the channel with which it was co-transfected.[28,31–35]

## 1.2. Incomplete penetrance and variable expressivity

It is widely accepted that many channelopathies display incomplete penetrance and variable expressivity.[36] The disease penetrance is the probability that individuals that carry the same disease-causing mutation will manifest the phenotypic features of that disorder. On the other hand, variable expressivity is the type and severity of the phenotypic features observed on the genotype-positive individuals who harbor the same mutation. For example, in cardiac channelopathies, this variable expressivity ranges from electrocardiogram (ECG) abnormalities (e.g. ST segment elevation) and arrhythmias (e.g.

syncope, sudden cardiac death (SCD)), to the absence of any abnormality and a lifelong asymptomatic state.[4] Although there's an underlying incomplete penetrance with genetic and phenotypical variability in channelopathies that still remains unknown,[36] the fact that the variability may be observed even among members of the same family[37] suggests that other genetic and environmental factors can influence the phenotype.[38]

### 1.2.1. Genetic factors

Some studies have focused on the co-inheritance of functional mutations, which can influence the phenotype, either by enhancing or repressing the effects of the potentially pathogenic mutation (compound mutations). These mutations can reside on the same or opposite allele of the affected gene, or in a completely different gene, thus acting in the gene transcriptional regulation, its splicing or affecting post-translational modifications composition. Variants in non-coding regions responsible for regulating channelopathy-susceptible genes may also function as genetic modifiers.[4,37]

Since ion channels do not function in isolation, mutations in any interacting protein could modulate the effect of a given mutation.[37] In the study by Gourraud *et al.,* in which they identified three loci associated with BrS susceptibility, it was shown that the cumulative effect on disease susceptibility was large. This demonstrated that the presence of different genetic polymorphisms can influence BrS phenotype.[36] Furthermore, several polymorphisms have been described in the *SCN5A* promoter. For example, Van den Boogaard *et al.* demonstrated that an *SCN10A* haplotype was an enhancer region for *SCN5A*.[39] Additionally, they verified that a variant in this locus alters a transcription factor binding site, which reduces *SCN5A* expression.[40] This haplotype has been linked to a reduced $I_{Na}$ in the presence of a potentially pathogenic mutation.[41]

Fernández-Marmiesse *et al*. proposed that the incomplete penetrance in brain diseases can be explained by the Knudson 2-hit mechanism. This mechanism suggests that an individual can inherit one variant from one progenitor, and a subsequent appearance of a second variant in the same gene or another can have an accumulative effect to the phenotype. Thus, the co-ocurrence of two mutations that are independently innocuous can give rise to a clinical phenotype.[42]

### 1.2.2. Environmental factors

The predominant environmental factor affecting the phenotype is temperature. Higher temperatures have been shown to accentuate premature $Na_V1.5$ inactivation. Thus, febrile states may increase the risk of an arrhythmogenic event, particularly in the pediatric individuals.[43,44] In epilepsies such as DS, the temperature has also been demonstrated to increase the risk of seizures.[45,46] Another environmental factor are medications such as antidepressants, antiarrhythmics and anesthetics. Taking these drugs has been associated with higher risk of ST segment elevation and arrhythmias in those individuals genetically predisposed.[43,47]

The focus of this Thesis are two different SNVs affecting the cardiac- and brain-type sodium currents. Thus, the following chapter summarizes the main characteristics of voltage-gated sodium channels (VGSC), and the properties of the currents that flow through them.

## 2. Voltage-gated sodium channels

Voltage-gated sodium ($Na_V$) channels are ion channels with selective permeability to $Na^+$ ions, allowing them to flow following their electrochemical gradient. $Na_V$ channels have a determinant role in the electrical activity of many cells, as they initiate APs in excitable cells.[48,49] They were first identified in 1952 by Hodgkin and Huxley, in their work studying the electric conductance in axons of giant squids.[50]

In 1980, Beneski and Catterall's biochemical experiments led to the discovery of the sodium channel protein. They identified the principal α subunit and the auxiliary β1 subunit of brain sodium channels (**Figure 1**).[51]

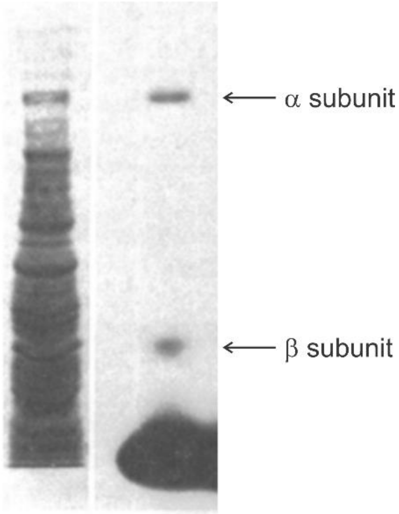

**Figure 1. The first SDS-polyacrylamide gel illustrating α and β1 subunits.** On the left is the molecular weight marker. On the right α and β1 subunits covalently labeled with $^{125}I_1$Sctx in standard binding medium containing 1 µM tetrodoxin. Adapted from Beneski and Catterall.[51]

### 2.1. Genes, molecular structure and function of α subunits

$Na_V$ channels are composed of a single α subunit and one or two β subunits.[52] The principal subunit of $Na_V$ channels is the α, it is large and accounts for all the defining properties of $Na_V$ channels.[53] So far ten genes of about 8000 bp, encoding for different $Na_V$ α subunit subtypes, have been identified.[54] Each of these genes is supposed to have arisen by a gene duplication followed by an evolutionary process to create a new specialized subtype. They are classified as *SCN1A* through *SCN11A*, and encode for the corresponding proteins $Na_V$1.1 through $Na_V$1.9. The resulting proteins contain around 2000 amino acids and have a molecular weight of about 260 kDa.[54] The different subtypes are represented in the dendrogram depicted in **Figure 2**, according to their aminoacid similarity.[53]

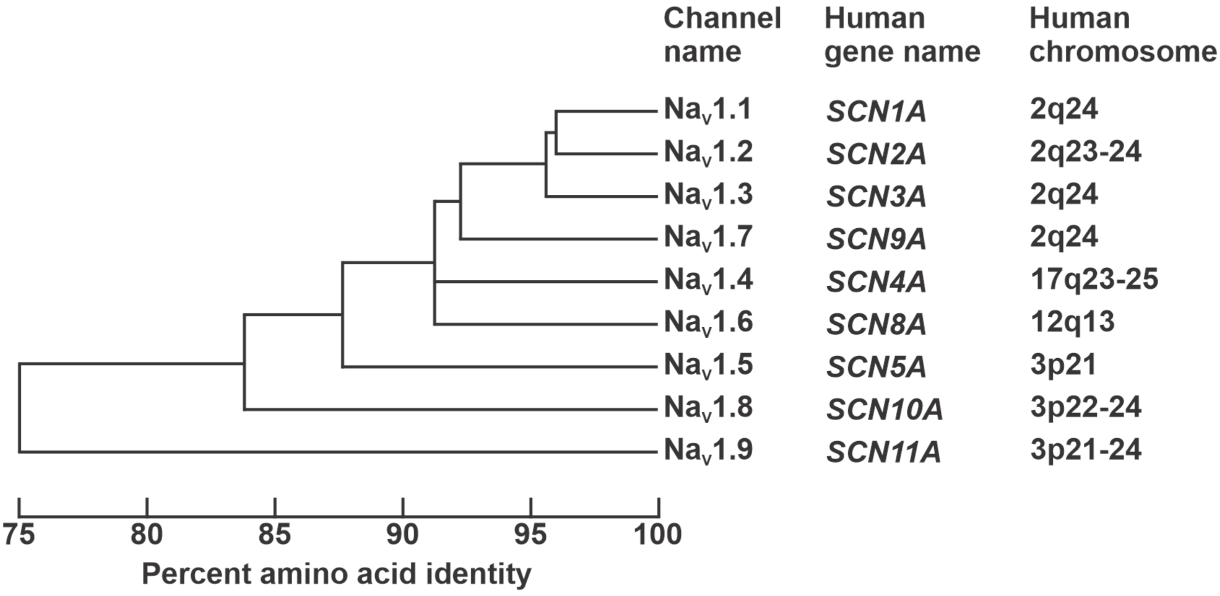

**Figure 2. Dendrogram of Na$_V$ channels family.** Adapted from Hille.[53]

**Figure 3** depicts the α subunit structure. It is organized into four homologous but non-identical domains (denoted I to IV) of 300 to 400 amino acids.[53,54] Each domain consists of six α-helix transmembrane segments (S1 to S6), connected by linker segments.

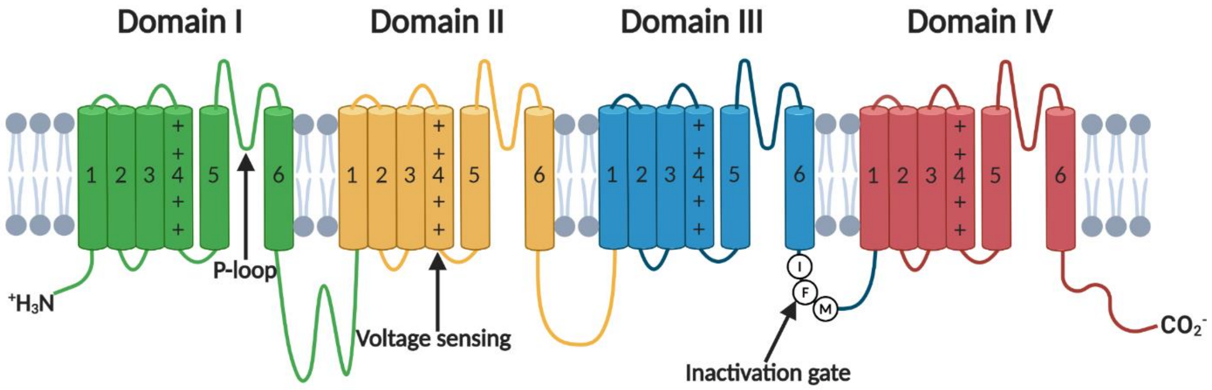

**Figure 3. Topology of the human VGSC α subunit.** Created with BioRender.com.

The S4 segment from each domain form the voltage-sensing domain (VSD), that regulates the channel opening upon depolarization of the membrane and triggers the pore opening. This segment includes four positively charged aminoacids at every third residue, carrying much of the gating charge of the VSD. Upon depolarization, the S4 segments move toward the extracellular surface. Even though S4 is the principal voltage sensor, S1-S3 enable the movement of VSD, allowing its exposure to the two sides of the membrane.[53–55]

The four VSDs fold around a central aqueous ion-conducting pore or pore domain (PD) (**Figure 4**), which is lined by the S5-S6 loop (known as P-loop).[56,57] This loop determines the ion selectivity and conductance properties of $Na_V$ channels.[58]

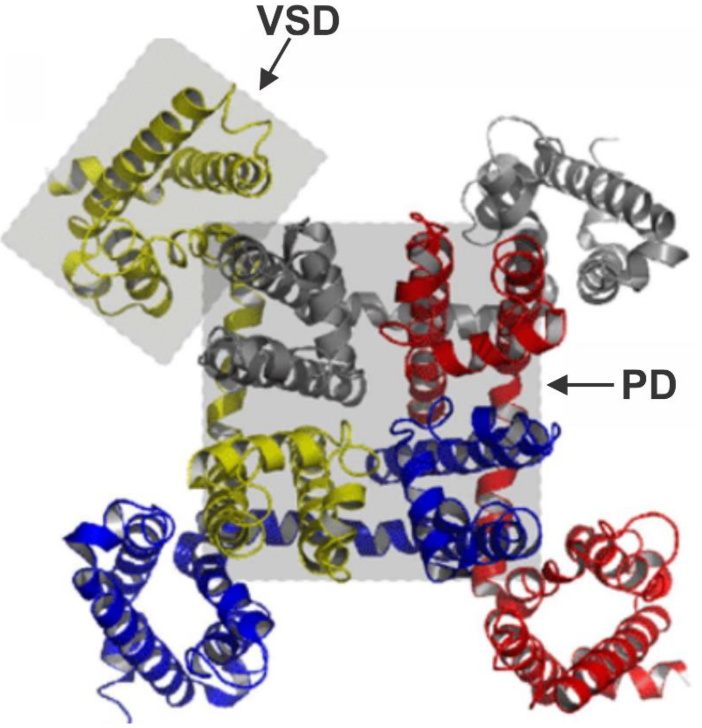

**Figure 4. Top view of a VGSC.** The channel consists of four homologous domains (DI-DIV), colored in yellow, grey, red and blue. The S4 segment of each domain forms the VSD, which folds around the PD. Adapted from Vetter *et al*.[59]

The fast inactivation of the channel is possible thanks to a short and highly conserved intracellular loop that connects domains III and IV, known as the inactivation gate.[55,57] This segment protrudes intracellularly and, upon membrane depolarization, it moves blocking the channel pore.[54]

## 2.2. Genes, molecular structure and function of β subunits

$Na_V$ channels are also composed of β subunits, which are referred to as auxiliary or regulatory.[53] These β subunits are small non-pore-forming proteins of 30 to 40 kDa, members of the immunoglobulin (Ig) superfamily of cell adhesion molecules (CAM).[54] To date, four genes encoding for β subunits have been identified: *SCN1B*, *SCN2B*, *SCN3B* and *SCN4B*. They encode for the proteins β1 and its splice variant β1b, β2, β3 and β4, respectively.[54,60] All five β subunits contain an extracellular Ig domain. With the exception of β1b, β subunits consist of a single polypeptide chain with an extracellular N-terminus domain, a transmembrane segment, and an intracellular C-terminus domain. β1b has an in-frame retention of intron 3, from which it generates an alternate C-terminus sequence that does not include a transmembrane domain (**Figure 5**).[61,62] Thus, β1b is expressed as a soluble molecule.[63] Subunits β1 and β3 associate noncovalently to the α subunit, whereas β2 and β4 bind covalently.[55]

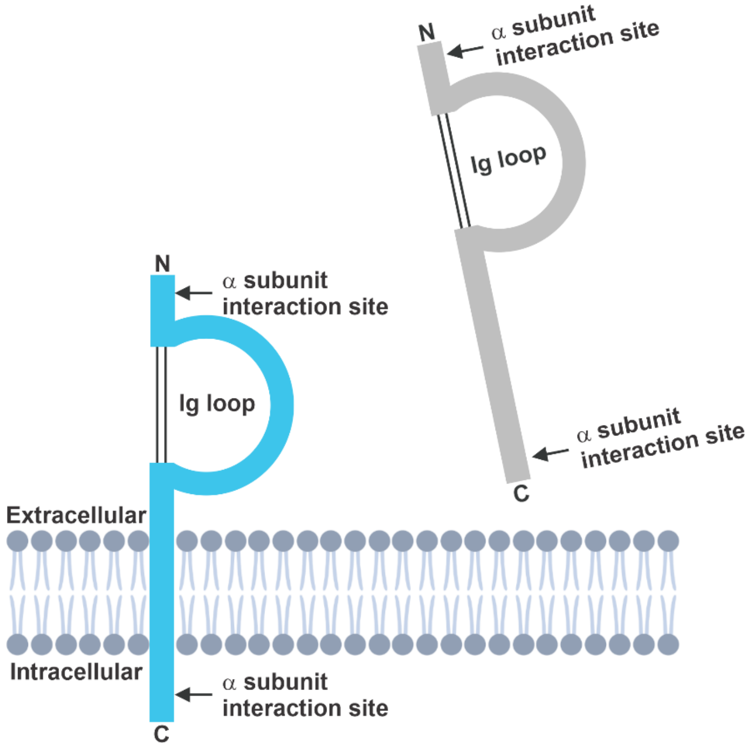

**Figure 5. Schematic representation of β (blue) and β1b (grey) subunits.** Parallel vertical lines correspond to the protein disulfide bonds. Own creation.

Although the α subunit expression is sufficient to reconstitute functional $Na_V$ channels in heterologous expression systems, β subunits modulate their function.[54] Coexpression of the β with the α subunit augments the number of functional channels that reach the plasma membrane, changes gating rate constants and shifts the midpoint of activation and inactivation curves.[53] The most important functions of the β subunits are to stabilize $Na_V$ channels in the cellular membrane, and to coordinate the interactions with other anchoring proteins.[54,64]

## 2.3. Biophysical properties of voltage-gated sodium channels

$Na_V$ channels are expressed in the cell membranes of both excitable and non-excitable cells. $Na_V$ channels can adopt conformational transitions between closed and open states in response to changes in the voltage of the membrane potential detected by the voltage sensor, also known as gating.[49,65] These transitions involve the opening or the closing of the pore, which will either block or allow the flow of ions through it and thus the electrical current.[55] As it will be described in further detail in **chapter 4**, the gating of $Na_V$ channels is the fundamental processes behind electrical phenomena such as the heartbeat.[65]

$Na_V$ channels have three characterizing features:[54,57]

- A voltage-dependent activation.
- A fast inactivation.
- Selective ion channel conductance.

In the 1950's, Hodgkin and Huxley developed a method to study the currents that underlie the changes of voltage across the membrane of the giant squid axon: the voltage clamp.[50] In this technique, the voltage that flows across the cell membrane is controlled as a mean to measure the electrical current that results from the flow of ions through the ion channels.[49,66] Three decades later, after the proposal of the modern membrane model, Hamill *et al*. developed the patch clamp technique. This technique used the principles of the voltage clamp, but allowed the recording of current across a small patch of the membrane as first reported by Neher and Sakmann.[67,68] Hamill *et al.* accomplished the creation of a high resistance seal between glass pipettes and the cell membrane, known as gigaseal.[67] The patch clamp technique has four main configurations that allow to study different channel properties. Among these, the whole-cell recording configuration allows to study of whole cell ion currents that flow through the cellular membrane, by creating access to the intracellular media after rupturing the fraction of membrane sealed to the pipette.[66] This is the most used voltage clamp technique, and is the technique used to study sodium current properties in this Thesis. Further information about cellular current recordings can be found in **Annex section 1.2**.

The work of Hodgkin and Huxley in 1952 using the voltage clamp technique allowed to describe a model to determine ion fluxes and permeability changes of the excitable membranes in terms of molecular mechanisms: the HH model. Their experiments showed that the conductance of the membrane changed gradually with time, with no large jumps. Although their model treats activation and inactivation as independent of each other, some experiments showed that both processes were interdependent.[53,69] Later, single sodium channel analysis demonstrated that the channel could go to the inactivated state from closed states, as well as from the open state.[70,71] These findings prompted the reformulation of the HH model, and lead to a coupled model, which postulated that the transition between closed and open states could be represented as:

$$\text{Closed} \leftrightarrow \text{Open}$$

But, since $Na_V$ channels are not symmetrical, they do not exactly follow this model. Each repeat or domain has its own transition.[53] Bezanilla and Armstrong proposed in 1977 the following diagram model, that incorporates several closed ($C_1$-$C_4$) states, and one open (O) and one inactivated (I) state:[72]

$$C_4 \leftrightarrow C_3 \leftrightarrow C_2 \leftrightarrow C_1 \leftrightarrow O \leftrightarrow I$$

Later, this model had several modifications and, in 1991, Vandenberg and Bezanilla introduced a new model that incorporated the knowledge on single and whole currents together with gating currents. The model incorporates several closed and inactivated states with one open state. As **Figure 6** shows, according to this model the inactivated states could be reached from a closed and/or the open states

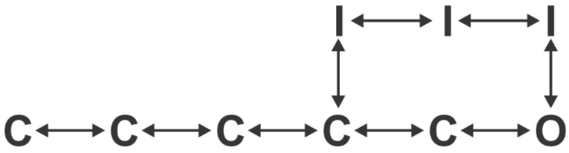

**Figure 6. Diagram model of the sodium channel conformations proposed by Vandenberg and Bezanilla.** Adapted from Bezanilla.[69]

A simple scheme showing the transitions between channel conformations is presented in the following **Figure**:

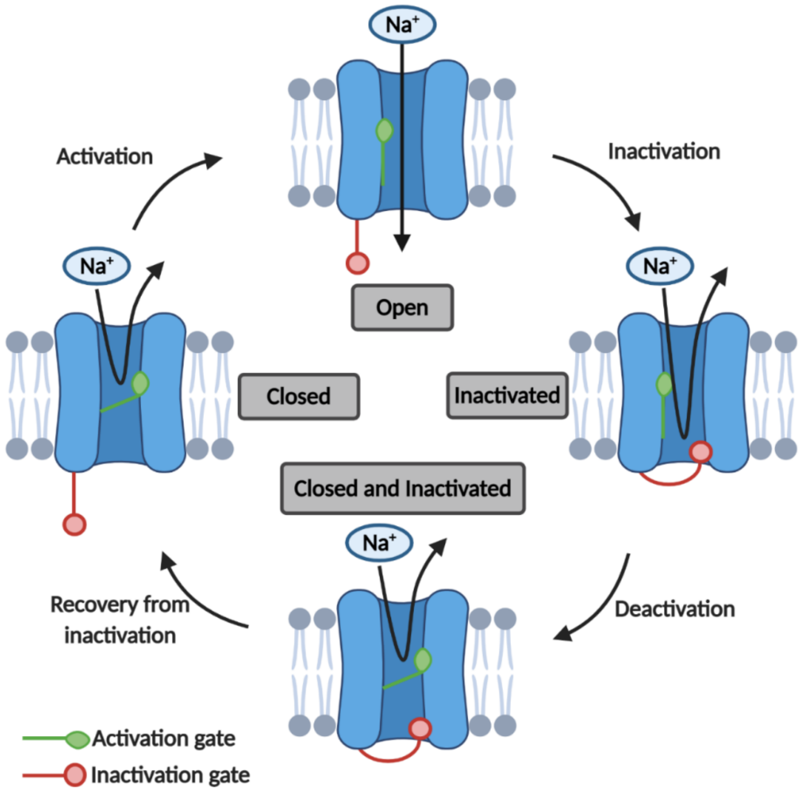

**Figure 7. Conformational transitions of $Na_V$ channels.** Created with BioRender.com.

### 2.3.1. Closed state

The cardiac sodium channel is at a closed state at negative potentials of about -90 mV. In this conformation, the inactivation gate is open but the activation gate is closed, there is no influx of $Na^+$ into the cell and therefore there is no current flow.[66]

Normally, in patch clamp experiments, a holding potential of -120 mV is applied to ensure that the channels are at a closed state and available to be activated.

### 2.3.2. Open state

At depolarizing potentials, both the activation and inactivation gates are open and the channel allows the communication between the intracellular and extracellular compartments. Thus, ions can cross the membrane following their electrochemical gradient. The amount of time that a channel remains open varies depending on the membrane voltage (referenced as open probability), and thus the ion flux will change at different voltages.[65]

Membrane conductance is a useful measure of how many channels are open in a given membrane area. Some channels present rectification, meaning that their conductance changes with voltage. A strong rectification would mean that the ion channels are open at some membrane potentials but closed at others.[53]

### I-V relationship

The current carried by the ions varies with the membrane voltage, and is represented as the current-voltage (I-V) relationship for that ion.[66] **Figure 8A** shows typical current traces, obtained during patch clamp experiments in the whole-cell configuration in response to a series of voltage steps. At negative pulses (-80 mV in red in this example), there is no influx of $I_{Na}$. As the depolarization increases to -40 mV (blue), $Na_V$ channels open and $I_{Na}$ becomes increasingly negative (inward). At -20 mV (green) the open probability of the channel increases and thus $I_{Na}$ is larger. As the potential reaches the sodium equilibrium potential ($E_{Na}$), the driving force for $Na^+$ decreases and thus the $I_{Na}$ decreases also, even when channels are open. At even more positive potentials of 80 mV (black), beyond the reversal potential, $I_{Na}$ is positive (outward). Thus, the I-V shape is given by the effect of the membrane potential on channel open probability and on the driving force.[66] The peak current at each applied voltage can be normalized by the cell capacitance, thus obtaining the $I_{Na}$ density (**Figure 8B**).

### Voltage-dependence of activation

Voltage-dependence of activation is different for each type of channel, and it refers to the response of the charged residues in S4 when the electric field across the membrane is perturbed. The relationship between channel activation and voltage can be determined from the same I-V protocol, which allows the calculation of the channel conductance (g) at each voltage from the modified Ohm's law:

$$g_{Na} = \frac{\text{Peak } I_{Na}}{V - E_{Na}}$$

where V is the membrane potential, peak $I_{Na}$ the maximum current value and $E_{Na}$ the $Na^+$ equilibrium potential. By measuring the current at each voltage, the conductance can be calculated. Then, the ratio $g/g_{max}$ can be plotted as a function of voltage, to obtain the activation curve (**Figure 8E**).

The activation curve can be fitted by a Boltzmann equation of the form:

$$g = \frac{g_{max}}{1 + \exp^{\frac{V_{1/2} - V}{k}}}$$

where $g_{max}$ is maximum conductance, $V_{1/2}$ is the voltage at which half of the activation occurs, and k is the slope factor that determines how steeply the activation curve changes with voltage.

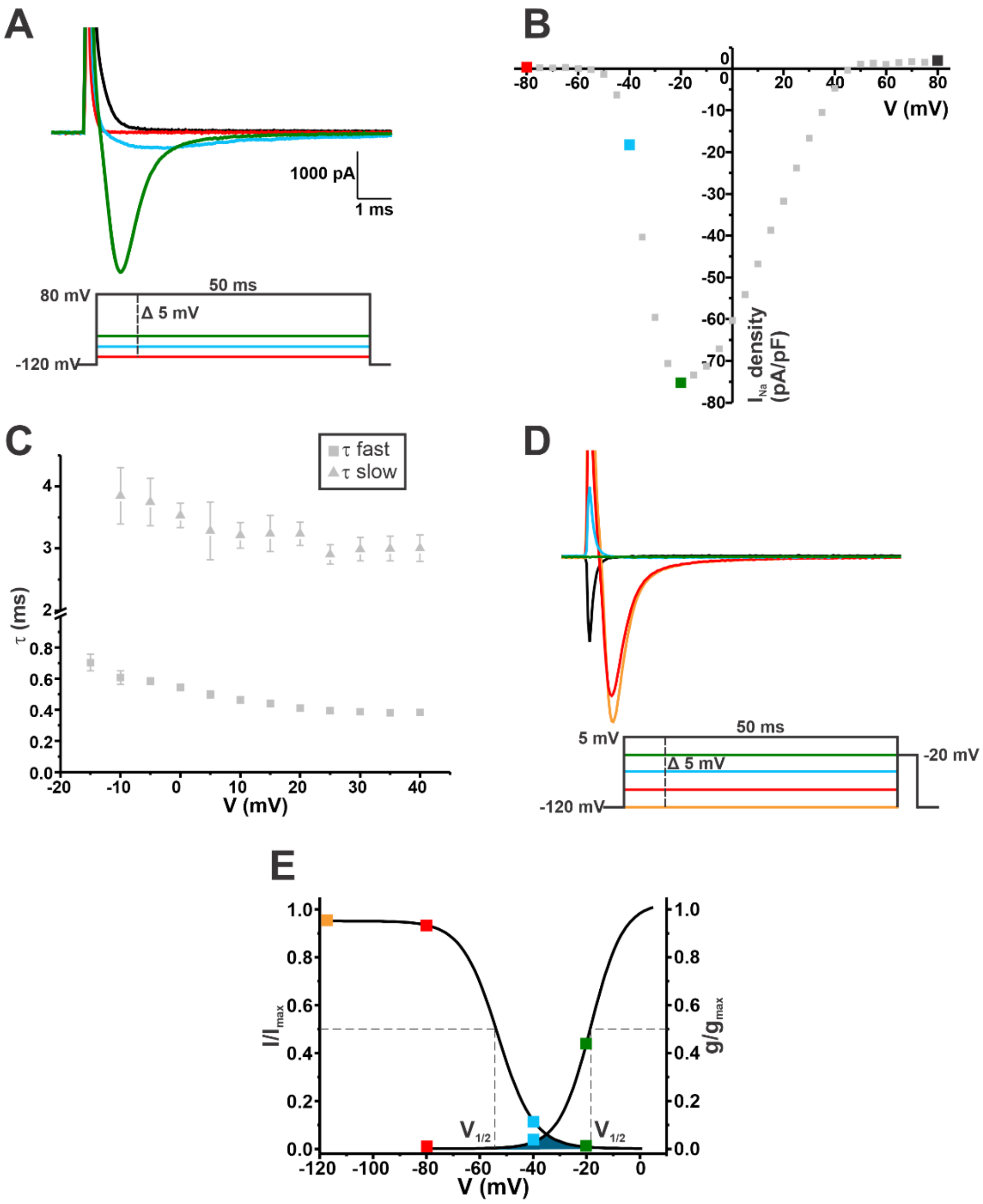

**Figure 8. Study of the biophysical properties of voltage-gated sodium channels using the whole-cell patch clamp technique. (A)** Macroscopic current traces obtained after depolarizing pulses of 50 ms with a 5 mV increment. The red line represents the current obtained at -80 mV, the blue line the current obtained at -40 mV, the green line the current obtained at -20 mV, and the black line the current obtained at 80 mV. **(B)** I-V relationship obtained from protocol A. Colored squares

correspond to the same-colored depolarizing pulses from protocol A. **(C)** Fast inactivation obtained from protocol A. Squares correspond to τ fast, and triangles to τ slow. **(D)** Macroscopic current traces obtained at -20 mV after a prepulse at different depolarizing potentials of 50 ms with a 5 mV increment. The orange line represents the current obtained after a prepulse of -120 mV, red line after a prepulse of -80 mV, blue line after a prepulse of -40 mV, green line after a prepulse of -20 mV and black line after a prepulse of 5 mV. **(E)** Voltage-dependence of activation graph ($g/g_{max}$) obtained from protocol A, and steady-state voltage-dependence of inactivation graph ($I/I_{max}$) obtained from protocol B. Colored squares correspond to the same-colored depolarizing pulses from protocol A and B. Discontinuous lines represent how $V_{1/2}$ is obtained. Dark blue area represents the window current.

### 2.3.3. Inactivated state

The inactivation of the channel starts a few milliseconds after the channel opening as a consequence of a conformational change of the channel upon depolarization. This impairs $Na^+$ conductance although the voltage sensor is in an active conformation. The inactivation gate closes folding into the channel pore, and the channel goes to an inactivated state.[55] The membrane must be repolarized to remove the inactivation.[53,73]

#### Fast inactivation

With the same protocol applied in Figure 8A, the inactivation time constant can be measured. It is the time that takes to the current to reach 63% of the inactivation upon maximum peak amplitude, at different voltages. By adjusting the current while it is inactivating to a double exponential, two time constants can be obtained: fast tau ($\tau_f$) and slow tau ($\tau_s$) (**Figure 8C**).

#### Steady-state voltage-dependence of inactivation

The steady-state voltage-dependence of inactivation represents the fraction of channels that remain open after a depolarizing voltage pulse, in which the current has reached a steady-state of inactivation. **Figure 8D** depicts the protocol used to measure $I_{Na}$ at -20 mV, after a series of depolarizing steps. This allows to obtain the fraction of viable channels that can be activated by a -20 mV pulse ($I/I_{max}$, **Figure 8E**). Following a -120 mV prepulse (orange), the channels are closed but are available to be opened, and thus peak $I_{Na}$ is maximum when a -20 mV pulse is applied. After a -80 mV prepulse (red) is applied, a small fraction of channels has already inactivated, and the peak $I_{Na}$ is smaller at the -20 mV pulse. With a more depolarizing prepulse (-40 mV blue, -20 mV green, and 5 mV black), peak $I_{Na}$ after the -20 mV pulse is very small or zero, as most or all the channels have already inactivated.

The steady-state inactivation data can also be fit to a Boltzmann equation of the form:

$$I = \frac{I_{max}}{1 + \exp\frac{V - V_{1/2}}{k}}$$

where I is peak current amplitude and $I_{max}$ is maximum current amplitude, $V_{1/2}$ is the voltage at which half of the inactivation occurs, and k is the slope factor that determines how steeply the inactivation curve changes with voltage.

### Window current

The window current (**Figure 8E**, painted in dark blue) is determined by the crossover of the voltage-dependence of activation and steady-state inactivation curves, which govern the opening of the sodium channel. In this area, there is a population of channels that are inactivated, but also a fraction of channels that have not inactivated and are in the closed state. Thus, there is a probability that any non-inactivated channel may open spontaneously at these voltages. The current that these few open channels carry defines the window current.

## 2.3.4. Closed-Inactivated state

Upon membrane repolarization, the gating charged residues of each S4 return to their resting positions closing the activation gate.[73] This causes the current deactivation and channels enter in the closed-inactivated state.

### Recovery from inactivation

After the current has deactivated, the channels require a certain time to recover and to do the transition to the closed conformation, and thus be available to open again. This lapse of time is known as recovery from inactivation. It can be measured with a two-pulse protocol (**Figure 9 left**). Between both pulses, a resting potential of -120 mV is applied for different duration times (1-40 ms). **Figure 9** shows that the recovery increases exponentially in a few milliseconds when the interpulse interval is increased. Plotting the current obtained at -20 mV (P2) normalized by the maximum current obtained at the first pulse (P1), allows to measure the recovery from inactivation time constant (τ) when data is adjusted to a mono- or biexponential function (**Figure 9 right**):

$$f(t) = 1 - e^{\frac{t}{\tau}}$$

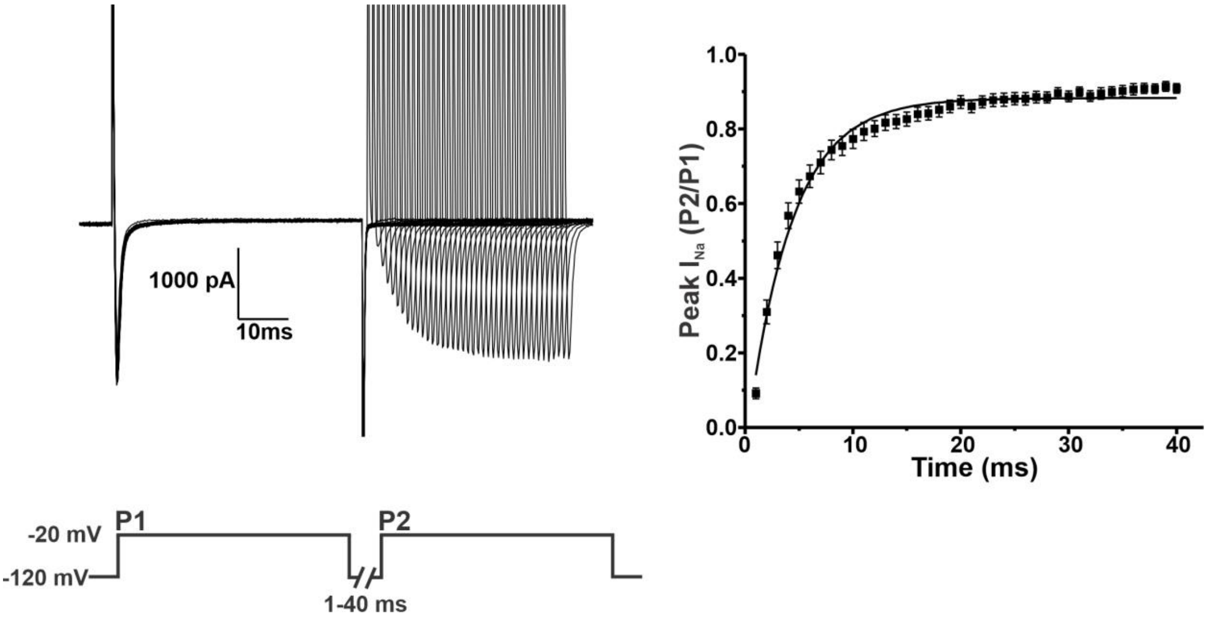

**Figure 9. Voltage protocols used to study the recovery from inactivation of voltage-gated sodium channels using the whole-cell patch clamp technique. Left:** Macroscopic currents obtained after a two-pulse protocol. **Right:** Graph plotting the P2/P1 quotient at each interpulse duration time, adjusted to a monoexponential function.

All the explained properties in this section may be changed by the appearance of a mutation in the VGSC or their regulatory subunits. Thus, this could contribute to an abnormal electrical behavior of the cells.

## 3. Experimental cellular models for the study of mutations affecting voltage-gated sodium channels

Numerous studies have been performed to understand the mechanisms underlying different channelopathies. Due to methodological and ethical limitations, these studies have been done in animal and cellular models. Murine models are commonly used to study several channelopathies, including cardiac and neuronal arrhythmias.[74–76] Other models such as porcine and canine, are used to study cardiac channelopathies.[77–81] Zebrafish and fruit fly animal models have been used in the study of neuronal channelopathies.[76,82,83]

In addition to the animal models, cellular models are also widely used. These models include heterologous expression systems and tissue-specific cells derived from induced pluripotent stem cells (iPSc). Since the experiments performed in this Thesis involve both cellular models, they will be explained in detail.

### 3.1. Heterologous expression systems

Vectors carrying mutations identified in voltage-gated sodium channels are usually transfected into heterologous expression systems (**Figure 10**). Cell types used in this approach include human embryonic kidney (HEK) cells, Chinese hamster ovary (CHO) cells and *Xenopus laevis* oocytes.[76,77,82,84] The current expressed in these cells is studied in patch clamp experiments. Indeed, this strategy has been widely used to study the effect of SNVs in genes associated to arrhythmogenic diseases.[28,29,93,85–92] This type of studies has provided a detailed analysis of the wild type and mutant channel's biophysical properties, and have contributed to increase our understanding of the molecular mechanisms underlying several channelopathies.

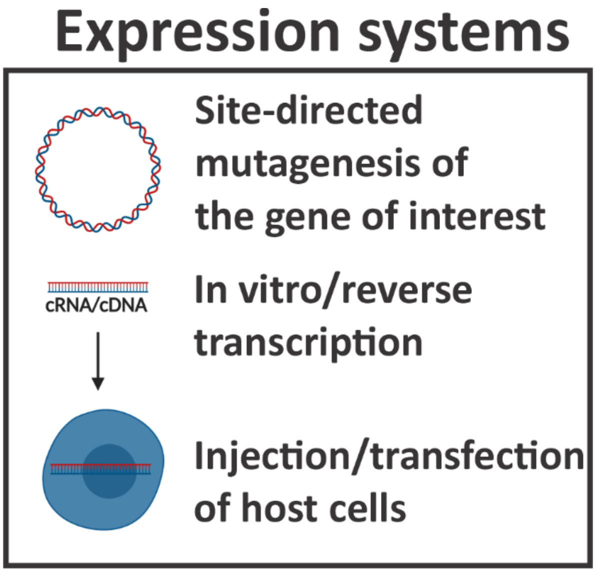

**Figure 10. Schematic representation of the heterologous expression system model.** Modified from Sendfeld et al.[77] using BioRender.com.

The principal advantages of using heterologous expression systems are that they are inexpensive, easy to maintain and to manipulate. Nevertheless, this model lacks the specific genetic background of the patient, and thus does not give insight into the incomplete penetrance that some arrhythmogenic diseases display. Furthermore, heterologous expression systems do not display the native environment of the cell types affected by the mutation, such as cardiomyocytes or neurons. To overcome these disadvantages, other model systems had to be applied to the study of mutations affecting voltage-gated sodium channels.

### 3.2. Tissue-specific cells derived from induced pluripotent stem cells (iPSc)

Since 1958, several approaches of cellular reprogramming have been attempted. The somatic cell nuclear transfer (SCNT) was the first method used, in which the nucleus of a somatic cell is transferred to an enucleated egg.[94,95] In the following years, the embryonic stem (ES) cells were discovered. These cell lines had a developmental capacity to generate all cell types, known as pluripotency.[96,97] Some studies also reported that somatic cells such as fibroblasts and T lymphocytes could be epigenetically reprogrammed by cell fusion with ES cells. The resulting reprogrammed cells expressed pluripotency-associated genes including Oct3/4.[98,99] This suggested the existence of reprogramming factors that could modify the memory of somatic cells.

All these works led Takahashi and Yamanaka to the generation, in 2006, of induced pluripotent stem cells (iPSc) from mouse embryos and adult fibroblasts, using four transcription factors (Oct3/4, Sox2, Klf4 and c-Myc).[100] These iPSc were derived from somatic cells and shared a functional resemblance to ES cells. Soon after, the same group reported the obtention of iPSc from human somatic cells using the same four transcription factors.[109] Posterior studies showed that it was feasible to obtain human iPSc by using different sets of transcription factors.[110]

iPSc hold the property of pluripotency, and they are capable to differentiate into all somatic cell types. Cells carrying a specific genetic profile can be obtained from patients and be reprogrammed into iPSc. Furthermore, these iPSc can then be differentiated to a specific cell type to mimic characteristic features of a disease. Thus, this approach allows the study of mutant proteins in their native environment.
Therefore, iPSc have become a valuable model to overcome several limitations present in the previously explained model. To date, iPSc suppose a promising approach for drug discovery, disease modelling and regenerative medicine, due to their capacity to differentiate in any type of cell, including neurons and cardiomyocytes (**Figure 11**).

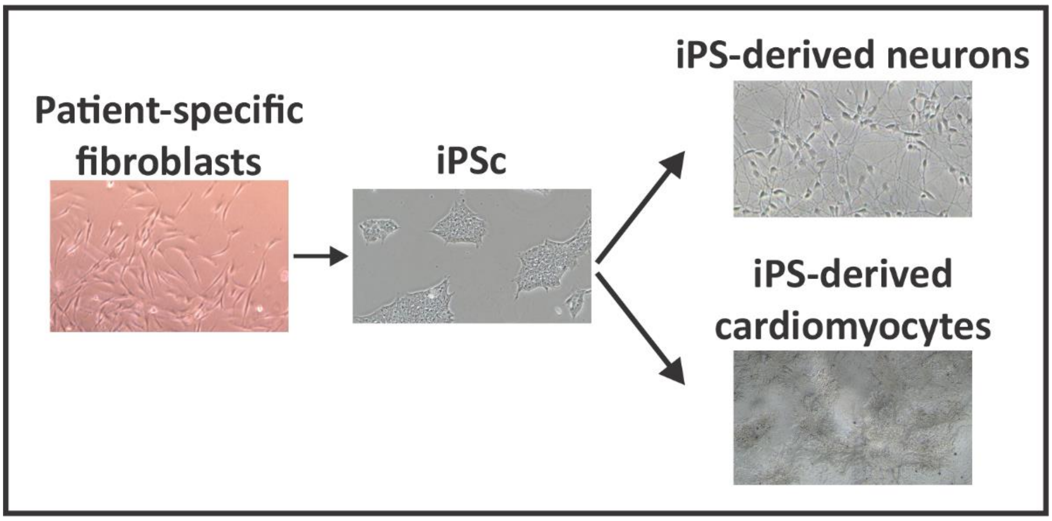

**Figure 11. Representation of the iPS-derived neurons and cardiomyocytes models.** The iPS-derived neurons image is adapted from https://www.appliedstemcell.com/.

### 3.2.1. iPSc-derived neurons

To study the cellular mechanisms of several neurological disorders, patient-specific iPSc-derived neurons have emerged as a valuable cell model. Multiple protocols have been developed to obtain patient-specific iPSc neurons, including spinal cord motor neurons, dopaminergic neurons and neural crest cells among others.[103–109] These protocols are based in two different approaches. The first one is based in a timed and controlled application of exogenous mitogens and morphogens in culture. The second method used relies in using transcription factors.[110]

iPSc-derived neurons have been used in the studies of sodium current-related genetic epilepsies, characterized by seizures and abnormal electroencephalograms.[111,112] The type of epilepsy most extensively studied using iPSc is DS, caused by mutations in the *SCN1A* gene.[113–115] Other studied epilepsies include febrile seizures caused by mutations in either *SCN1A* or *SCN8A*,[116,117] or developmental and epilepsy encephalopathies linked to mutations in *SCN1B*.[118]

### 3.2.2. iPSc-derived cardiomyocytes (iPS-CM)

In the last years, several protocols for ES cells and iPSc differentiation into cardiomyocytes have been established. One of the first protocols that were developed, was focused in the formation of embryoid bodies. The differentiation in this protocol was achieved by suspending a small number of ES cells within hanging droplets, mirroring the embryonic cell growth conditions. The principal disadvantage of this protocol, was that the cardiomyocyte generation was low (<5%) and with a significant variability.[119]

Other differentiation protocols focused on using specific growth factors to recapitulate the temporal changes that occur in embryonic cardiogenesis. Although these protocols yielded more than 70% cardiomyocytes, they relied on the use of expensive recombinant proteins and required several steps of cell dissociation and passages.[120–122]

More recently, differentiation protocols focused on precise temporal modulation of the canonical Wnt pathway. Early activation of this pathway through the molecule CHIR-99021 followed by its inhibition through Wnt-C59 led to a population of cardiomyocytes with >90% purity. The great advantage of these protocols in comparison to previous ones, was that a monolayer culture was obtained with the use of affordable small molecules.[123–125]

One of the main advantages in the iPS-CM cell model, is that patient-specific iPS-CMs carry the patient's genetic background. Also, these cells reproduce a cardiomyocyte-like environment. Additionally, this cell model offers the possibility of drug toxicity screening, testing their toxic effects on cardiomyocytes before going into clinical trials.[77]
Patient-specific iPS-CM have been used in the study of channelopathies linked to sodium current mutations. Gain of function mutations in *SCN5A* have been linked to LQT3,[126] and several studies have elucidated the effect of mutations in this gene using iPS-CM as a cell model.[127–130] Furthermore, this cell model has allowed to study an *SCN5A* mutation related to an overlap syndrome of both LQT3 and BrS.[131] The majority of studies of *SCN5A* mutations are related to BrS, and will be further discussed in **section 6.2**.

Nevertheless, the main disadvantage is that iPS-CM cultures present cardiac cell type heterogeneity and an immature phenotype compared to adult cardiomyocytes. Indeed, their gene expression profile is more similar to fetal cardiomyocytes.[77,132] They display spontaneous beating, their membrane potential is more depolarized than adult cardiomyocytes, and they present a poor ultrastructural organization.[77] Yang *et al.* summarized the differences observed between iPS-CM and adult cardiomyocytes.[133]

To increase cardiomyocyte purity and exclude or reduce non-cardiomyocytes within the cellular population, a glucose-free lactate-dependent survival metabolic selection has been approached.[134–136] Several efforts to promote iPS-CM maturation have been made, including prolonged culture duration, electrical stimulation, mechanical stretch, adrenergic and thyroid hormone stimulation, forced overexpression of microRNAs expressed in adult cardiomyocytes, and vascularized 3D engineered cardiac tissues. The review published by Liang *et al*. summarizes all these aproaches.[126]

## 4. Electrical heart activity

The electrical activity of the heart is initiated by an electrical impulse in the sinoatrial node (SAN), located in the right atrium (**Figure 12**). This impulse is generated by the spontaneous excitation of the pacemaker cells, which have intrinsic automatic activity to generate cardiac APs.[137] The electrical impulse originated in the SAN travels through intercellular gap junctions and depolarizes the adjacent atrial cells, causing the atria excitation and contraction. The wave is propagated through the atrioventricular node (AVN), the His bundle and the Purkinje fibers to the ventricles. The ventricular myocytes are depolarized, resulting in the ventricular excitation and contraction. The whole process leads to the beat of the heart.[3,138,139]

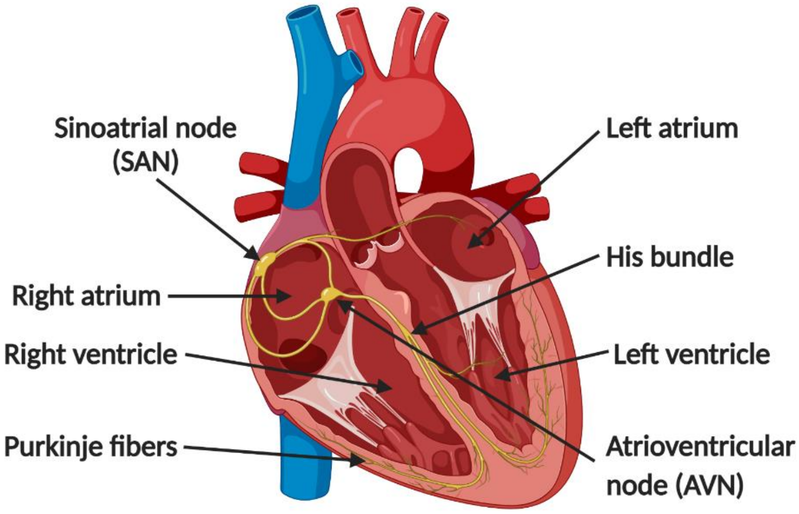

**Figure 12. Schematic representation of the human heart.** Created with BioRender.com.

### 4.1. Cardiac action potential (AP)

The cardiac AP is defined as the coordinated changes that take place in the cardiomyocytes membrane potential ($V_m$). It is triggered by the electrical interaction of the ion channels, transmembranal voltage-gated channels that allow the passive flow of ions following the electrochemical gradient.[1,139] The ion channels are composed by pore-forming α subunits (**Figure 13**), which are ion-selective mainly for sodium ($Na^+$), calcium ($Ca^{2+}$) or potassium ($K^+$), and regulatory β subunits. In normal physiological conditions, both $Na^+$ and $Ca^{2+}$ ions flow inside the cell (inward or depolarizing current), and the $K^+$ ions outside the cell (outward or repolarizing current) through the channels.[38,139] In excitable cells, such as neurons and cardiomyocytes, the electrical current is due to the electrochemical gradient that exists across the surface membrane of each cell, and the transmembranal voltage-gated ion channels.[139]

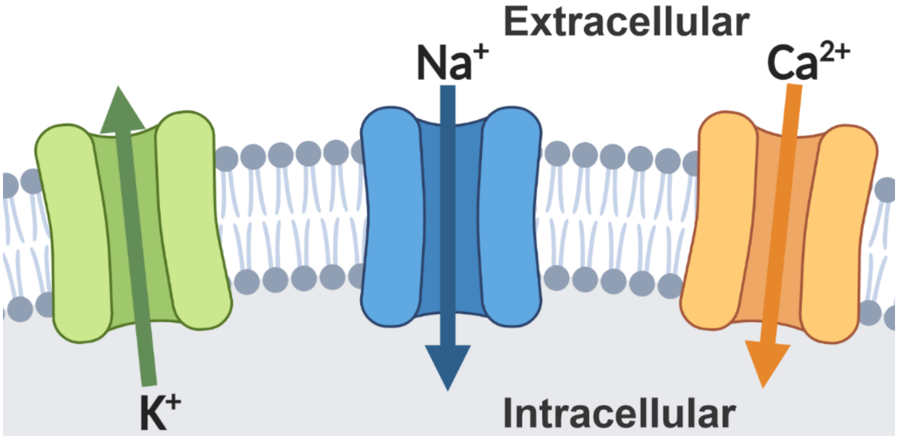

**Figure 13. The key ion channels in cardiac cells.** The outward current carried by the $K^+$ channel (colored in green) repolarizes the cell membrane. The inward current carried by $Na^+$ channels and $Ca^{2+}$ channels (colored in blue and in orange, respectively) depolarizes the cell membrane. Created with BioRender.com.

The ventricular AP is divided in 5 phases, numbered 0-4 (**Figure 14, right**). Here are summarized the main events that drive the AP:[3,138–140]

- **Phase 0 or Depolarization (Initial upstroke):** In a resting heart, the cardiomyocyte's membrane is permeable to $K^+$ ions through the inward rectifier $K^+$ channel ($I_{K1}$ current). The $V_m$ inside the cell is approximately 85 millivolts (mV) more negative with respect to the outside. During cardiac excitation, the membrane becomes permeable to $Na^+$ ions due to the rapid opening or activation of the voltage-gated $Na^+$ channels ($Na_V$). These ions flow into the cardiomyocytes, generating the $Na^+$ current ($I_{Na}$), and reverting the $V_m$ to more positive values of approximately +40 mV: this process is called depolarization and starts the AP.
- **Phase 1 or Partial membrane repolarization (Notch):** The inactivation of the $Na_V$ channels a few milliseconds after the start of the AP and the activation of the transient outward $K^+$ current ($I_{to}$) in response to the depolarization causes a small repolarization, and the $V_m$ is subtly reverted to more negative potentials.
- **Phase 2 or Plateau:** In this phase there's a gradual activation of different voltage-gated $K^+$ channels. The $K^+$ ions exit the cell and produce the outward rectifier current $I_K$, starting the repolarization of the membrane. In ventricular cardiomyocytes, $I_K$ is

formed by the rapid ($I_{Kr}$) and slow ($I_{Ks}$) components. At this point the membrane potential is returning to its basal state, but since there's still an inward current through L-type voltage-gated $Ca^{2+}$ channels ($I_{CaL}$), the change of $V_m$ is subtle.

- **Phase 3 or Repolarization:** In this phase, the voltage-gated $Ca^{2+}$ channels are inactivated. The complete membrane repolarization starts with the sum of $I_{Kr}$ and $I_{Ks}$, which is completed by the delayed rectifier and the rectifier currents ($I_{Kp}$ and $I_{K1}$, respectively).
- **Phase 4 or Resting:** As the final phase, the $V_m$ returns to its baseline of approximately -85 mV. This potential stability is given by the inward rectifier current $I_{K1}$.

The cardiac AP shape is different among cell types present in every heart region. This is a consequence of the differences in expression and biophysical properties of the ion channels in every region. Figure shows characteristic APs for SAN, atrial and ventricular cells, including which channels underlie each phase of the AP. Of note, in atrial cardiomyocytes the ultra-rapidly rectifier $K^+$ current ($I_{Kur}$) is expressed, and thus the repolarization is faster than in ventricular cardiomyocytes. In SAN and AVN cells, the rectifier current $I_{K1}$ is not expressed and this enables a slow depolarization in phase 4 of the AP mediated by the hyperpolarization-activated cyclic nucleotide-gated channels, called funny current ($I_f$).[3] **Figure 14 left and middle** shows the AP of the SAN and atrium.

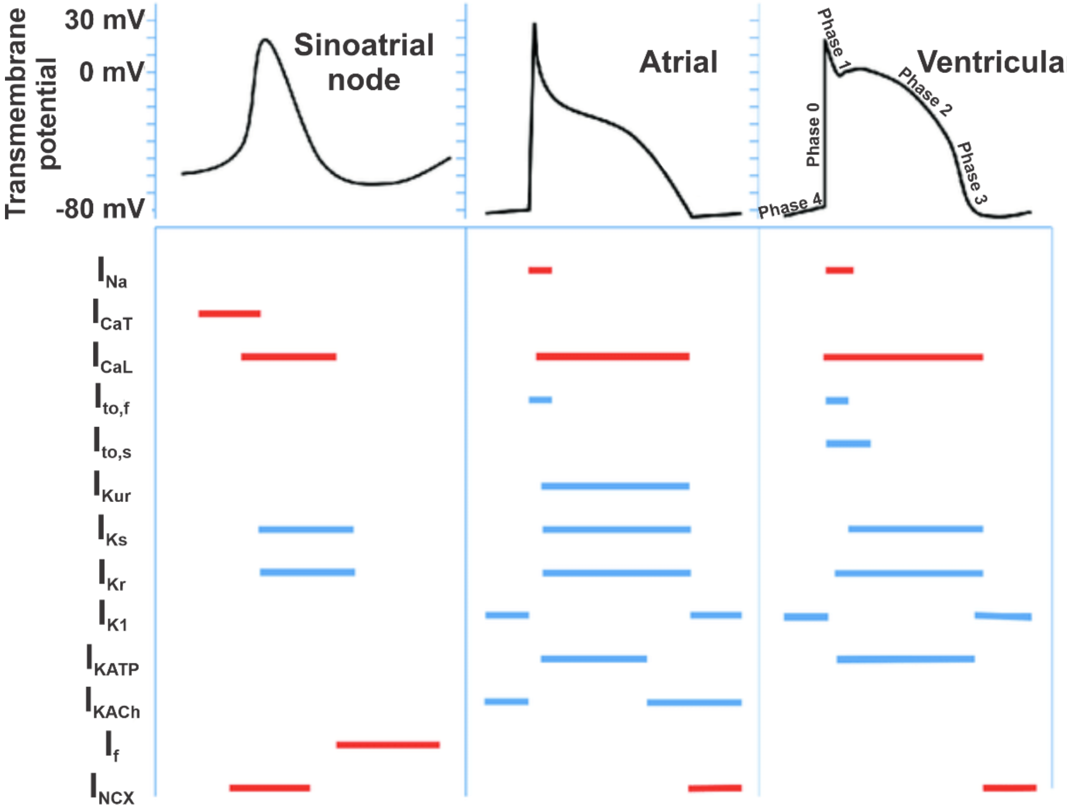

**Figure 14. Schematic representation of cardiac APs. Top:** SAN (left), atrial (middle) and ventricular (right) AP waveforms. **Bottom:** Representation of inward (red lines) and outward (blue lines) currents that contribute to the AP formation. Adapted from Lane et al.[141]

### Excitation-contraction (E-C) coupling

The AP triggers the cardiomyocyte contraction. In phase 2 of the AP, $Ca^{2+}$ ions enter the cell through the L-type voltage-gated $Ca^{2+}$ channels, which triggers the activation of the ryanodine receptor located in the sarcoplasmic reticulum (SR). This allows the release of $Ca^{2+}$ ions to the cytosol, which activates the cellular contractile machinery. The whole process is known as the excitation-contraction (E-C) coupling. For cardiac relaxation, the cytosolic $Ca^{2+}$ concentration must decline. This is achieved through the $Na^+/Ca^{2+}$ exchanger, which is activated by the increase of the cytosolic $Ca^{2+}$ and allows the entry to the cell of 3 $Na^+$ ions for every released $Ca^{2+}$ ion generating a net inward current.[3,139] The SR calcium transport ATPase (SERCA) pump reloads $Ca^{2+}$ from the cytoplasm into the SR. This contributes to muscle relaxation by lowering the cytosolic $Ca^{2+}$, and refills the SR with $Ca^{2+}$ ions that will be released in the next heartbeat.[142]

## 4.2. Electrocardiogram (ECG)

The ECG represents the sum of the electrical activity at any given time generated by the cardiomyocytes in the different heart regions (**Figure 15A**). The ECG can be recorded through 10 electrodes placed in the body: 4 limb electrodes and 6 precordial electrodes around the chest. The electrodes are used to make 12 angles or leads, and each lead shows the electrical heart activity from a different location.[139]

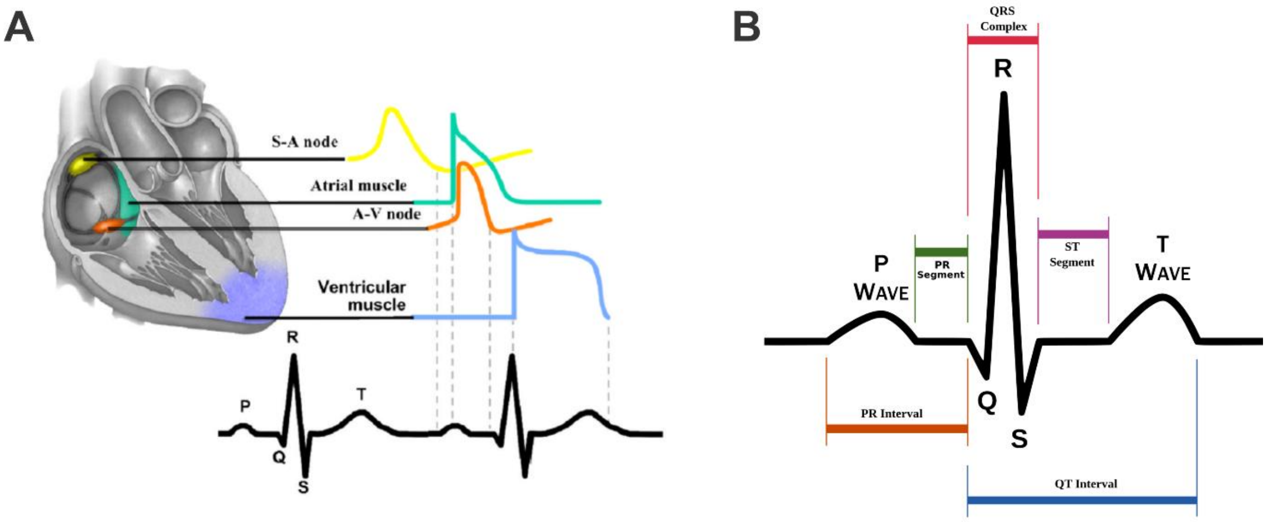

**Figure 15. ECG representation. (A)** Schematic representation of the cardiac conduction system and the correlation between the action potentials of cardiomyocytes in the areas of the heart (SAN in yellow, atrium in green, AVN in orange and ventricles in blue) and the surface electrocardiogram. Adapted from Giudicessi et al.[4] **(B)** Schematic diagram of the intervals, waves, segments and complexes that conform the ECG. Extracted from https://a-fib.com/.

The ECG can be described by means of waves and segments (**Figure 15B**). The P wave in the ECG results from the atria depolarization, and is followed by a flat line (PR segment, green) when the electrical impulse is conducted to the ventricles. The QRS complex (red) represents the ventricular depolarization (phase 0 of the previously explained ventricular AP). Since atria repolarization is faster than ventricular repolarization, it is masked in the ECG by the ventricular depolarization. The ventricular repolarization (phase 1, 2 and 3 of the ventricular AP) corresponds to the T wave. Finally, the basal line is the ventricular resting (phase 4) where the resting membrane potential recovery happens.[139]

The duration between the QRS complex and the T wave is used to calculate the ventricular depolarization-repolarization duration, also named as the QT interval (blue). The ST segment (purple) connects the QRS complex and the T wave and corresponds to the period when the ventricles are depolarized.[139]

The ECG is a useful tool to detect cardiac abnormalities such as blocked arteries, heart damage, heart failure, heart attack and arrhythmias. Alterations in the QT interval have been associated with LQT and short QT (SQT) syndromes, and alterations in the ST segment to BrS.[4]

## 5. Sudden cardiac death (SCD)

The World Health Organization defines sudden cardiac death (SCD) as a sudden unexpected natural death from a cardiovascular cause, in a patient with or without a previously diagnosed cardiovascular disease, that occurs within one hour of symptoms onset when witnessed. If unwitnessed, it is considered a SCD when the individual was observed to be alive within the previous 24 hours. A sudden cardiac arrest occurs when the heart stops beating, or is not beating sufficiently to maintain perfusion and life, and can lead to SCD.[143]

SCD is a leading cause of mortality, responsible for 50-60% of all deaths worldwide from cardiovascular diseases.[143–145] Furthermore, it accounts for up to 15-20% of all natural deaths in Western societies[146], being its incidence lower in Asian individuals.[147]

SCD results from two factors: an underlying substrate and a transient event. The substrate is a cardiac condition, and the transient event can be any external factor that induces electrical instability in the heart (for example, increasing sympathetic activity).[6,148–150] In the past decades, substantial progress has been made in SCD prevention and multiple clinical and genetic risk factors that compromise the heart have been identified.[143]

### 5.1. SCD risk factors

Family history of SCD may represent a risk factor.[151] It has been found that the SCD risk is two-fold higher if an individual had one parent who died suddenly, and nine-fold if both parents did. This supports the idea that heritable factors play an important role in determining SCD risk.[143]

Among the clinical risk factors, hypertension, diabetes, smoking and obesity are associated with SCD in both men and women.[143,147] Other clinical comorbidities can be atrial fibrillation (AF), chronic kidney disease and obstructive sleep apnoea.[144] Depression, anxiety and psychosis are mental illnesses that have been linked to SCD, as well as lifestyle factors such as dietary patterns, emotional stress and air pollution.[147] Gender also plays a fundamental role, being the risk in men three- to four-fold higher compared to women, as well as age.[143,152]

### 5.2. SCD cases

The majority of SCD cases occur in adults older than 35 years, and its incidence increases with age.[153] However, in individuals under 35 years of age, the highest incidence of SCD is in the age group of 0-5 years.[147] SCD in infants younger than 1 year old represent 90% of the cases. The principal cause is the sudden infant death syndrome (SIDS). It is defined as the death of a child younger than 1 year for unknown causes after performing an autopsy and revising the clinical history of both the child and the family.[154] It is considered a multifactorial death. Among these factors are included: child vulnerability (premature or infections), environmental and genetic risk factors and biochemical anomalies. Between 10-20% of the SIDS cases are associated to variants in genes related to channelopathies.[154,155] In infants older than 1 year and in young teenagers, the main substrates of SCD are cardiomyopathies and channelopathies. [156,157]

The major cause of SCD in the adult population is coronary heart disease, which represents 75% of the SCD cases.[149,150] The remaining 25% of the SCD cases in the adults are caused by cardiomyopathies and cardiac channelopathies. Cardiomyopathies are more frequent, and are characterized by anomalies in the heart structure. The principal cardiomyopathies are hypertrophic cardiomyopathy, dilated cardiomyopathy and arrhythmogenic right ventricular cardiomyopathy. Given that these diseases, as well as CHD, are characterized by heart abnormalities, the SCD cause can be explained when an autopsy is performed. These heart abnormalities can be caused by mutations in genes encoding for structural proteins or by clinical factors such as metabolism diseases, pregnancy complications, alcohol and drugs abuse and infections among others.[150] When no alterations in heart structure are identified, a cardiac channelopathy is suspected.

### 5.3. Cardiac channelopathies

Cardiac channelopathies can be defined as electrical diseases in an apparently healthy heart caused by variants in genes that encode for ion channels or other modulatory proteins, as previously described. The principal cardiac channelopathies are BrS, LQT and SQT syndromes, and catecholaminergic polymorphic ventricular tachycardia (CPVT).

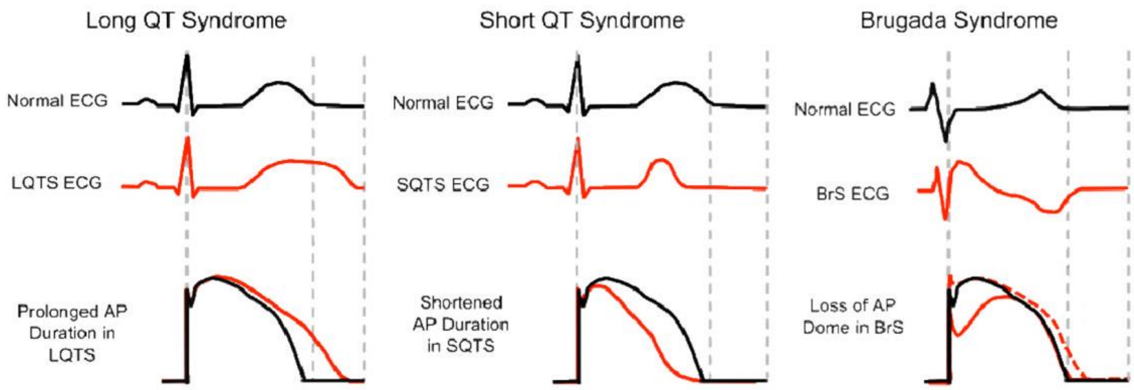

**Figure 16. Electrocardiogram in health and disease.** The upper trace is the schematic representation of a healthy ECG (black) and of LQT, SQT and BrS Type 1 patients (red). The lower, the schematic representation of healthy (black) and diseased (red) ventricular AP. Adapted from Giudicessi *et al*.[4]

Since the electrical activity of the cells in the different heart regions are perfectly synched, any abnormality in the AP of any of the regions could cause an arrhythmia.[139] These abnormalities, that can be due to alterations in the expression levels or biophysical properties of the ion channels, can disrupt the ion currents balance, which is essential for a normal AP.[3,38] These disturbances can lead to an heterogeneity in the AP amplitude and time course and/or coupling between cardiomyocytes of the different heart regions, causing an abnormal cardiac rhythm or arrhythmia that favors SCD (**Figure 16**).[1,3,38] Thus, ion channels have to be finely orchestrated for a correct heart function.[38]

As previously mentioned, one of the main causes of channelopathies are mutations in ion channels or their regulatory proteins. However, the sole identification of a mutation does not suffice for the diagnosis of a channelopathy, neither it provides a conclusive prediction of pathogenicity. Information gathered through genetic analyses, as well as the ECG and clinical information of the patient need to be integrated in order to predict the pathogenicity of the mutation. Genetic analyses are particularly useful on giving support to the clinical diagnosis, defining a treatment and identifying mutation carriers at risk of suffering SCD.[6,158,159] Hundreds of mutations associated to cardiac diseases affecting $Na^+$, $K^+$ and $Ca^{2+}$ ion currents have been identified. These mutations affect either the generation and propagation of the AP or the calcium homeostasis.[38]

### 5.3.1. Diseases associated with sodium channel dysfunction

$Na^+$ channel dysfunction is linked to several inherited arrhythmia syndromes. These are caused by mutations in *SCN5A*, the gene that encodes for the α subunit of the cardiac sodium channel, or by mutations in the β subunits or other sodium channel modulatory proteins.[160] These mutations can cause either a loss of function, where channel conductance is diminished or abolished, or a gain of function, with an enhanced channel conductance.

An example of these inherited syndromes linked to $Na^+$ channel dysfunction is BrS, where $I_{Na}$ is reduced mainly by loss of function mutations in the *SCN5A* gene or its regulatory subunits.[3,4] This may lead to ventricular fibrillation (VF) and SCD in the young population.[38] Since it is the main identified disease I have worked on in this Thesis, BrS will be further explained in **Chapter 6**.

$I_{Na}$ reduction is not only involved with BrS, but also with acquired diseases such as AF. This is the most prevalent arrhythmia in elderly patients, caused by both loss and gain of function mutations in the *SCN5A* gene.[161] Other gain of function mutations can cause LQT3.[3]

### 5.3.2. Diseases associated with potassium channel dysfunction

Loss of function mutations on six different $K^+$ channel-encoding genes are associated to 50-60% of the LQTS cases.[4,38] Mutations in *KCNQ1*, the gene encoding for the α subunit of the channel responsible for $I_{Ks}$, can cause LQT1.[3] Gain of function mutations in this gene are also involved in SQT2.[4] Loss of function mutations in *KCNH2/hERG*, the gene encoding for the α subunit of the channel responsible for $I_{Kr}$, can cause LQT2.[3,38] Mutations in this gene can also cause SQT1.[3] Mutations in *KCNJ2*, encoding for the α subunit of the channel responsible for $I_{K1}$, may trigger arrhythmias and cause SQT3 and AF.[3,38]

Mutations in the genes that encode for the $K^+$ channels are also involved in other diseases. Gain of function mutations in *KCNE3*, a modulator of the $I_{to}$ current, have been found in patients with BrS and AF.[3,4] Other patients with AF carried mutations in *KCNA5*, the gene that encodes for the α subunit of $K_V1.5$.[3]

### 5.3.3. Diseases associated with calcium channel dysfunction

Loss of function mutations in *CACN1C* and *CACNB2b* (the genes that encode for the α and β subunits of the L-type $Ca^{2+}$ channel, respectively) have been found in BrS and STQ patients.[3,4,38]

Gain of function mutations in *CACN1C* and *CACNB2b* have been found in LQT patients.[4]

Mutations in intracellular ion channels can also cause arrhythmias. Gain and loss of function mutations in *RyR2* , the gene that encodes for the ryanodine receptor of the SR, are linked to CPVT.[3,4,38]

## 6. Brugada Syndrome (BrS)

BrS is a rare inherited cardiac channelopathy characterized by prolonged conduction intervals and an ST segment elevation in the right precordial leads ($V_1$-$V_3$) of the ECG. It predisposes to a high risk of SCD, secondary polymorphic ventricular tachycardia and VF, in a structurally normal heart.[3,162–164]

This disease was first reported in 1992, known as "right bundle branch block, persistent ST segment elevation and sudden death syndrome". It was observed in 8 individuals resuscitated from SCD who presented a ST segment elevation in the ECG.[165] In 1996, the disease was referenced as BrS for the first time.[166]

In 1998 the first mutation linked to this disease was reported.[167] BrS usually displays autosomal dominant inheritance, which was suggested from the first description in 1992.[165] The dominance pattern was later supported by Kobayashi *et al.*, who reported a two-generation family with both SCD and ST segment elevation.[168] It has been reported that 20-50% of the patients suffering this disease have a familiar history of SCD.[38]

Although its prevalence is low, with 1-5 per 10,000 in Europe and the USA, it has been considered responsible of 4-12% of all SCD cases.[163,169]

### 6.1. Phenotype, diagnosis and treatment

The phenotypical presentation of BrS is heterogenous, ranging from patients that suffer SCD to asymptomatic individuals. It is associated with palpitations, syncope, dizziness, malignant ventricular arrhythmias and SCD, which often occur during sleep or at rest.[169–171] Only a little percentage of BrS patients have an arrhythmogenic event per year: it has been reported a frequency of 0.5% in patients who, until that event, were asymptomatic; 1.9% in patients that had already experienced a syncope and 7.7% in aborted SCD patients.[172] Aborted SCD is often the first symptom, although a third of the patients are diagnosed after syncope. The majority are asymptomatic at the time of the diagnosis, which in 36% of the cases is done during familial genetic screening.[36]

BrS is 8-10 times more prevalent in men, which may be explained by differences in ion channel expression and/or hormone levels (e.g., higher $I_{to}$ density and testosterone levels in men).[160,163] The symptoms typically occur during adulthood (41 ± 15 years), but in some cases are present in children and aged individuals.[163,173] Indeed, the first cases of BrS in 1992 included three pediatric patients[165], but after that, few pediatric cases have been reported.

Although the majority of BrS patients have a structurally normal heart, some studies have described minor structural alterations in the ventricles.[174,175]

The diagnosis criteria of BrS apply to children as well as adults, and are based on ECG abnormalities without requiring any further evidence of malignant arrhythmias.[163] In 2012 a consensus document was published establishing three ECG abnormalities for BrS (**Figure 17**):[176]

- **Type 1 (coved type):** Characterized by a ≥ 2 mm ST segment elevation in the right precordial leads ($V_1$-$V_3$) followed by a concave or straight T wave. This can occur spontaneously or can be evoked with an intravenous antiarrhythmic drug test (ajmaline, flecainide, pilsicainide).[160,163,169] These drugs block the cardiac sodium channel $Na_V1.5$, indicating the crucial role of $I_{Na}$ in BrS.[160] The ECG change can also be triggered by fever, as some *SCN5A* mutations alter the gating properties of $Na_V1.5$ in a temperature-dependent manner.[56,177] Physical exercise has also been reported to unmask the ST segment elevation.[160] This type of ECG abnormality is the only pattern that is diagnostic for BrS, although it is spontaneously observed only in 25% of the cases.[43]
- **Type 2 (saddle-back type):** Characterized by a ≥ 1 mm ST segment elevation followed by a convex T wave. This anomaly is only suggestive for BrS. When a patient displays this ECG morphology, a drug test is performed, and it may change from type 2 to type 1. If this is the case, the patient is diagnosed with BrS.[163]
- **Type 3:** Characterized by an ≤ 1 mm ST segment elevation, with either a coved type or saddle-back morphology. Similar to type 2, this anomaly is only suggestive for BrS and a drug test is performed to try to unmask the type 1 ECG.

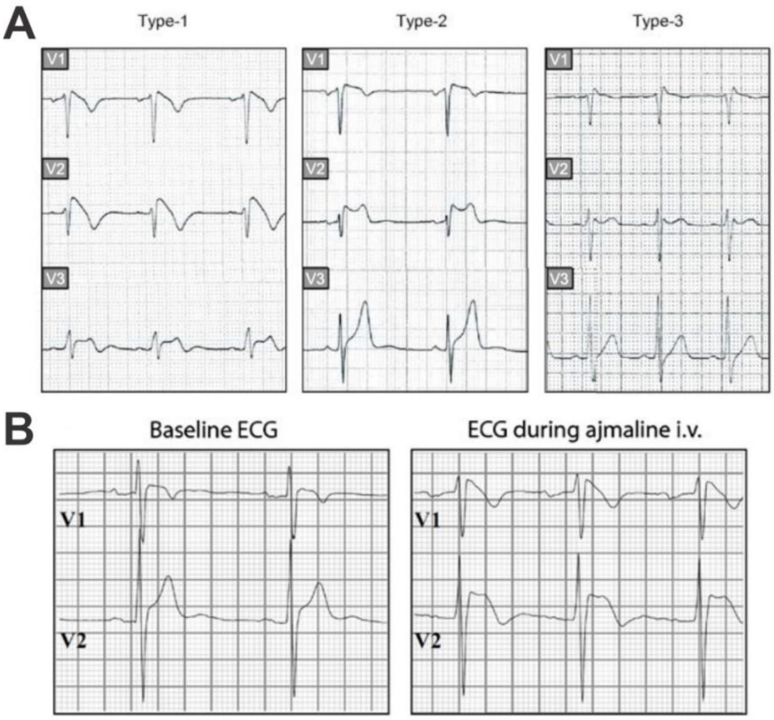

**Figure 17. ECG patterns in BrS. (A) Left:** Type 1 with ≥ 2 mm ST elevation and concave T wave. **Middle:** Type 2 with ≥ 1 mm ST elevation and convex T wave. **Right:** Type 3 with ≤ 1 mm ST elevation and concave or convex T wave. Adapted from Brugada et al.[178] **(B)** ST segment elevation before and after intravenous (i.v.) administration of ajmaline in an individual with BrS. Adapted from Amin et al.[160]

First degree relatives of BrS patients are recommended to undergo a clinical screening. Those patients with a normal ECG should undergo a drug provocative test. They are also recommended to go under a genetic screening, and carriers of a potentially pathogenic mutation should be closely followed.[43]

The implantation of a defibrillator is the only efficient therapy known in patients with high risk (who had a history of either VF or aborted SCD),[43] but it comes with a high cost and complications in 30% of the cases. These complications can be due to dysfunction of the defibrillator, inappropriate therapy or infection.[36,43,179] Pharmacological therapies that could reduce arrhythmia and prevent SCD by ionic current rebalance are still needed. Since most of BrS patients carry loss of function mutations, it is difficult to compensate for the missing healthy allele.[43,180] Both isoproterenol and quinidine are the most recommended options to treat BrS.[158] Another approach is the radiofrequency catheter ablation, where there's a disconnection of the right ventricular outflow tract (RVOT), preventing VF.[181]

## 6.2. Implicated genes

Approximately 35% of all the BrS cases are caused by missense and nonsense mutations and small nucleotide insertions or deletions.[160,169] Truncation mutations lead to a more severe phenotype.[180] Of the patients diagnosed with BrS, 20-25% carry a mutation in the gene *SCN5A*.

Up to date, more than 400 identified genetic variants have been identified in this gene.[77,170,182] When the mutations in *SCN5A* identified in BrS patients are expressed heterologously, most of them lead to loss of function of the cardiac sodium channel, with a reduced peak $I_{Na}$ and/or an alteration in other channel properties.[77,160] The loss of function may be produced by three different mechanisms:

- **Decreased membrane $Na_V$1.5 protein expression**. This can be caused by either a premature degradation of the protein in the endoplasmic reticulum, or because the protein fails to interact with β subunits or other regulatory proteins that are essential for the protein trafficking to the cell membrane.[160,183]
- **Non-functional channels** that reach the membrane, but conduct a small amount of $Na^+$ ions or none at all.[86,91,92,183]
- **Channels with altered gating properties,** which reach the membrane, but display delayed activation, earlier or faster inactivation, or enhanced slow inactivation. These alterations decrease the probability of the channels to be in the activated stage, thus reducing $I_{Na}$. [86,91,92,160,183]

In the *SCN5A* gene there is no hot spot for mutations. Kapplinger *et al.* published in 2010 a compendium of *SCN5A* mutations in patients with BrS which showed that the mutations can be localized throughout the whole protein (**Figure 18**).[184]

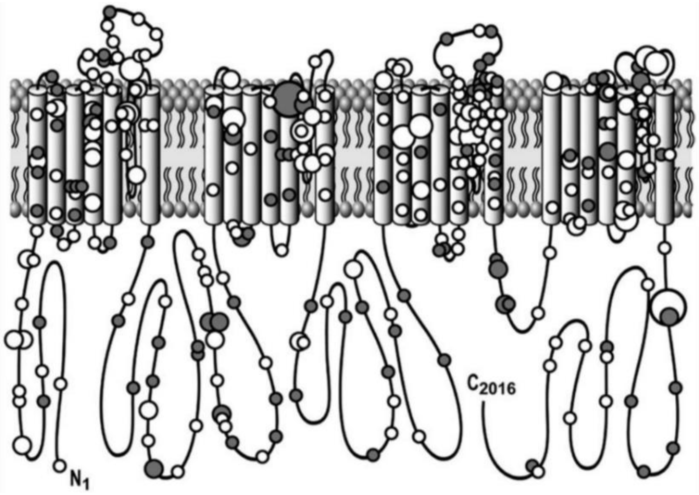

**Figure 18. Location of BrS mutations in Na$_V$1.5 channel topology.** Missense SNVs are indicated by white circles, other mutation types in gray. The smallest circles indicate a mutation only seen once; medium circles mutations seen in 2-4 patients; large circles mutations observed in 5-9 patients; the largest circle indicates mutations observed in at least 10 patients. Adapted from Kapplinger et al.[184]

Besides *SCN5A*, more than 20 genes have been also associated to BrS, although mutations in them are rare and only explain 5-10% of the cases:[169,182]

- **Other ion channels:** For example, *CACNA1C* and *CACNB2*. Both genes encode for L-type calcium channels and thus mutations in these genes would have an effect in phase 2 and 3 of the AP.[36,163]. A mutation in *KCNE3*, which encodes for MiRP2 (a protein that interacts with K$_v$4.3), have been proven to increase I$_{to}$ thus predisposing to BrS.[185]
- **Sodium channel β subunits:** I$_{Na}$ reduction may also by caused by mutations in the genes encoding for the Na$_V$ β subunits.[160,162] Variants in the gene *SCN1B* encoding for the splice variants β1 and β1b, in *SCN2B* encoding for the β2 and in *SCN3B* encoding for the β3 subunit, are known to cause BrS. These mutations can impede the proper interaction of the β subunits with Na$_V$1.5 proteins.[160,162,186–188] Furthermore, *SCN1B* can modulate some *SCN5A* mutations, by aggravating the loss of function of the channel as demonstrated by Wan *et al.*[189]
- **Na$_V$1.5 modulators:** mutations in genes such as *GPD1L*, *RANGRF*, *PKP2*, *SLMAP* and *FGF12* can have an effect on I$_{Na}$.[36]

Hosseini *et al.* published a study in 2018 where they performed an evidence-based curation of 21 genes reported as single gene causes for BrS, involving 3 curator teams and a clinical expert panel. Only the *SCN5A* gene presented enough evidence to be classified as a definitive diagnostic gene.[190]

### 6.3. Pathophysiological mechanisms of BrS

BrS is usually caused by a loss of function of $Na_V$ channels. The reduction of $I_{Na}$ leads to a decrease of the AP phase 0 depolarization magnitude, slowing atrial and ventricular electrical conduction[160]. Two hypotheses have been proposed to try to explain the ST segment elevation, characteristic of BrS (**Figure 19**):

- The **repolarization hypothesis**: It claims that there's an unbalanced repolarization on the right ventricle. According to this hypothesis, APs are shorter in the right ventricle epicardium, where the repolarizing $I_{to}$ is larger, compared to the endocardium.[191] In normal conditions, the membrane rapid depolarization activates $I_{to}$, opposing the depolarization mediated by $I_{Na}$. Thus, since in the epicardium there's a higher $I_{to}$ density than in the endocardium, the reduction in $I_{Na}$ given by the loss of function of the channel causes an ionic decompensation. This provokes an early repolarization leading to a change in the AP morphology. On the other hand, $I_{to}$ is less relevant in the endocardium so the ionic balance decompensation by $I_{Na}$ reduction is not as prominent, and the AP morphology remains similar. This $I_{Na}$ reduction would further shorten depolarization duration and facilitate reentrant waves between depolarized endocardium and prematurely repolarized epicardium. In summary, the $Na_V$ loss of function leads to an altered AP morphology in the epicardium, which, in turn, causes a transmural voltage gradient between the epicardium and endocardium. This results in the ST segment elevation observed in the ECG (**Figure 19A**).[160,170,192,193]
- The **depolarization hypothesis:** It states that there's an unbalance in the AP depolarization. $I_{Na}$ reduction would cause a conduction delay in the RVOT, which would lead to a ST segment elevation (**Figure 19B**). This hypothesis is supported by subclinical structural abnormalities in the right ventricles found in some BrS patients.[160,171]

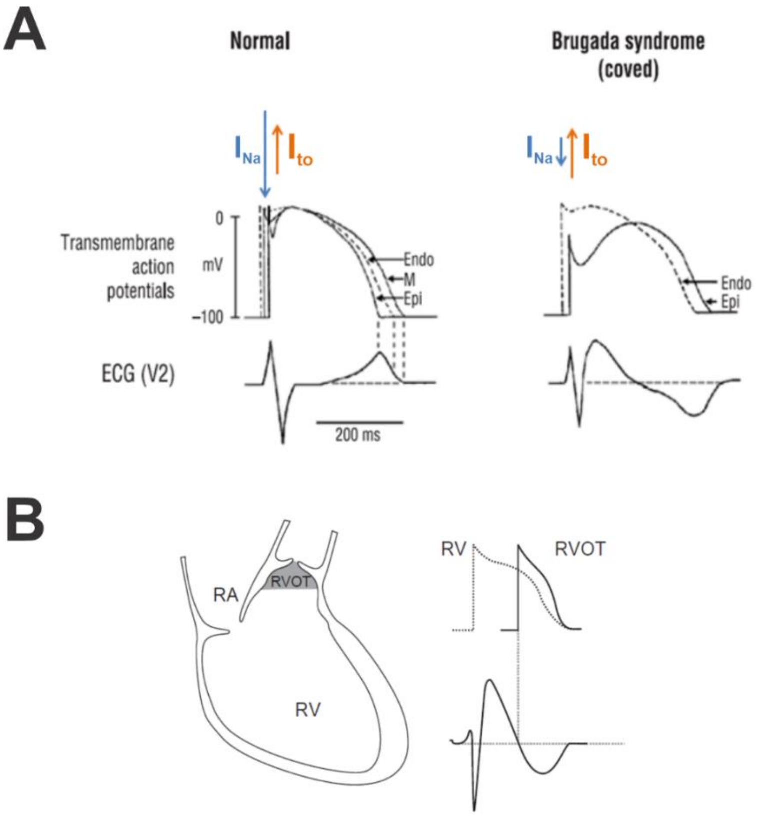

**Figure 19. Schematic representation of the ST segment elevation hypotheses. (A) Repolarization hypothesis:** $I_{Na}$ dysfunction (blue arrow) shortens the repolarization duration potentially causing BrS. Adapted from Benito *et al.*[194] **(B) Depolarization hypothesis:** $I_{Na}$ reduction causes a conduction delay in the RVOT, resulting in a coved-type ST elevation. Adapted from Meregalli *et al.*[171]

## 6.4. Experimental cellular models in Brugada Syndrome

Many models have been used to study BrS. A detailed description regarding the two cellular models used in this Thesis is provided.

### 6.4.1. Heterologous expression systems in BrS

Our group published in 2019 a compendium of *SCN5A* mutations related to BrS studied in heterologous expressions systems.[77] Around one-third of the mutations that had been characterized until that publication caused a reduction in $I_{Na}$ density. The observed reduction was proposed to be caused by either a defect in channel trafficking or by alterations in channel's gating properties.

Besides a reduction in $I_{Na}$, other alterations in the sodium channel properties have been reported for mutations associated with BrS. As an example, the studies of Bezzina *et al.*[195] and Tarradas *et al.*[92] showed *SCN5A* mutations that produced shifts in the voltage dependence of activation and steady-state inactivation curves. Other mutations either accelerated or decelerated the speed of inactivation[196,197], or prolonged the recovery from inactivation.[198,199]

Genes other than *SCN5A* associated with BrS have been functionally studied. These studies demonstrated that reduction in $I_{Na}$ can also be caused by mutations in *SCN1B*, *SCN2B*, *SCN3B* and *GPD1-L*.[162,186,200,201]

### 6.4.2. iPS-CM in BrS

Loss of function mutations located in the *SCN5A* gene and linked to BrS have been studied using the iPS-CM model. Similar to what has been studied in heterologous expression systems, the loss of function has been proposed to be caused by a channel trafficking defect or gating properties alterations.[77]

The first BrS mutation studied in iPS-CM caused a LQT3/BrS overlap phenotype, as previously stated in section 3.2.2, which caused a decrease in peak and persistent $I_{Na}$.[131] Our group has reported a SNV in *SCN5A* that lead to $I_{Na}$ reduction, a shift in both the activation and steady-state inactivation curves, and a faster recovery from inactivation.[91] The $I_{Na}$ reduction as well as a shift in the activation curve, caused by an *SCN5A* mutation, has also been observed in other studies.[85,202,203]

Kosmidis *et al*. reported two *SCN5A* mutations that caused loss of sodium current. Furthermore, they explored the effect of drugs over the mutations, corroborating the use of iPS-CM as a model to study therapeutic tools.[204]

As over 70% of BrS patients remain without an identified mutation, this cell model allows the study of possible cellular mechanisms and can provide candidate susceptibility genes.[204,205] The work by Belbachir *et al*. using iPS-CM from BrS patients, allowed the identification of the *RRAD* gene as a potential new susceptibility gene. The SNV located in this gene caused a reduction in $I_{Na}$ and $I_{CaL}$.[206]

# II. Rationale of the research

Genetic analysis has been very useful for identifying mutations that can potentially cause a disease in a patient, and to detect the mutations in relatives. Furthermore, functional analysis of these mutations has given evidence for their role in several arrhythmogenic diseases.

Nevertheless, severity of the clinical phenotype resulting from a mutation in an ion channel or associated proteins can vary among carriers[37]. In this situation, the mutation is said to exhibit incomplete penetrance and/or variable expressivity, which are common features of channelopathies. One of the possible explanations of these differences, is that the specific genetic background of each individual, plays a determinant role on the phenotypical expression of a given mutation.

The advent of the next generation sequencing techniques has allowed researchers to obtain information on the genetic background when a candidate mutation is identified. Later on, the possibility of studying patient specific iPSc-derived cardiomyocytes, brought the advantage of studying a given mutation in a patient-specific model.

In this thesis, we used these tools to study two different SNVs linked to arrhythmogenic diseases. First, we characterized the effect of an SNV located in the *SCN1B* gene on both cardiac- and brain-type sodium currents in a heterologous expression system. We discussed our results in view of the whole-exome data obtained from the proband and the detection of specific SNVs in the proband's relatives. Our second study was focused on an SNV located in *SCN5A* that had been related to Brugada Syndrome. We studied the cardiac sodium current properties in iPSc-derived cardiomyocytes of three SNV carriers and a related control from the same family, as well as in heterologous expression systems. In addition, we interpreted these results in the context of data from a genetic panel customized for cardiac arrhythmogenic diseases, performed in the family members to detect other SNVs that could influence the cardiac sodium current properties.

## 1. *SCN1B* variant associated with concomitant brain and cardiac disorders

This study was based on the SNV *SCN1B*_c.308A>T, referenced as rs1057519457 in SNP Report (https://www.ncbi.nlm.nih.gov/snp). This SNV was identified in a whole exome sequencing study of an 8-year-old male. This child (from now on referenced as proband) carried the SNV in heterozygosis. The whole exome study showed that the proband also carried two *POLR1C* variants in heterozygosis. The protein encoded by the *POLR1C* gene is a subunit of both RNA polymerase I and RNA polymerase III complexes. It is involved in the transcription of DNA into RNA, including ribosomal RNA and transfer RNA which are essential for the normal functioning and survival of the cells. Genetic screening of his progenitors evidenced that he had inherited two of the SNVs (*SCN1B*_c.308A>T and *POLR1C*_c.88C>T) from his father, and one of the SNVs (*POLR1C*_c.614delG) from his mother (**Figure 20**).[207]

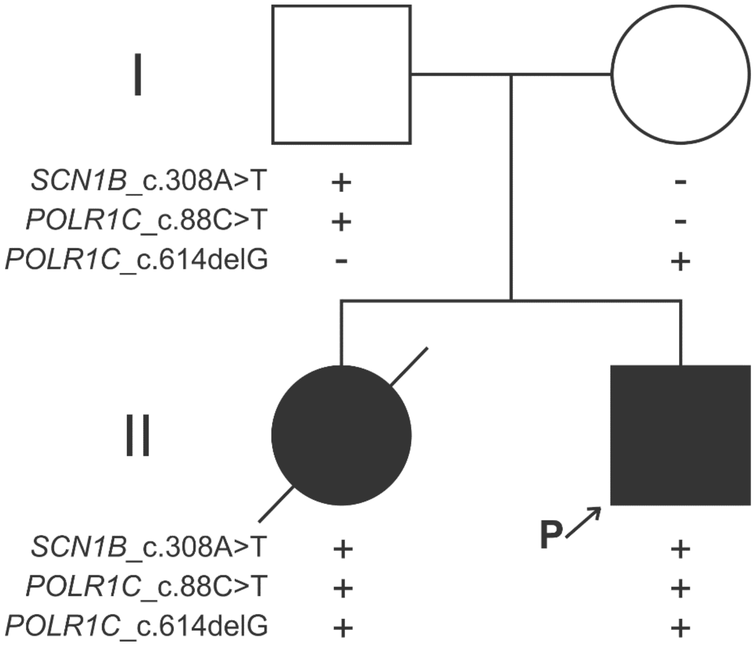

**Figure 20. Pedigree of the family carrying the SCN1B and POLR1C SNVs.** Circles represent females, and squares represent males. Clinically affected individuals are shown in black. The + symbol represents SNV carriers, and – symbol the non-carriers of the different SNVs. Arrow indicates the proband. The diagonal line indicates a deceased patient.

The clinical picture of the proband is complex and includes both cardiac and neurological impairment. Both parents are completely asymptomatic, while the proband's elder sister, who carried the three afore mentioned SNVs, had a fetal diagnosis of bradycardia and subsequent postnatal finding of complete AV block, leading to early neonatal death from multi-organ failure.

The major clinical features of the proband included bradycardia from variable AV conduction disturbance, borderline prolongation of the QTc interval and intraventricular conduction delay, which presented early in the neonatal stage. By the 2nd year of life, he presented global developmental delay and increased tone in the lower extremities. At age 5, neurological examination demonstrated significant cognitive deficits, persistent large-amplitude horizontal nystagmus with primary gaze, normal tone in the upper extremities with mixed spasticity and dystonia in the lower extremities. Brain MRI revealed extensive polymicrogyria involving the bilateral cerebral hemispheres, extensive T2 hyperintense signal throughout the supratentorial white matter with less in the cerebellar white matter and dorsal brainstem, and markedly delayed myelination. At 7 years of age, he also developed recalcitrant atrial tachycardia.

The identified SNV (*SCN1B*_c.308A>T) leads to a substitution of an Aspartic Acid for a Valine at position 103 of the protein (β1_p.D103V and β1b_p.D103V). This changes the hydropathy of the aminoacid at this position from hydrophilic to hydrophobic, and the polarity from negative to neutral. The SNV is located in exon 3 of the gene. This exon is part of the Ig-like loop of the extracellular domain (ECD) of the protein, which is shared by the two *SCN1B* splice variants: β1 and β1b subunits. These subunits have been described to modulate different sodium channels, among which the cardiac-type $Na_V1.5$ and brain-type $Na_V1.1$ channels.

Additionally, the substitution is located in a highly conserved region of the protein which is highly conserved among β subunits in humans and also among β1 subunits of different species (**Figure 21**). NCBI dbSNP (https://www.ncbi.nlm.nih.gov/snp/) reports a frequency of this SNV of 0%. The PolyPhen-2 (Polymorphism Phenotyping v2, http://genetics.bwh.harvard.edu/pph2) tool, which predicts the possible impact of a SNV on the protein structure and function, predicted this SNV to be probably damaging. The SNV was also catalogued as deleterious by the PROVEAN (Protein Variation Effect Analyzer, http://provean.jcvi.org/index.php) software, which predicts the impact of a SNV on the biological function of the cells. Additionally, the pathogenicity predictor MutationTaster (http://www.mutationtaster.org) classified the SNV as disease causing. Taking all this information into account, this SNV can be considered as possibly pathogenic and could modify the regulatory properties of the β1 and/or β1b subunits on the $Na_V1.5$ and/or $Na_V1.1$ channels.

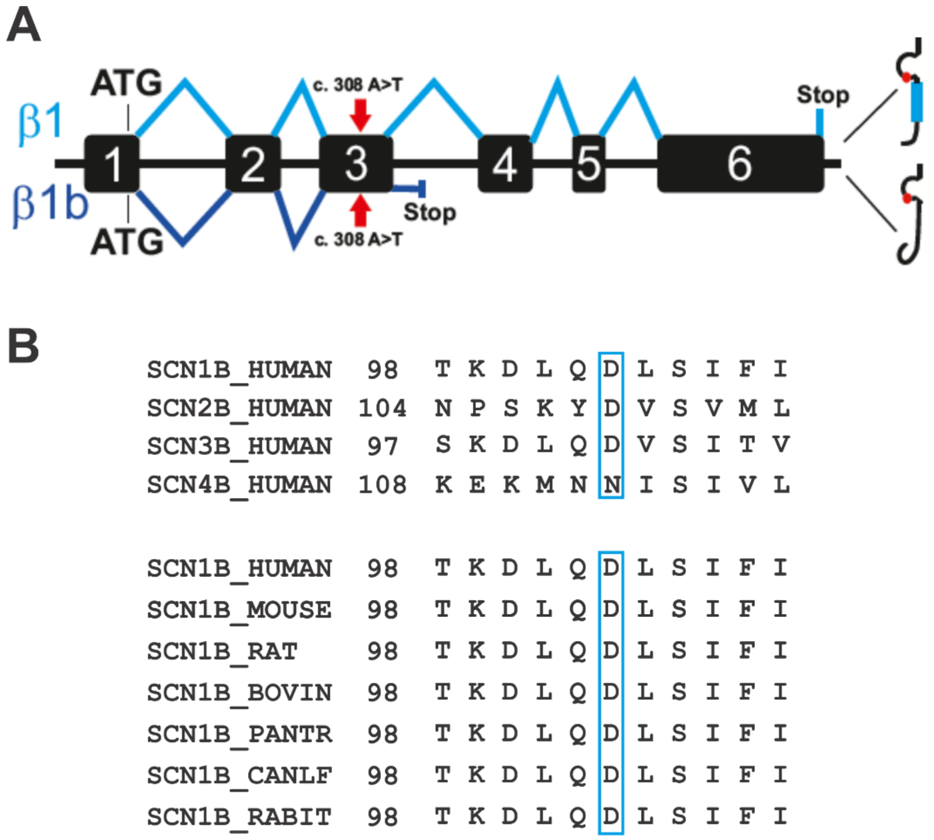

```
SCN1B_HUMAN   98   T K D L Q D L S I F I
SCN2B_HUMAN  104   N P S K Y D V S V M L
SCN3B_HUMAN   97   S K D L Q D V S I T V
SCN4B_HUMAN  108   K E K M N N I S I V L

SCN1B_HUMAN   98   T K D L Q D L S I F I
SCN1B_MOUSE   98   T K D L Q D L S I F I
SCN1B_RAT     98   T K D L Q D L S I F I
SCN1B_BOVIN   98   T K D L Q D L S I F I
SCN1B_PANTR   98   T K D L Q D L S I F I
SCN1B_CANLF   98   T K D L Q D L S I F I
SCN1B_RABIT   98   T K D L Q D L S I F I
```

**Figure 21. The protein region that includes the SNV SCN1B_c.308A>T is shared by β1 and β1b isoforms and is highly conserved. (A)** Schematic representation of the genomic (left) and protein (right) structure of β1 and β1b isoforms. The black boxes represent the exons of the gene. The blue rectangle indicates the transmembrane domain of β1. The red arrows indicate the location of the mutation in the gene, and the red circle the approximate location of the mutation in the protein. The β1b isoform is characterized by a partial retention of intron 3, which renders a protein lacking a transmembrane domain. **(B)** Sequence alignments of the region shared by β1 and β1b containing the *SCN1B*_p.D103V mutation were performed using Uniprot. The position of the first amino acid of each sequence is indicated on the left side. The aminoacid affected by the SNV is marked with a blue square. **Top:** Sequence alignment of human voltage-gated sodium channel β-subunit family members. **Bottom:** Sequence alignment of voltage-gated sodium channel β1 subunit of different species.

## 2. *SCN5A* variant associated with Brugada Syndrome

The second part of this thesis is focused on the SNV *SCN5A*_c.4573G>A. This variant was reported by Kapplinger *et al.*[208] and it is included in an international compendium of *SCN5A* SNVs found in patients tested for BrS. The SNV reference in SNP Report is rs199473269. We identified a family with several carriers of this SNV (**Figure 22**).

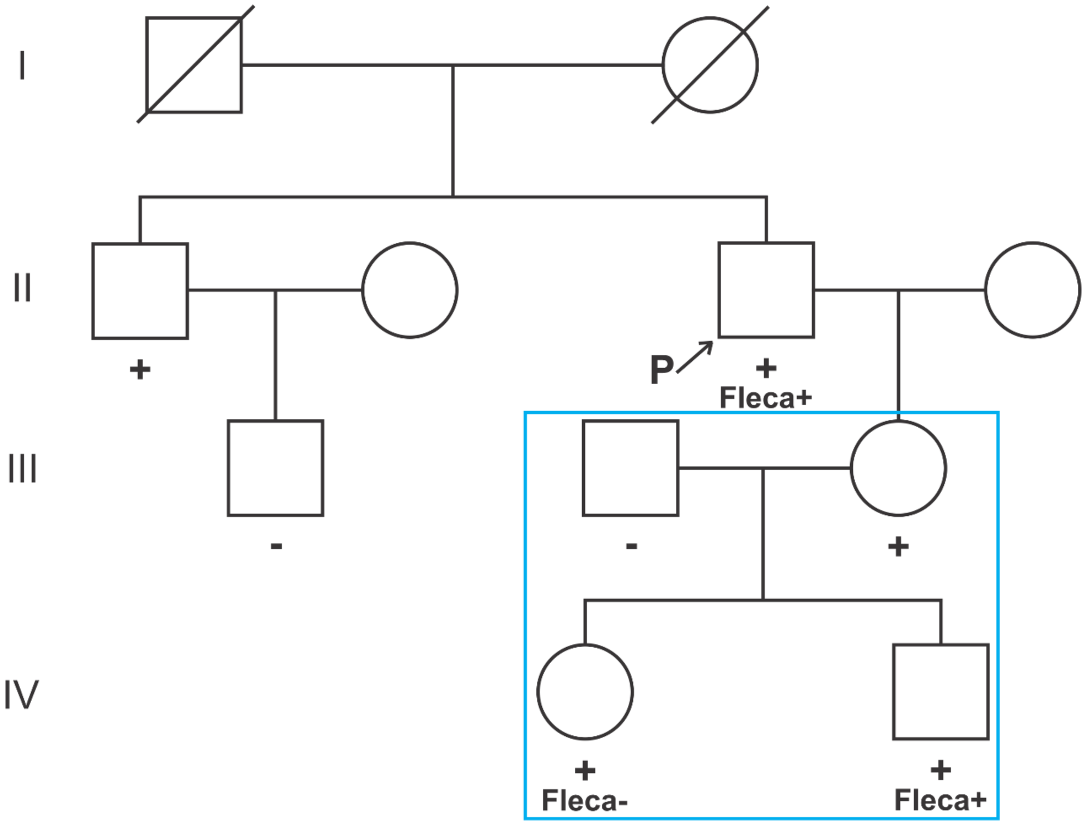

**Figure 22. Pedigree of the family carrying the *SCN5A* SNV.** Circles represent females, and squares represent males. The + symbol represents SNV carriers, and – symbol the non-carriers. Fleca designates patients which underwent a flecainide test, and the + or – symbols next to it indicate whether the result was positive or negative, respectively. Arrow indicates the proband. Diagonal lines indicate deceased patients. Blue square indicates the individuals that were studied in this Thesis.

The proband had been previously diagnosed with AF. He displayed the typical BrS ECG pattern when he was being treated with flecainide. A genetic analysis of the proband was performed by LABGENETICS in Madrid, and the SNV *SCN5A*_c.4573G>A was identified in heterozygosis. The brother of the proband is also a carrier of the SNV, but it was not inherited by his son.

The daughter of the proband also carries the SNV in heterozygosis. She remains asymptomatic to date. Her husband is not a carrier of the SNV. Their daughter and son, grandsons of the proband, were also genetically tested and both are heterozygous carriers of the SNV. Both children underwent a Flecainide test, which unmasked the typical BrS type 1 ECG only for the boy. To date, both the girl (18 years old) and the boy (15 years old) remain asymptomatic. However, as stated in the Introduction, BrS symptoms typically develop in the adulthood. Therefore, we cannot discard that these patients will eventually develop symptoms of the disease. In this Thesis, we focused on this latter family unit, which is identified with a blue square in **Figure 22**.

The SNV investigated in this study (*SCN5A*_c.4573G>A) is located in exon 27 of the *SCN5A* gene. It leads to an aminoacidic change from a Valine to a Methionine ($Na_V$1.5_p.V1525M), which changes the hydropathy from hydrophobic to moderate, although the polarity remains neutral. At the protein level, the SNV is localized in a cytoplasmic loop of $Na_V$1.5, which connects domains III and IV (**Figure 23A**). This region of the protein contains the inactivation gate of the channel. The Valine in this position is in a region that is highly conserved among different species and among α subunit-encoding genes (**Figure 23B**). This SNV has a frequency in the population of 0.001% according to the Genome Aggregation Database (https://gnomad.broadinstitute.org), and of 0.008% according to the NHLBI Exome Sequencing Project (ESP) Exome Variant Server (https://evs.gs.washington.edu/EVS). The PolyPhen-2 tool predicted this SNV to be probably damaging, and was catalogued as deleterious by the PROVEAN software. Furthermore, MutationTaster classified the SNV as disease causing. Taking all this information into account, this SNV can be considered as possibly pathogenic and could modify the properties of the $Na_V$1.5 channel.

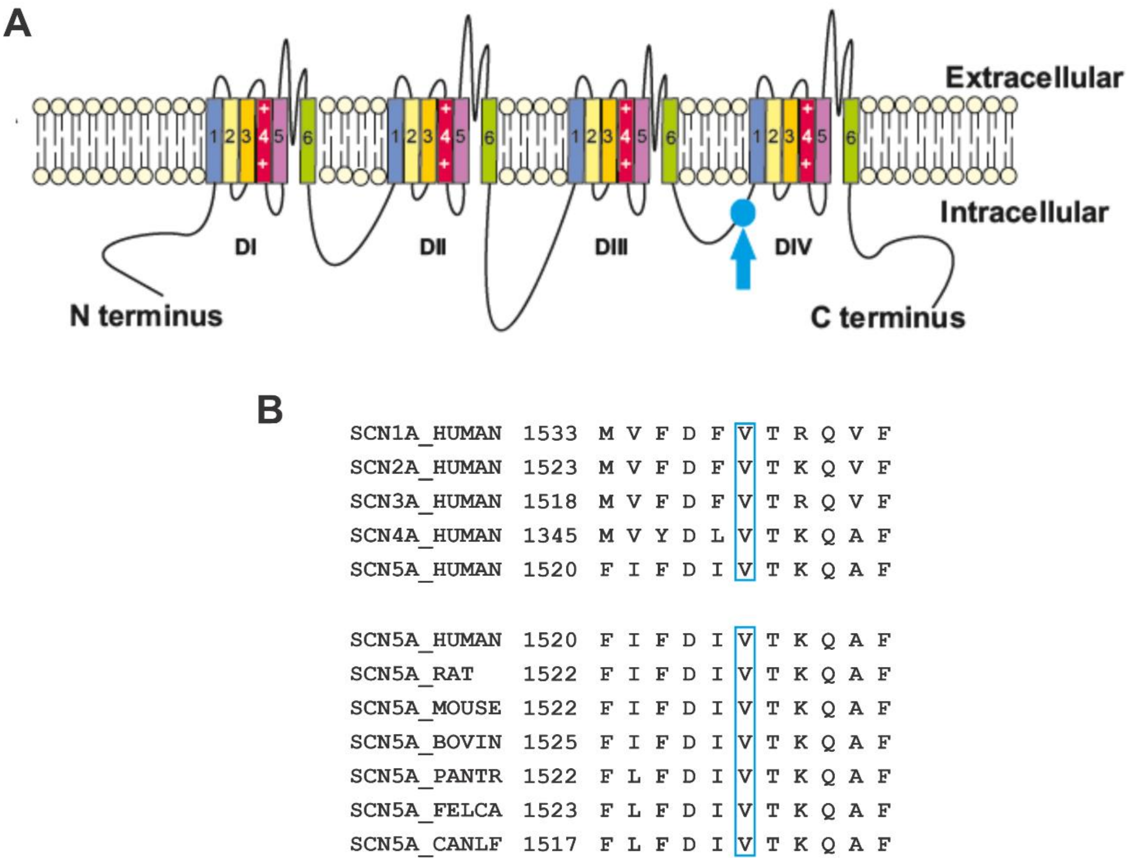

**Figure 23. The SNV SCN5A_c.4573G>A is located in a highly conserved region. (A)** The approximate location of the SNV in the Na$_V$1.5 protein is marked with a blue dot and an arrow. **(B)** Sequence alignments of the region in Na$_V$1.5 containing the p.V1525M mutation were performed using Uniprot. The position of the first amino acid of each sequence is indicated on the left side. The aminoacid affected by the SNV is marked with a blue square. **Top:** Sequence alignment of human voltage-gated sodium channel family members. **Bottom:** Sequence alignment of voltage-gated sodium channel Na$_V$1.5 of different species.

**Thus, current data on channelopathies related to inherited arrhythmogenic diseases together with the evidence presented in this chapter, lead us to propose the hypotheses and specific aims exposed in the following chapter.**

# III. Hypotheses and Specific Aims

In the previous section, we presented data on two different SNVs associated to inherited arrhythmogenic diseases. Pathogenicity prediction for both mutations suggested that they could explain at least part of the clinical phenotype of the probands. However, the pedigrees of both families, in which clinical and genetic data are shown together, suggested that the SNVs exhibited incomplete penetrance and/or variable expressivity. We propose that this phenotypical difference results from a modulatory effect of the patient-specific genetic background.

Thus, the central hypothesis of this thesis is that **the effect of sodium channel SNVs associated to inherited arrhythmogenic diseases is modulated by the individual's specific genetic background.**

To test this general hypothesis, we proposed separate sub-hypotheses and specific aims related to the SNVs under study as follows:

## 1. *SCN1B* variant associated with concomitant brain and cardiac disorders

We propose the following specific hypotheses for this study:

**1.1.** The SNV *SCN1B*_c.308A>T alters the regulatory properties of the β1 and β1b subunits over $Na_V1.5$ and $Na_V1.1$ channels.

**1.2.** The clinical manifestation of the mutant β1 and β1b subunits is aggravated by the presence of other patient-specific SNVs.

To assess these hypotheses, we propose the following specific aims:

**Specific aim 1**. To characterize the effect of the wild type β1 and β1b subunits on the electrophysiological properties of the sodium current in HEK-293T cells expressing these β subunits together with either $Na_V1.5$ or $Na_V1.1$.

**Specific aim 2.** To characterize the effect of the SNV *SCN1B*_c.308A>T in β1 and β1b subunits on the electrophysiological properties of the sodium current in HEK-293T cells expressing these mutant β subunits together with either $Na_V1.5$ or $Na_V1.1$.

## 2. *SCN5A* variant associated with Brugada Syndrome

We propose the following specific hypotheses for this study:

**2.1.** The SNV *SCN5A*_c.4573G>A modifies the sodium current properties of the $Na_V1.5$ channel.

**2.2.** The effect of the SNV on the sodium current properties of the $Na_V1.5$ channel will be different in the three carrier individuals of the same family.

**2.3.** The effect of the SNV on the $Na_V1.5$ current in the iPS-CM derived from the family carriers will be different to the effect observed in HEK-293T cells heterologously expressing the SNV.

**2.4.** The three carrier family members hold other variants that could influence the cellular phenotypical effect of the SNV.

To assess these hypotheses, we propose the following specific aims:

**Specific aim 3.** To characterize the effect of the SNV *SCN5A*_c.4573G>A on the electrophysiological properties of the sodium current, in HEK-293T cells expressing the wild type or mutant $Na_V1.5$ channel either in homozygosis or heterozygosis.

**Specific aim 4.** To differentiate patient-specific iPSc to iPS-CM suitable for electrophysiological experiments from the four members of the same family.

**Specific aim 5.** To characterize the effect of the SNV *SCN5A*_c.4573G>A on the electrophysiological properties of the sodium current, in the patient-specific iPS-CM.

**Specific aim 6.** To identify differences in the genetic background among the four members of the family, using a sequencing panel that includes genes related to cardiac arrhythmias.

# IV. Methods

# 1. Materials

## 1.1. Cellular lines

### 1.1.1. Bacteria

The bacteria used in this thesis to obtain the different expression vectors were XL-10 gold ultracompetent cells (Agilent Technologies, Santa Clara, CA, USA), which were grown in the following media:

**Table 1. Media used for bacterial culture**

| Media | Composition | Company | Additional information |
|---|---|---|---|
| **NZY⁺ Broth** | 0.22 g in 10 ml mQ water | Fisher BioReagents™-Thermo Fisher Scientific (Waltham, MA, USA) | Adjust pH to 7.5 with NaOH. Once autoclaved and cold add 125 µl $MgCl_2$ and 200 µl of 20% w/v glucose. |
| **LB-Agar** | 3.5 g in 100 ml mQ water | NZYTech (Lisboa, Portugal) | Dispense 20 ml/10cm dish |
| **LB-Broth** | 2 g in 100 ml mQ water | Sigma-Aldrich-Merck (Darmstadt, Germany) | N/A |

### 1.1.2. HEK-293T

The cellular model to heterologously study the *SCN1B* and *SCN5A* SNVs was human embryonic kidney-293 tsA201 cells (HEK-293T, Health Protection Agency Culture Collections-Salisbury, UK).

The cells were routinely maintained in TC-treated T25 flasks (Corning, New York, NY, USA) at 37°C with 5% $CO_2$, with Dulbecco's Modified Eagle's Medium (DMEM, **Table 2**).

**Table 2. HEK-293T medium composition**

| Composition | Company |
|---|---|
| **DMEM** | **Sigma-Aldrich-Merck** |
| **10% Fetal bovine serum (FBS)** | **Gibco-Thermo Fisher Scientific** |
| **1% Penicillin - Streptomycin (Pen-Strep)** | **Gibco-Thermo Fisher Scientific** |
| **1% Glutamax** | **Gibco-Thermo Fisher Scientific** |

### 1.1.3. Fibroblasts

Fibroblasts were obtained from skin samples from all the patients and controls used in this Thesis, and maintained with fibroblasts medium (**Table 3**).

**Table 3. Fibroblasts medium composition**

| Composition | Company |
|---|---|
| **DMEM, high glucose plus Glutamax and HEPES** | Gibco-Thermo Fisher Scientific |
| **50 µg/ml Gentamicin** | Gibco-Thermo Fisher Scientific |
| **1.25 µg/ml Amphotericin B** | Gibco-Thermo Fisher Scientific |
| **1% Pen-Strep** | Gibco-Thermo Fisher Scientific |
| **10% HyClone FBS** | GE Healthcare Life Sciences (Utah, USA) |

In the reprogramming protocol to induced pluripotent stem cells (iPSc), 10% DMEM (**Table 4**) and stem cell selection medium (TeSR-E8, STEMCELL Technologies, Vancouver, Canada) were used.

**Table 4. 10% DMEM composition**

| Composition | Company |
|---|---|
| **DMEM, high glucose plus L-glutamine** | Gibco-Thermo Fisher Scientific |
| **10% FBS** | Gibco-Thermo Fisher Scientific |
| **1% Pen-Strep** | Gibco-Thermo Fisher Scientific |

### 1.1.4. Induced pluripotent stem cells

iPSc were routinely maintained in TC-treated 6-well plates (Falcon-Corning) with mTeSR1 medium (STEMCELL Technologies).

### 1.1.5. Induced pluripotent stem cell-derived cardiomyocytes

The differentiation of iPSc to iPSc-derived cardiomyocytes (iPS-CM) was done in TC-treated 12-well plates (Falcon-Corning) and included 3 different media (**Table 5**, **Table 6**, **Table 7**). The digestion media to replate the cells is described in **Table 8**.

**Table 5. Differentiation media composition**

| Composition | Company |
|---|---|
| **DMEM: Nutrient Mixture F-12** | Gibco-Thermo Fisher Scientific |
| **0.064 mg/ml L-ascorbic acid** | Sigma-Aldrich-Merck |
| **0.01344 µg/ml sodium selenite** | Sigma-Aldrich-Merck |
| **10 µg/ml holo-transferrin** | Sigma-Aldrich-Merck |
| **1X chemically defined lipid concentrate** | Gibco-Thermo Fisher Scientific |
| **1% Glutamax** | Corning |
| **1% Pen-Strep** | Corning |

**Table 6. Starving media composition**

| Composition | Company |
|---|---|
| **SILAC basal medium** | Gibco-Thermo Fisher Scientific |
| **0.0615 mg/ml L-ascorbic acid** | Sigma-Aldrich-Merck |
| **0.00844 µg/ml sodium selenite** | Sigma-Aldrich-Merck |
| **2.5 µg/ml holo-transferrin** | Sigma-Aldrich-Merck |
| **1X chemically defined lipid concentrate** | Gibco-Thermo Fisher Scientific |
| **1% Glutamax** | Corning |
| **1% Pen-Strep** | Corning |
| **147.5 mg/ml L-Arginine** | Thermo Fisher Scientific |
| **91.25 mg/ml L-Lysine** | Thermo Fisher Scientific |

**Table 7. Maturation media composition.**

| Composition | Company |
|---|---|
| **Differentiation media** | Described in **Table 5** |
| **10 µg/ml insulin** | Sigma-Aldrich-Merck |
| **1 µM Dexamethasone (Dex)** | Tocris Bioscience (Bristol, UK) |
| **0.1 µM 3,3’,5-Triiodo-L-thyronine (T3)** | Sigma-Aldrich-Merck |

**Table 8. Digestion media composition**

| Composition | Company |
|---|---|
| **Differentiation media** | Described in **Table 5** |
| **20% FBS** | Gibco-Thermo Fisher Scientific |
| **10 µM Y-27632 2HCl ROCK1 inhibitor (ROCKi)** | Deltaclon (Madrid, Spain) |
| **10 µg/ml insulin** | Sigma-Aldrich-Merck |
| **1 µM Dex** | Tocris-Bio-Techne (Minneapolis, MN, USA) |
| **0.1 µM T3** | Sigma-Aldrich-Merck |

### 1.2. Expression vectors

The pcDNA3 vector harboring the cDNA of human *SCN5A* (pCDNA3-SCN5A) was a generous gift from Dr. Matteo Vatta (Baylor College of Medicine, Houston, TX, USA).

The pCMV vector harboring the complementary DNA (cDNA) of human *SCN1A* was a generous gift from Dr. Alfred George Jr. (Vanderbilt, University Division of Genetic Medicine, Nashville, TN, USA).

The cDNA of the human *SCN1B* in a commercially available pCMV6-XL4-SCN1B (OriGene Technologies Inc., Rockland, MD, USA) was subcloned into a bicistronic vector encoding enhanced green fluorescent protein (GFP, pIRES-GFP, Clontech Laboratories Inc., Mountain View, CA, USA). Human *SCN1Bb* cDNA was previously amplified in our group from human heart right ventricle and cloned into pIRES-GFP[209].

### 1.3. Antibodies

The primary antibodies used in this thesis were: rabbit anti-human $Na_V1.1$ antibody (Alomone Labs, Jerusalem, Israel) and rabbit anti-human $Na_V1.5$ (Alomone Labs).

The secondary antibody used was a horseradish peroxidase-conjugated anti-rabbit (Thermo Fisher Scientific).

### 1.4. Western Blot and Biotinylation assay buffers

The lysis buffer used to collect the HEK-293T cells is described in **Table 9**.

**Table 9. HEK-293T cells lysis buffer composition**

| Composition | Company |
|---|---|
| **50 mM Tris/HCl pH 6.8** | Sigma-Aldrich-Merck |
| **10% Glycerol** | Sigma-Aldrich-Merck |
| **2% SDS** | Sigma-Aldrich-Merck |

The buffers used in the western blot are described in **Table 10**.

**Table 10. Western Blot Buffers**

| Buffer | Composition | Company |
|---|---|---|
| **5X Loading Buffer** | 50 mM Tris/HCl, pH 6.8; 10% Glycerol; 2% SDS; 5% β-Mercaptoethanol; 0.004% Bromophenol blue | Sigma-Aldrich-Merck |
| **10X Electrolyte Buffer** | 25 mM Tris base; 192 mM Glycine; 0.1% SDS | Sigma-Aldrich-Merck |
| **10X Transfer Buffer** | 25 mM Tris base; 192 mM Glycine | Sigma-Aldrich-Merck |

The following reagents were used in the biotinylation assay:

**Table 11. Reagents used in the Biotinylation assay**

| Reagent | Composition | Company |
|---|---|---|
| **DPBS$^+$** | 2.68 mM KCl; 1.47 mM $KH_2PO_4$; 0.49 mM $Na_2HPO_4 \cdot 7H_2O$; 137 mM NaCl; 0.49 mM $MgCl_2 \cdot 6H_2O$; 0.9 mM $CaCl_2$ | Sigma-Aldrich-Merck |
| **LB1** | 50 mM Tris/HCl, pH 7.4; 150 mM NaCl; 1 mM EDTA | Sigma-Aldrich-Merck |
| **LB2** | LB1; 1% Triton X-100 | Sigma-Aldrich-Merck |
| **LB3** | LB2; 1 tablet of Protease Inhibitor Cocktail (for 10 ml) | Roche-Merck |
| **SWS** | 350 mM NaCl; 5 mM EDTA; 0.1% Triton X-100 | Sigma-Aldrich-Merck |

### 1.5. Patch Clamp solutions

For the HEK-293T cells the bath solution used was a normal saline solution (140 NK, **Table 12**), while a low $Na^+$ solution (**Table 12**) was used for the iPS-CM. For both cells, we used a pipette solution with the composition listed in **Table 13** (130 CsCl).

**Table 12. Bath solutions used in the electrophysiological studies. All components are from Sigma-Aldrich-Merck.**

| Solution | Composition | Company |
|---|---|---|
| **140 NK** | 140 mM NaCl; 3 mM KCl; 10 mM HEPES; 1.8 mM $CaCl_2$; 1.2 mM $MgCl_2$ | Sigma-Aldrich-Merck |
| **Low Na$^+$** | 40 mM NaCl; 3 mM KCl; 100 mM NMdG; 10 mM HEPES; 1.8 mM $CaCl_2$; 1.2 mM $MgCl_2$ | Sigma-Aldrich-Merck |

**Table 13. Pipette solution used in the electrophysiological studies.**

| Solution | Composition | Company |
|---|---|---|
| **130 CsCl** | 130 mM CsCl; 1 mM EGTA; 10 mM HEPES; 10 mM NaCl; 2 mM ATP-$Mg^{2+}$ | All from Sigma-Aldrich-Merck, except CsCl from EMSURE - Merck |

Both bath solutions were adjusted to pH 7.4 with NaOH using a SympHony pH meter (VWR - West Chester, PA, USA), pipette solution was adjusted to pH 7.2 with CsOH. Osmolality of bath and pipette solutions was adjusted with glucose (Sigma-Aldrich-Merck) to 325 and 308 mOsm respectively, using a VAPRO 5520 Osmometer (Wescor – ELITech Group).

## 1.6. Other material references

All other reagents, expendables and equipment are numerically referenced in the methods text according to the following list.

### 1.6.1. Reagents

1. β-Mercaptoethanol: Sigma-Aldrich-Merck
2. 0.05% Trypsin/EDTA: Corning
3. 0.25% Trypsin: Sigma-Aldrich-Merck
4. Amaxa NHDF Nucleofector Kit: Lonza (Basel, Switzerland)
5. Ampicillin: Sigma-Aldrich-Merck
6. Biotin solution: EZ-Link Sulfo-NHS-SS-Biotin (Thermo Fisher Scientific)
7. BSA: Pierce Protein Biology-Thermo Fisher Scientific
8. Clarity: Western ECL Substrate (Bio-Rad Laboratories, Hercules, CA, USA)
9. CHIR99021: Selleckchem (Houston, TX, USA)
10. Chloroform: Sigma-Aldrich-Merck
11. Collagenase B: Roche-Merck
12. DMSO: Sigma-Aldrich-Merck
13. EDTA: Life Technologies-Thermo Fisher Scientific
14. Ethanol: Scharlab,S.L. (Barcelona, Spain)
15. ExoZAP: PureIT ExoZAP PCR CleanUp (AMPLIQON, Odense M, Denmark)
16. FCS: Sigma-Aldrich-Merck
17. Gel-Dye Mix: Agilent Technologies
18. Gelatin: Sigma-Aldrich-Merck
19. Genecellin transfection kit: BioCellChallenge (Toulon, France)
20. Glycine: Sigma-Aldrich-Merck
21. Heparin: Sigma-Aldrich-Merck
22. Hi-Di™ Formamide: Life Technologies-Thermo Fisher Scientific
23. Isopropanol: Scharlab,S.L.
24. IWP2: Tocris-Bio-Techne
25. KAPA SYBR FAST qPCR: Roche – Merck
26. KOSR: Gibco-Life Technologies
27. Lipofectamine 2000: Invitrogen-Thermo Fisher Scientific
28. Matrigel: BD Biosciences (Franklin Lakes, NJ, USA)

29. Methanol: Scharlab,S.L.
30. Molecular weight marker: PageRuler Plus (Thermo Fisher Scientific)
31. NeutrAvidin Ultralink beads: Gibco-Thermo Fisher Scientific
32. Nuclease-free $H_2O$: Ambion-Life Technologies
33. NucleoSpin® Tissue kit: Macherey-Nagel GmbH & Co KG (Duren, Germany)
34. Opti-MEM: Gibco-Thermo Fisher Scientific
35. PBS: Sigma-Aldrich-Merck
36. Pierce BCA protein assay kit: Thermo Fisher Scientific
37. Poly-L-lysine: Sigma-Aldrich-Merck
38. QIAGEN Plasmid Maxi Kit: QIAGEN (Hilden, Germany)
39. QIAGEN Plasmid Mini Kit: QIAGEN
40. Qiazol: QIAGEN
41. QuantiTect Reverse Transcription kit: QIAGEN
42. QuikChange Site-Directed Mutagenesis kit: Stratagene (La Jolla, CA, USA)
43. RNeasy Mini Kit kit: QIAGEN
44. Skimmed milk powder: Scharlab,S.L.
45. Sodium acetate: Sigma-Aldrich-Merck
46. SureSelect XT Target Enrichment System: Agilent Technologies Inc.
47. TaqMan™ Gene Expression Assay: Applied Biosystems-Thermo Fisher Scientific
48. TE Buffer: QIAGEN
49. TripLE select: Gibco-Thermo Fisher Scientific
50. Tween-20: Sigma-Aldrich-Merck

### 1.6.2. Consumables

51. 1.5 ml tubes: SARSTEDT AG & Co. KG (Nümbrecht, Germany)
52. 70 µm strainer: Falcon-Corning
53. 100 mm culture dish: Falcon-Corning
54. 15 ml tube: Falcon-Corning
55. 19G needle: Sigma-Aldrich-Merck
56. 21G needle: Sigma-Aldrich-Merck
57. 2 ml tubes: Eppendorf (Hamburg, Germany)
58. 35 mm dishes: Falcon-Corning

59. 50 ml tubes: Falcon-Corning
60. 96-well plate: Axygen-Corning
61. Borosilicate glass capillaries: Sutter Instrument (Novato, CA, USA)
62. Coverslip: Thermo Fisher Scientific
63. Cryovials: SARSTEDT AG & Co. KG
64. Forceps: Heinz Herenz Medizinalbedarf GmbH-VWR
65. Pre-cast SDS acrylamide gels: 4-15% Mini-PROTEAN TGX Stain-Free (Bio-Rad Laboratories)
66. PVDF membrane: GE Healthcare Life Sciences (Chicago, IL, USA
67. Scraper: Falcon-Corning
68. TC-treated 12-well plates: Falcon-Corning
69. TC-treated 4-well plates: Falcon-Corning
70. TC-treated 6-well plates: Falcon-Corning
71. TC-treated T75 flask: Falcon-Corning
72. RNA chip: Agilent Technologies

### 1.6.3. Equipments

73. Amaxa Nucleofector 2b: Lonza
74. Axopatch 200B amplifier: Axon Instruments-Molecular Devices (Sunnyvale, CA, USA)
75. Bioanalyzer Agilent 2100: Agilent Technologies
76. Bioruptor®: Diagenode (Belgium)
77. ChemiDoc Imaging System: Bio-Rad Laboratories
78. Cell counter: Invitrogen-Thermo Fisher Scientific
79. Genetic Analyzer 3130XL: Applied Biosystems-Thermo Fisher Scientific
80. Microforge MF-900: Narishige International Limited (London, UK)
81. Microplate reader: Cytation 5 Imaging Reader (BioTek, Winooski, VT, USA)
82. MiSeq platform: Illumina Inc. (California, USA)
83. Mr. Frosty: Freezing container (Nalgene-Sigma-Aldrich-Merck)
84. NANODROP-1000: Thermo Fisher Scientific
85. Narishige PC-10 puller: Narishige International Limited
86. Nikon Eclipse TE300 light microscope: Nikon (Tokyo, Japan)

87. Nikon Eclipse Ti: Nikon
88. pClamp10.2/Digidata 1440A acquisition system: Axon Instruments-Molecular Devices
89. Plate reader: Cytation 5 imaging reader (BioTek, Winooski, VT, USA)
90. Rotating wheel: OVAN (Barcelona, Spain)
91. Sequencer: Genetic Analyzer 3130XL (Applied Biosystems-Thermo Fisher Scientific)
92. Scepter automatic counter: Merck
93. Thermoblock: TS1 ThermoShaker (Biometra, Göttingen, Germany)
94. Veriti™ Thermal Cycler: Applied Biosystems-Thermo Fisher Scientific
95. Vortexer: IKA (Agilent Technologies)

### 1.6.4. Software

96. Image J: National Institutes of Health
97. Origin 2019: OriginLab Corporation (Northampton, MA, USA)
98. pClamp10.2: Molecular Devices
99. Seqscape v.2.5: Applied Biosystems-Thermo Fisher Scientific
100. Sequencing Analysis v.5.2: Applied Biosystems-Thermo Fisher Scientific

## 2. Heterologous expression of the SNVs

### 2.1. Site-directed mutagenesis

pIRES-GFP-SCN1B and pIRES-GFP-SCN1Bb were used as a template to engineer the *SCN1B*_c.308A>T SNV. *SCN5A*_c.4573G>A was introduced in pcDNA3.1-SCN5A. Forward (FW) and reverse (RV) primers (**Table 14**, SNV underlined) to perform the mutagenesis were resuspended and diluted to a final concentration of 100 ng/µl with 50% mQ ultrapure water and 50% TE Buffer (**48**).

**Table 14. Primers used to engineer the SNVs**

| SNV | Primer |
|---|---|
| *SCN1B*_c.308A>T | FW: 5’ CACCAAAGACCTGCAGGTTCTGTCTATCTTCATCA 3’ |
| | RV: 5’ TGATGAAGATAGACAGAACCTGCAGGTCTTTGGTG 3’ |
| *SCN5A*_ c.4573G>A | FW: 5’ CATATTCGACATTATGACCAAGCAGGCCTTTGACGTCACCATCATG 3’ |
| | RV: 5’ CTGCTTGGTCATAATGTCGAATATGAAGCCCTGGTACTTGTTCAGG 3’ |

The mutagenesis reaction was done using the QuikChange Lightning Site-Directed Mutagenesis Kit (**42**). The mix for the mutagenesis reaction was done in a 1.5 ml tube (**51**) and had the following composition (**Table 15**):

**Table 15. Mutagenesis reaction composition**

| Components | Final concentration |
|---|---|
| **10X Reaction Buffer** | 1X |
| **50 ng/µl Template vector** | 50 ng |
| **100 ng/µl Primer FW** | 125 ng |
| **100 ng/µl Primer RV** | 125 ng |
| **dNTP mix** | N/A |
| **Quiksolution reagent** | N/A |

After that, 1 µl of QuikChange Lightning Enzyme was added and all components were transferred to 1 well of a 96-well plate (**60**). The mutagenesis reaction was performed using a Veriti™ Thermal Cycler (**93**) with a profile based on an initial template denaturalization, followed with an 18-cycle program of denaturalization, hybridization and elongation, and ended with a final elongation (**Table 16**).

**Table 16. Mutagenesis thermal cycler profile**

| Step | Temperature | Duration | Cycles |
|---|---|---|---|
| **Initial denaturalization** | 95°C | 2’ | 1 |
| **Denaturalization** | 95°C | 20” | 18 |
| **Hybridization** | 60°C | 10” | |
| **Elongation** | 68°C | 9.5’ | |
| **Final elongation** | 68°C | 5’ | 1 |
| **Final** | 4°C | Infinite | 1 |

The mutagenesis was purified with 10 U/µl *Dpn I* restriction enzyme (final concentration 20 U), to digest the nonmutated parental template. The plate was incubated at 37°C for 1h.

### 2.2. Transformation of bacterial culture

XL-10 gold ultracompetent cells were transformed with the purified mutated *SCN1B*, *SCN1Bb* or *SCN5A* vectors. Cells were gently thawed on ice, and 45 µl of cells were aliquoted in a pre-chilled 1.5 ml tube (**51**). To increase the transformation efficiency, 2 µl β-Mercaptoethanol (**1**) was added to the tubes. The tubes were gently swirled and incubated on ice for 2’. Five microliters of the purified mutagenesis reaction were added and incubated on ice for 30’. The tubes were heat-pulsed at 42°C for 30” and incubated on ice for 2’. NZY$^{+}$ broth (**Table 1**) pre-heated at 42°C was added and incubated at 220 rpm 37°C for 1h.

After that, the tubes were centrifuged at 4000 rpm for 3’. Most part of the supernatant was removed, and 50 µl of the medium with bacteria of each tube were plated in LB-Agar plates (**Table 1, 52**) with 100 mg/ml Ampicillin (Amp) (**5**) and incubated at 37°C overnight (O/N).

### 2.3. Vector purification

A colony from each LB-Agar plate was picked and grown in 4 ml of LB medium (**Table 1**) containing 100 mg/ml Amp (**5**), and incubated at 220 rpm 37°C O/N.

To purify the vector DNA introduced in the XL-10 gold ultracompetent cells, the QIAGEN Plasmid Mini Kit was used (**39**). A glycerol stock composed by 50% glycerol and 50% culture was stored at -80 ºC before proceeding. The bacterial cells were harvested by centrifugation at 5400 x g for 10’ at 4ºC. The pellet was resuspended in Buffer P1 containing RNase A to remove RNA. Buffer P2 was added and mixed by inverting the tube

4-6 times. These two buffers lysate the bacteria under alkaline conditions. Buffer N3 was added and mixed to neutralize the lysate and the tube was centrifuged at 16000 x g for 10’ at room temperature (RT). The supernatant was added to a QIAprep spin column which use a silica membrane, and centrifuged for 1’. The column was washed using Buffer PE to remove salts and centrifuging for 1’. Flow-through was discarded, and the column was centrifuged for 1’ at full speed to remove residual wash buffer. The column was placed in a 1.5 ml tube (**51**), and DNA was eluted by adding Buffer EB (10 mM Tris-Cl, pH 8.5) and centrifuging for 1’.

Eluted DNA was quantified using NANODROP-1000 (**84**). Concentration measures were performed using an absorbance (A) of 260 nm, a wavelength where nucleic acids absorb. $A_{260nm}/A_{280nm}$ was used to assess protein contamination: a pure DNA preparation shows a ratio between 1.8 and 2.0. $A_{260nm}/A_{230nm}$ is a secondary measure to assess nucleic acid purity. Values between 2.0 and 2.2 are indicators of DNA purity, while lower values indicate presence of organic solvents. Upon quantification, vector DNA was stored at -20°C.

The eluted DNA was sequenced as described in **section 4.1.2** to verify the presence of the desired SNV and the absence of additional variations.

Upon validation of the presence of the desired SNV, the previously stored bacteria glycerol stock was scratched and grown in 4 ml of LB medium (**Table 1**) containing 100 mg/ml Amp (**5**) at 220 rpm 37 ºC for 5-6h. This starter culture was diluted into a 100 ml of LB medium with 100 mg/ml Amp (**5**) and grown at 220 rpm 37°C O/N. The QIAGEN Plasmid Maxi Kit (**38**) was used to purify the vector DNA.

The bacterial cells were harvested by centrifugation at 6000 x g 4°C for 15’ and the pellet resuspended with buffer P1. Buffer P2, that helps with cell lysis, was added and mixed by inverting the tube until it results in a homogeneous colored suspension, and incubated at RT for 5’. Pre-chilled buffer P3 was added to the lysate and mixed by inverting the tube. The lysate was poured into the barrel of a cartridge with a cap and incubated at RT for 10’. The cap was removed and the plunger inserted filtering the cell lysate into a 50 ml tube. Buffer ER was added to the filtered lysate and mixed by inverting the tube, incubated on ice for 30’. While the sample was incubated, a QIAGEN-tip was equilibrated by applying buffer QBT and allowing the column to empty by gravity flow. The filtered lysate was added to the tip and allowed to enter by gravity flow. The tip was washed twice with buffer QC and the DNA was eluted with buffer QN. Eluted DNA was precipitated adding RT isopropanol and centrifuged at 15000 x g 4°C for 30’. DNA pellet was washed with endotoxin-free RT 70% ethanol and centrifuged at 15000 x g for 10’. The pellet was air-dried and buffer TE was added and incubated at 4°C O/N. The volume was transferred to a 1.5 ml tube (**51**) and quantified using NANODROP-1000 (**84**) as previously described.

### 2.4. HEK-293T cell culture

The HEK-293T cells to perform the molecular studies of the SNVs were plated with DMEM medium (**Table 2**) on 6-well plates (**70**), while the cells to perform the electrophysiological studies were plated on 35 mm dishes (**58**) coated with poly-L-lysine (**37**). They were transiently transfected 24h after plating using Lipofectamine 2000 (**27**) and Opti-MEM (**34**) (**Table 17**). The effect of the β1b subunit on Na$_V$1.5 current was studied using the Genecellin transfection kit (**19**). The medium of the 6-well plates was changed 24h after transfection, and cells were collected 48h after with lysis buffer (**Table 9**) for western blot, or for biotinylation assay as indicated in **section 4.4**. The cells plated on 35 mm dishes were split and plated again on 35 mm dishes, to obtain isolated single cells that allowed the electrophysiology experiments. These experiments were performed approximately 18h after splitting.

**Table 17. Transfection conditions studied**

| Conditions | Amount of vectors used (µg) |
|---|---|
| Na$_V$1.5$^{WT}$ + GFP | 1.54 + 0.1 |
| Na$_V$1.5$^{WT}$ + β1 or β1b$^{WT}$ | 1.54 + 0.46 |
| Na$_V$1.5$^{WT}$ + β1 or β1b$^{D103V}$ | 1.54 + 0.46 |
| Na$_V$1.1$^{WT}$ + GFP | 1.54 + 0.1 |
| Na$_V$1.1$^{WT}$ + β1 or β1b$^{WT}$ | 1.54 + 0.46 |
| Na$_V$1.1$^{WT}$ + β1 or β1b$^{D103V}$ | 1.54 + 0.46 |
| Na$_V$1.5$^{V1525M/V1525M}$ + GFP | 1.54 + 0.1 |
| Na$_V$1.5$^{WT/V1525M}$ + GFP | 0.77 + 0.77 + 0.1 |

## 3. Obtaining of patient-specific iPS-CM

### 3.1. Obtaining of skin biopsies

Our collaborators at Hospital Sant Joan de Déu obtained the skin biopsies. Before performing the biopsy, the skin area of the patients and control was cleaned with ethanol. A scalpel was used to perform an incision that included the dermis, and the blood excess was washed. The biopsies were extracted using forceps and collected in fibroblasts medium (**Table 3**), and were kept on ice until processing.

### 3.2. Obtaining of fibroblasts

Tissue with a small volume of fibroblasts medium was poured onto the cover of a 100 mm dish (**53**). The sample was dissected into 12-15 pieces with two sterile scalpels. Four tissue pieces were transferred into each of the 3 top wells of a 6-well plate (**70**) using forceps (**64**) and covered with a sterile coverslip (**62**). The coverslips were pressed with the forceps and fibroblasts medium was slowly added. The tissue pieces were cultured at 37°C and 5% $CO_2$. The first medium change was done 7 days after, and subsequently every 4-5 days. Around day 21, fibroblasts covered the whole surface under the coverslip and were ready for the first passage.

On the first passage, Phosphate-buffered saline (PBS) (**35**) was added to all the wells from the 6-well plate. Coverslips were transferred using forceps from the top wells to the bottom wells, upside-down. PBS was aspirated and TripLE select (**49**) was added and incubated at 37°C for 3'. Fibroblasts medium was added on top and the fibroblasts were detached using a cell scraper (**67**). Medium with fibroblasts and skin pieces was collected in a 15 ml tube (**54**) and centrifuged at 1000 rpm for 4'. The supernatant was aspirated and the cell pellet resuspended in fibroblasts medium, and transferred to a TC-treated T75 flask (**71**). Medium was changed twice a week.

The fibroblasts were ready for freezing when they covered the whole surface of the T75 flask. They were detached as described above and centrifuged at 1000 rpm for 4'. Supernatant was discarded, cell pellet was resuspended with fibroblasts freezing medium composed by fetal calf serum (FCS) (**16**) + 10% Dimethyl sulfoxide (DMSO) (**12**) and distributed into 2 cryovials (**63**). They were stored in a Mr. Frosty (**83**) at -80ºC, to be transferred the day after into the $LN_2$ tank.

### 3.3. Fibroblasts reprogramming to iPS cells

Fibroblasts were reprogrammed to iPS cells using the Yamanaka factors and the Amaxa NHDF Nucleofector Kit (**4**). Fibroblasts maintained in a T75 flask were detached as described above. Cells were counted doing a 1:10 dilution and using the Scepter automatic counter (**91**).

500.000 fibroblasts were aliquoted in a new 15 ml tube (**54**) and centrifuged at 200 x g for 10'. Cell pellet was resuspended with 100 µl of nucleofection solution (82 µl solution + 18 µl supplement) and transferred to a 1.5 ml tube. A total of 5 µg of the episomal vectors pCXLE-hOCT3/4-shp53-F, pCXLE-hSK and pCXLE-hUL were added to the tube (**Table 18**, equal amounts of each vector).

**Table 18. Vectors used for reprogramming**

| Vector | Genes encoded | Quantity | Addgene reference |
|---|---|---|---|
| **pCXLE-hOCT3/4-shp53-F** | Oct4 and shp53 | 1.7 µg | #27077 |
| **pCXLE-hSK** | Sox2 and Klf | 1.6 µg | #27078 |
| **pCXLE-hUL** | LMyc and Lin28 | 1.7 µg | #27080 |

The mix was gently pipetted up and down and transferred to the cuvette provided by the kit. The cuvette was inserted in an Amaxa Nucleofector 2b (**73**) and the U023 protocol was selected for maximum nucleofection efficiency. Nucleofected fibroblasts were plated in one well of a 6-well plate (**70**) coated with 1% gelatin (**18**) with pre-warmed fibroblasts medium.

Twenty-four hours after nucleofection, medium was replaced with 10% DMEM (**Table 4**). Media was changed again 3 days later.

Seven days after nucleofection, cells were incubated with 0.05% Trypsin/Ethylenediamine-tetraacetic acid (EDTA) (**2**) at 37°C for 5'. Medium was poured on top of the cells to detach them, and were collected in a 15 ml tube (**54**). The tube was centrifuged at 1000rpm for 5' and the cell pellet was resuspended in 10% DMEM. The cells were plated onto a 0.1% gelatin-coated 100 mm culture dish (**53**). After 24 hours, medium was changed to TeSR-E8. Medium changes were done every two days and cell morphology was assessed using a Nikon Eclipse TE300 light microscope (**86**).

iPS-like colonies started to appear 20-25 days after nucleofection. Individual colonies were manually picked into separate wells of Matrigel (**28**) coated TC-treated 4-well plates (**69**) in TeSR-E8 medium. Colonies were treated as individual clones and expanded to give rise to independent cell lines. Medium changes were done daily and cells were passaged using 0.5 mM EDTA (**13**) and a cell scraper (**67**).

Cells of passages 7-9 were frozen to have a cell stock. Wells were washed with PBS and 0.5 mM EDTA (**13**) was added and incubated at 37°C for 4’. EDTA was aspirated and cells were collected with TeSR-E8 medium in a 15 ml tube (**54**) and centrifuged at 200 x g for 5’. Cell pellet was resuspended in freezing medium composed by 90% knock out serum replacement (KOSR) (**26**) and 10% DMSO (**12**) and transferred to a cryovial (**63**). They were kept for 24 hours in a Mr. Frosty (**83**) at -80°C and stored in a $LN_2$ tank.

Cell pellets of passages 7 – 11 of each clone were collected for RNA or DNA extraction. Wells were washed with PBS (**35**), cells were collected into a 15 ml tube (**54**) by pipetting and centrifuged at 200 x g for 5’. Cell pellets were kept at -80°C until needed.

## 3.4. Differentiation of iPS cells to iPS-CM

### 3.4.1. iPSc culture

As needed, iPS clones were thawed. mTeSR1 + 10 µM ROCKi medium was prepared in a 15 ml tube (**54**). A small volume of this medium was aspirated to continue aspirating the cells from the cryovial, and then returned to the tube, which was then centrifuged at 200 x g for 5’. Cell pellet was resuspended with mTeSR1 + ROCKi medium and distributed in the wells of a matrigel-coated 6-well plate (**70**). Before starting the cardiomyocyte differentiation, a couple of passages were performed to allow cells to adapt from the TeSR-E8 to the mTeSR1 medium.

iPS cells maintained in the 6-well plate were fed every day with mTeSR1, and passaged every 4-7 days. For passaging, cells were washed with PBS (**35**) and incubated with prewarmed 0.5 mM EDTA (**13**) at 37°C for 4’. After aspirating EDTA, the plate was gently tapped from all four sides to facilitate cell detachment. mTeSR1 + ROCKi medium was poured on top of the cells and collected in a 50 ml tube (**59**). Cells were counted using a cell counter (**78**). 100.000-300.000 cells were plated in mTeSR1 + ROCKi in a matrigel-coated 6-well plate (**70**) for maintenance.

### 3.4.2. Cardiomyocyte differentiation

Two clones of each patient and of the control were differentiated into cardiomyocytes. To obtain high yield and pure cardiomyocyte monolayers, a 3-step protocol was followed, based on three previous publications. First, iPSc were differentiated to cardiomyocytes[210]. In order to enhance the purity of the culture, a starvation protocol was followed, using a medium without glucose[136]. Finally, we aimed to increase the cardiomyocyte maturity by using the differentiation medium with two hormones[211], and replating the cells on day 16 of differentiation.

The first step consisted in: after iPS cells reached a 90% confluence, they were detached as described above, and 625.000-800.000 cells were plated in each well of a matrigel-coated 12-well plate (**68**). This was counted as day -3/-2 of the differentiation protocol. mTeSR1 medium was changed every day.

Differentiation began in 2-3 days, when 100% optical confluence was reached, and consisted in changing the differentiation medium (**Table 5**) with a specific composition every day after exactly 24 hours. This was counted as day 0.

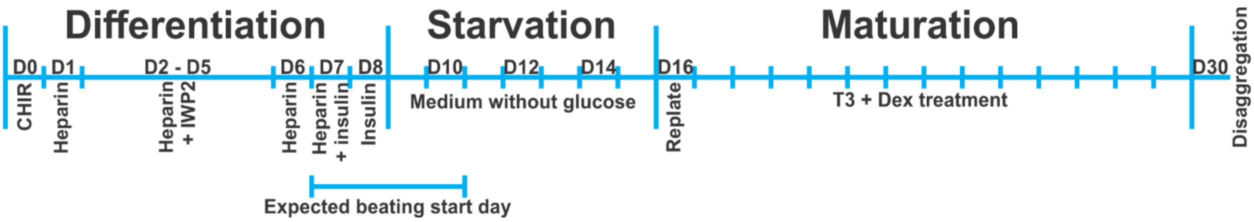

**Figure 24. Schematic representation of the optimized differentiation protocol.** Protocol based on the studies published by Lin et al, Sharma et al, and Parikh et al, and including our modifications.

**Figure 24** summarizes the differentiation protocol followed. On day 0, differentiation started incubating the cells with differentiation medium that contained 4µM CHIR99021 (**9**).

24h later, medium was changed to differentiation medium containing 3 µg/ml heparin (**21**). On days 2, 3, 4 and 5, the differentiation medium contained 3µg/ml heparin and 3 µM IWP2 (**24**).

On day 6, the differentiation medium only contained 3 µg/ml heparin.

On day 7, differentiation medium contained 3 µg/ml heparin and 10 µg/ml insulin.

On day 8, differentiation medium contained 10 µg/ml insulin. Cells were expected to beat between day 7 and day 10.

On days 10, 12 and 14, the medium SILAC without glucose (**Table 6**) was used to purify the cardiomyocyte population, due to the ability of this cell type to metabolize lactate as the primary energy source, while other cell types can't.

On day 16, iPS-CM were replated to a new 12-well plate (**68**). With this, the matrigel from the plate is renewed and a monolayer of beating cells is obtained, which improves their survival. Every well was treated with 400U/mg Collagenase B (**11**) at 37°C for 30'-2h. To allow detachment, cells were slightly shaked every 10'. When the cardiomyocyte monolayer was detached, it was transferred to a 15 ml tube (**54**) and centrifuged at 200 x g for 4'. 0.25% Trypsin (**3**) was added to the cell pellet and the tube was incubated at 37°C for 11'. After that, double volume of previously warmed digestion medium (**Table 8**) was added and cells were gently pipetted up and down. Cells were centrifuged at 200 x g for 4' and cell pellet was resuspended with digestion medium. Cardiomyocytes were strained with a 70 µm strainer (**52**) into a 50 ml tube (**59**), and the strainer was washed with digestion medium. Cells were counted as above and approximately $2.5 \cdot 10^6$ cells were plated on each matrigel-coated well of a 12-well plate.

From day 17 to day 30, medium was changed every day with maturation medium (**Table 7**).

On day 30, cells were plated for functional studies or collected for DNA or RNA extraction.

- For the functional studies, cells were disaggregated using the Collagenase B-based protocol previously described. On the final step, $1 \cdot 10^5$ cells were plated in 0.1% gelatin-coated 35 mm dishes (**58**).
- For DNA extraction, cells were harvested in PBS by centrifugation at 200 x g for 5' and stored at -80°C until used.
- For RNA extraction, cells were pipetted in Qiazol (**40**), collected in 2 ml tubes (**57**) and stored at -80°C until used.

# 4. Molecular studies

## 4.1. *SCN5A* sequencing

### 4.1.1. Genomic DNA extraction

Genomic DNA extraction of iPSc pellets collected and frozen at -80°C was performed following the NucleoSpin® Tissue kit specifications (**33**). The cell pellets were lysed with buffer T1 that contains SDS. Proteinase K solution was added as well as buffer B3. The sample was vortexed and incubated at 70°C for 15’. 96-100% ethanol (**14**) was added and the sample was vortexed vigorously. The sample was applied in a NucleoSpin® Tissue column placed in a collection tube, and the DNA was bound to the silica membrane. The column was centrifuged at 11000 x g for 1’ and placed into a new collection tube. The silica membrane of the column was washed to eliminate possible contaminations. First, with buffer BW and centrifuging at 11000 x g for 1’, then with buffer B5 and centrifuging at 11000 x g for 1’. The membrane was dried by a centrifugation at 11000 xg for 1’, and it was placed in a 1.5 ml tube (**51**). To elute the DNA, buffer BE was added to the column and incubated at RT for 1’, and centrifuged at 11000 x g for 1’.

Genomic DNA was quantified using NANODROP-1000 (**84**). Upon quantification, DNA samples were stored at -20°C.

### 4.1.2. Amplification, purification and sequencing

Genetic analysis of all exons of the *SCN5A* gene was performed on all iPSc clones. DNA amplification was performed using the polymerase chain reaction (PCR) technique in 96-well plates (**60**). Every amplification reaction had the composition specified in **Table 19** and a final volume of 12.5 µl adjusted with mQ water. The amplifications were performed using a Veriti™ Thermal Cycler (**93**) with a profile based on an initial DNA denaturalization, followed with a 40-cycle program (**Table 20**). The correct fragment amplification was verified with a 1.2% agarose electrophoresis gel, run at a voltage of 90 V for 30’.

Table 19. PCR components

| Component | Final concentration | Reference |
|---|---|---|
| **GoTaq G2 Hot Start Colorless Master Mix 2X** | 1X | Promega (Madison, WI, USA) |
| **10 µM Primers** | 0.8 µM | N/A |
| **10 ng/µl DNA** | 0.8 ng/µl | N/A |
| **Nuclease-Free water** | N/A | Promega |

Table 20. PCR thermal cycler profile

| Step | Temperature | Duration | Cycles |
|---|---|---|---|
| **Initial denaturalization** | 95°C | 3’ | 1 |
| **Denaturalization** | 94°C | 30” | 40 |
| **Hybridization** | 60°C | 30” | |
| **Elongation** | 72°C | 45” | |
| **Final elongation** | 72°C | 5’ | 1 |
| **Final** | 4°C | Infinite | 1 |

Amplicons were purified using ExoZAP (**15**). This reagent contains two enzymes: exonuclease I that degrades single stranded DNA, and shrimp alkaline phosphatase that degrades any remaining dNTP. The reaction was performed in a final volume of 3.5 µl (1 µl reagent and 2.5 µl PCR product). The reaction was performed in a 96-well plate (**60**) on a Veriti™ Thermal Cycler (**93**), and the protocol consists of two steps: first the purification reaction at 37°C for 5’, and second the enzymes inactivation at 80°C for 5’.

The sequencing reaction was done with the Sanger method using the BigDye Terminator v3.1 kit. The reaction was done in a final volume of 5 µl in 96-well plates (**Table 21**), using a Veriti™ Thermal Cycler (**93**). Sequence reaction profile was based in an initial denaturalization, followed by 25 cycles of denaturalization, hybridization and elongation (**Table 22**).

Table 21. Sequence reaction components

| Component | Final concentration | Company |
|---|---|---|
| **5X Sequence Buffer** | 1X | Life Technologies |
| **BigDye® Terminator v3.1 Ready Reaction Mix** | 1X | Applied Biosystems-Thermo Fisher Scientific |
| **10 mM primer forward or reverse** | 1mM | N/A |
| **PCR purified product** | 0.8 ng/µl | N/A |
| **$H_2O$** | N/A | N/A |

**Table 22. Sequence reaction profile**

| Step | Temperature | Duration | Cycles |
|---|---|---|---|
| **Initial denaturalization** | 96°C | 1’ | 1 |
| **Denaturalization** | 96°C | 10” | 25 |
| **Hybridization** | 50°C | 5” | |
| **Elongation** | 60°C | 4’ | |
| **Final** | 4°C | Infinite | 1 |

Once the sequencing reaction was finished, DNA was precipitated using 80 µl per well of an 70% ethanol – sodium acetate solution (**45**). It was centrifuged at 2000 x g for 45’. The previous solution was eliminated and 150 µl of 70% ethanol (**14**) was added and centrifuged at 2000 x g for 10’. The precipitated product was resuspended in 10 µl Hi-Di™ Formamide (**22**) and incubated at 95°C for 10’.

The product was analyzed with capillary electrophoresis using the sequencer (**90**).

The resulting data was analyzed using Sequencing Analysis v.5.2 (**99**) and Seqscape v.2.5 (**98**) software. Data was compared with the reference sequence for *SCN5A* of the NM000335 isoform to determine genetic variations with respect to the human genome.

### 4.2. Genetic panel associated to arrhythmogenic diseases

This experimental procedure was provided by the Genetic diagnostics section of our group. Briefly, iPSc DNA was fragmented with Bioruptor® (**76**) and libraries were prepared following the SureSelect XT Target Enrichment System (**46**) for Illumina Paired-End Sequencing Library protocol. The panel was designed by the group of bioinformaticians in our lab and then validated (SureSelect XT Custom 0.5–2.9 Mb library). All coding regions of described isoforms and intronic positions up to 6 base pairs of the following genes were interrogated:

*ABCC9, ACTA2, ACTC1, ACTN2, AKAP9, ANK2, ANKRD1, BAG3, BRAF, CACNA1C, CACNA2D1, CACNA1G, CACNA1H, CACNA1I, CACNB2, CALM1, CALM2, CALM3, CALR3, CASQ2, CAV3, CBL, COL3A1, CRYAB, CSRP3, CTNNA3, GJA1, CTF1, DES, DMD, DMPK, DPP6, DSC2, DSG2, DSP, DTNA, ECE1, EMD, EN1, EYA1, EYA4, FBN1, FBN2, FHL2, FKTN, FLNA, FLNC, GAA, GJA5, GLA, GPD1L, HCN1, HCN2, HCN4, HRAS, JPH2, JUP, KCNA5, KCND3, KCNE1, KCNE2, KCNE3, KCNE4, KCNE5, KCNH2, KCNJ2, KCNJ5, KCNJ8, KCNQ1, KRAS, LAMA4, LAMP2, LDB3, LMNA, MAP2K1, MAP2K2, MYBPC3, MYH11, MYH6, MYH7, MYL2, MYL3, MYLK2, MYOZ2, MYPN, NEBL, NEXN, NF1, NOS1AP, NOTCH1, NPPA, NRAS, NUP155,*

*PDLIM3, PHOX2A, PHOX2B, PITX2, PKP2, PLN, PRKAG2, PTPN11, RAF1, RANGRF, RBM20, RET, RIT1, RYR2, SCN1B, SCN2B, SCN3B, SCN4B, SCN5A, SCN10A, SDHA, SGCD, SHOC2, SLC22A5, SLC6A4, SLC8A1, SLMAP, SLN, SMAD3, SNTA1, SOS1, SOS2, SPRED1, TAZ, TCAP, TGFB2, TGFB3, TGFBR1, TGFBR2, TGFBR3, TLX3, TMEM43, TMPO, TNNC1, TNNI3, TNNT2, TP63, TPM1, TRDN, TRIM63, TRPM4, TTN, TTR, VCL.*

Indexed libraries were sequenced in ten-sample pools per cartridge. Paired-end sequencing process was performed on a MiSeq platform (**82**), with a read length of 2 × 76 bp.

An in-house developed pipeline algorithm was used for the analysis of SNVs and indels. Adaptors and low-quality bases from raw FASTQ files were trimmed and reads were mapped with BWA-MEM (http://bio-bwa.sourceforge.net/). Only properly mapped read pairs were selected. The SNV and indel detection was performed with SAMtools v.1.2 (http://samtools.sourceforge.net/), together with an ad hoc developed script. The SNVs and indels identified were annotated with dbSNP Build 142 (http://www.ncbi.nlm.nih.gov/SNP/), Exome Sequencing Project ESP6500SI-V2 (http://evs.gs.washington.edu/EVS/), 1000 Genomes Phase 3 (http://www.1000genomes.org/), ExAC v.0.3 (http://exac.broadinstitute.org/), Human Gene Mutation Database (http://www.hgmd.cf.ac.uk/ac/index.php), ClinVar (http://www.ncbi.nlm.nih.gov/clinvar/), ENSEMBL and in-home database IDs.

## 4.3. *SCN5A* mRNA expression

### 4.3.1. RNA extraction

Two different protocols of RNA extraction were used depending on the cell line. For the RNA extraction of iPSc pellets collected and frozen at -80°C, the RNeasy Mini Kit kit (**43**) protocol was followed. Buffer RLT with β-Mercaptoethanol was added and pipetted up and down. The lysate was transferred into a Qiashredder spin column placed in a collection tube and centrifuged at 16000 x g for 2’. 70% ethanol (**14**) was added into the sample in the collection tube and pipetted up and down. The sample was transferred into an RNeasy spin column placed in a collection tube and centrifuged at 8000 x g for 15”. Flow-through was discarded and DNase solution (70 µl buffer RDD + 10µl DNase I) was added to the column and incubated at RT for 15’. Buffer RW1 was added to the column and centrifuged at 8000 x g for 15”, discarding the flow-through. Buffer RPE was added twice, centrifuging at 8000 x g for 15” the first time and 2’ the second. Column was centrifuged at 16000 x g for 1’ and placed in a new 1.5 ml tube (**51**). The column membrane was incubated with RNase-free water at RT for 1’ and centrifuged at 8000 x g for 1’.

A protocol based on Qiazol (**40**) was used to extract RNA of iPS-CM. Previously collected samples were thawed on ice and cells were fragmented with a syringe and a needle if any clumps remained. First, a 19G needle (**55**) was used, and then a 21G (**56**) until no fragments were seen. Upon fragmentation, samples were incubated at RT for 5’. After that, 100% chloroform (**10**) was added and the sample was vortexed for 45” followed by an incubation at RT for 10’. Samples were centrifuged at 12000 x g 4°C for 15’. The superior transparent phase was trespassed to a 1.5 ml tube (**51**) and 100% isopropanol (**23**) was added. The tubes were inverted 3-4 times and incubated at RT for 10’. Samples were centrifuged at 12000 x g 4°C for 10’. Cell pellet was washed with 70% ethanol (**14**) and centrifuged at 12000 x g 4°C for 10’. Ethanol was discarded and the washing step was repeated 4 more times. Samples were incubated on a thermoblock (**92**) at 55°C until ethanol was evaporated and the pellet looked transparent. Nuclease-free $H_2O$ was added and the pellet was dissolved at 55°C for 10’.

Extracted RNA from both protocols was quantified using the NANODROP-1000 (**84**). Concentration measures were performed using an A of 260 nm. $A_{260nm}/A_{280nm}$ was used to assess protein contamination: a pure RNA preparation shows a ratio of 2.1. $A_{260nm}/A_{230nm}$ shows salts and phenol contaminants, the ideal ratio should be greater than 1.5. Upon quantification, RNA samples were stored at -80°C.

RNA quality from iPS-CM samples was assessed using the Bioanalyzer (**75**). First, a Gel-Dye Mix (**17**) consisting of RNA gel matrix and RNA dye concentrate was prepared. Then, it was added in the well, marked as a circled G of an RNA chip (**Figure 25**) (**72**). RNA marker was loaded in all 12 sample wells and in the well marked with stairs in the figure. RNA ladder was added in the well, marked with stairs, and each sample in each of the 12 sample wells. The chip was vortexed in a vortexer (**94**) for 1’ at 2400 rpm, and loaded in the bioanalyzer.

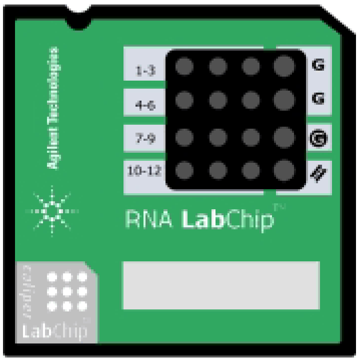

**Figure 25. Picture of the Bioanalyzer RNA chip used to assess RNA quality.** Adapted from https://ipmb.sinica.edu.tw/microarray/workshop/workshop-11.pdf

### 4.3.2. Retrotranscription

RNA samples were first retrotranscribed to cDNA using the QuantiTect Reverse Transcription kit (**41**). All samples at a concentration of 500 ng/µl were first incubated with gDNA wipeout buffer 7X in a 96-well plate (**60**) on a Veriti™ Thermal Cycler (**93**) at 42°C for 2’. Retrotranscription master mix (**Table 23**) was added to each well and incubated at 42°C for 15’ and at 95°C for 3’. Samples were collected in a 1.5 ml tube (**51**) and used for quantitative PCR (qPCR) or stored at -20°C.

**Table 23. Retrotranscription components**

| Component | Final concentration |
|---|---|
| **Quantriscript Reverse Transcriptase** | N/A |
| **Quantriscript RT Buffer 5X** | 1X |
| **RT Primer Mix** | N/A |

### 4.3.3. qPCR

Two different kits were used for the qPCR experiments, which differed in the assay chemistry.

The first kit, KAPA SYBR FAST qPCR (**Table 24**) (**25**) contains a dye (SYBR Green) that binds to the double stranded DNA and thus allows the detection of the PCR product. When using this kit, *GAPDH* was used as a housekeeping gene (HKG). All the sequences of the primers used can be found in **Annex Table 2**.

Table 24. KAPA SYBR FAST qPCR Kit components.

| Component | Final concentration |
|---|---|
| **KAPA SYBR FAST qPCR Master Mix (2X) Universal** | 1X |
| **10 µM forward primer** | 200 nM |
| **10 µM reverse primer** | 200 nM |
| **Template DNA** | 25 ng |
| **50X ROX Low** | 1X |
| **PCR-grade water** | N/A |

The other assay chemistry used was the TaqMan™ Gene Expression Assay (**47**), which use a gene-specific fluorogenic probe (**Table 25**). In these experiments, the HKG used were *PPIA* and *18S*. More information about the probes used can be found in **Annex Table 3**.

Table 25. TaqMan™ Gene Expression Assay components.

| Component | Final concentration |
|---|---|
| **TaqMan® Fast Advanced Master Mix (2X)** | 1X |
| **TaqMan® Assay (20X)** | 1X |
| **Template DNA** | 25 ng |
| **Nuclease-Free Water** | N/A |

qPCR data analysis was performed with the ThermoFisher Connect tool (https://www.thermofisher.com/es/es/home/digital-science/thermo-fisher-connect.html).

## 4.4. *SCN5A* protein expression

### 4.4.1. Western blot

HEK-293T cells were collected with the lysis buffer described in **Table 9**. HEK-293T cells were lysed in a rotating wheel (**89**) at slow speed for 1h in the cold room. Lysates were centrifuged at 16000 x g 4°C for 15’ and supernatant was transferred to a new 1.5 ml tube (**51**).

Protein concentration was determined with the Pierce BCA protein assay kit (**36**) using a standard curve with quantities from 0.5 to 7 µg of bovine serum albumin (BSA) (**7**) protein in 96-well plates (**60**).

Diluted samples were added to the plate next to the standard curve wells. BCA reagent was added to each well and the plate was covered with an adhesive plastic and incubated at 37°C for 30’. The wells’ absorbance was read in the microplate reader (**81**) at 562 nm.

Proteins were separated by electrophoresis in pre-cast SDS acrylamide gels (**65**) that include a trihalo compound that reacts with the tryptophan residues in proteins. This allows rapid fluorescence detection of proteins in gels or membranes without staining. Samples were diluted using 5X Loading buffer (**Table 10**) and were heated at 70°C for 10’. Between 20 – 60 µg of protein were loaded in the gel next to molecular weight marker (**30**). Protein separation was done in 1X running buffer (**Table 10**) in two steps. First, a voltage of 100 V was applied for 10’ to allow protein concentration. Second, to separate the proteins, a voltage of 160 V was applied until the blue dye front nearly ran out from the gel.

Once the proteins were separated, they were transferred to a PVDF membrane (**66**) in 1X western blot transfer buffer (**Table 10**) with 20% methanol (**29**) at 30 V O/N at 4°C. Gels were read by exposure to UV light in a ChemiDoc Imaging System (**77**) before and after transference, to ensure that most of the proteins were transferred to the membrane.

The membrane was then blocked with 5% skimmed milk powder (**44**) in PBS with 0.1% Tween-20) (PBS-T, **50**) at RT for 1h. It was incubated with either the rabbit anti-human $Na_V1.1$ antibody at a 1:100 dilution O/N at 4°C, or the rabbit anti-human $Na_V1.5$ at a 1:1000 dilution for 1h at RT.

Membranes were washed twice with PBS-T and once with PBS for 10’. Membranes were further incubated with the secondary horseradish peroxidase-conjugated anti-rabbit antibody at a 1:10000 dilution for 1h at RT. The membranes were washed twice with PBS-T and once with PBS for 10’. Chemiluminescent signal was obtained with Clarity (**8**) and detected using the ChemiDoc Imaging System (**77**). Expression of $Na_V1.1$ and $Na_V1.5$ was quantified using ImageJ software (**95**). Membrane intensity values for each sample were normalized by the total lane density read in the membrane after protein transfer.[212] Taylor and Posch demonstrated that this method is a valid approach to normalize western blot data. Furthermore, total lane density normalization rendered better results than the traditional data normalization with housekeeping proteins. Protein bands linearity was far superior in stain-free total protein measurement than in immunodetection of housekeeping proteins.[213]

### 4.4.2. Cell surface protein biotinylation

HEK-293T cells were plated in 6-well plates (**70**). All procedures were done in cold conditions. Cells were washed twice with cold DPBS$^+$ (**Table 11**) and incubated with 1 mg/ml of biotin solution (**6**) for 30' with gentle rocking. Cells were washed three times with cold 100 mM glycine (**20**) in DPBS$^+$ for 5' with gentle rocking. They were detached from the plate in lysis buffer LB3 (**Table 11**) with the help of scrapers (**67**), and collected in 1.5 ml tubes (**51**). Tubes were placed in a rotating wheel (**89**) at slow speed for 1h to allow cell lysis.

While the cell lysis was performed, the NeutrAvidin Ultralink beads (**31**) were prepared. They were washed twice with DPBS$^+$ and twice with LB2 (**Table 11**), and were centrifuged at 3000 x g 4°C for 30”. After the last wash, they were resuspended with LB3 (**Table 11**).

Cell lysates were centrifuged at 16000 x g 4°C for 15'. Supernatant was transferred to a new 1.5 ml tube (**51**), keeping 10% of the volume in another tube as the input sample and stored at -80°C. The rest of the sample was referred as the pull-down sample. Pull-down samples were incubated with NeutrAvidin beads O/N in the rotating wheel. Samples were centrifuged at 16000 x g 4°C for 30”. Beads were washed by centrifugation at 16000 x g 4°C for 30”, once with LB3, twice with LB2, twice with SWS (**Table 11**) and once with LB1 (**Table 11**). Precipitated proteins were resuspended in 5X loading buffer (**Table 10**) and heated at 95°C for 5'. Pull-down samples were kept at -80°C until the western blot was performed as described above.

## 5. Functional studies

### 5.1. Sodium current recordings

Sodium currents from HEK-293T cells displaying green fluorescence and from patient-specific iPS-CM were studied at RT using the whole cell patch clamp technique, 48h after transfection or disaggregation respectively. Bath solutions used are described in **Table 12**. Pipettes were pulled from borosilicate glass capillaries (**61**) with a puller (**85**), and further polished using a microforge (**80**) to obtain a resistance that ranged 2-4 MΩ when filled with pipette solution (**Table 13**).

Experiments were conducted with an Axopatch 200B amplifier (**74**) and pClamp10.2/Digidata 1440A acquisition system (**88**, **97**), at a sampling rate of 25 kHz.

Data was filtered at 5 kHz. The series resistance compensation of 80-90% was used when necessary, and the leak subtraction was not used.

To permit current stabilization, recordings were performed at least 5 minutes after entering the whole cell configuration. Membrane potentials were not corrected for junction potentials that arose between the bath and the pipette solution.

Sodium currents were studied with voltage-clamp step protocols. To determine the current-voltage (IV) relationship and voltage dependence of activation, cells were held at -120 mV and currents were elicited with depolarizing pulses of 50 ms from -80 to 80 mV in 5 mV increments (**Figure 26, left**). The voltage dependence of inactivation was determined by applying 50-ms prepulses from -140 to 5 mV in 5 mV increments, followed by a -20-mV test pulse (**Figure 26, middle**). Recovery from inactivation was studied with a two-pulse protocol consisting of a first -20 mV pulse of 50 ms from a holding potential of -120 mV, followed by a -120 mV interpulse of varying duration (1-40 ms), and a second -20 mV pulse of 50 ms (**Figure 26, right**).

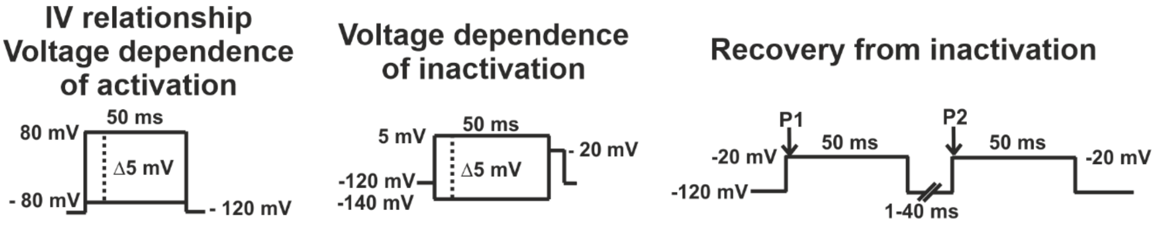

**Figure 26. Protocols used for the electrophysiological characterization of the sodium current.** Left inset was used to study the IV relationship and the voltage dependence of activation, middle for the voltage dependence of inactivation and right for the recovery from inactivation.

### 5.2. Data analysis

Data obtained in the sodium current functional studies was analyzed using the Origin 2019 software (**96**).

Current density was obtained by normalizing the current at each potential by the cell capacitance and plotted against the applied voltage. Voltage dependence of activation data was plotted against the applied voltage and fitted to a Boltzmann equation of the form:

$$g = \frac{gmax}{\dfrac{1 + \exp\,(V_{\frac{1}{2}} - V)}{k}}$$

where g is conductance, $g_{max}$ is maximum conductance, $V_{1/2}$ is the voltage at which half of the channels are activated, V is membrane potential and k is the slope factor.

Voltage dependence of inactivation data was plotted against the applied voltage and fitted to a Boltzmann equation of the form:

$$I = \frac{Imax}{\dfrac{1 + \exp\,(V - V_{\frac{1}{2}})}{k}}$$

where I is peak current amplitude, $I_{max}$ is maximum current amplitude, $V_{1/2}$ is the voltage at which half of the channels are inactivated, V is membrane potential and k is the slope factor.

Recovery from inactivation data was fitted to a mono- or bi-exponential function to obtain the time constant. P1/P2 peak current values were plotted against different interpulse intervals.

## 6. Statistical analyses

Data normality was verified with the Kolmogorov-Smirnov test. Statistical comparisons of the means between two groups were performed using the parametric test t-test, for the analysis of electrophysiological data of **Study 1** and the iPS-CM of **Study 2**, Western blot and cell surface biotinylation assay. The parametric test one-way ANOVA with a post-hoc Tukey test was used for comparisons that included three or more groups. This test was used for the analysis of electrophysiological data of the HEK-293T cells of **Study 2** and the qPCR experiments. Differences were considered statistically significant when p value was lower than 0.05 ($p<0.05$).

# V. Results

# Study 1: *SCN1B* variant associated with concomitant brain and cardiac disorders

As mentioned in the **Rationale of the research section**, the SNV *SCN1B*_c.308A>T was found in a patient with concomitant heart and brain disorders. Given the clinical phenotype of the proband, and since the SNV affects the resulting protein in a region that compromises both β1 and β1b subunits, one of the main hypotheses in this study is that the SNV *SCN1B*_c.308A>T alters the regulatory properties of both β1 and β1b subunits over $Na_V1.5$ and $Na_V1.1$ channels. To test this hypothesis, we investigated the effect of these two mutant subunits on the electrophysiological properties of the sodium current heterogously expressed in HEK-293T cells.

HEK-293T cells were transiently transfected with the vector encoding $Na_V1.5$ or $Na_V1.1$ alone, or in combination with either the wild type (WT) or mutated β1 and β1b subunits (see **Methods section 2.4**). We recorded sodium currents using the whole cell configuration of the patch clamp technique, 48h after transfection. Isolated cells were bathed in normal sodium solution (for a complete explanation, see **Methods chapter 5**).

## 1. $Na_V1.5$ current properties are modified by $\beta1^{WT}$ and $\beta1b^{WT}$ subunits

Although the effect of both $\beta1^{WT}$ and $\beta1b^{WT}$ on $Na_V1.5$ sodium current properties had been previously characterized by several groups, we studied these effects in HEK-293T cells to have a direct control of our experiments with the mutated subunits.

We studied the current-voltage (I-V) relationship of the sodium current. Peak $I_{Na}$ was normalized to cell capacitance and plotted against the applied voltage. Co-expression of $Na_V1.5$ with either $\beta1^{WT}$ or $\beta1b^{WT}$ increased peak $I_{Na}$ density (41.2 and 42.8%, respectively) compared to $Na_V1.5$ alone (**Figure 27B** and **Table 26**).

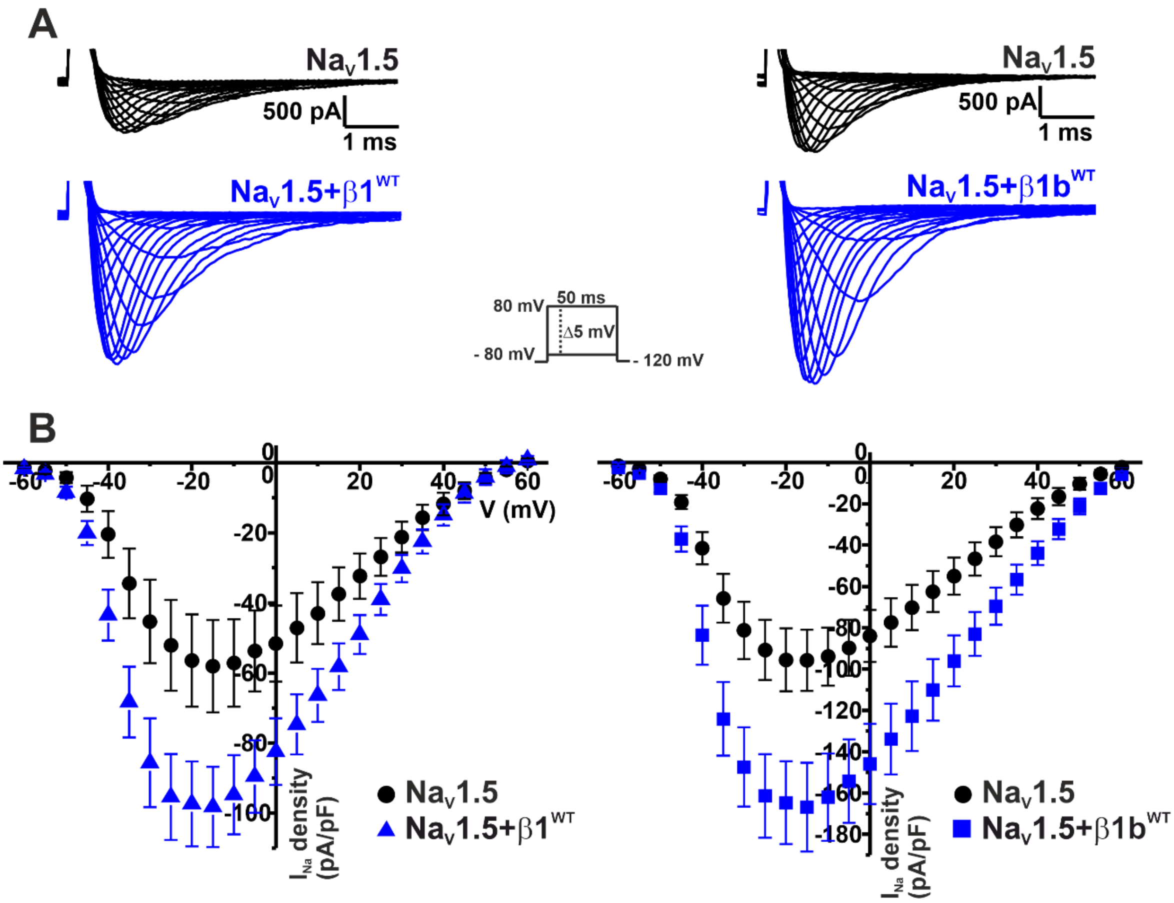

**Figure 27. Both $\beta1^{WT}$ and $\beta1b^{WT}$ increase $Na_V1.5$ peak $I_{Na}$.** Whole cell currents were elicited by depolarizing potentials as shown in the insets. Black circles depict data for $Na_V1.5$ alone, blue tringles represent $Na_V1.5+\beta1^{WT}$ and blue squares represent $Na_V1.5+\beta1b^{WT}$. Values are expressed as mean ± SEM. **(A)** Representative whole cell $Na^+$ current traces from $Na_V1.5$ alone (top), $Na_V1.5+\beta1^{WT}$ (bottom left) and $Na_V1.5+\beta1b^{WT}$ (bottom right). **(B)** Mean current-voltage relationship of the $\beta1^{WT}$ studies (left) and $\beta1b^{WT}$ studies (right). Peak $I_{Na}$ amplitude was normalized by the cell capacitance to obtain Peak $I_{Na}$ density values.

We next studied the voltage-dependence of activation (g/gmax) and steady-state inactivation (I/Imax). Data obtained was plotted against the applied voltage and fitted to a Boltzmann equation to obtain $V_{1/2}$ and k values (see **Methods section 5.2**). Of note, the $\beta1^{WT}$ subunit induced a negative shift of 5 mV in the voltage dependence of activation compared to $Na_V1.5$ alone (**Figure 28A left panel** and **Table 26**). No changes were observed in voltage dependence of activation upon expression of $Na_V1.5+\beta1b^{WT}$ (**Figure 28A right panel** and **Table 26**). Voltage dependence of inactivation was not altered by either $\beta1^{WT}$ or $\beta1b^{WT}$ subunits (**Figure 28A** and **Table 26**).

We also measured the recovery from inactivation. **Figure 28B** shows P2/P1 peak current values plotted against different interpulse intervals. Tau (τ) was obtained by fitting the data to a monoexponential function. Both Na$_V$1.5+β1$^{WT}$ and Na$_V$1.5+β1b$^{WT}$ currents displayed faster recovery from inactivation compared to Na$_V$1.5 alone (**Figure 28B** and **Table 26**).

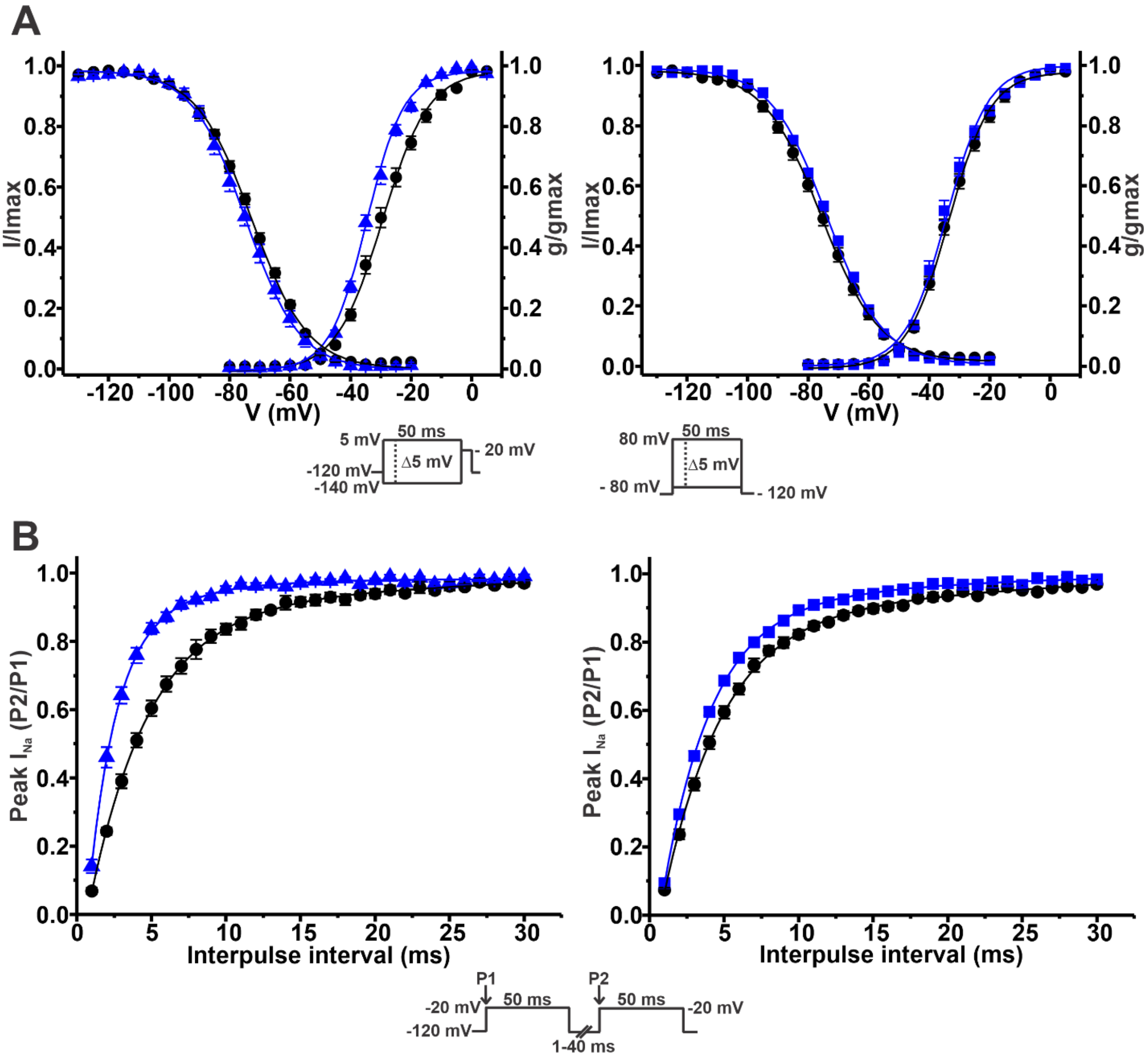

**Figure 28. β1$^{WT}$ and β1b$^{WT}$ modulate Na$_V$1.5 sodium current properties.** Whole cell currents were elicited by depolarizing potentials as shown in the insets. Black circles depict data for Na$_V$1.5 alone, blue tringles represent Na$_V$1.5+β1$^{WT}$ and blue squares represent Na$_V$1.5+β1b$^{WT}$. Values are expressed as mean ± SEM. **(A)** Steady-state voltage dependence of activation and inactivation plots of the β1$^{WT}$ studies (left) and β1b$^{WT}$ studies (right). Data was fitted to a Boltzmann equation (solid lines). **(B)** Recovery from inactivation curves of the β1$^{WT}$ studies (left) and β1b$^{WT}$ studies (right). Data was fitted to a monoexponential function (solid lines).

**Table 26. Biophysical parameters of HEK cells expressing $Na_V1.5$ alone or together with $β1^{WT}$ (left) or $β1b^{WT}$ (right).**

| | $β1^{WT}$ | | $β1b^{WT}$ | |
|---|---|---|---|---|
| **Parameter** | **$Na_V1.5$ alone** | **$Na_V1.5+β1^{WT}$** | **$Na_V1.5$ alone** | **$Na_V1.5+β1b^{WT}$** |
| **Peak $I_{Na}$ density** | | | | |
| **pA/pF** | -58.51±13.02 | -99.50±12.05* | -97.44±14.91 | -170.41±22.22$^{Ψ}$ |
| **n** | 8 | 13 | 15 | 20 |
| **Activation** | | | | |
| **$V_{1/2}$ (mV)** | -29.61±1.10 | -34.61±0.68* | -33.20±0.88 | -34.69±0.89 |
| **k** | 6.95±0.06 | 6.40±0.14 | 6.80±0.26 | 6.14±0.28 |
| **n** | 6 | 11 | 15 | 20 |
| **Steady-state inactivation** | | | | |
| **$V_{1/2}$ (mV)** | -73.00±0.75 | -74.90±1.33 | -75.69±1.12 | -73.71±0.62 |
| **k** | 9.07±0.21 | 8.57±0.25 | 9.32±0.20 | 9.25±0.21 |
| **n** | 6 | 11 | 14 | 18 |
| **Recovery from inactivation** | | | | |
| **τ (ms)** | 4.42±0.28 | 2.27±0.16* | 4.56±0.19 | 3.72±0.11$^{Ψ}$ |
| **n** | 6 | 10 | 12 | 10 |

Data is presented as Mean ± SEM. $I_{Na}$ = sodium current; n = number of cells; k = slope factor; $V_{1/2}$ = voltage for half-maximal activation or steady-state inactivation; τ = time constant. Differences between data were analyzed with a t-test. *vs $Na_V1.5$ (β1); $^{Ψ}$vs $Na_V1.5$ (β1b). Significantly different, p-value < 0.05.

## 2. The mutant $β1^{D103V}$ subunit decreases $Na_V1.5$ sodium current density

To determine whether the *SCN1B* SNV identified in the patient had an effect on the cardiac $Na_V1.5$ sodium current, we performed a functional characterization in HEK-293T cells expressing $Na_V1.5+β1^{D103V}$ compared to those expressing $Na_V1.5+β1^{WT}$.

$β1^{D103V}$ decreased $Na_V1.5$ sodium current density by 45.7% compared to $β1^{WT}$ (Figure **29B** and **Table 27**). Also, $β1^{D103V}$ induced a 3.37-mV positive shift of the voltage dependence of activation compared to $β1^{WT}$ (Figure **29C** and **Table 27**). The voltage dependence of steady state inactivation was similar in the two conditions studied ($Na_V1.5+β1^{WT}$ and $Na_V1.5+β1^{D103V}$) (**Figure 29C** and **Table 27**). Likewise, the recovery from inactivation time constants were similar when $I_{Na}$ was measured in both experimental conditions (**Figure 29D** and **Table 27**).

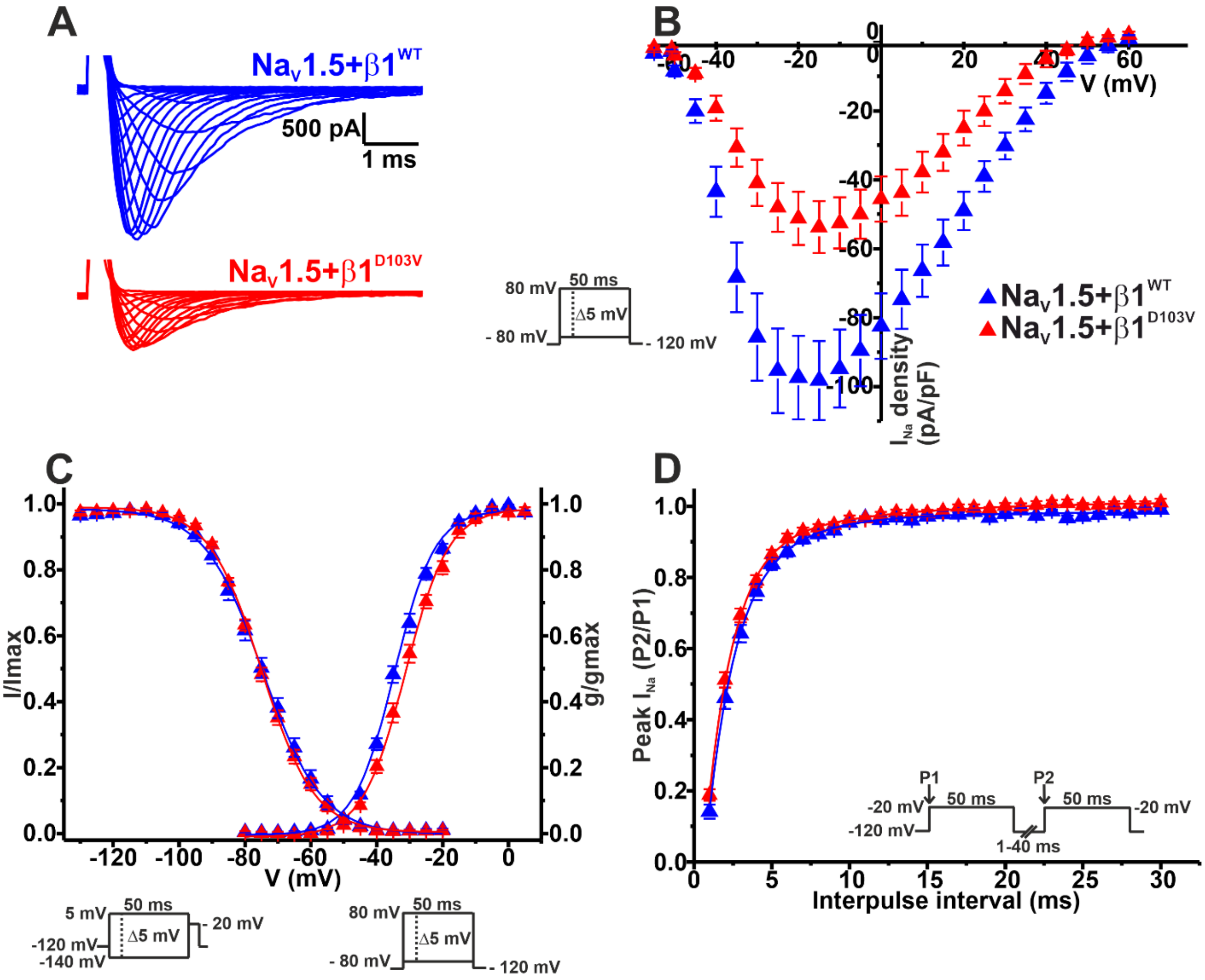

**Figure 29. β1$^{D103V}$ modifies the gating properties of Na$_V$1.5 channel.** Whole cell currents were elicited by depolarizing potentials as shown in the insets. Blue triangles depict data for Na$_V$1.5+β1$^{WT}$ and red triangles represent Na$_V$1.5+β1$^{D103V}$. Values are expressed as mean ± SEM. **(A)** Representative whole cell Na$^+$ current traces for Na$_V$1.5+β1$^{WT}$ (top) and Na$_V$1.5+β1$^{D103V}$ (bottom). **(B)** Mean current-voltage relationship. Peak $I_{Na}$ amplitude was normalized by the cell capacitance to obtain Peak $I_{Na}$ density values. **(C)** Steady-state voltage dependence of activation and inactivation plots. Data was fitted to a Boltzmann equation (solid lines). **(D)** Recovery from inactivation curves. Data was fitted to a monoexponential function (solid lines).

**Table 27. Biophysical parameters of HEK cells expressing Na$_V$1.5+β1$^{WT}$ or Na$_V$1.5+β1$^{D103V}$.**

| **Parameter** | **Na$_V$1.5+β1$^{WT}$** | **Na$_V$1.5+β1$^{D103V}$** |
|---|---|---|
| **Peak I$_{Na}$ density** | | |
| **pA/pF** | -99.50±12.05 | -54.04±7.63* |
| **n** | 13 | 10 |
| **Activation** | | |
| **V$_{1/2}$ (mV)** | -34.61±0.68 | -31.24±0.78* |
| **k** | 6.40±0.14 | 6.52±0.24 |
| **n** | 11 | 6 |
| **Steady-state inactivation** | | |
| **V$_{1/2}$ (mV)** | -74.90±1.33 | -74.76±0.75 |
| **k** | 8.57±0.25 | 7.88±0.25 |
| **n** | 11 | 10 |
| **Recovery from inactivation** | | |
| **τ (ms)** | 2.27±0.16 | 2.14±0.10 |
| **n** | 10 | 10 |

Data is presented as Mean ± SEM. I$_{Na}$ = sodium current; n = number of cells; k = slope factor; V$_{1/2}$ = voltage for half-maximal activation or steady-state inactivation; τ = time constant. Differences between data were analyzed with a t-test. *vs Na$_V$1.5+β1$^{WT}$. Significantly different, p-value < 0.05.

Notably, we did not detect any sodium current in 34 of 75 cells transfected with Na$_V$1.5+β1$^{D103V}$. However, only 11 of 81 cells expressing Na$_V$1.5+β1$^{WT}$ had no detectable I$_{Na}$. This effect on the sodium current could be prompted by either an electrical malfunction of the channel, or a decrease in total Na$_V$1.5 protein expression in the cell and in the membrane. To assess total and membrane protein expression, we performed Western Blot analysis 48h after transfection (see **Methods 4.4.1**).

These experiments showed that the β1$^{D103V}$ mutation did not affect total protein expression. We observed approximately the same amount of total Na$_V$1.5 in all three conditions (Na$_V$1.5 alone, Na$_V$1.5+β1$^{WT}$, and Na$_V$1.5+β1$^{D103V}$, **Figures 30A and 30C**). Moreover, immunoblotting analysis of biotinylated surface membrane proteins evidenced that the amount of Na$_V$1.5 in the plasma membrane was unaffected by the β1 mutation (**Figures 30B and 30C**).

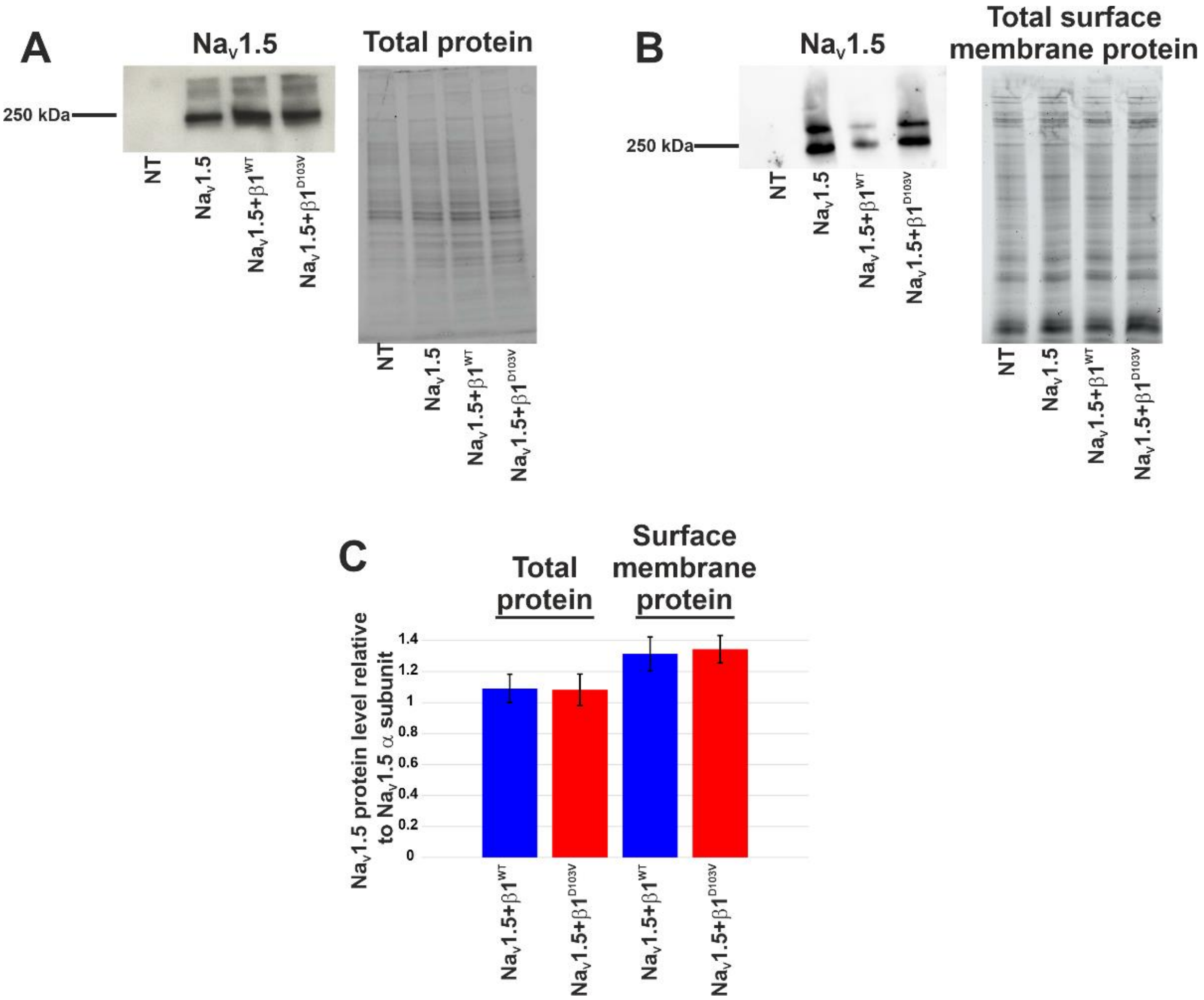

**Figure 30. Na$_V$1.5 protein expression is not affected by β1$^{D103V}$. (A)** Western blot detection of Na$_V$1.5 (left) and corresponding total protein stain-free gel (right), from HEK-293T cells transfected with either Na$_V$1.5, Na$_V$1.5+β1$^{WT}$, or Na$_V$1.5+β1$^{D103V}$ or non-transfected cells (NT). **(B)** Western blot detection of Na$_V$1.5 after cell surface biotinylation (left) and corresponding total protein stain-free gel (right), from HEK-293T cells transfected with either Na$_V$1.5, Na$_V$1.5+β1$^{WT}$, or Na$_V$1.5+β1$^{D103V}$ or non-transfected cells (NT). **(C)** Bar graph depicts the relative protein expression normalized by the Na$_V$1.5 α subunit protein level. Left two bars correspond to total protein (n = 2) and right two bars correspond to biotinylated protein (n = 4) from HEK-293T cells transfected with either Na$_V$1.5+β1$^{WT}$ or Na$_V$1.5+β1$^{D103V}$. Both visible bands from the biotinylated samples were used for quantification, and the ratio was obtained by normalizing each condition with its respective input. Differences between data were analyzed with a t-test. Significantly different, p-value < 0.05.

## 3. The mutant β1b$^{D103V}$ isoform does not modify Na$_V$1.5 properties

To further investigate all the possible effects of the SNV on Na$_V$1.5 current, we also evaluated the effects of the mutant β1 alternative isoform (β1b$^{D103V}$) on Na$_V$1.5 sodium current features.

We did not observe any changes in I$_{Na}$ density from cells expressing β1b$^{D103V}$ compared to β1b$^{WT}$. Likewise, voltage dependence of activation, steady state inactivation, and recovery from inactivation were not altered by this mutant subunit compared to the wildtype subunit (**Figure 31** and **Table 28**).

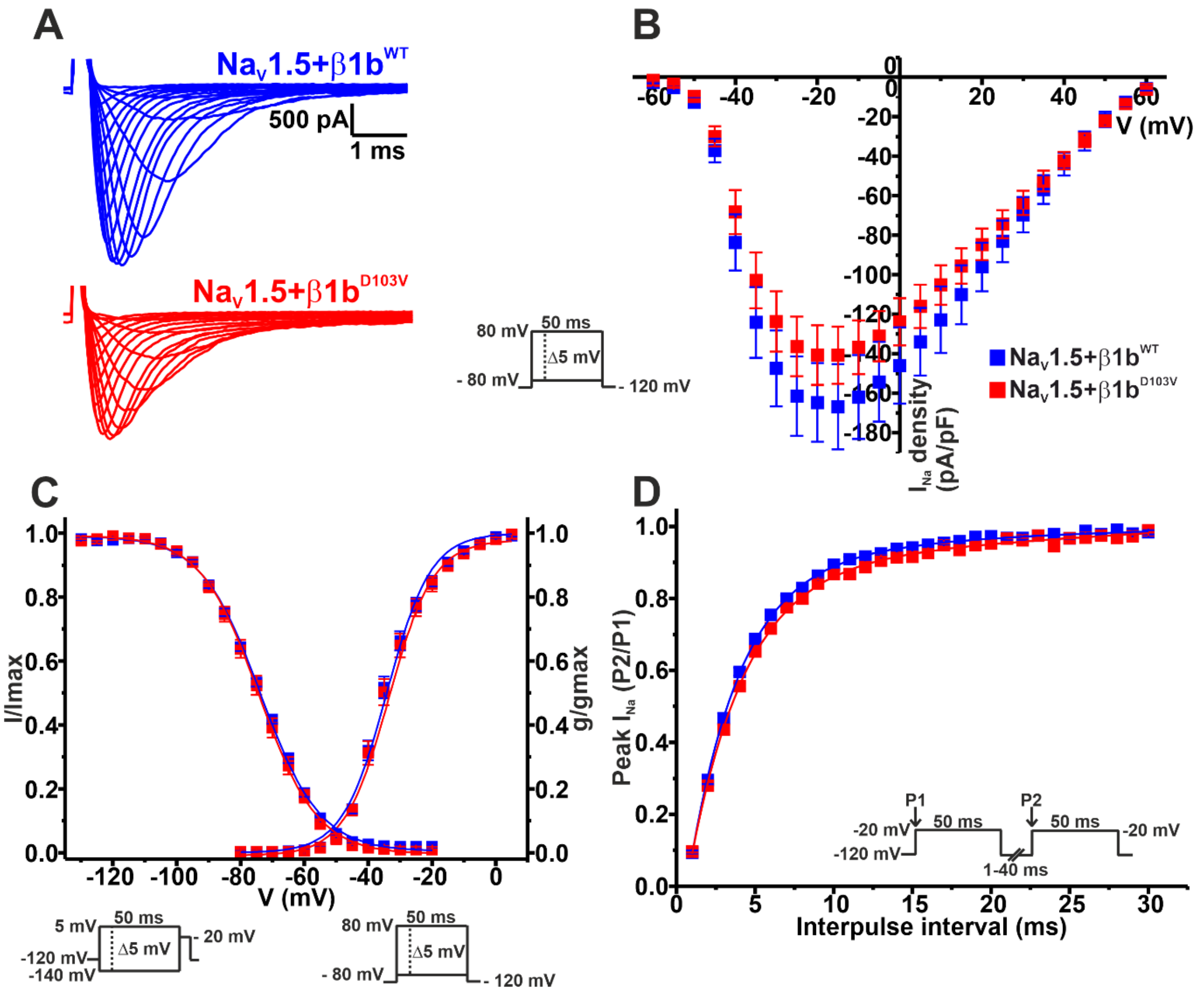

**Figure 31. Na$_V$1.5 current properties are not modified by β1b$^{D103V}$.** Whole cell currents were elicited by depolarizing potentials as shown in the insets. Blue squares depict data for Na$_V$1.5+β1b$^{WT}$ and red squares represent Na$_V$1.5+β1b$^{D103V}$. Values are expressed as mean ± SEM. **(A)** Representative whole cell Na$^+$ current traces from Na$_V$1.5+β1b$^{WT}$ (top) and Na$_V$1.5+β1b$^{D103V}$ (bottom). **(B)** Mean current-voltage relationship. Peak I$_{Na}$ amplitude was normalized by the cell capacitance to obtain Peak I$_{Na}$ density values. **(C)** Steady-state voltage dependence of activation and inactivation plots. Data was fitted to a Boltzmann equation (solid lines). **(D)** Recovery from inactivation curves. Data was fitted to a monoexponential function (solid lines).

**Table 28. Biophysical parameters of HEK cells expressing Na$_V$1.5+β1b$^{WT}$ or Na$_V$1.5+β1b$^{D103V}$.**

| Parameter | Na$_V$1.5+β1b$^{WT}$ | Na$_V$1.5+β1b$^{D103V}$ |
|---|---|---|
| **Peak I$_{Na}$ density** | | |
| **pA/pF** | -170.41±22.22 | -143.03±14.84 |
| **n** | 20 | 14 |
| **Activation** | | |
| **V$_{1/2}$ (mV)** | -34.69±0.89 | -34.41±1.15 |
| **k** | 6.14±0.28 | 6.29±0.27 |
| **n** | 20 | 13 |
| **Steady-state inactivation** | | |
| **V$_{1/2}$ (mV)** | -73.71±0.62 | -74.21±1.16 |
| **k** | 9.25±0.21 | 8.84±0.20 |
| **n** | 18 | 10 |
| **Recovery from inactivation** | | |
| **τ (ms)** | 3.72±0.11 | 4.15±0.14 |
| **n** | 10 | 8 |

Data is presented as Mean ± SEM. I$_{Na}$ = sodium current; n = number of cells; k = slope factor; V$_{1/2}$ = voltage for half-maximal activation or steady-state inactivation; τ = time constant. Differences between data were analyzed with a t-test. *vs Na$_V$1.5+β1$^{WT}$. Significantly different, p-value < 0.05.

## 4. The β1 and β1b subunits modulate Na$_V$1.1 sodium current properties

Because we hypothesized that the neurological features of the patient could be related to the SNV, we investigated whether the p.D130V mutation in β1 and β1b isoforms also affected one of the most predominant brain-type sodium channels: Na$_V$1.1. Similar to the Na$_V$1.5 experiments, the effect of the β1 on Na$_V$1.1 sodium current properties had been studied before. However, we studied the effect of both β1 and β1b in HEK-293T cells as an internal control.

We detected a 45.9% and 47.2% increase of peak I$_{Na}$ density when Na$_V$1.1 was co-expressed with β1$^{WT}$ or β1b$^{WT}$, respectively, compared to Na$_V$1.1 alone (**Figure 32B** and **Table 29**).

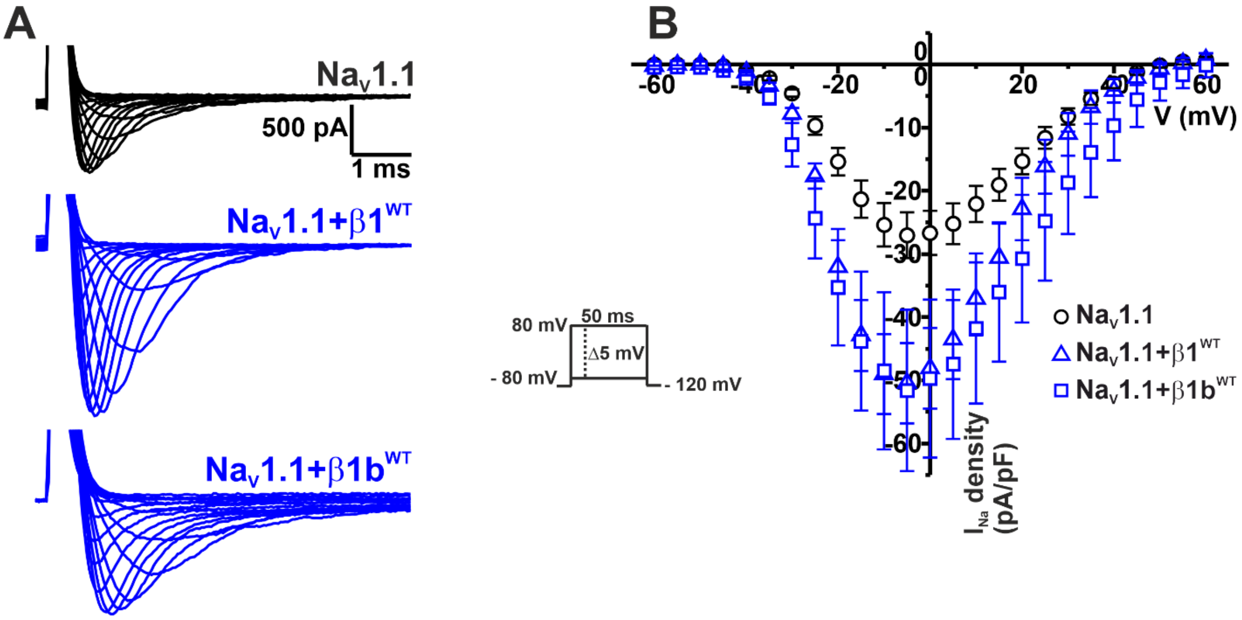

**Figure 32. β1$^{WT}$ and β1b$^{WT}$ increase Na$_V$1.1 sodium current density.** Whole cell currents were elicited by depolarizing potentials as shown in the insets. Black open circles depict data for Na$_V$1.1 alone, blue open triangles represent Na$_V$1.1+β1$^{WT}$ and blue open squares represent Na$_V$1.1+β1b$^{WT}$. Values are expressed as mean ± SEM. **(A)** Representative whole cell Na$^+$ current traces from Na$_V$1.1 (top), Na$_V$1.1+β1$^{WT}$ (middle) and Na$_V$1.1+β1b$^{WT}$ (bottom). **(B)** Mean current-voltage relationship. Peak I$_{Na}$ amplitude was normalized by the cell capacitance to obtain Peak I$_{Na}$ density values.

Neither β1$^{WT}$ nor β1b$^{WT}$ caused any significant changes in the voltage dependence of activation (**Figure 33A** and **Table 29**). Steady-state inactivation of the Na$_V$1.1 current was not altered by β1$^{WT}$. On the contrary, co-expression of the β1b$^{WT}$ isoform caused a 7.21 mV negative shift of the voltage dependence of inactivation compared to Na$_V$1.1 alone (**Figure 33A** and **Table 29**). β1$^{WT}$ markedly decreased the recovery from inactivation time in comparison to Na$_V$1.1 alone. However, this decrease was not observed when Na$_V$1.1 was co-expressed with β1b$^{WT}$ (**Figure 33B** and **Table 29**).

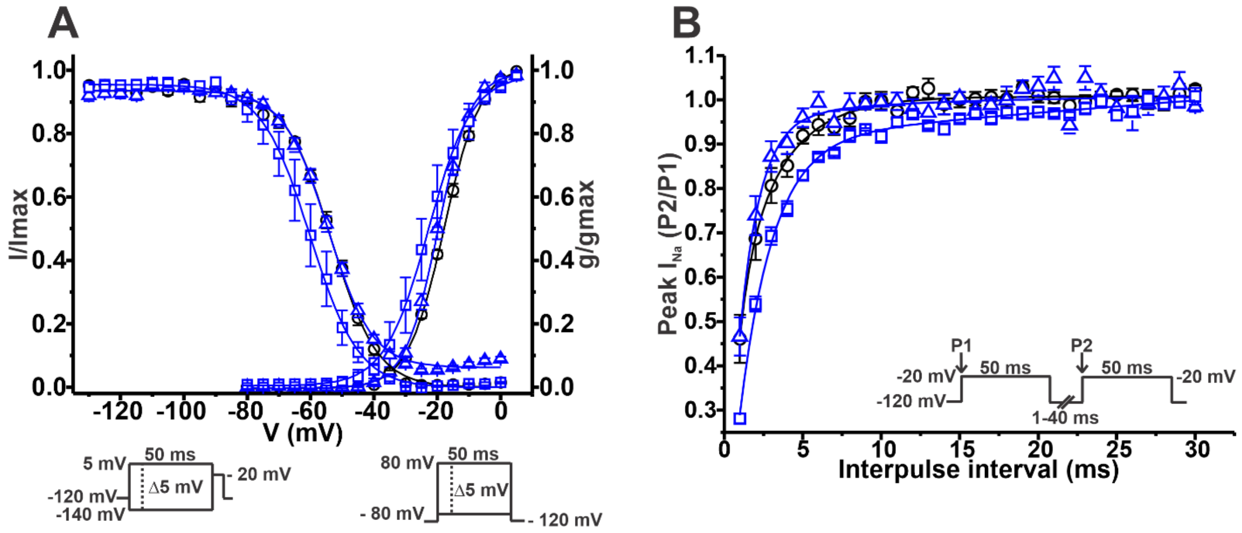

**Figure 33. β1$^{WT}$ and β1b$^{WT}$ differently modulate Na$_V$1.1 sodium current properties.** Whole cell currents were elicited by depolarizing potentials as shown in the insets. Black open circles depict data for NaV1.1 alone, blue open triangles represent Na$_V$1.1+β1$^{WT}$ and blue open squares represent Na$_V$1.1+β1b$^{WT}$. Values are expressed as mean ± SEM. **(A)** Steady-state voltage dependence of activation and inactivation plots. Data was fitted to a Boltzmann equation (solid lines). **(B)** Recovery from inactivation curves. Data was fitted to a monoexponential function (solid lines).

**Table 29. Biophysical parameters of HEK cells expressing Na$_V$1.1 alone or together with β1$^{WT}$ or β1b$^{WT}$.**

| **Parameter** | **Na$_V$1.1 alone** | **Na$_V$1.1+β1$^{WT}$** | **Na$_V$1.1+β1b$^{WT}$** |
|---|---|---|---|
| **Peak I$_{Na}$ density** | | | |
| **pA/pF** | -27.39±3.55 | -50.67±6.38* | -51.90±12.75* |
| **n** | 13 | 14 | 5 |
| **Activation** | | | |
| **V$_{1/2}$ (mV)** | -17.71±0.41 | -19.69±0.67 | -22.78±2.91 |
| **k** | 5.79±0.19 | 5.24±0.14 | 6.05±0.45 |
| **n** | 7 | 9 | 5 |
| **Steady-state inactivation** | | | |
| **V$_{1/2}$ (mV)** | -52.93±0.80 | -54.17±0.73 | -60.14±2.98* |
| **k** | 7.21±0.31 | 7.28±0.38 | 6.75±0.42 |
| **n** | 7 | 9 | 6 |
| **Recovery from inactivation** | | | |
| **τ (ms)** | 2.30±0.12 | 1.31±0.26* | 3.17±0.52 |
| **n** | 6 | 7 | 5 |

Data is presented as Mean ± SEM. I$_{Na}$ = sodium current; n = number of cells; k = slope factor; V$_{1/2}$ = voltage for half-maximal activation or steady-state inactivation; τ = time constant. Differences between data were analyzed with a t-test. *vs Na$_V$1.1 alone. Significantly different, p-value < 0.05.

## 5. The β1$^{D103V}$ subunit decreases Na$_V$1.1 current density

To determine whether the *SCN1B* SNV identified in the patient had an effect on the neuronal Na$_V$1.1 sodium current, we first performed functional characterization in HEK-293T cells expressing Na$_V$1.1+β1$^{D103V}$ compared to those expressing Na$_V$1.1+β1$^{WT}$.

Peak current density measured from cells expressing Na$_V$1.1+β1$^{D103V}$ was 66.9% smaller than that in Na$_V$1.1+β1$^{WT}$-expressing cells (**Figure 34B** and **Table 30**). Voltage dependence of activation and steady-state inactivation were not altered by β1$^{D103V}$ (**Figure 34C** and **Table 30**). Recovery from inactivation time constants were similar in both experimental conditions (**Figure 34D** and **Table 30**).

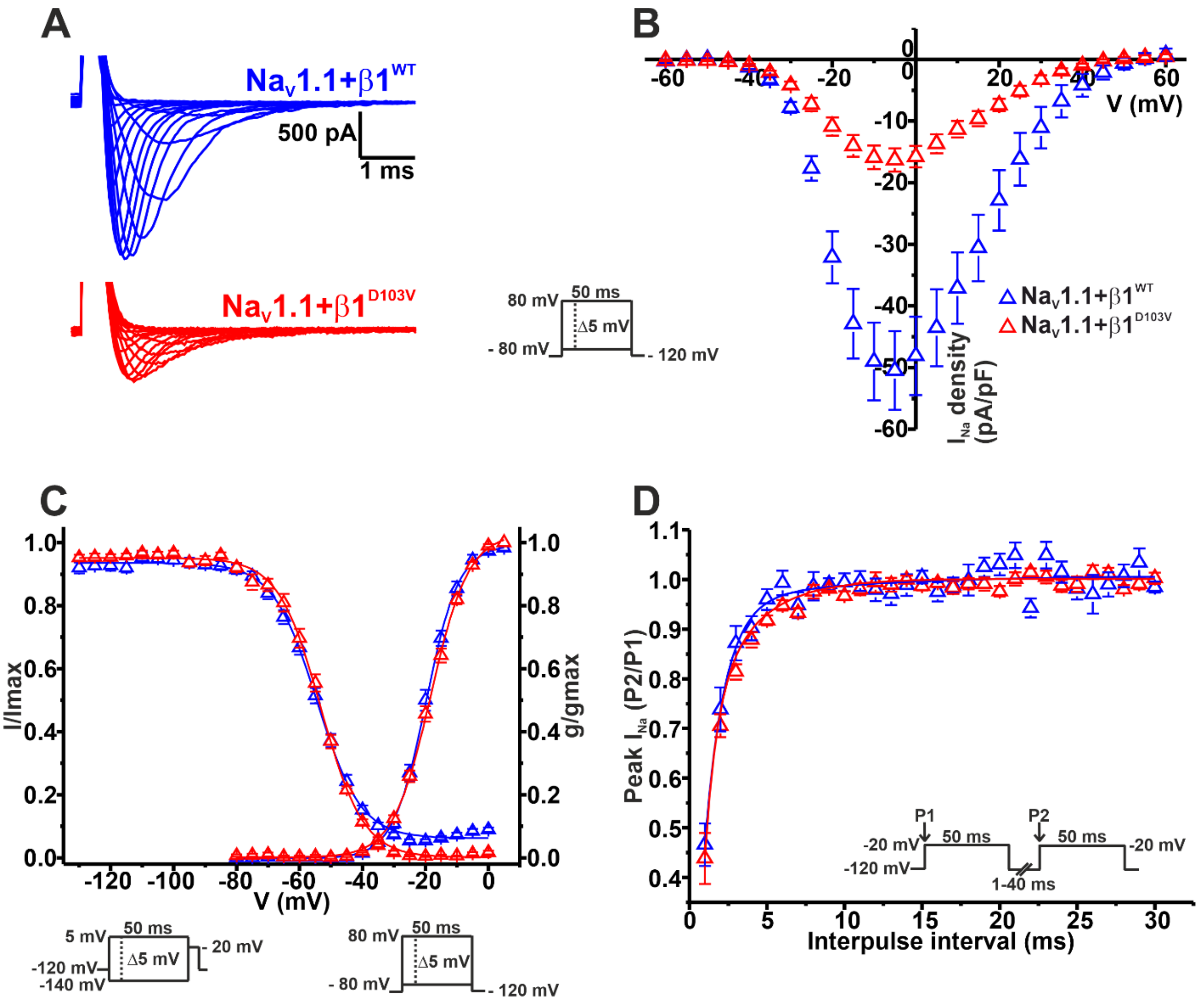

**Figure 34. β1$^{D103V}$ significantly decreases Na$_V$1.1 I$_{Na}$.** Whole cell currents were elicited by depolarizing potentials as shown in the insets. Blue triangles depict data for Na$_V$1.1+β1$^{WT}$ and red triangles represent Na$_V$1.1+β1$^{D103V}$. Values are expressed as mean ± SEM. **(A)** Representative whole cell Na$^+$ current traces from Na$_V$1.1+β1$^{WT}$ (top) and Na$_V$1.1+β1$^{D103V}$ (bottom). **(B)** Mean current-voltage relationship. Peak I$_{Na}$ amplitude was normalized by the cell capacitance to obtain Peak I$_{Na}$ density values. **(C)** Steady-state

voltage dependence of activation and inactivation plots. Data was fitted to a Boltzmann equation (solid lines). **(D)** Recovery from inactivation curves. Data was fitted to a monoexponential function (solid lines).

**Table 30. Biophysical parameters of HEK cells expressing Na$_V$1.1+β1$^{WT}$ or Na$_V$1.1+β1$^{D103V}$.**

| **Parameter** | **Na$_V$1.1+β1$^{WT}$** | **Na$_V$1.1+β1$^{D103V}$** |
|---|---|---|
| **Peak I$_{Na}$ density** | | |
| **pA/pF** | -50.67±6.38 | -16.76±1.88* |
| **n** | 14 | 22 |
| **Activation** | | |
| **V$_{1/2}$ (mV)** | -19.69±0.67 | -18.18±0.61 |
| **k** | 5.24±0.14 | 5.91±0.21 |
| **n** | 9 | 13 |
| **Steady-state inactivation** | | |
| **V$_{1/2}$ (mV)** | -54.17±0.73 | -53.06±0.34 |
| **k** | 7.28±0.38 | 7.09±0.54 |
| **n** | 9 | 13 |
| **Recovery from inactivation** | | |
| **τ (ms)** | 1.31±0.26 | 1.79±0.18 |
| **n** | 7 | 7 |

Data is presented as Mean ± SEM. I$_{Na}$ = sodium current; n = number of cells; k = slope factor; V$_{1/2}$ = voltage for half-maximal activation or steady-state inactivation; τ = time constant. Differences between data were analyzed with a t-test. *vs Na$_V$1.1+β1$^{WT}$. Significantly different, p-value < 0.05.

Similar to what we observed in Na$_V$1.5 experiments, we did not detect any current in 23 out of 59 cells expressing Na$_V$1.1+β1$^{D103V}$. However, when cells were transfected with Na$_V$1.1+β1$^{WT}$, only 4 of 56 cells showed no current. Western blot analysis showed no significant differences in Na$_V$1.1 expression between the three experimental conditions (**Figure 35**).

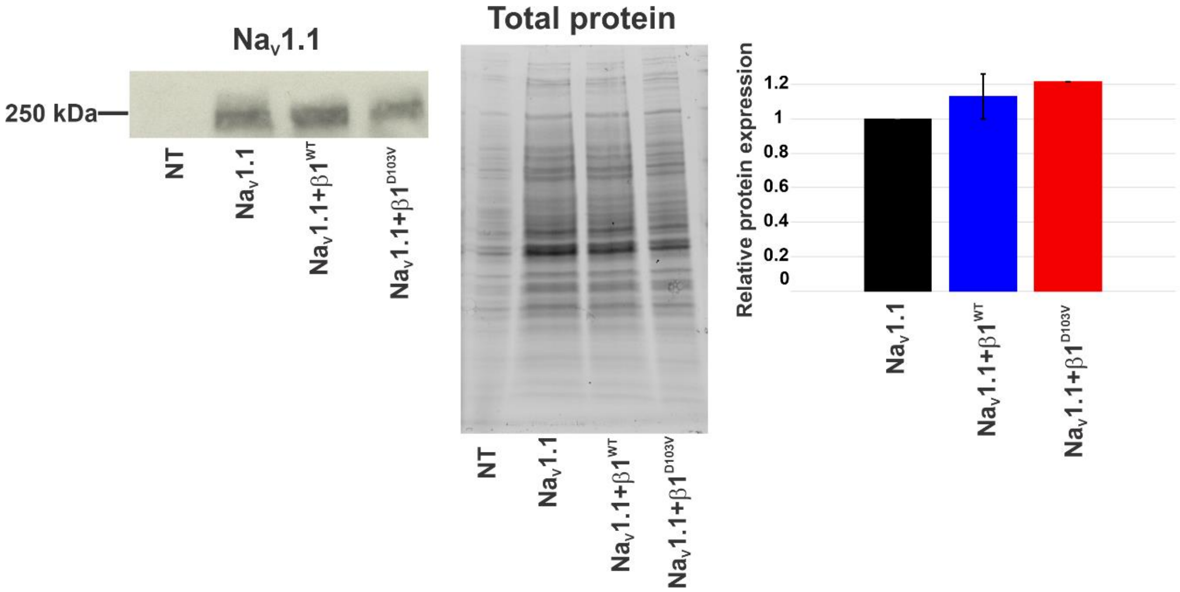

**Figure 35. Na$_V$1.1 protein expression is not affected by β1$^{D103V}$.** Western blot detection of Na$_V$1.1 (left) and corresponding total protein stain-free gel (middle) from HEK-293T cells transfected with either Na$_V$1.1, Na$_V$1.1+β1$^{WT}$, or Na$_V$1.1+β1$^{D103V}$ or non- transfected cells (NT). Bar graph on the right depicts the relative protein expression normalized by Na$_V$1.1 alone (n = 2). Differences between data were analyzed with a t-test. Significantly different, p-value < 0.05.

## 6. Mutant β1 isoform b (β1b$^{D103V}$) modifies Na$_V$1.1 properties

Because the p.D103V mutation is located in a region shared by both β1 and β1b subunits, we also assessed the effect of β1b$^{D103V}$ on Na$_V$1.1 current properties.

Co-expression of β1b$^{D103V}$ with Na$_V$1.1 did not change I$_{Na}$ density compared to Na$_V$1.1+β1b$^{WT}$ (**Figure 36B** and **Table 31**). Likewise, the β1b$^{D103V}$ subunit did not significantly change the voltage dependence of activation compared to β1b$^{WT}$ (**Figure 36C** and **Table 31**). However, β1b$^{D103V}$ caused a 6.04-mV right shift of the voltage dependence of steady-state inactivation when compared to the wildtype subunit (**Figure 36C** and **Table 31**). This change resulted in a positive shift of the window current of Na$_V$1.1+β1b$^{D103V}$ compared to Na$_V$1.1+β1b$^{WT}$ (**Figure 36D**). β1b$^{D103V}$ significantly reduced the recovery from inactivation time constant compared to Na$_V$1.1+β1b$^{WT}$ (**Figure 36E** and **Table 31**).

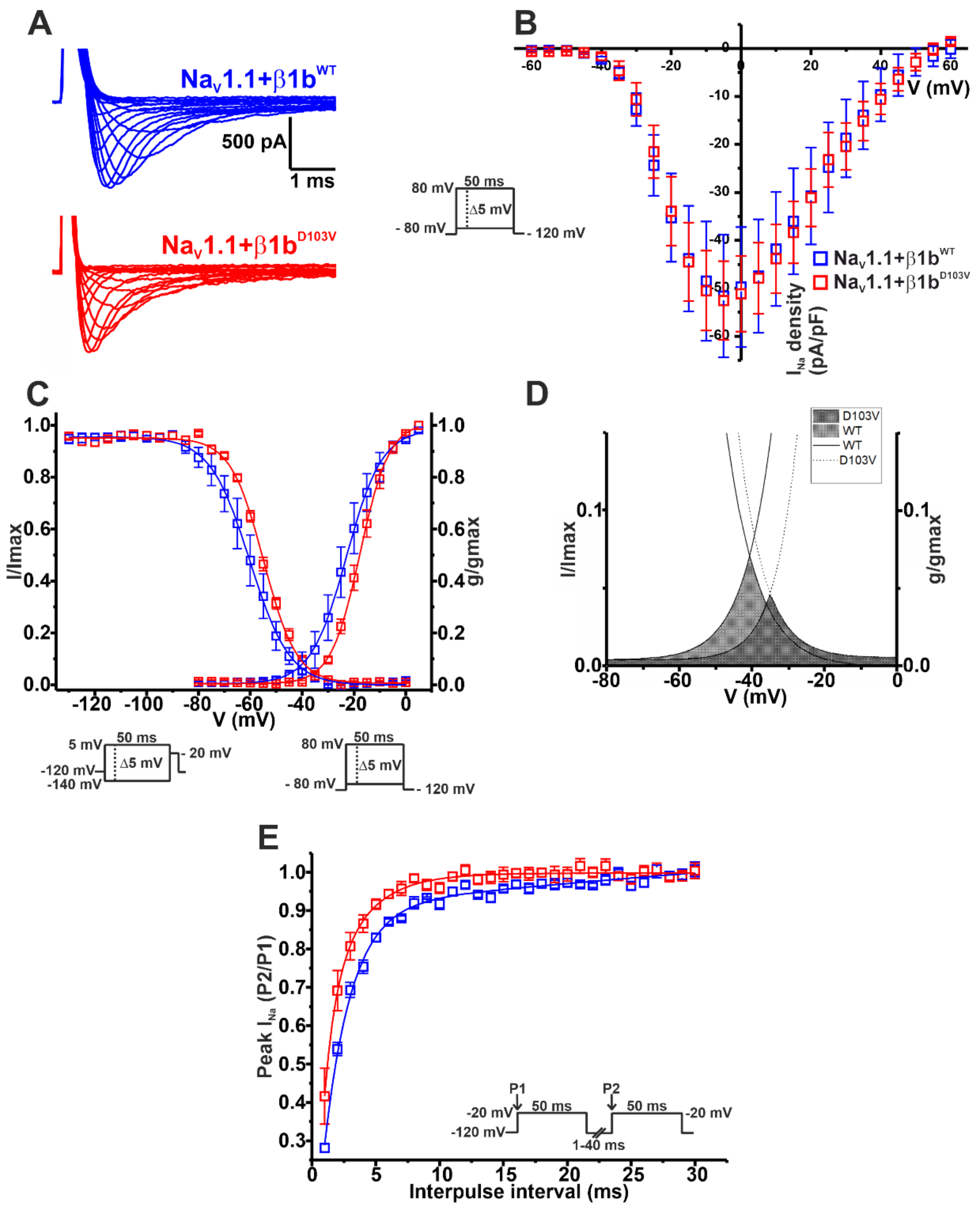

**Figure 36. β1b$^{D103V}$ modifies the gating properties of Na$_V$1.1 channel.** Whole cell currents were elicited by depolarizing potentials as shown in the insets. Blue squares depict data for Na$_V$1.1+β1b$^{WT}$ and red squares represent Na$_V$1.1+β1b$^{D103V}$. Values are expressed as mean ± SEM. **(A)** Representative whole cell Na$^+$ current traces from Na$_V$1.1+β1b$^{WT}$ (top) and Na$_V$1.1+β1b$^{D103V}$ (bottom). **(B)** Mean current-voltage relationship. Peak I$_{Na}$ amplitude was normalized by the cell capacitance to obtain Peak I$_{Na}$ density values. **(C)** Steady-state voltage dependence of activation and inactivation plots. Data was fitted to a Boltzmann equation (solid lines). **(D)** Window region bounded by the activation and steady state inactivation voltage dependent curves (Na$_V$1.1+β1b$^{WT}$ light gray and Na$_V$1.1+β1b$^{D103V}$ dark gray). **(E)** Recovery from inactivation curves. Data was fitted to a monoexponential function (solid lines).

**Table 31. Biophysical parameters of HEK cells expressing Na$_V$1.1+β1b$^{WT}$ or Na$_V$1.1+β1b$^{D103V}$.**

| Parameter | Na$_V$1.1+β1b$^{WT}$ | Na$_V$1.1+β1b$^{D103V}$ |
|---|---|---|
| **Peak I$_{Na}$ density** | | |
| **pA/pF** | -51.90±12.75 | -54.06±8.41 |
| **n** | 5 | 9 |
| **Activation** | | |
| **V$_{1/2}$ (mV)** | -22.78±2.91 | -17.34±1.16 |
| **k** | 6.05±0.45 | 5.36±0.30 |
| **n** | 5 | 8 |
| **Steady-state inactivation** | | |
| **V$_{1/2}$ (mV)** | -60.14±2.98 | -54.10±0.82* |
| **k** | 6.75±0.42 | 6.36±0.29 |
| **n** | 6 | 7 |
| **Recovery from inactivation** | | |
| **τ (ms)** | 3.17±0.52 | 1.67±0.23* |
| **n** | 5 | 6 |

Data is presented as Mean ± SEM. I$_{Na}$ = sodium current; n = number of cells; k = slope factor; V$_{1/2}$ = voltage for half-maximal activation or steady-state inactivation; τ = time constant. Differences between data were analyzed with a t-test. *vs Na$_V$1.1+β1b$^{WT}$. Significantly different, p-value < 0.05.

## Study 2: *SCN5A* variant associated with Brugada Syndrome

As explained in the **Rationale of the research section**, we were also interested in studying the effects of an SNV that had been previously related to BrS (*SCN5A*_c.4573G>A). We hypothesized that the SNV modifies the sodium current properties of the $Na_V1.5$ channel. To assess this, we used two cellular approaches. First, we studied HEK-293T cells transiently transfected with the SNV. This allowed us to determine the changes in the sodium current properties induced by the SNV. However, we were also interested in approaching the effect of patient-specific genetic background over the sodium current properties, in a cardiomyocyte-like cellular environment. For that purpose, we obtained skin samples of four individuals of the same family, three of which were carriers of the SNV (**Figure 37**). We reprogrammed their dermal fibroblasts into iPSc, and studied the electrophysiological properties of the iPS-CM of these four individuals. From now on the father, which is a related control, will be referenced as Rb20237, the mother as Rb20236, the daughter as Rb20234 and the son as Rb20235.

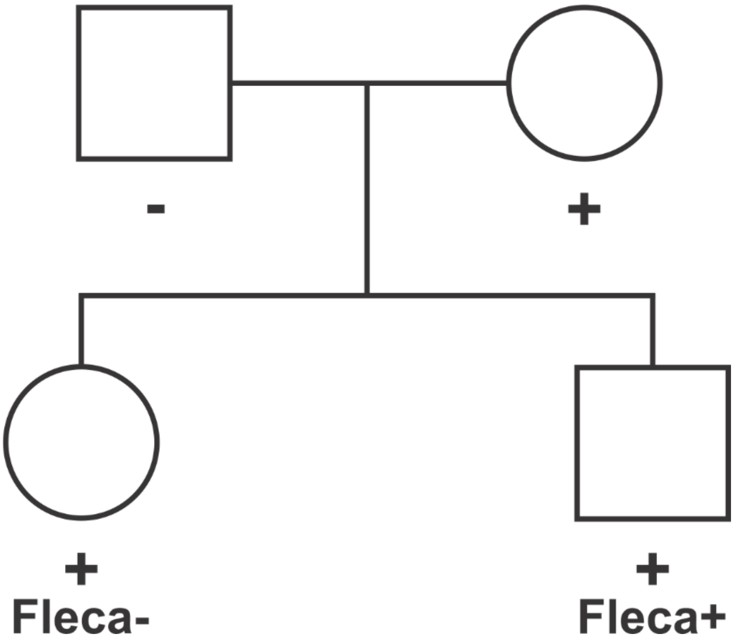

**Figure 37. Partial pedigree of the family carrying the SCN5A SNV, showing the individuals from whose we obtained skin samples.** Circles represent females, and squares represent males. The + symbol represents SNV carriers, and – symbol the non-carriers. Fleca designates patients which underwent a flecainide test, and the + or – symbols next to it indicates whether the result was positive or negative, respectively.

## 1. Characterization of the SNV *SCN5A*_c.4573G>A in HEK-293T cells

Before studying the mutation in patient-specific iPS-CM, we characterized the effect of the SNV *SCN5A*_c.4573G>A on the electrophysiological properties of the $Na_V1.5$ sodium current in HEK-293T cells transiently transfected with a vector encoding the *SCN5A* SNV.

We used the pcDNA3-SCN5A vector as a template to introduce the SNV by site-directed mutagenesis. We sequenced the vector to ensure the presence of the SNV under study (**Figure 38**) and the absence of additional variants.

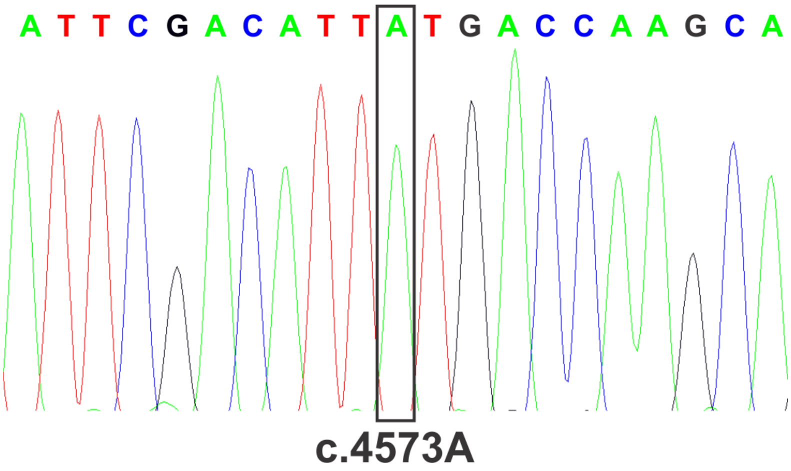

**Figure 38. Region of the pcDNA3.1-SCN5A vector harboring the SNV SCN5A_c.4573G>A.** The SNV SCN5A_c.4573G>A was identified in the pcDNA3.1-SCN5A mutated vector.

We transiently transfected HEK-293T cells with a GFP vector and either one of the vectors encoding $Na_V1.5^{WT}$ (homozygous WT cells), or $Na_V1.5^{V1525M}$ (homozygous V1525M cells) or with both vectors (heterozygous WT/V1525M cells). We recorded sodium currents using the whole cell configuration of the patch clamp technique, as previously explained.

As shown in **Figure 39B** and **Table 32**, the SNV markedly decreased $I_{Na}$ density. In the cells where the SNV was expressed in homozygosis, the decrease in $I_{Na}$ density compared to the WT was of 46.9%. As expected, the decrease in $I_{Na}$ in heterozygosis (24.2%) was near half of the reduction we observed in homozygosis.

Using the same I-V pulse protocol, we measured the inactivation time constant at different voltages of fifteen randomly selected cells out of the total. We fitted the data to a double exponential function, obtaining two time constants: τ fast and τ slow.

We did not detect any significant changes in τ fast, with respect to the WT, when the SNV was expressed in heterozygosis or homozygosis. However, τ slow was slightly increased at 20 mV when the SNV was expressed in heterozygosis (identified with the symbol *), compared to the WT (**Figure 39C**).

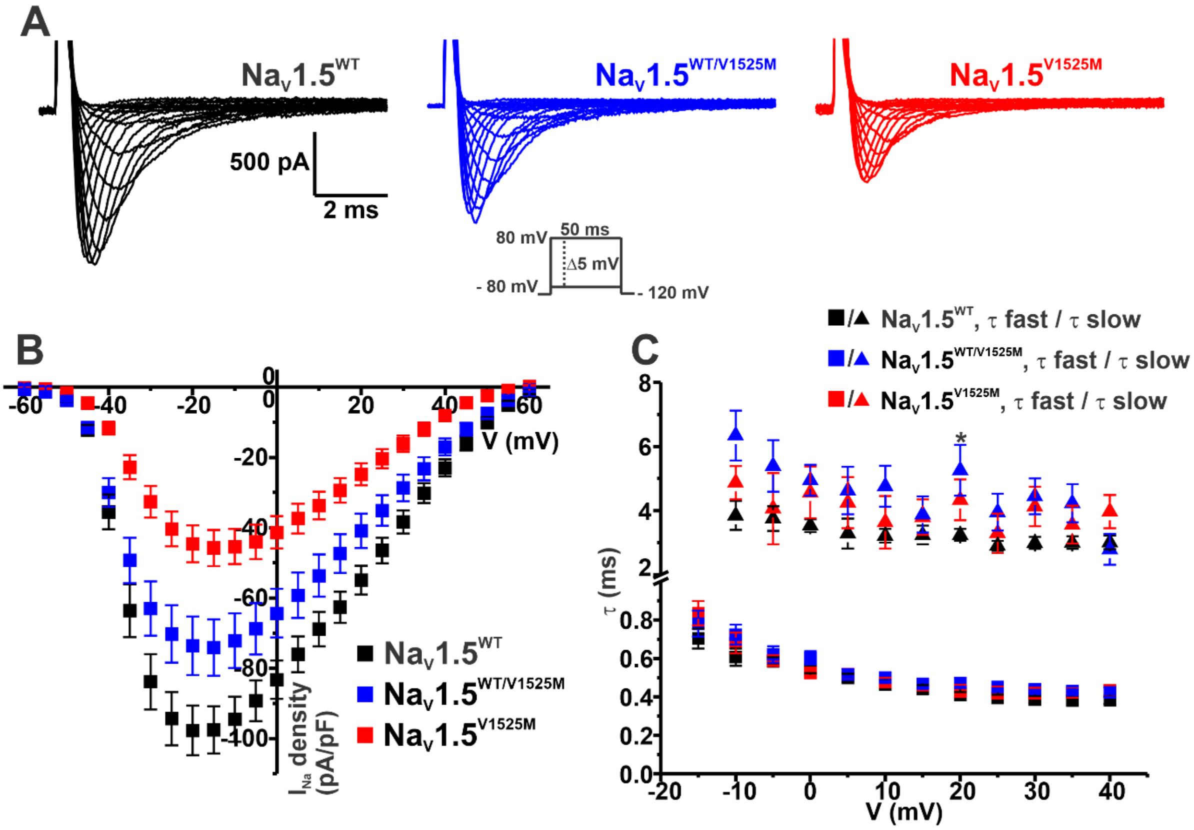

**Figure 39. The SNV *SCN5A*_ c.4573G>A decreases Na$_V$1.5 peak I$_{Na}$.** Whole cell currents were elicited by depolarizing potentials as shown in the insets. Black squares depict data for Na$_V$1.5$^{WT}$, blue squares represent Na$_V$1.5$^{WT/V1525M}$ and red squares represent Na$_V$1.5$^{V1525M}$. Values are expressed as mean ± SEM. **(A)** Representative whole cell Na$^+$ current traces from Na$_V$1.5$^{WT}$ (left), Na$_V$1.5$^{WT/V1525M}$ (middle) and Na$_V$1.5$^{V1525M}$ (right). **(B)** Mean current-voltage relationship. Peak I$_{Na}$ amplitude was normalized by the cell capacitance to obtain Peak I$_{Na}$ density values. **(C)** I$_{Na}$ inactivation plot. τ fast and slow values were plotted against voltage. Squares depict data for τ fast, and triangles for τ slow. Differences between data were analyzed with a t-test. *vs Na$_V$1.5$^{WT}$. Significantly different, p-value < 0.05.

The voltage dependence of activation curve was shifted towards more depolarizing potentials when the SNV was expressed in homozygosis, but not in heterozygosis, compared to the WT (**Figure 40A** and **Table 32**). No significant changes were observed in the steady-state inactivation parameters (**Figure 40A** and **Table 32**).

Surprisingly, the recovery from inactivation time constant was only increased when the SNV was expressed in heterozygosis, compared to the WT (**Figure 40B** and **Table 32**).

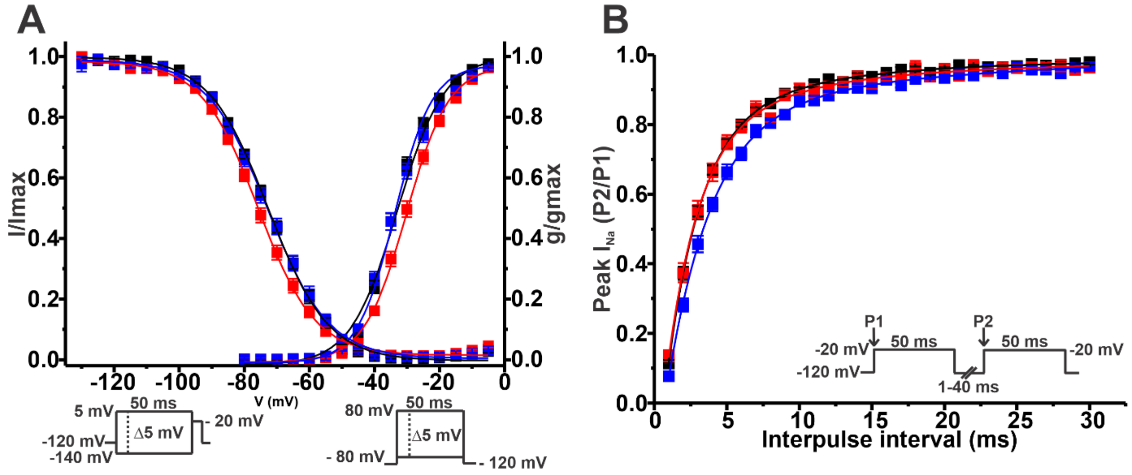

**Figure 40. The homozygous and heterozygous expression of *SCN5A*_ c.4573G>A have different effects in Na$_V$1.5 sodium current properties.** Whole cell currents were elicited by depolarizing potentials as shown in the insets. Black squares depict data for Na$_V$1.5$^{WT}$, blue squares represent Na$_V$1.5$^{WT/V1525M}$ and red squares represent Na$_V$1.5$^{V1525M}$. Values are expressed as mean ± SEM. **(A)** Voltage dependence of activation and steady-state inactivation plots. Data was fitted to a Boltzmann equation (solid lines). **(B)** Recovery from inactivation curves. Data was fitted to a monoexponential function (solid lines).

**Table 32. Biophysical parameters of HEK-293T cells expressing Na$_V$1.5$^{WT}$, Na$_V$1.5$^{WT/V1525M}$ or Na$_V$1.5$^{V1525M}$.**

| Parameter | Na$_V$1.5$^{WT}$ | Na$_V$1.5$^{WT/V1525M}$ | Na$_V$1.5$^{V1525M}$ |
|---|---|---|---|
| **Peak I$_{Na}$ density** | | | |
| **pA/pF** | -97.67±7.09 | -74.07±8.04* | -45.77±5.18*‡ |
| **n** | 23 | 28 | 19 |
| **Activation** | | | |
| **V$_{1/2}$ (mV)** | -33.60±0.63 | -33.10±0.78 | -30.01±0.68*‡ |
| **k** | 5.49±0.21 | 6.26±025* | 6.37±0.18* |
| **n** | 23 | 28 | 19 |
| **Steady-state inactivation** | | | |
| **V$_{1/2}$ (mV)** | -72.07±0.87 | -72.23±1.19 | -74.90±0.91 |
| **k** | 8.81±0.24 | 8.89±0.17 | 8.36±0.27 |
| **n** | 17 | 22 | 17 |
| **Recovery from inactivation** | | | |
| **τ (ms)** | 2.48±0.18 | 3.34±0.22*$^{\Psi}$ | 2.44±0.23 |
| **n** | 13 | 17 | 13 |

Data is presented as Mean ± SEM. I$_{Na}$ = sodium current; n = number of cells; V$_{1/2}$ = voltage for half-maximal activation or steady-state inactivation; k = slope factor; τ = time constant. Differences between data were analyzed with a one-way ANOVA with a post-hoc Tukey test. *vs Na$_V$1.5$^{WT}$; ‡vs Na$_V$1.5$^{WT/V1525M}$; $^{\Psi}$vs Na$_V$1.5$^{V1525M}$. Significantly different, p-value < 0.05.

Given the noteworthy loss of function observed in $I_{Na}$ when the SNV was expressed both in heterozygosis and in homozygosis, we wanted to rule out that the WT and the mutant Na$_V$1.5 expressed differently in the transfected cells. To assess that, we performed western blot analysis 48h after transfection.

One representative experiment is shown in **Figure 41**. Of note, total Na$_V$1.5 protein expression was not decreased when the SNV was expressed heterozygously (Na$_V$1.5$^{WT/V1525M}$) or homozygously (Na$_V$1.5$^{V1525M}$). Thus, a lower expression level does not explain the $I_{Na}$ decrease observed in these cells.

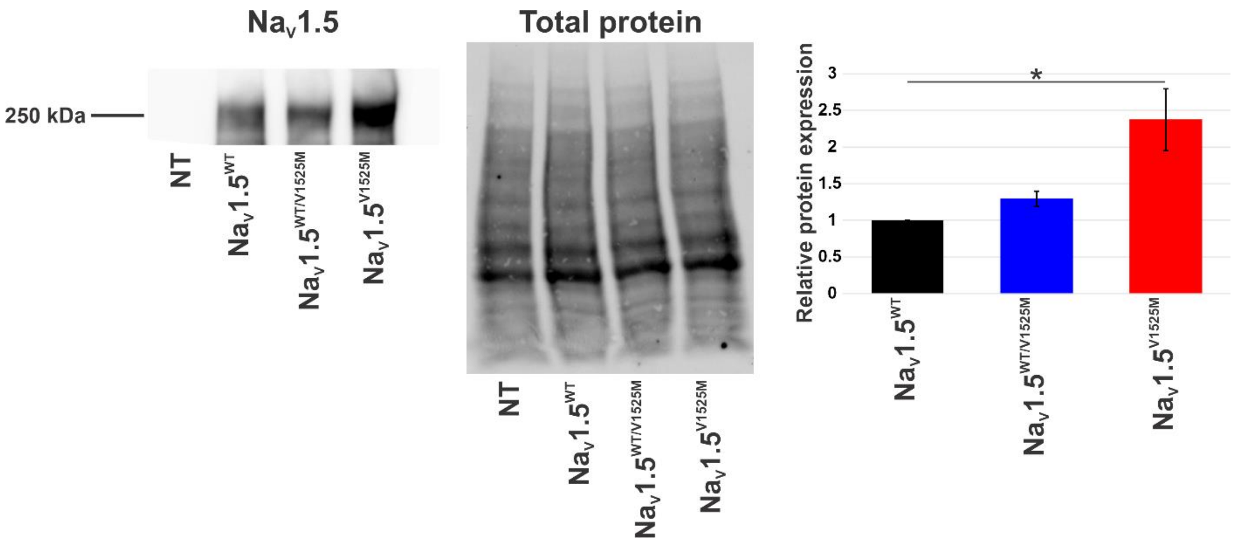

**Figure 41. Na$_V$1.5 protein expression was not decreased in cells transfected with the vectors carrying the SNV.** Western blot detection of Na$_V$1.5 (left) and corresponding total protein stain-free blot (middle), from HEK-293T cells transfected with either Na$_V$1.5$^{WT}$, Na$_V$1.5$^{WT/V1525M}$, or Na$_V$1.5$^{V1525M}$ or non-transfected cells (NT). Bar graph on the right depicts the relative protein expression normalized by Na$_V$1.5$^{WT}$ (n = 3). Differences between data were analyzed with a t-test. *vs Na$_V$1.5$^{WT}$. Significantly different, p-value < 0.05.

## 2. Generation of iPS cell lines

Based on the evidence for a loss of sodium current function of the mutant Na$_V$1.5 in heterologous conditions, and with aim to study the effects of the SNV in a more cardiomyocyte-like cellular environment carrying the patient-specific genetic background, we pursued with the patient-specific iPSc studies. As stated previously, the SNV *SCN5A*_c.4573G>A has been associated to BrS and is carried in heterozygosis by several members of the family under study.

We successfully obtained fibroblasts from skin samples of the four members of the family under study (**Figure 42A**). We sequenced the *SCN5A* coding region of the four individual's fibroblasts to confirm the presence of *SCN5A*_c.4573G>A in the SNV carriers (Rb20234, Rb20235, Rb20236), and the absence of the SNV in the non-carrier Rb20237 (related control) (**Figure 42B**).

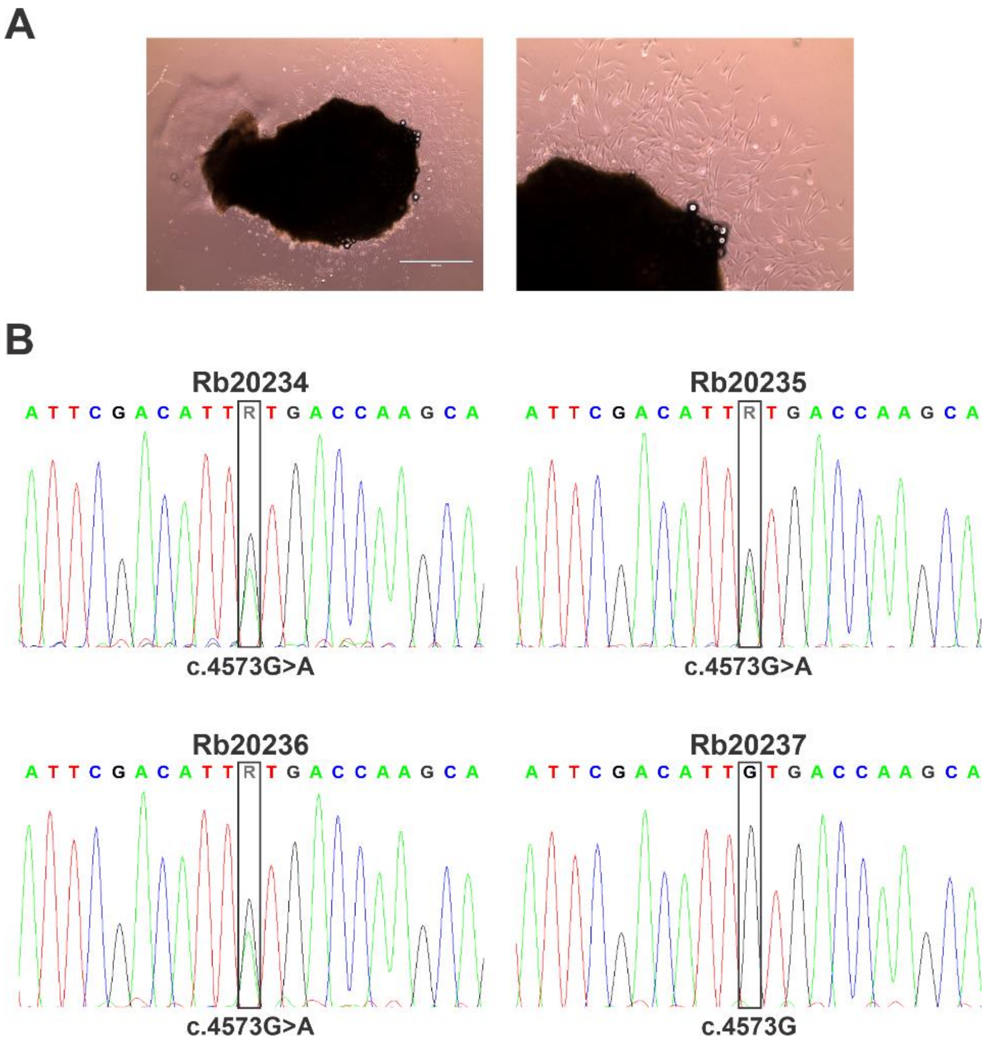

**Figure 42. Sequences of the *SCN5A* region harboring the SNV from the fibroblasts of the 4 family members. (A) Left:** Representative bright field microscopy image of fibroblasts in culture growing from a skin sample (dark area). Scale bar represents 1000 µm. **Right:** Magnification of the upper right section

of left image. **(B)** The SNV *SCN5A*_c.4573G>A was identified in genomic DNA isolated from fibroblasts in individuals Rb20234 (top left), Rb20235 (top right) and Rb20236 (bottom left), but not in individual Rb20237 (bottom right).

By day 26-28 after skin plating, fibroblasts were ready to be reprogrammed to iPS cells following the protocol explained in **Methods section 3.3**. iPS cell-like colonies appeared around day 20 after reprogramming, and were manually picked and treated as individual clones.

### 2.1. Clone selection

To obtain consistent molecular biology and electrophysiological results, we selected two clones for each patient. To select these clones, we used as a reference a non-related control iPS cell line (GPG1) that was previously generated in the laboratory. We first characterized the pluripotency transcription factors expression of this control. As shown in **Figure 43** and **Annex Table 4,** the pluripotency markers *Nanog*, *Sox-2* and *POU5F1* (encoding Oct-4) were widely overexpressed in the GPG1 iPS cells compared to the fibroblasts from the same individual.

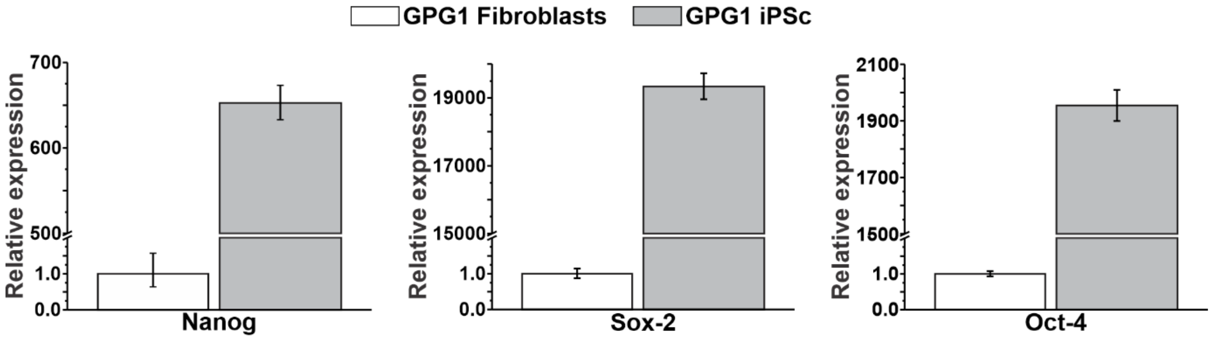

**Figure 43. The non-related control GPG1 iPSc overexpresses pluripotency transcription factors compared to the fibroblasts from the same individual.** The relative expression of pluripotency transcription factors Nanog (left), Sox-2 (middle) and Oct-4 (right) is shown as mean values of biological triplicates ± minimum and maximum relative quantification.

This cell line was further characterized at Centre De Medicina Regenerativa de Barcelona (CMRB) and this comprehensive characterization confirmed the suitability of these cells as an iPSc control (data not shown).

To choose which clones to select among the newly generated iPSc clones, we checked which of them expressed pluripotency markers at a similar level as GPG1 iPSc.

We selected the two iPSc clones for each of the individuals under study that showed the most similar levels of the transcription factors compared to the non-related control. Results obtained for the two clones from a representative patient are depicted in **Figure 44,** and all the relative quantification values of the chosen clones are defined in **Table 33**. The relative levels of the pluripotency transcription factors of the discarded clones can be found in the **Annex Tables 5-8**.

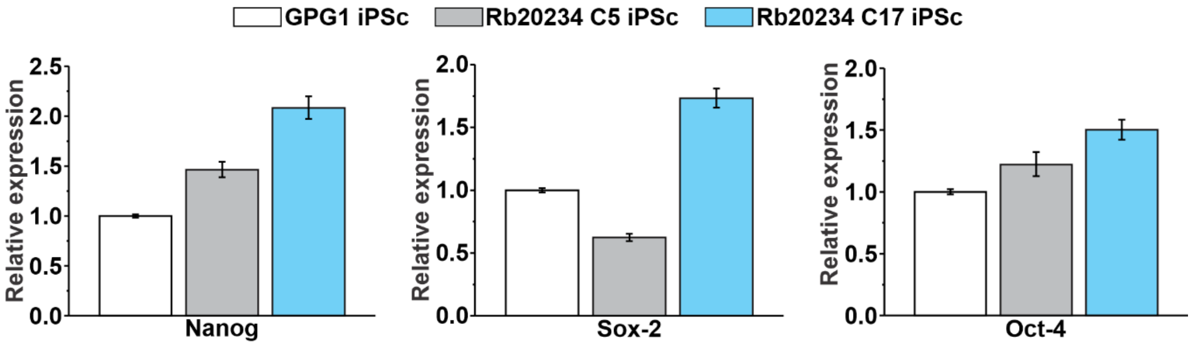

**Figure 44. Bar graph of two representative selected clones, showing that they display expression levels of the pluripotency transcription factors that are similar to those of the non-related control.** The relative expression of pluripotency transcription factors Nanog (left), Sox-2 (middle) and Oct-4 (right) is shown as mean values of biological triplicates ± minimum and maximum relative quantification.

**Table 33. Expression levels of the pluripotency transcription factors obtained by relative quantification (Rq) of the selected clones for each individual of the family under study with respect to the non-related control iPSc.**

| Individual | Selected clones | Nanog | | | Sox-2 | | | Oct-4 | | |
|---|---|---|---|---|---|---|---|---|---|---|
| | | Rq | Rq min | Rq max | Rq | Rq min | Rq max | Rq | Rq min | Rq max |
| **Rb20234** | **C5** | 1.463 | 1.389 | 1.542 | 0.624 | 0.595 | 0.654 | 1.220 | 1.127 | 1.322 |
| | **C17** | 2.083 | 1.972 | 2.200 | 1.731 | 1.657 | 1.808 | 1.502 | 1.423 | 1.584 |
| **Rn20235** | **C5** | 2.171 | 2.042 | 2.307 | 1.529 | 1.432 | 1.633 | 0.846 | 0.807 | 0.886 |
| | **C39** | 0.869 | 0.838 | 0.900 | 0.938 | 0.892 | 0.986 | 0.515 | 0.503 | 0.527 |
| **Rb20236** | **C21** | 2.351 | 1.979 | 2.793 | 1.093 | 0.925 | 1.292 | 1.361 | 1.155 | 1.603 |
| | **C24** | 3.987 | 3.628 | 4.382 | 1.548 | 1.426 | 1.682 | 2.033 | 1.853 | 2.230 |
| **Rb20237** | **C2** | 1.577 | 1.318 | 1.886 | 0.818 | 0.745 | 0.899 | 0.379 | 0.364 | 0.394 |
| | **C5** | 1.427 | 1.373 | 1.483 | 0.845 | 0.793 | 0.900 | 0.529 | 0.507 | 0.552 |

In order to ensure the presence or absence of the *SCN5A*_c.4573G>A SNV in the selected clones, we sequenced exon 27 of *SCN5A* in genomic DNA samples. We confirmed the presence of *SCN5A*_c.4573G>A in Rb20234, Rb20235 and Rb20236 iPSc selected clones, and its absence in Rb20237 iPSc selected clones (**Figure 45**).

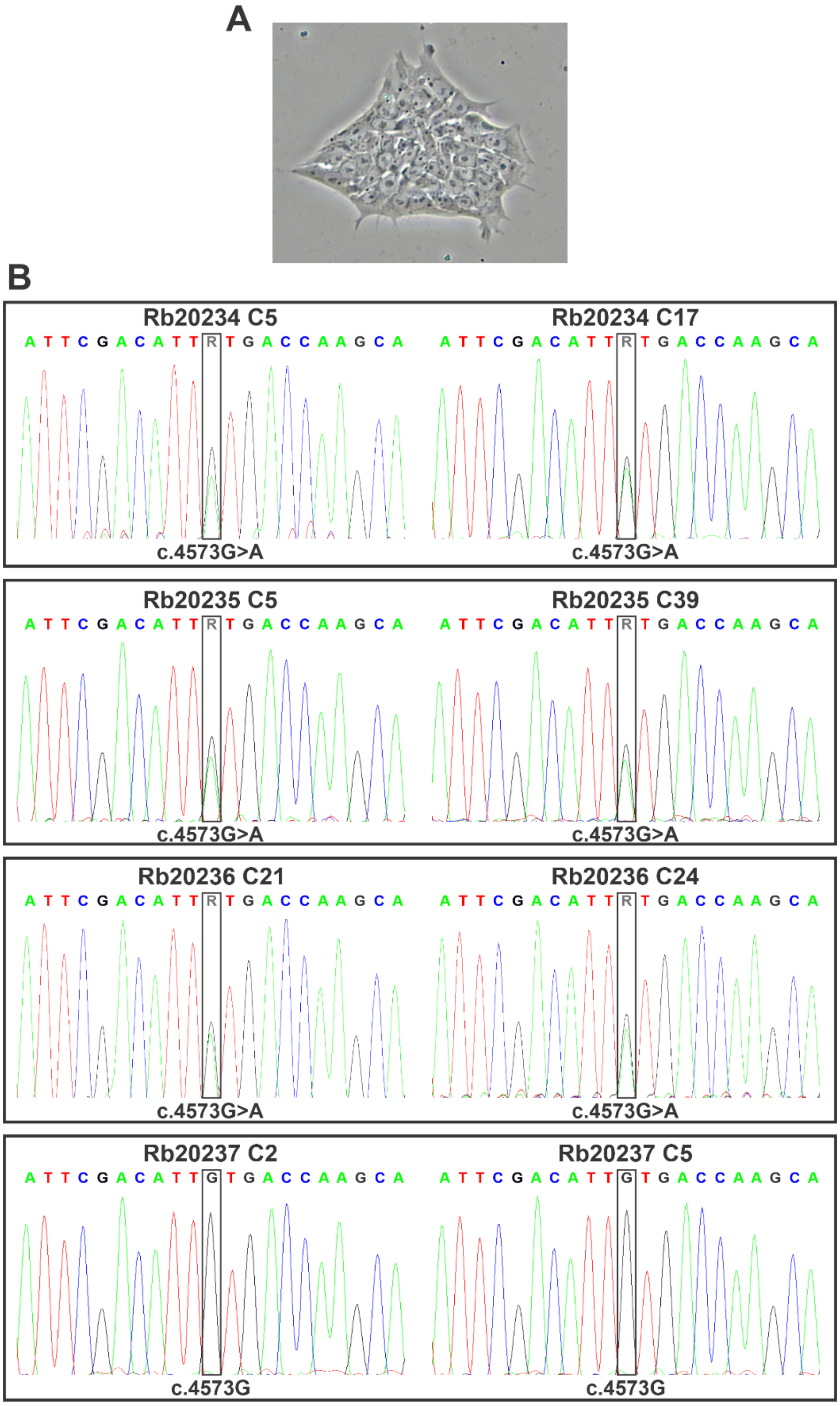

**Figure 45. Sequencing of the *SCN5A* region harboring the SNV in iPSc selected clones. (A)** Representative bright field microscopy image of iPSc colonies in culture. **(B)** The SNV

*SCN5A*_c.4573G>A was identified in genomic DNA isolated from iPSc clones in individuals Rb20234 (first row), Rb20235 (second row) and Rb20236 (third row), but not in individual Rb20237 (fourth row).

### 2.2. Clone characterization

To assure that our iPSc were suitable for differentiation, we sent one of the two selected iPSc clones of each patient for a thorough characterization in Centre De Medicina Regenerativa de Barcelona (CMRB). The results from this characterization are summarized in **Table 34**.

**Table 34. Summary of the results of the iPSc characterization.**

| | **Rb20234 C17** | **Rb20235 C5** | **Rb20236 C21** | **Rb20237 C5** |
|---|---|---|---|---|
| **Mycoplasma analysis** | Negative | Negative | Negative | Negative |
| **Reprogramming plasmids presence** | Negative | Negative | Negative | Negative |
| **Alkaline phosphatase** | Positive | Positive | Positive | Positive |
| **Karyotype** | 46, XX | 46, XY | 46, XX | 46, XY |
| **Pluripotency test** | Positive for Oct-4, SSEA-3, SSEA-4, Nanog, Sox-2, TRA-1-60, TRA-1-81 | Positive for Oct-4, SSEA-3, SSEA-4, Nanog, Sox-2, TRA-1-60, TRA-1-81 | Positive for Oct-4, SSEA-3, SSEA-4, Nanog, Sox-2, TRA-1-60, TRA-1-81 | Positive for Oct-4, SSEA-3, SSEA-4, Nanog, Sox-2, TRA-1-60, TRA-1-81 |
| **In vitro differentiation** | Ectoderm positive: Tuj1, GFAP | Ectoderm positive: Tuj1 | Ectoderm positive: Tuj1 | Ectoderm positive: Tuj1 |
| | Endoderm positive: AFP, FOXA2 | Endoderm positive: AFP, FOXA2 | Endoderm positive: AFP, FOXA2 | Endoderm positive: AFP, FOXA2 |
| | Mesoderm positive: ASMA, ASA | Mesoderm positive: ASMA | Mesoderm positive: ASMA | Mesoderm positive: ASMA |

**Table 34** shows the absence of mycoplasma contamination and reprogramming plasmids in the four iPSc clones studied. The selected iPSc clones stained positive for alkaline phosphatase activity (**Table 34**). This enzyme's activity is up-regulated in pluripotent stem cells, thus it is a method widely used to identify iPSc. Moreover, the iPSc clones displayed a normal karyotype (**Table 34**). **Figure 46** shows the alkaline phosphatase staining and karyotype from a representative iPSc clone, and **Annex Figure 6** depicts the other three clones.

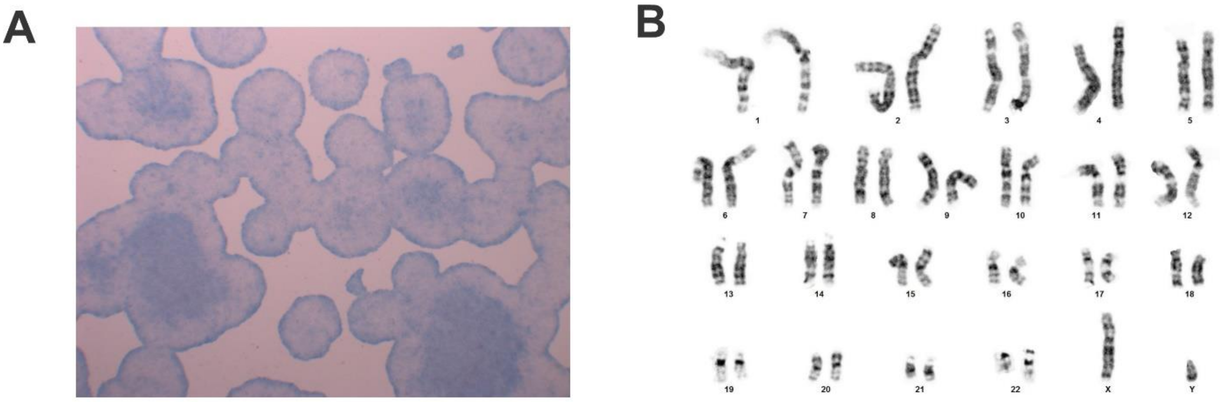

**Figure 46. Alkaline phosphatase staining (A) and karyotype (B) of Rb20235 C5 iPSc.**

In agreement with our qPCR results presented in **section 2.1**, the iPSc clones tested positive in immunohistochemical studies for several pluripotency transcription factors (**Figure 47**).

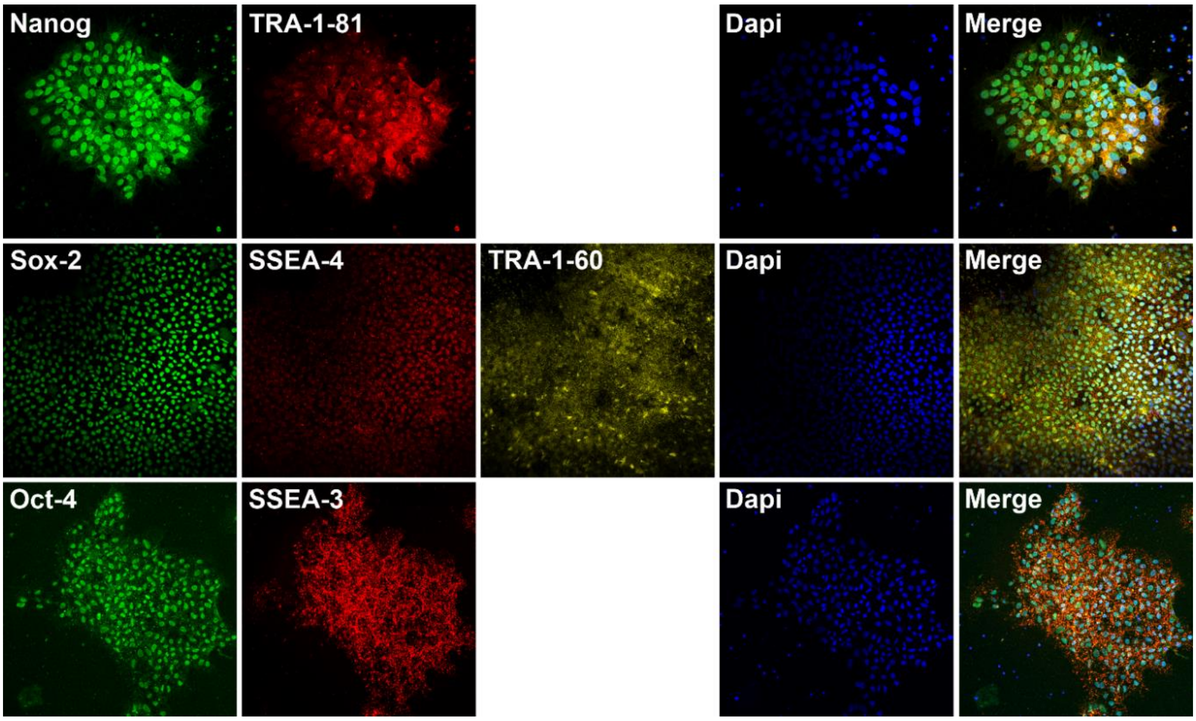

**Figure 47. Pluripotency characterization of Rb20234 C17 iPSc clone.** iPSc clone Rb20234 C17 tested positive for pluripotency markers Nanog and TRA-1-81 (upper panel), Sox-2, SSEA-4 and TRA-1-60 (middle panel), and Oct-4 and SSEA-3 (bottom panel).

Furthermore, immunohistochemical staining for characteristic markers of cells derived from the three germ layers after in vitro differentiation confirmed the ability of the selected clones to differentiate into cells of the three germ layers (**Figure 48**).

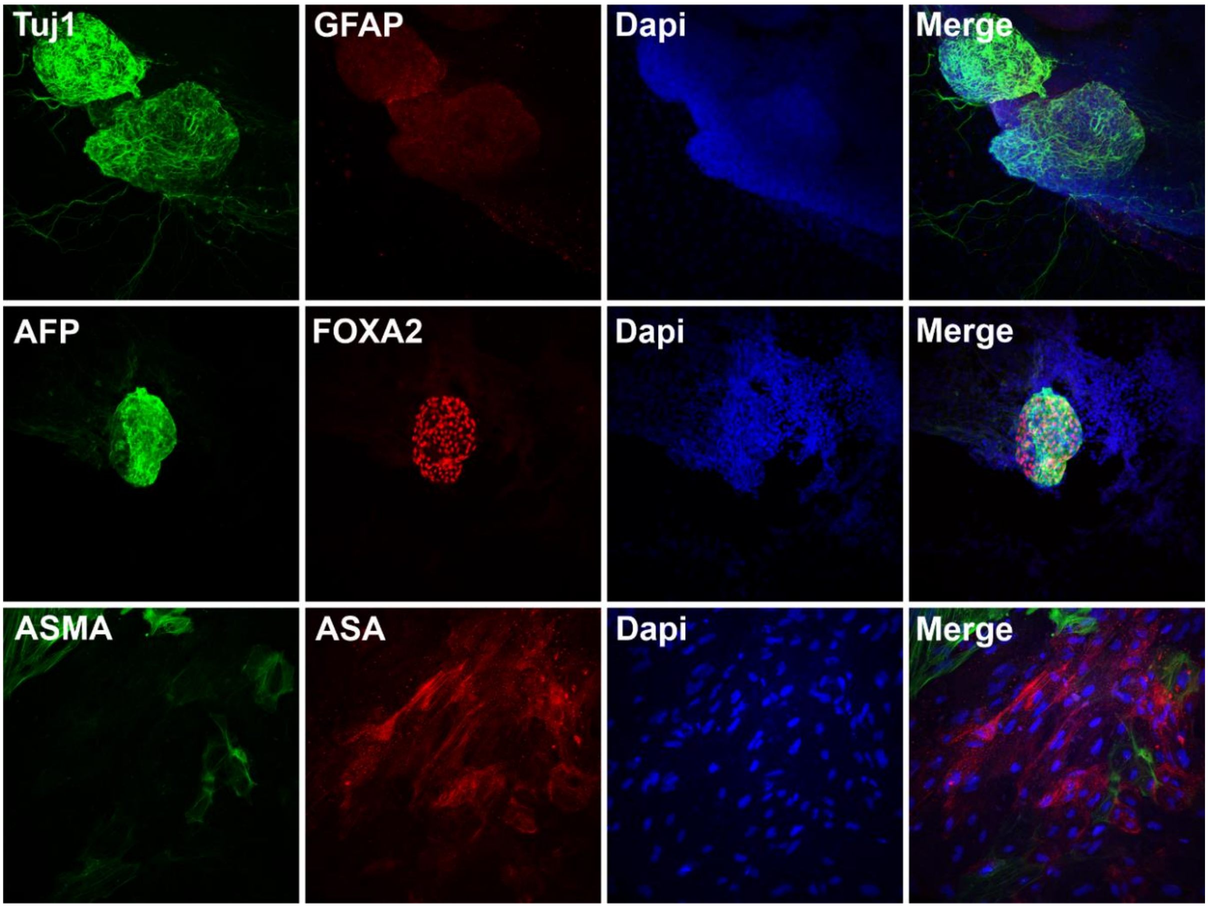

**Figure 48. In vitro differentiation of Rb20234 C17 iPSc clone into the three germ layers.** Studies of in vitro differentiation to cells of the three germ layers showed the capacity of the studied iPSc to differentiate into cells of the ectoderm (positive staining for Tuj1 and GFAP, upper panel), endoderm (positive staining for AFP and FOXA2, middle panel), and mesoderm (positive staining for ASMA and ASA, bottom panel).

The complete immunohistochemical studies of the other iPSc clones can be found in **Annex Figures 7-9**.

## 3. iPS cell differentiation to cardiomyocytes

Characterization of the newly generated iPS cell lines indicated that they displayed the expected features for iPSc. Therefore, we proceeded with the differentiation of these iPSc into cardiomyocytes. This would allow us to characterize the effect of the SNV on the electrophysiological properties of the cardiac sodium current, in a cardiomyocyte-like environment holding the patient-specific genetic background.

### 3.1. Optimization of the differentiation protocol

We used the non-related control GPG1 iPSc to optimize a differentiation protocol which would render a high yield of pure mature cardiomyocytes. To do so, we tried different published differentiation protocols. First we followed Xu *et al.*[214] protocol, based in the formation of embryoid bodies. Although we obtained beating iPS-CM, the yield was low, so we switched to a monolayer-based differentiation protocol, published by Zanella *et al*.[215]

Since the results with these protocols were below optimal, we implemented a different protocol published by Lin *et al*.[210] A full description of the protocol is explained in **Methods section 3.4.2**. However, to improve the yield of healthy beating iPS-CM, we introduced some modifications. First, we added ROCK inhibitor (ROCKi) from day 2 to 5 to increase cell survival. This improvement yielded a monolayer of beating cells. To obtain a purer and more homogeneous iPS-CM culture, we used glucose starvation as reported by Sharma *et al*.[136] This protocol is based on the capacity of cardiomyocytes to metabolize lactate, while other, non-differentiated cells cannot survive in the absence of glucose. Thus, we fed the cells with a medium without glucose (**Methods Table 6**) on differentiation days 10, 12 and 14.

Ongoing work in the lab by David Carreras is focused on maturating iPS-CM, as it is known that these differentiated cells display a structural and electrical immature phenotype. He validated that replating the cells to a new matrigel-coated well on differentiation day 16, and adding T3 and Dex from day 16 to day 30 as reported by Parikh *et al*.[211] increased cardiomyocyte maturity. Therefore, we introduced these improvements to our protocol.

On differentiation day 30, cells were either collected for the cardiomyocyte characterization or disaggregated for the electrophysiological studies. All the experiments shown in this thesis were performed using the iPS-CM obtained with the complete protocol, which included all the improvements (**Figure 49**).

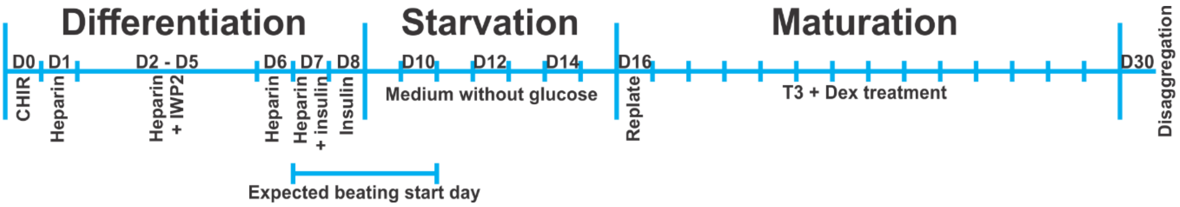

**Figure 49. Schematic representation of the optimized differentiation protocol.** Protocol based on the studies published by Lin et al, Sharma et al, and Parikh et al, and including our modifications.

### 3.2. Cardiomyocyte characterization

To assess whether the optimized differentiation protocol yielded a good population of iPS-CM, we measured the absence and presence of pluripotency and cardiomyocyte markers, respectively. For this purpose, we performed qPCRs on three differentiation rounds of each selected clone on day 30 of differentiation. We first compared the expression levels of pluripotency transcription factors in iPS-CM samples with their respective iPS cell clones.

**Figure 50 and Annex Tables 9-12** show that the expression levels of the pluripotency transcription factors studied were severely decreased in iPS-CM compared to the iPSc clones. Thus, iPS-CM did not express pluripotency markers, as expected.

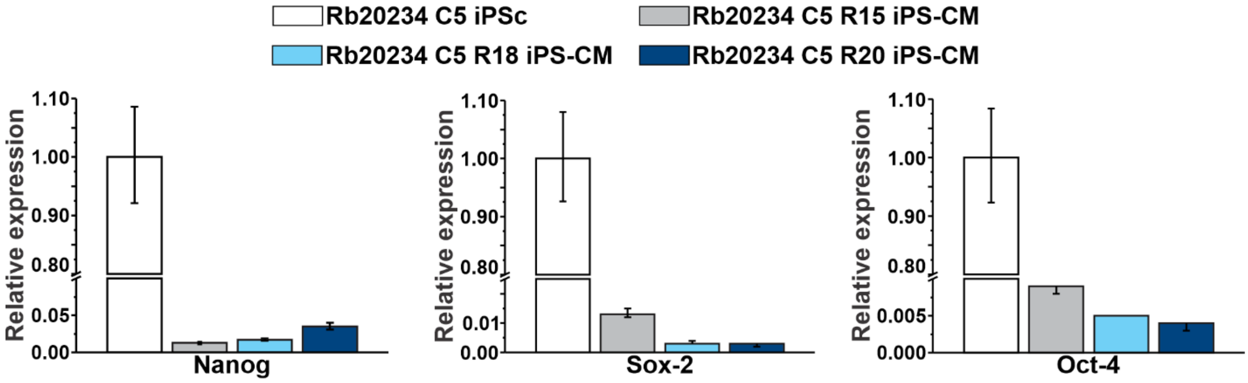

**Figure 50. iPS-CM do not express pluripotency transcription factors compared to the iPSc.** The relative expression of pluripotency transcription factors Nanog (left), Sox-2 (middle) and Oct-4 (right) is shown as mean values of biological triplicates ± minimum and maximum relative quantification for 3 rounds of differentiation of one representative clone.

To confirm that the obtained cells showed characteristics of cardiomyocyte type cells, we assessed the expression of three cardiac gene markers (*MYBPC3*, *TNNI3* and *SCN5A*) in iPS-CM in comparison to the iPSc clones.

All three cardiac genes were overexpressed in the iPS-CM compared to iPS cell clones (**Figure 51 and Annex Tables 13-16**), being *MYBPC3* the most expressed gene.

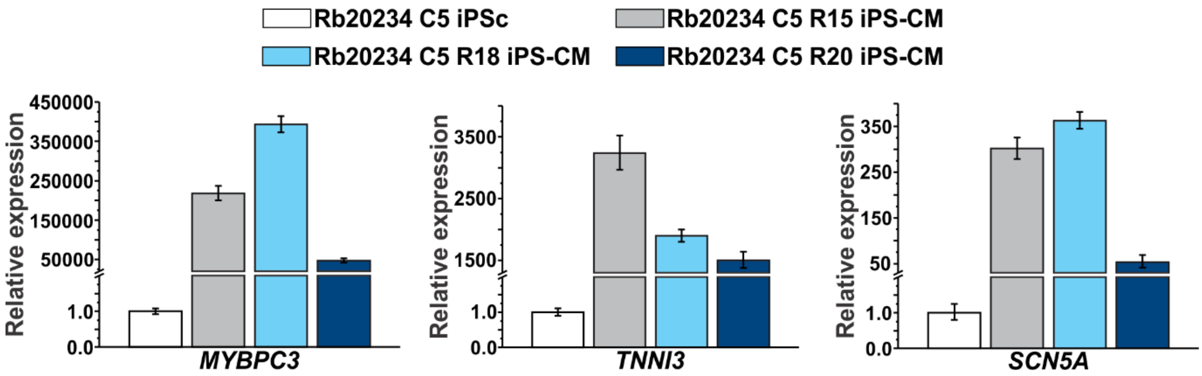

**Figure 51. iPS-CM overexpress cardiac gene markers compared to the iPSc.** The relative expression of cardiac gene markers MYBPC3 (left), TNNI3 (middle) and SCN5A (right) is shown as mean values of biological triplicates ± minimum and maximum relative quantification for 3 rounds of differentiation of one representative clone.

## 4. Electrophysiological characterization of iPS-CM

Once we confirmed that the iPS-CM obtained for each clone of the four family members showed characteristics of cardiomyocyte-type cells, we aimed to study the sodium current properties on this cellular model. Between 6 and 12 differentiation rounds for each individual were studied.

### 4.1. Evaluation of individual Rb20237 as a suitable control

First, we evaluated whether the non-carrier member of the family (Rb20237) was a suitable control for the electrophysiological experiments. To assess this, we studied and compared the sodium current properties of iPS-CM from the related control Rb20237 with the non-related control GPG1 using the whole cell patch clamp technique.

Our electrophysiological studies evidenced that iPS-CM from both Rb20237 iPSc clones displayed similar sodium current properties (**Table 35**). Thus, we pooled the results from the two clones for all the experiments analyses.

Both Rb20237 and GPG1 iPS-CM displayed similar peak $I_{Na}$ density (**Figure 52B** and **Table 35**), and no differences were observed in the voltage dependence of activation (**Figure 52C** and **Table 35**). However, voltage dependence of steady-state inactivation of GPG1 showed a positive shift of 4 mV compared to Rb20237 (**Figure 52C** and **Table 35**). Recovery from inactivation values were similar (**Figure 52D** and **Table 35**).

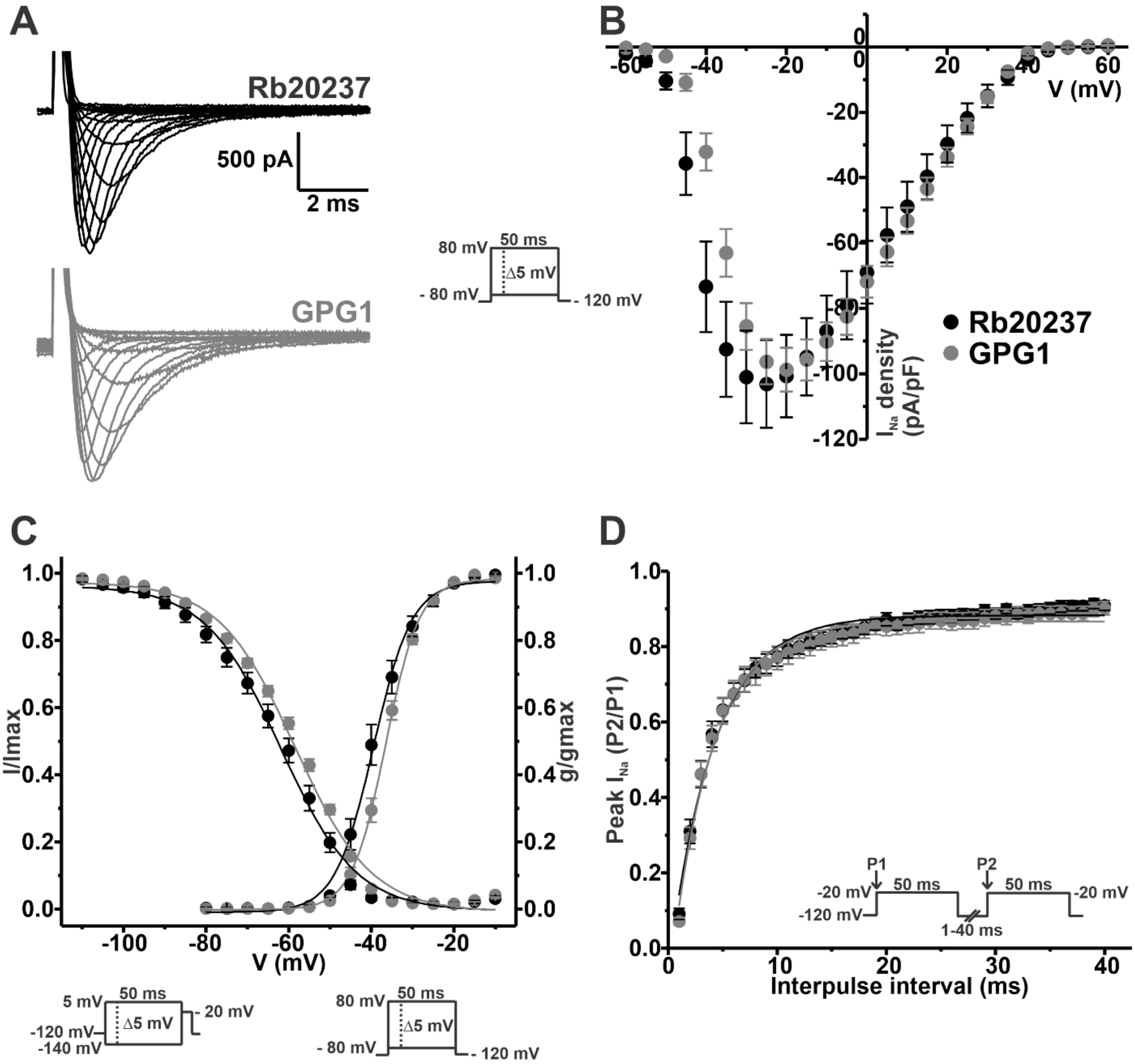

**Figure 52. The family-related and non-related controls display similar sodium current properties.** Whole cell currents were elicited by depolarizing potentials as shown in the insets. Black circles depict data for Rb20237 iPS-CM, and grey circles represent GPG1 iPS-CM. Values are expressed as mean ± SEM. **(A)** Representative whole cell $Na^+$ current traces from RB20237 (top) and GPG1 (bottom). **(B)** Mean peak current density-voltage relationship. $I_{Na}$ amplitude was normalized by the cell capacitance to obtain $I_{Na}$ density values. **(C)** $I_{Na}$ steady-state voltage dependence of activation and inactivation plots. Data was fitted to a Boltzmann equation (solid lines). **(D)** Recovery from inactivation curves. Data was fitted to a monoexponential function (solid lines).

**Table 35. Biophysical parameters of both Rb20237 clones, Pooled Rb20237 and GPG1 iPS-CM.**

| Parameter | Rb20237 C2 | Rb20237 C5 | Pooled Rb20237 | GPG1 |
|---|---|---|---|---|
| **Peak $I_{Na}$ density** | | | | |
| **pA/pF** | -94.69±17.36 | -109.17±19.69 | -103.10±13.41 | -98.74±6.70 |
| **n** | 13 | 18 | 31 | 28 |
| **Activation** | | | | |
| **$V_{1/2}$ (mV)** | -37.28±1.51 | -39.94±1.38 | -38.77±1.04 | -36.60±0.57 |
| **k** | 3.63±0.37 | 3.46±0.42 | 3.54±0.28 | 3.65±0.14 |
| **n** | 13 | 18 | 31 | 28 |
| **Steady-state inactivation** | | | | |
| **$V_{1/2}$ (mV)** | -61.07±1.48 | -62.54±2.23 | -62.43±1.40 | -58.54±0.76* |
| **k** | 8.51±0.48 | 7.42±0.55 | 8.10±0.37 | 8.99±0.18* |
| **n** | 12 | 12 | 24 | 25 |
| **Recovery from inactivation** | | | | |
| **τ (ms)** | 3.66±0.51 | 4.62±0.64 | 4.17±0.42 | 4.30±0.53 |
| **n** | 8 | 9 | 17 | 19 |

Data is presented as Mean ± SEM. $I_{Na}$ = sodium current; n = number of cells; $V_{1/2}$ = voltage for half-maximal activation or steady-state inactivation; k = slope factor; τ = time constant. Differences between data were analyzed with a t-test. *vs Pooled Rb20237. Significantly different, $p\text{-value} < 0.05$.

### 4.2. Sodium current density is decreased in Rb20234 and Rb20235 individuals

After confirming that Rb20237 was suitable as a related-control, we aimed to determine whether the SNV *SCN5A*_c.4573G>A affected the cardiac $Na_V1.5$ sodium current density in the carrier individuals Rb20234, Rb20235 and Rb20236. Similar to Rb20237, both selected clones of Rb20234, Rb20235 and Rb20236 displayed similar sodium current properties and thus data was pooled for all the electrophysiological experiments (**Annex Tables 18-20**).

To avoid clamp artifacts or recordings saturation, especially in control iPS-CMs where the currents were expected to be large, cells were bathed in low sodium solution to decrease $I_{Na}$. Surprisingly, we observed that a high percentage of iPS-CM from individuals Rb20234 and Rb20235 did not display recordable $I_{Na}$ (**Figure 53**). While more than 60% of iPS-CM from Rb20234 and Rb20235 failed to show recordable $I_{Na}$, this was not reproduced in individuals Rb20237 and Rb20236, as the percentage was of 10% and 5% respectively.

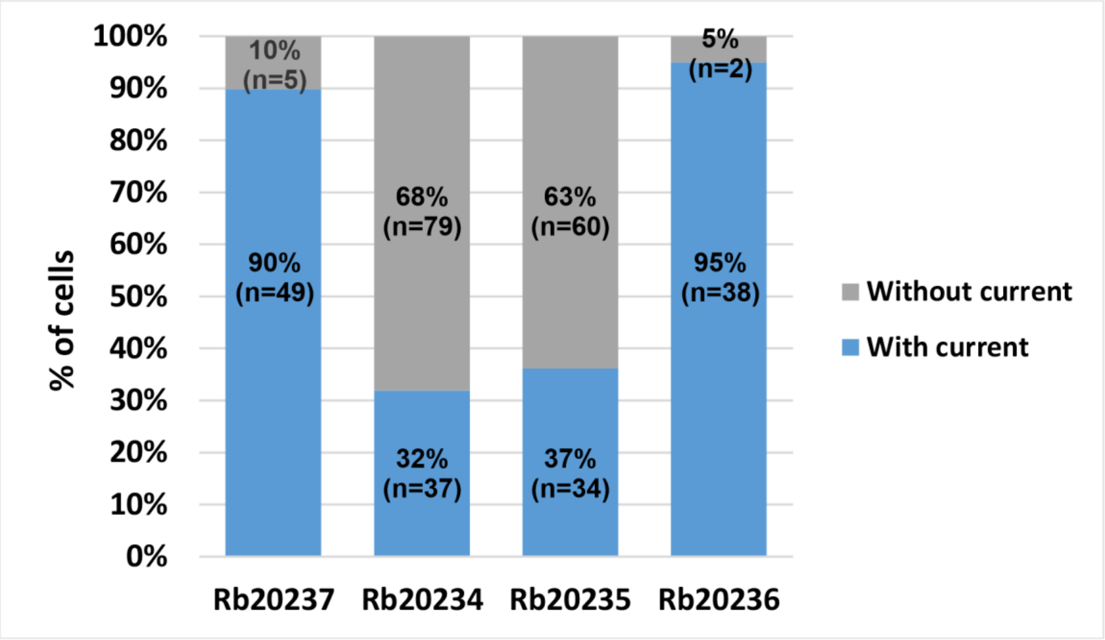

**Figure 53. More than 60% of Rb20234 and Rb20235 iPS-CM did not show recordable $I_{Na}$.** Grey portion of the bar graph represents percentage and number of cells without recordable $I_{Na}$. Blue portion represents percentage and number of cells with recordable $I_{Na}$.

We investigated if the lack of recordable $I_{Na}$ in Rb20234 and Rb20235 iPS-CM was due to the presence of different cardiomyocyte types among the cells studied. It is known that nodal cells do not display $Na_V1.5$ sodium current. A heterogeneous population of cardiomyocytes, potentially enriched in nodal cells, could have been obtained during iPS-CM differentiation, and could explain the absence of recordable $I_{Na}$ in these 2 patients. To rule out this hypothesis, we assessed the expression of ventricular, atrial and nodal markers (*MYL2*, *MYL7* and *HCN4* genes, respectively) in 5 rounds of each individual by qPCR. *MYL2* and *MYL7* relative quantification values for each differentiation round were normalized by those of *HCN4*. We measured the expression of the markers in the Rb20234, Rb20235 and Rb20236 iPS-CM, relative to the control Rb20237.

As shown in **Figure 54**, the studied ventricular and atrial markers are similarly overexpressed in the three individuals in comparison to the control Rb20237. Thus, the lack of recordable $I_{Na}$ in iPS-CM from individuals Rb20234 and Rb20235 cannot be attributed to a diminished expression of ventricular or atrial-type cells in any of the patient-specific iPS-CM. The complete Rq values can be found in **Annex Table 17**.

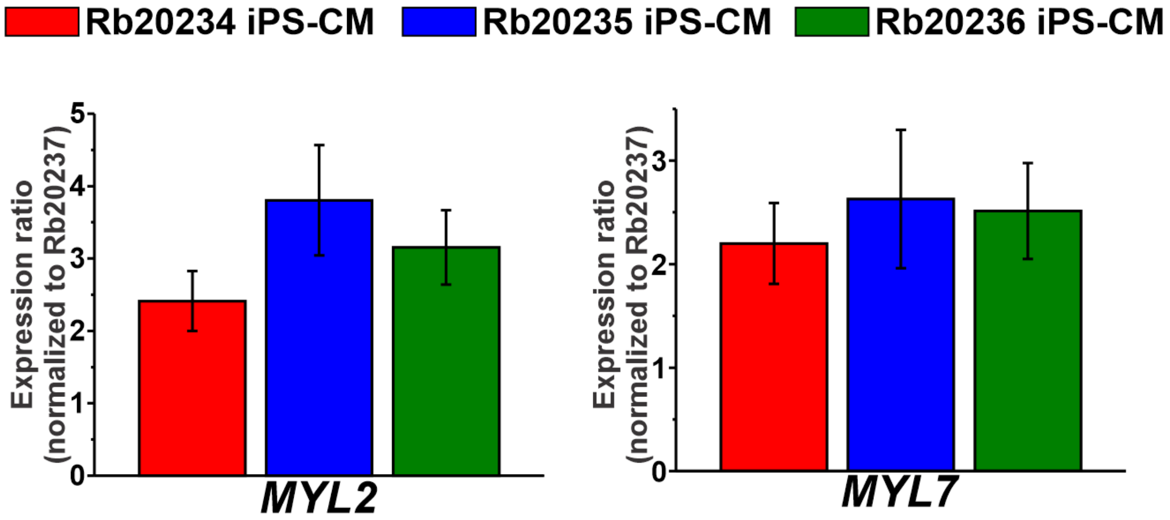

**Figure 54. Rb20234, Rb20235 and Rb20236 iPS-CM overexpress ventricular and atrial markers compared to the nodal marker.** The ratio between the ventricular marker *MYL2* or the atrial marker *MYL7* and the nodal marker *HCN4* for individuals Rb20234, Rb20235 and Rb20236 was normalized by the ratios obtained for individual Rb20237 to obtain the relative expression. The relative expression of *MYL2* (left) and *MYL7* (right) is shown as mean values of biological triplicates ± SEM for 5 rounds of differentiation. Differences between data were analyzed with a one-way ANOVA with a post-hoc Tukey test.

The analysis of the sodium current properties for individuals Rb20234 and Rb20235 was performed using the cells that did show recordable $I_{Na}$. Analysis of the data revealed a reduction of $I_{Na}$ density in Rb20234 and Rb20235 iPS-CM of 77.7% and 78.1%, respectively compared to Rb20237 (**Figure 55B** and **Table 36**). On the contrary, $I_{Na}$ density of Rb20236 was increased by 68.3% compared to Rb20237 (**Figure 55B** and **Table 36**).

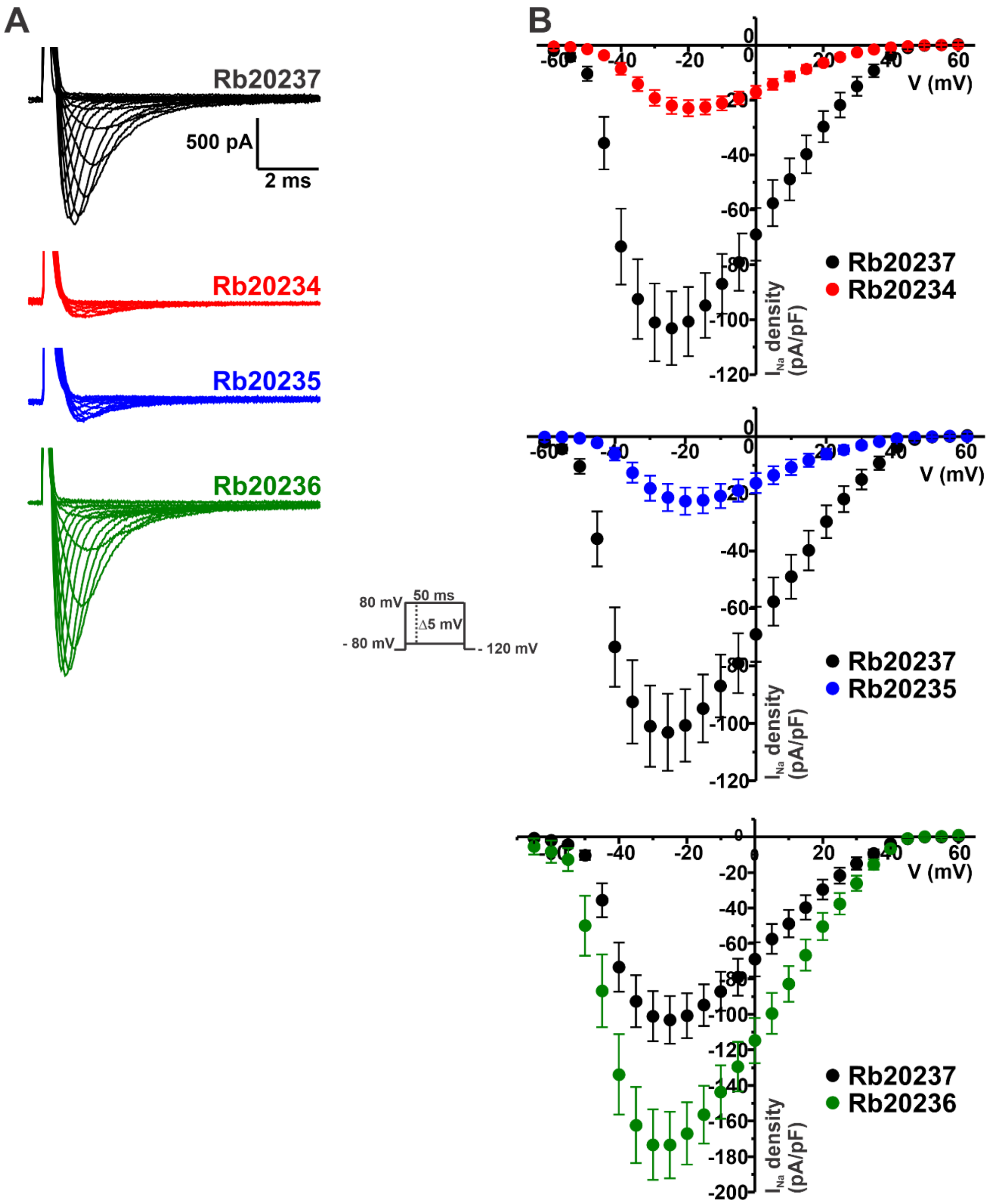

**Figure 55. SNV *SCN5A*_c.4573G>A drastically decreases $I_{Na}$ density in Rb20234 and Rb20235, and increases $I_{Na}$ density in Rb20236.** Whole cell currents were elicited by depolarizing potentials as shown in the insets. Black circles depict data for Rb20237, red circles represent Rb20234, blue circles represent Rb20235, and green circles represent Rb20236 iPS-CM. Values are expressed as mean ± SEM. **(A)** Representative whole cell $Na^+$ current traces from RB20237 (top left), Rb20234 (top right), Rb20235 (bottom left) and Rb20236 (bottom right). **(B)** Mean peak current density-voltage relationship compared to Rb20237 of Rb20234 (top left), Rb20235 (top right) and Rb20236 (bottom). Peak $I_{Na}$ amplitude was normalized by the cell capacitance to obtain peak $I_{Na}$ density values.

**Table 36. Sodium current density parameters of the four individuals of the family.**

| Parameter | Rb20237 | Rb20234 | Rb20235 | Rb20236 |
|---|---|---|---|---|
| **Peak $I_{Na}$ density** | | | | |
| **pA/pF** | -103.10±13.41 | -22.96±2.90* | -22.53±4.72* | -173.55±18.73* |
| **n** | 31 | 21 | 20 | 24 |

Data is presented as Mean ± SEM. $I_{Na}$ = sodium current; n = number of cells. Differences between data were analyzed with a t-test. *vs Rb20237. Significantly different, p-value < 0.05.

We measured the inactivation time constant at different voltages using the same I-V pulse protocol. We fitted the data to a double-exponential function. However, since the current of Rb20234 and Rb20235 iPS-CM was so small, the fit of the slow component was not accurate. Thus, we are representing only the time constant for the fast component (τ fast). As shown in **Figure 56**, τ fast was significantly increased in Rb20234 and Rb20235 iPS-CM at more negative potentials (identified with the symbol *), compared to Rb20237. In addition, τ fast was also significantly increased in Rb20235 iPS-CM at more positive potentials, with respect to Rb20237.

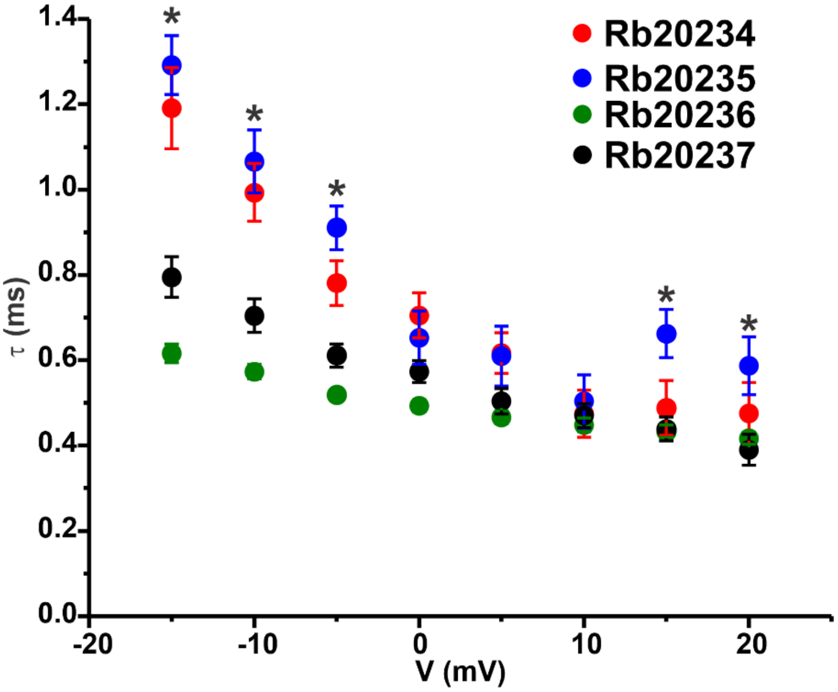

**Figure 56. SNV *SCN5A*_c.4573G>A increases τ fast in Rb20234 and Rb20235.** Black circles depict data for Rb20237, red circles represent Rb20234, blue circles represent Rb20235, and green circles represent Rb20236 iPS-CM. Values are expressed as mean ± SEM. Differences between data were analyzed with a t-test. *vs Rb20237. Significantly different, p-value < 0.05.

### 4.3. Voltage dependence of activation and steady-state inactivation are positively shifted in Rb20234 and Rb20235 iPS-CM

We next assessed whether the SNV *SCN5A*_c.4573G>A modified the voltage dependence of activation and steady-state inactivation sodium current properties. Since the steady-state inactivation values between the control Rb20237 and the non-related control GPG1 were significantly different, we compared the values obtained for the iPS-CM corresponding to the carriers with both the related and non-related controls.

As shown in **Figure 57** and **Table 37**, we observed a positive shift of the voltage dependence of the activation curve for Rb20234 and Rb20235 respect to Rb20237 ($V_{1/2}$ increased 5 mV and 8 mV, respectively) and also respect to GPG1 ($V_{1/2}$ increased 2.5 mV and 6 mV, respectively). Fitting of the steady-state voltage dependence of inactivation data to a Boltzmann equation also evidenced a positive shift of the curve in the SNV carriers Rb20234 and Rb20235 compared to Rb20237 ($V_{1/2}$ increased 8 mV and 7 mV, for Rb20234 and Rb20235 respectively; **Figure 57** and **Table 37**) and to GPG1 ($V_{1/2}$ increased 4 mV and 3 mV, for Rb20234 and Rb20235 respectively; **Table 37**).

Neither of these shifts was observed in the iPS-CM from SNV carrier Rb20236, compared to both Rb20237 (**Figure 57** and **Table 37**) or GPG1 (**Table 37**).

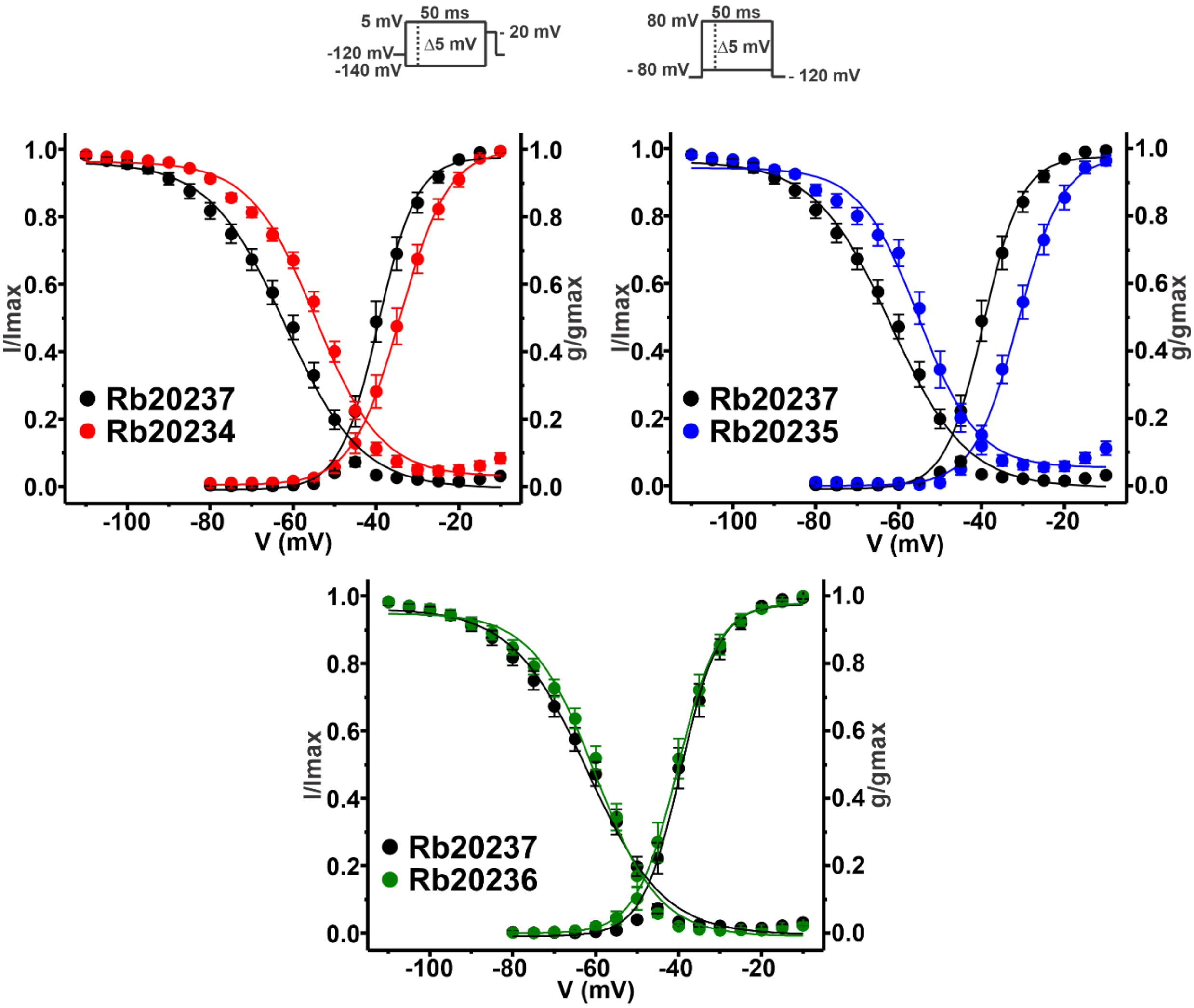

**Figure 57. SNV *SCN5A*_c.4573G>A shifts voltage dependence of activation and steady-state inactivation in Rb20234 and Rb20235.** $I_{Na}$ steady-state voltage dependence of activation and inactivation plots for Rb20234 (top left), Rb20235 (top right) and Rb20236 (bottom), compared to Rb20237. Whole cell currents were elicited by depolarizing potentials as shown in the insets. Black circles depict data for Rb20237, red circles represent Rb20234, blue circles represent Rb20235, and green circles represent Rb20236 iPS-CM. Solid lines represent the fitted Boltzmann curves. Values are expressed as mean ± SEM.

**Table 37. Sodium current voltage dependence of activation and steady-state inactivation parameters of the four individuals of the family.**

| Parameter | Rb20237 | Rb20234 | Rb20235 | Rb20236 | GPG1 |
|---|---|---|---|---|---|
| **Activation** | | | | | |
| **$V_{1/2}$ (mV)** | -38.77±1.04 | -34.09±1.23*$^{\Psi}$ | -30.33±1.23*$^{\Psi}$ | -40.10±1.22 | -36.60±0.57 |
| **k** | 3.54±0.28 | 4.81±0.25*$^{\Psi}$ | 4.92±0.34*$^{\Psi}$ | 4.04±0.39 | 3.64±0.14 |
| **n** | 31 | 22 | 19 | 20 | 29 |
| **Steady-state inactivation** | | | | | |
| **$V_{1/2}$ (mV)** | -62.43±1.40 | -54.66±0.99*$^{\Psi}$ | -55.14±1.46*$^{\Psi}$ | -60.34±1.16 | -58.54±0.76* |
| **k** | 8.10±0.37 | 7.46±0.29*$^{\Psi}$ | 6.25±0.65*$^{\Psi}$ | 7.18±0.50 | 8.99±0.18 |
| **n** | 24 | 18 | 15 | 18 | 25 |

Data is presented as Mean ± SEM. $V_{1/2}$ = voltage for half-maximal activation or steady-state inactivation; k = slope factor; n = number of cells. Differences between data were analyzed with a t-test. *vs Rb20237. $^{\Psi}$vs GPG1. Significantly different, $p$-value < 0.05.

### 4.4. Recovery from Inactivation is only affected in Rb20234 iPS-CM

We then assessed the Recovery from Inactivation, illustrated in **Figure 58** and summarized in **Table 38**.

Data fitted to a monoexponential function showed a significant increase in the time constant of Rb20234 iPS-CM, compared to Rb20237. Interestingly, we did not detect this increase in the iPS-CM of the remaining SNV carriers Rb20235 and Rb20236.

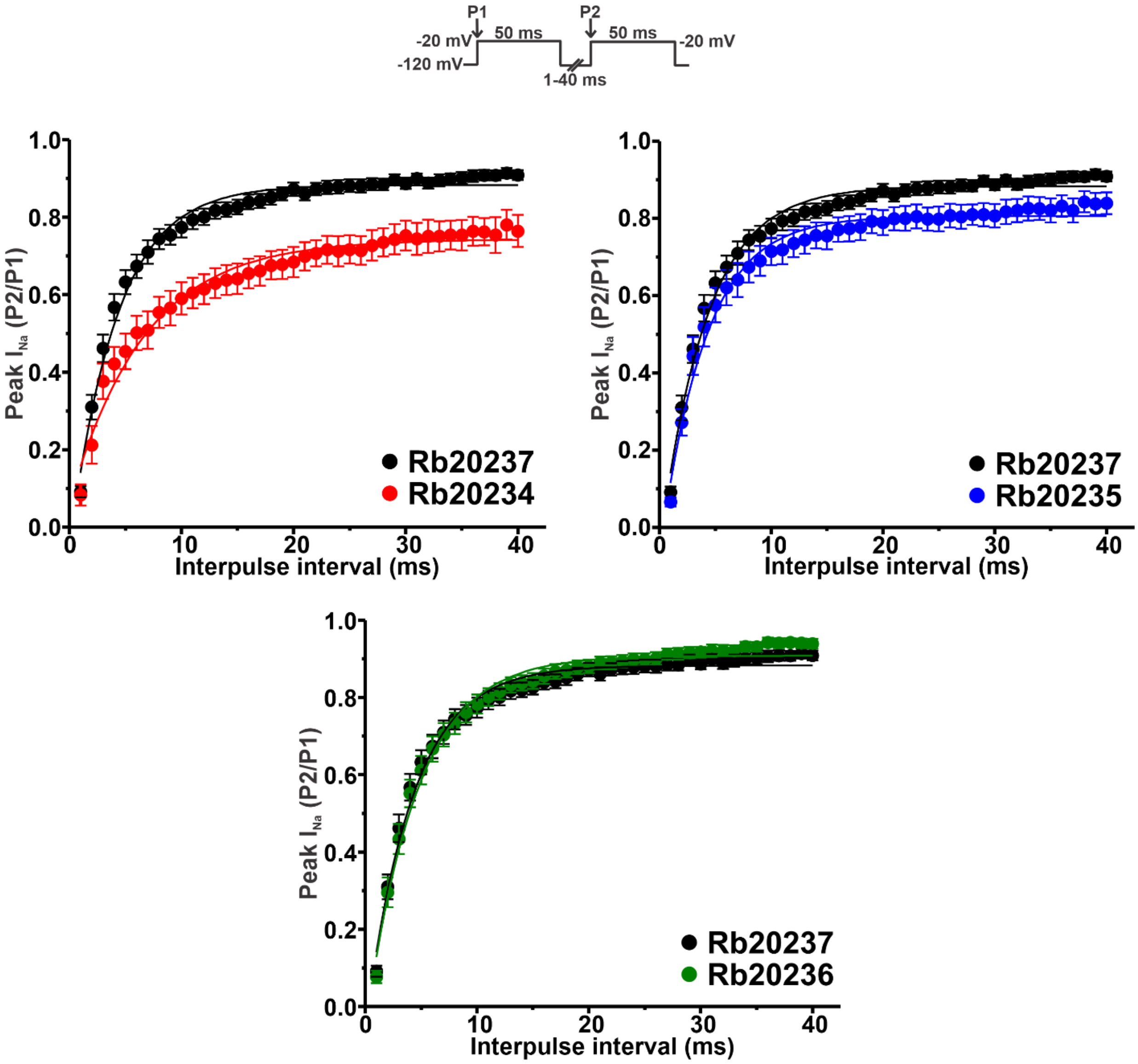

**Figure 58. Recovery from inactivation time constant is only increased in Rb20234 iPS-CM.** Recovery from Inactivation plots comparing Rb20237 with Rb20234 (top left), Rb20235 (top right) or Rb20236 (bottom). Whole cell currents were elicited by depolarizing potentials as shown in the insets. Black circles depict data for Rb20237, red circles represent Rb20234, blue circles represent Rb20235, and green circles represent Rb20236 iPS-CM. Solid lines in panels represent the fitted monoexponential curves. Values are expressed as mean ± SEM.

**Table 38. Recovery from inactivation time constant of the four individuals of the family.**

| Parameter | Rb20237 | Rb20234 | Rb20235 | Rb20236 |
|---|---|---|---|---|
| **Recovery from inactivation** | | | | |
| **τ (ms)** | 4.17±0.42 | 6.68±0.88* | 4.79±0.67 | 4.37±0.47 |
| **n** | 17 | 13 | 15 | 17 |

Data is presented as Mean ± SEM. τ = time constant; n = number of cells. Differences between data were analyzed with a t-test. *vs Rb20237. Significantly different, p-value < 0.05.

### 4.5. The relative expression of *SCN5A* is not decreased in Rb20234 and Rb20235 iPS-CM

We observed a dramatic loss of function of the $Na_V1.5$ channel in the electrophysiological studies in Rb20234 and Rb20235 iPS-CM. Thus, we aimed to assess by qPCR whether the reduction in $I_{Na}$ density in these individuals could be caused by a decrease in *SCN5A* expression.

As shown in **Figure 59**, *SCN5A* relative expression compared to Rb20237 is not decreased in iPS-CM from Rb20234, Rb20235 and Rb20236. Thus, the decrease in $I_{Na}$ density observed in Rb20234 and Rb20235 iPS-CM is not caused by a reduction in *SCN5A* expression. The Rq values of each of the 5 rounds of differentiation studied for each patient can be found in **Annex Table 21**.

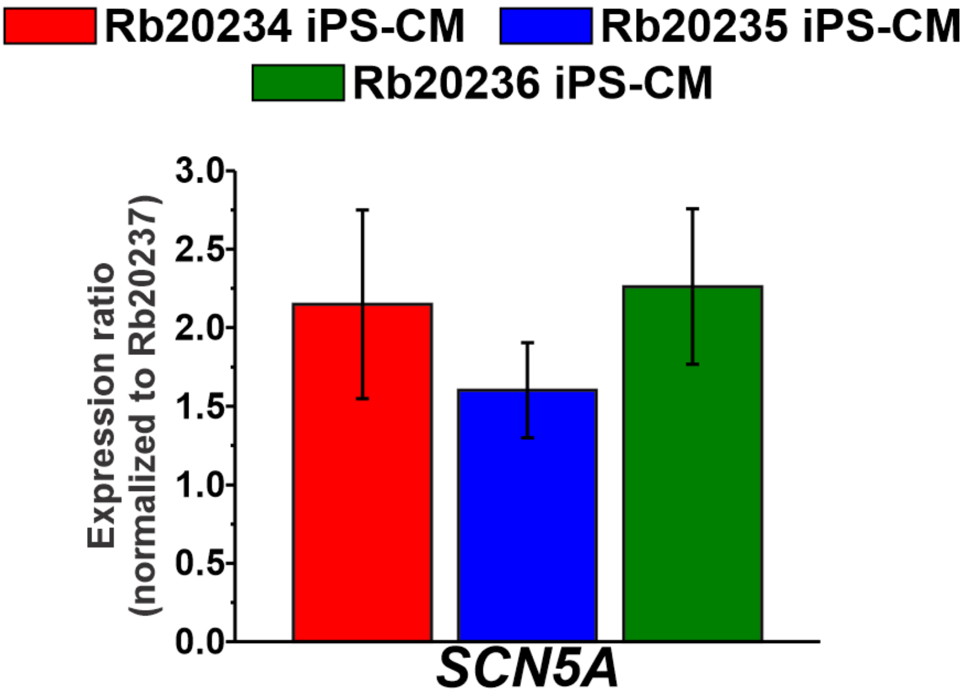

**Figure 59. *SCN5A* expression in Rb20234, Rb20235 and Rb20236 iPS-CM is not decreased, compared to Rb20237.** The relative expression of *SCN5A* is shown as mean values of biological triplicates ± SEM for 5 rounds of differentiation. Differences between data were analyzed with a one-way ANOVA with a post-hoc Tukey test.

## 5. Study of the genetic background with a panel of genes related to cardiac arrhythmias

The complete pedigree of the family (**Rationale of the research Figure 22**) showed incomplete penetrance of *SCN5A*_c.4573G>A. Given that a possible explanation of this feature is the individual-specific genetic background, we sequenced 85 genes associated to cardiac arrhythmogenic diseases using a customized panel (see **Methods section 4.2**) in search for additional genetic variants that could be related to the differences observed between the three SNV carriers in the electrophysiological experiments.

We identified 12 rare SNVs, which are found in less than 1% of the population according to ExAC database (**Table 39**). As expected, the SNV in this study *SCN5A*_c.4573G>A was also identified in the panel.

**Table 39. Rare SNVs found in the four individuals of the study.** Green filled cells indicate the individual as carrier of the SNV.

| SNV | Rb20234 | Rb20235 | Rb20236 | Rb20237 |
|---|---|---|---|---|
| *CACNB2*_c.711G>A | 🟩 |  | 🟩 |  |
| *FBN1*_c.8176C>T | 🟩 |  |  | 🟩 |
| *FLNC*_c.6175G>A |  | 🟩 | 🟩 | 🟩 |
| *KCNH2*_c.2989A>G |  |  | 🟩 |  |
| *SCN5A*_c.4573G>A | 🟩 | 🟩 | 🟩 |  |
| *SCN5A*_c.1587T>C |  | 🟩 |  | 🟩 |
| *SCN5A*_c.717C>T |  | 🟩 |  | 🟩 |
| *TTN*_c.99478G>A | 🟩 | 🟩 |  | 🟩 |
| *TTN*_c.81314G>A | 🟩 | 🟩 |  | 🟩 |
| *TTN*_c.61114G>A | 🟩 |  | 🟩 |  |
| *TTN*_c.95876T>C |  |  |  | 🟩 |
| *TTN*_c.28892C>T |  |  |  | 🟩 |

We also identified multiple common variants, found in more than 1% of the population. Among them, 40 were carried by the four members of the family (**Annex Tables 22-23**) and 59 were carried by some but not all the four members of the family (**Annex Tables 24-25**). From all these variants, what we found more revealing is that the mother Rb20236 is the only carrier of the SNV *SCN5A*_c.1673A>G. The resulting protein $Na_V$1.5_p.H558R is a known modulator of the sodium current that restores abnormal channel properties caused by other *SCN5A* SNVs[216].

Other identified variants worth mentioning will be further explained in the discussion.

# VI. Discussion

# Study 1: *SCN1B* variant associated with concomitant brain and cardiac disorders

In the first study of this Thesis, we presented the effect of an *SCN1B* SNV (c.308A>T; leading to p.D103V), affecting both β1 and β1b regulatory subunits, over the heart- and brain-type sodium currents. We showed evidence of the deleterious effect of the SNV on both heart and brain sodium currents. This strongly suggests that the variant affecting the β1 and β1b subunits is underlying the concomitant brain and cardiac disorders observed in the proband. These data have been published in a scientific paper, in which I am the first author.[217]

The following sections include a point-by-point discussion of our results in relation to our hypotheses.

## 1. The SNV *SCN1B*_c.308A>T alters the regulatory properties of the β1 and β1b subunits over $Na_V1.5$ and $Na_V1.1$ channels

To assess the first hypothesis proposed for this study, we aimed to determine whether the mutant $\beta1^{D103V}$ and $\beta1b^{D103V}$ subunits affected $Na_V1.5$ and $Na_V1.1$ sodium current properties, compared to the wild type subunits. To have a direct control of our experiments with the mutated subunits, we first characterized the effect of the WT β subunits over the cardiac and neuronal sodium channel α subunit's properties.

The effect of the WT β1 subunit over the biophysical properties of $Na_V1.5$ and $Na_V1.1$ sodium current has been widely characterized. As expected, our results are in agreement with previously published data.[28,186,218–223] Summarizing, $\beta1^{WT}$ expressed in HEK-293T cells caused an increase in $I_{Na}$, shifted the voltage dependence of activation towards hyperpolarizing potentials and reduced the recovery from inactivation time constant of $Na_V1.5$. When $\beta1^{WT}$ was co-expressed with $Na_V1.1$, it increased $I_{Na}$ density and accelerated the recovery from inactivation.

The effect of the WT β1b subunit on $Na_V1.5$ current has not been studied extensively. Some groups have reported the presence of the β1b subunit in human and rat adult hearts.[61,220] However, there are some controversies in the literature. Yuan *et al.* showed that the expression levels of β1b in the atria and ventricle are greater than those of β1.[220] On the contrary, Watanabe *et al*. detected a relative low expression level of *SCN1Bb* compared with *SCN1B* in human ventricle.[186] In this study, we observed an increase in $Na_V1.5$ current density in the presence of $\beta1b^{WT}$ larger than that detected when $\beta1^{WT}$ was co-transfected with the α subunit. Co-expression of the α subunit with $\beta1b^{WT}$ also caused a decrease in the recovery from inactivation time constant, which has not been previously reported for the $Na_V1.5$ channel.

Data on the modulatory effect of the β1b subunit on $Na_V1.1$ is scarce and controversial. Some groups propose that β1b expression predominates in embryonic development and early life and is thus essential for brain development.[61–63] Patino *et al*.[63] studied an epilepsy-related SNV that only affects the β1b subunit. Although their co-immunoprecipitation studies did not detect an association between β1b and $Na_V1.1$ or $Na_V1.3$ channels, they showed that β1b modulates the $Na_V1.3$ sodium current in heterologous systems. Our study shows that the $\beta1b^{WT}$ subunit modulates voltage dependence of inactivation by shifting the curve to more negative potentials. These data increase our current knowledge about the effects of β1b subunit on $Na_V1.1$ channel.

### 1.1. $\beta1^{D103V}$ but not $\beta1b^{D103V}$ produces a loss of function of the cardiac sodium current

Mutations in the β1 subunit have been implicated in various cardiac arrhythmias, such as BrS, AD, SIDS, LQT syndrome, and cardiac conduction defect.[62,186,224–226] Here we show that the $\beta1^{D103V}$ subunit caused a reduction in $I_{Na}$ with respect to $\beta1^{WT}$. In addition, the mutant subunit shifted the voltage dependence of activation towards more positive potentials, suggesting a physical interaction between $\beta1^{D103V}$ and the alpha subunit. This interaction, however, appears not to disrupt $Na_V1.5$ trafficking to the plasma membrane. This is supported by our data showing that relative plasma membrane levels of $Na_V1.5$ were similar in the presence of either $\beta1^{WT}$ or $\beta1^{D103V}$. Thus, the mutant β1 is likely to exert its effect over $Na_V1.5$ directly on the channel electrical properties. Taking into account that the β1 subunit is normally present in cardiac cells, this difference between $\beta1^{WT}$ and $\beta1^{D103V}$ would be considered a loss of function of the channel, which would be consistent with the progressive atrial standstill and cardiac conduction disorder observed in the patient.

Regarding the effects of β1b$^{D103V}$ on Na$_V$1.5, we observed a decrease of the sodium current in the presence of this mutated subunit. We believe that this effect is not due to a lack of interaction between both subunits, since β1b$^{D103V}$ also produced an acceleration in the recovery from inactivation. Thus, the decrease in Na$_V$1.5 current is not likely due to a lower expression of the β1b$^{D103V}$ subunit but to an interaction between the α and β subunits at the plasma membrane.

### 1.2. Effect of β1$^{D103V}$ and β1b$^{D103V}$ on Na$_V$1.1 properties could impair normal neuronal activity

We show that the mutant β1 subunit strongly decreased Na$_V$1.1 sodium current density compared to the WT β1 subunit, which represents a loss of function of the channel, in agreement with Meadows *et al.*[31] On the contrary, β1b$^{D103V}$ did not have any effects on Na$_V$1.1 current density, but it shifted the voltage dependence of inactivation in the depolarizing direction, thus causing the channel to be available for activation in a larger voltage range. The observed reduction in the recovery from inactivation time constant caused by the β1b$^{D103V}$ subunit also increases the availability of the channels for their activation. Assuming that β1b is normally present and interacts with Na$_V$1.1 in the native tissue[61], both effects would contribute to gain of function of the channel. β1 subunit mutations that induce a gain of function of Na$_V$1.1 have been reported to cause brain dysfunction.[31,227] Thus, it is possible that β1b$^{D103V}$ causes neuron hyperexcitability, destabilizing normal neuronal behavior of the brain. Also, given the importance of this subunit in brain development[62], this mutation may impair brain formation at embryonic stages, provoking the brain phenotype at an early age, and may be involved in the patient's polymicrogyria.

Our results showed that the modulatory effects of β1$^{D103V}$ and β1b$^{D103V}$ on Na$_V$1.1 $I_{Na}$ are different, even opposing each other. Considering that β1b is predominantly expressed during embryonic development, we expect that the gain of function effect of β1b$^{D103V}$ is more important during that stage. A loss of function caused by β1$^{D103V}$ would be more important later in development. Therefore, since the *SCN1B*_c.308A>T SNV affects both β1 and β1b isoforms, it could differentially compromise neuronal electrical activity during development.

## 2. The clinical manifestation of the β1 and β1b subunit SNV is aggravated by the presence of other patient-specific mutations

Although the father and his children are carriers of the *SCN1B*_c.308A>T SNV, they displayed huge differences at the clinical level. While both the proband and his elder sister presented a complex clinical picture, the father was asymptomatic. This is an example of incomplete penetrance. To assess the second hypothesis of this study, regarding the influence of the genetic background on the phenotypical expression of a disease-causing mutation, we reviewed the whole exome data available for the proband to assess whether the effect of the SNV of this study on both neuronal and cardiac sodium currents could be affected by additional variants.

This family was part of a sequencing re-analysis project, from which the *SCN1B* variant along with variants in *POLR1C* were flagged as the best candidates that potentially contributed to the clinical phenotypes manifested by both the proband and his elder sister.[207] Indeed, these two individuals carried the *SCN1B* SNV along with two SNVs in *POLR1C*.

The proband's father carries the c.88C>T SNV in *POLR1C* in heterozygosis along with the c.308A>T SNV in *SCN1B*, and his mother is heterozygous for the c.614delG SNV in *POLR1C*. Both mother and father are asymptomatic. Therefore, neither the *SCN1B* variant nor the *POLR1C* variants found in the proband could be the sole cause of his complex clinical picture. Indeed, the idea of monogenetic diseases has changed in recent years. Nowadays, it is accepted that genetic modifiers can cause phenotypic variability among individuals harboring the same mutation, and should be identified to perform an integrated clinical interpretation.[228] As explained in **section 1.2.1 of the Introduction**, a mechanism, named the Knudson 2-hit, has been proposed to explain the incomplete penetrance in brain diseases.[42] Thus, the *POLR1C* mutations as well as the variant located in *SCN1B* could have an accumulative effect to the phenotype.

*POLR1C* has been associated with autosomal recessive hypomyelinating leukodystrophy.[229] This gene has also been described to cause recessive Treacher Collins syndrome 3 (OMIM #248390). Our proband did not show clinical manifestations of either of these conditions.[207] However, the patient exhibited several neurological phenotypes consistent with *POLR1C* mutations, including hypomyelination, ataxia, and nystagmus, but the patient's other clinical features are not described in *POLR1C* related cases. Thus, it is possible that the electrical disturbances observed in the patient are caused, at least in part, by the *POLR1C* mutations, and become aggravated by the loss of function of the sodium current caused by the *SCN1B* variant. Also, three-dimensional voltage mapping at baseline rhythm revealed extensive scarring of the right atrium and coronary sinus (**Figure 60**). Thus, electrical dysfunction potentially caused by the mutant β1 and β1b subunits could be aggravated by a damaged tissue substrate.

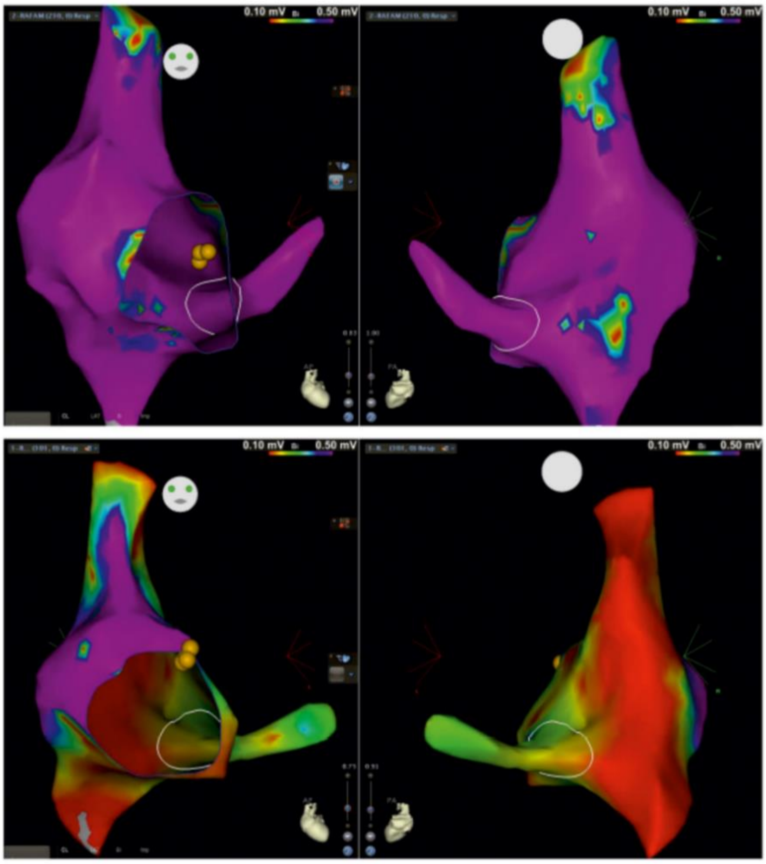

**Figure 60. Intracardiac three-dimensional voltage mapping.** Antero-posterior (left) and postero-anterior (right) projections of voltage map of right atrium and coronary sinus in baseline rhythm from the proband (top) and a healthy age-matched peer (bottom) for comparison (voltage color scale range: 0.1 – 0.5 mV, purple indicates voltage >0.5 mV). Adapted from Martinez-Moreno *et al.*[217]

In summary, although the overall pathophysiology of the patient is complex, the $Na_V1.5$ loss of function caused by the mutant β1 subunit largely explains the clinical manifestations related to the patient's heart dysfunction. In addition, loss and gain of function of $Na_V1.1$ caused by the β1 and β1b mutant subunits might aggravate a brain condition caused by the combination of the two *POLR1C* mutations.

# Study 2: *SCN5A* variant associated with Brugada Syndrome

In the second study of this Thesis, we presented the effect of the SNV *SCN5A*_c.4573G>A on the cardiac sodium channel properties. This SNV was identified in several members of a family, and had been previously related to BrS.[184] Our results in both HEK-293T cells and patient-specific iPS-CM showed a deleterious effect of this SNV on the sodium current. This suggests that the SNV may create a substrate for cardiac arrhythmias.

The following sections include a point-by-point discussion of our results in relation to our hypotheses.

## 1. The SNV *SCN5A*_c.4573G>A modifies the sodium current properties of the $Na_V1.5$ channel

To assess the first hypothesis proposed for this study, we aimed to determine whether the SNV *SCN5A*_c.4573G>A had an effect on the electrophysiological properties of the cardiac $Na_V1.5$ channel.
Mutations in the *SCN5A* gene have been implicated in several cardiac arrhythmogenic diseases, including LQT3, BrS, progressive cardiac conduction disease, dilated cardiomyopathy, sick sinus syndrome, AF and SIDS.[160] Furthermore, mutations in *SCN5A* account for 20-25% of the BrS cases.[77] Indeed, the first mutation associated to BrS was located in this gene.[167] Moreover, most of the BrS-associated mutations studied in heterologous models cause a loss of function of the cardiac sodium channel.[77,160]

In our study, HEK-293T cells expressing the mutant $Na_V1.5$ in heterozygosis showed a decrease in $I_{Na}$ of 24.2%, compared to $Na_V1.5^{WT}$. As expected, this decrease was further accentuated to a 46.9% when the SNV was expressed in homozygosis. In addition, $\tau$ slow was slightly increased when the SNV was expressed in heterozygosis at the 20 mV voltage.

$Na_V1.5^{V1525M}$ shifted the activation curve to more depolarizing potentials, compared to both $Na_V1.5^{WT}$ and $Na_V1.5^{WT/V1525M}$. These data is in agreement with has been widely observed in mutations associated to BrS, recently reviewed by our group.[77]

Surprisingly, while the recovery from inactivation time constant was unaffected when the SNV was expressed in homozygosis, it was increased in the heterozygous expression of the SNV.

Clatot *et al*. demonstrated that sodium channel α subunits form dimers through an interaction site located in the domain I-II linker. Furthermore, these dimers present coupled gating properties.[230] Thus, the interaction between the mutant and WT α subunits in the heterozygous condition, could explain the increase observed in the recovery from inactivation time constant. This possible interaction between α subunits will be further discussed later in this section.

Overall, both the heterozygous and homozygous $Na_V1.5$ mutants lead to a loss of function of the channel. Our western blot data rules out the possibility that the WT and the heterozygous and homozygous mutants are expressed differently in the transfected cells. Thus, taking all these data into account, the loss of function observed in the mutant $Na_V1.5$ is likely due to a defective channel and not to a decrease in the number of channels.

## 2. The effect of the SNV on the sodium current properties of the $Na_V1.5$ channel is different in the three carrier individuals of the same family

From the clinical information that we had for the four individuals studied, we couldn't identify large phenotypical differences among the mutation carriers. Nevertheless, although the mother as well as her children are asymptomatic, the children are still younger than the average age for the onset of BrS symptoms. Thus, the absence of clinical manifestations of the disease cannot be taken as definitive. Moreover, the boy tested positive for flecainide while his sister tested negative. These differences were enough to prompt us to propose that the effect of the SNV on the sodium current properties of the $Na_V1.5$ channel would be different among the three carriers. To assess that, we studied the electrophysiological properties of $Na_V1.5$ in patient-specific iPS-CMs from the three SNV carriers and the non-carrier related control.

We observed that a high percentage of iPS-CM derived from the girl (Rb20234) and from the boy (Rb20235), both carriers of the SNV, did not show recordable $I_{Na}$. This was not observed in the iPS-CM derived from the mother (Rb20236), who is also a carrier of the SNV. To our knowledge, the lack of recordable $I_{Na}$ has not been previously reported by any study using iPS-CM from BrS patients. The presence of increased number of cells with non-recordable $I_{Na}$ could be caused by an enrichment of nodal cells in the cardiomyocyte population. It is known that this type of cells does not display $Na_V1.5$ current, and could have been obtained during iPSc differentiation together with ventricular and atrial-type cells.[210] Our data assessing the expression of ventricular (*MYL2*), atrial (*MYL7*) and nodal (*HCN4*) markers does not support this interpretation, as the ratios between ventricular and nodal cells, and atrial and nodal cells are similar in the three SNV carriers in comparison to the father (control Rb20237).

Another possible explanation could be a decrease in sodium channel expression at the plasma membrane. This mechanism has been observed for several BrS-associated mutations. Unfortunately, we could not address this possibility for our iPS-CM model, and it should be further investigated.

Taking all our results into account, a DN effect exerted by the SNV over the WT α subunit is the most plausible explanation for the lack of recordable $I_{Na}$ in iPS-CM from the girl and the boy. This reasoning will be further discussed ahead in this section.

We characterized the sodium current from the iPS-CMs obtained from the girl and the boy that showed recordable $I_{Na}$. Whole cell current recordings showed a strong reduction of $I_{Na}$ density in the iPS-CM derived from both children, compared to the father's derived iPS-CM which do not carry the SNV. This represents a loss of function of the current, which is in agreement with other studies performed with SNV-carrier BrS patient-specific iPS-CM.[85,91,203] Our data demonstrates that the loss of function observed in the children's derived iPS-CM is not caused by a reduction of *SCN5A* expression. Nevertheless, this loss of function could be attributed to a deficiency at the protein translation level, which could not be assessed with our iPS-CM model. τ fast was increased in both children's derived iPS-CM at negative potentials. In addition, this parameter was also increased in the boy's derived iPS-CM at more positive potentials. At more negative potentials, where the current peak is at its maximum value, this effect could be explained by the presence of the SNV. However, it could also be attributed to the fact that both patient-specific iPS-CM displayed a small $I_{Na}$. At positive potentials the current is minimal, and thus the fitting of the time course is less accurate. Therefore, the observed difference may not be real and needs to be further investigated.

Selga *et al.*[91], de la Roche *et al.*[85] and Li *et al.*[203] reported a shift in the voltage dependence of activation curve in iPS-CM from BrS related mutation carriers. We also observed this effect, but only in the children's derived iPS-CM, compared to the father. In addition, the voltage dependence of steady-state inactivation curve was positively shifted in the iPS-CM from the children's derived iPS-CM. This is in contrast with the three afore mentioned studies, which show either a negative shift of the inactivation curve or no shift at all. The two effects that we report would further contribute to a loss of function of the $Na_V1.5$ channel. In addition, the recovery from inactivation time constant was only increased in the iPS-CM derived from the girl. The explanation for this needs to be further investigated.

All these differences in the sodium current properties observed among the three SNV carriers iPS-CM strongly support the main hypothesis of this thesis, that states that the effect of sodium channel SNVs associated to inherited arrhythmogenic diseases is modulated by the individual's specific genetic background. The influence of the genetic background over the effects of the SNV on the cardiac sodium current will be further discussed in **section 4**.

Since the current reduction in the children's derived iPS-CM was greater than 50%, we suggest that the mutant channel could exert a DN effect over the WT $Na_V1.5$. As previously mentioned, Clatot *et al*. reported that voltage-gated sodium channels α subunits physically interact, assembling, functionating and gating as dimers.[230]

Assuming that $Na_V1.5$ α subunits interact, the proposed mechanism for the DN effect postulates that the mutant protein (known as dominant) is capable to inhibit the functions of the WT protein, causing it to be deficient.[231,232] The DN effect can be caused by a trafficking-deficient channel[233] or by an impaired coupled gating and gating probability of the WT and mutant channels.[234] A DN effect of the $Na_V1.5$ protein due to a BrS *SCN5A* SNV was first reported by Keller *et al.*[196], and several other studies have reported this effect since.[78,233,235,236]

Taking this information into account, we surmise that the mutant $Na_V1.5$ could exert a DN effect over the WT protein. Since the SNV in our study is carried in heterozygosis by three of the family members, the mutant protein could be preventing the WT to reach the plasma membrane and/or disrupt its gating properties. Either mechanism could explain the lack of recordable $I_{Na}$ and the loss of function observed in the children's derived iPS-CM.

## 3. The effect of the SNV on the Nav1.5 current in the iPS-CM derived from carrier individuals of the same family is different to the effect observed in HEK-293T cells heterologously expressing the SNV

In our laboratory, we had previously characterized the electrophysiological properties of the sodium current in iPS-CM derived from a BrS patient who harbored a different SNV in *SCN5A*, and from HEK-293T transiently expressing this SNV. This study showed that HEK-293T failed to display all the changes in the sodium current properties observed in the iPS-CM.[91] Similarly, de la Roche *et al.* also exposed that HEK-293T cells expressing an *SCN5A* SNV related to BrS failed to fully recapitulate the effects observed in iPS-CM derived from the patients harboring that SNV.[85]

Based on these findings, as well as from other groups, we proposed our hypotheses stating that HEK-293T cells heterologously expressing the SNV would not replicate the effect of the SNV on the $Na_V1.5$ current in the iPS-CM derived from carrier individuals. Thus, we used both HEK-293T and patient-specific iPS-CM as a cellular model. HEK-293T cells allow us to study the changes in the sodium current properties induced by the SNV. iPS-CM, in addition, provide both tissue and patient specificity, not present when the SNV is studied heterologously (**Figure 61**).

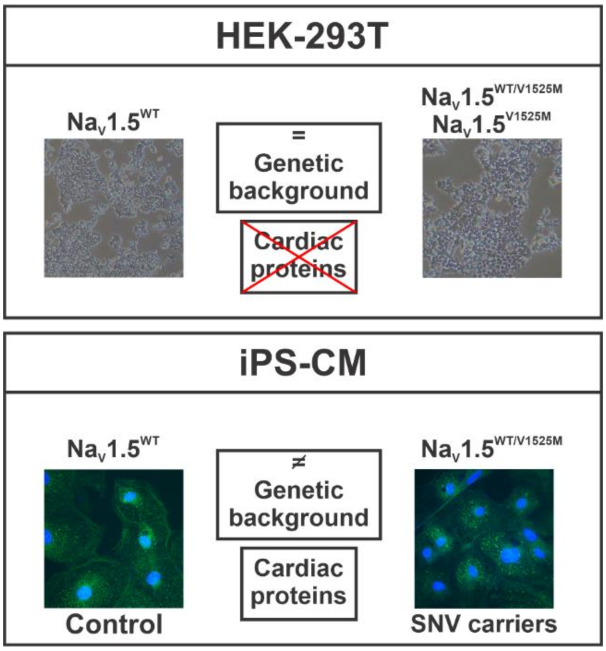

**Figure 61. Cellular models used for the study of the SNV *SCN5A*_c.4573G>A.** HEK-293T cells (up) share the same genetic background and do not express cardiac proteins; patient-specific iPS-CM (bottom) display different genetic background and express cardiac proteins.

Given that the SNV *SCN5A*_c.4573G>A is carried heterozygously by the three family individuals, we could expect that the effects over the sodium current properties would be similar to those observed in HEK-293T expressing $Na_V1.5^{WT/V1525M}$. This is not what we observed. While the mother's derived iPS-CM showed a gain of function compared to the control, the children's derived iPS-CM displayed a dramatic loss of function of $Na_V1.5$. This loss of function was greater than that observed in HEK-293T expressing the SNV in heterozygosis, and even in homozygosis.

Our results suggest that the differences detected in sodium current properties in both cellular models could be attributed to the presence of cell-specific molecules in iPS-CM that are absent in HEK-293T cells. Moreover, a DN effect mediated by a modulatory molecule could explain the disparity of the observed effects. Indeed, Mercier *et al.* demonstrated that β1 subunits promote α-α subunit interaction in heterologous expression systems. This interaction leads to a DN effect when one of the α subunits harbors a SNV, that is not present when α subunits are expressed alone.[235] Thus, the β1-mediated DN effect would be present in patient-specific iPS-CM but not in HEK-293T cells, and this could explain the differences that we observed in the effects of the SNV on the sodium current properties in both cellular models. Although the β1 subunit is a good candidate to explain these differences, it does not suffice to address the disparity of effects observed among mutation carriers. This will be further discussed in the following subsection.

## 4. The three carrier individuals of the same family hold other variants that could influence the cellular phenotypical effect of the SNV

As previously exposed, our data revealed a dramatic loss of function in the children's derived iPS-CM, not observed in the mother's. Thus, we hypothesized that other individual-specific variants could influence the cellular phenotypical effect of the SNV. We performed a genetic panel which included genes related to cardiac arrhythmias with the iPSc of the four members of the family. This allowed us to identify other variants in each of the individuals. The information provided by the panel opens some possible explanations on how different variants may impact the effects of the SNV on the sodium current characteristics and clinical phenotype in the SNV carriers.

The genetic panel revealed that the mother was the only carrier of the SNV *SCN5A*_c.1673A>G (**Annex Table 25**). This genetic change leads to $Na_V$1.5_p.H558R, which is a common polymorphism present in 20-32% in the white population, 29% in the black population and 10.4% in the Chinese population.[237] In vitro studies proved that this polymorphism modulates the effect of other mutations in *SCN5A*, even when those are located in a different allele.[238,239] Furthermore, different studies provided evidences that $Na_V$1.5_p.H558R fully or partially restores $I_{Na}$ impaired by co-expressed mutants, thus acting as a disease-modifying gene.[232,239,240] The improved sodium channel activity in mutated channels could be caused either by the polymorphism's ability to modify mutant $Na_V$1.5 gating kinetics or by its role in rescuing trafficking abnormalities.[239–241] Matsumura *et al.* proposed that $Na_V$1.5_p.H558R could be modulating *SCN5A* expression and methylation, thus offering protection against the occurrence of ventricular fibrillation in BrS patients.[216] In addition, Lizotte *et al*. demonstrated that it also modulates the electrocardiographic and clinical parameters in BrS patients.[237]

Thus, taking all these data into account, the presence of this polymorphism in the mother could explain the absence of the $Na_V$1.5 loss of function in the iPS-CM obtained from her. Furthermore, the lack of any clinical manifestations in the mother could also be explained by the modulatory role of this polymorphism on cardiac sodium current properties in the context of the SNV *SCN5A*_c.4573G>A. It is worth noting that the iPS-CM derived from her children, who do not carry this protective polymorphism, displayed a dramatic $Na_V$1.5 loss of function. Thus, the two children should be carefully clinically monitored in the future.

Both siblings showed clinical dissimilarities. While the boy tested positive for flecainide, which unmasked the BrS ECG pattern, his sister tested negative. Since the loss of function of the cardiac sodium channel observed in the iPS-CM obtained from both individuals was similar, we speculate that variants other than the shared SNV *SCN5A*_c.4573G>A could be causing the clinical differences.

We found some genetic differences between the siblings. Although none on their own helps us to explain the dissimilarities that we observed in the sodium current properties among the iPS-CM derived from the three carriers of the family, and taking into account that their effects on the sodium current properties have not been characterized, there are some variants that are worth discussing.

The girl carries a SNV in the gene *CACNB2* (**Results Table 39**), which encodes the β subunit of the L-type sodium current ($Ca_V\beta2$). While loss of function mutations in *CACNB2* have been associated to BrS[242], Hu *et al*. reported a polymorphism that caused a gain of function of $I_{Ca}$ by slowing its inactivation. In that study, the patients carried an SNV in *SCN5A* as well as the polymorphism in *CACNB2*, but none displayed the BrS ECG.[243] Moreover, it has been demonstrated that an increase in $I_{Ca}$ mediated by the administration of some drugs suppresses the BrS phenotype. In the ECG, $I_{Ca}$ increment avoids loss of the AP dome or restores it, preventing the development of ST elevation.[244]

The SNV in *CACNB2* identified in the girl has not been previously reported nor characterized, thus we do not know if it causes either a loss of function or a gain of function of $I_{Ca}$. Nevertheless, if it was the latter case, it could be suppressing the BrS ECG, which could explain the difference in the flecainide test between she and her brother. A functional characterization of this variant in a cellular model such as HEK-293T cells or iPS-CM could elucidate its role.

The boy carries common variants in the genes *MYBPC3*, *MYH6*, *MYH7* and *TNNI3* that were not identified in the other family members (**Annex Table 24**). Mutations in these genes have been related to Hypertrophic Cardiomyopathy, which is characterized by similar abnormalities in the ECG as BrS, including an abnormal ST segment and negative T waves.[245,246] Although all these variants are reported to be likely benign, in the context of the damaged cellular phenotype observed in the boy they could be contributing to the observed response to flecainide, either by compromising the heart conductivity or the junction between cardiomyocytes, and thus affecting the ECG.

Alterations in the *PKP2* gene, encoding for the protein plakophilin-2, have been associated principally to arrhythmogenic cardiomyopathy (AC).[247] Nevertheless, Corrado *et al*. reported that AC may present phenotypic features typically observed in BrS patients, such as non-exercise-related cardiac arrest and polymorphic ventricular tachycardia.[248] In 2014, Cerrone *et al*. suggested that *PKP2* mutations may be involved in BrS, as this gene interacts with the voltage-gated sodium channel complex.[249] Additionally, they had already demonstrated in 2012 that a mouse model of haploinsufficiency for *PKP2* displayed $I_{Na}$ deficit, leading to flecainide-induced ventricular arrhythmias and SCD.[250] Thus, similar to the previously discussed set of genes, the variant identified in the boy in *PKP2* (**Annex Table 24**) could be modifying the son's ECG.

Although the variants discussed in these genes carried by the children are not conclusive and would need further investigation, they could potentially explain the differences observed between them in the flecainide test.

In summary, the *SCN5A*_c.4573G>A SNV causes a loss of function of $Na_V1.5$ in both studied cellular models. This effect was greater in the children's derived iPS-CM than in HEK-293T cells, possibly due to the fact that iPS-CM carry both tissue specificity and patient-specific background. Since the mother's derived iPS-CM did not display this loss of function, other genetic variants identified in the genetic panel may be modulating the cellular phenotype. These identified variants could be preventing the $Na_V1.5$ loss of function in the iPS-CM derived from the mother, and contributing to the differences observed in the flecainide test of the siblings.

## Overall discussion

It is known that several channelopathies have an underlying genetic component.[251] To date, genetic analysis has been the principal approach to identify mutations in individuals affected by channelopathies. Furthermore, a genetic diagnosis enables clarification of the risk for relatives, in special the asymptomatic ones.[251] Nevertheless, some channelopathies display incomplete penetrance and variable expressivity, probably due to a combination of genetic, environmental and lifestyle factors. Additionally, rare and/or common variants located in the same gene or even another one can modify the cellular phenotype caused by a disease-linked mutation. All these variables represent additional challenges in the interpretation of genetic results, and should thus be taken in context of all the clinical information and familiar history.[251,252]

Having all this information in mind, and focusing in diseases potentially caused by alterations in the voltage gated sodium channels, we formulated the main hypothesis of this Thesis. We stated that the individual's specific genetic background modulates the effect of sodium channel SNVs linked to arrhythmogenic diseases, which could explain the incomplete penetrance and variable expressivity of a given SNV in a family. The study of the two SNVs characterized in this Thesis provides evidence for a role of patient-specific genetic background in the clinical phenotype caused by a given mutation.

Both studied SNVs were identified in families displaying incomplete penetrance. The SNVs, when expressed heterologously in HEK-293T cells, altered the biophysical properties of the studied sodium channels: $Na_V1.5$ and $Na_V1.1$ in the study involving the β1/β1b subunits SNV, and $Na_V1.5$ in the study of the *SCN5A* SNV. Furthermore, the *SCN5A* SNV displayed cellular phenotypical variability in the iPS-CM derived from the iPSc from the three carriers. While a dramatic loss of function of the channel in the children's derived iPS-CM was observed, such effect was not seen in those derived from the mother.

In both studies, additional analyses involving whole exome sequencing in the first study and a genetic panel in the second, allowed us to discuss the possible reasons behind such variability. In the first study, two variants in the *POLR1C* gene were identified, and could modulate the complex clinical phenotype observed in the proband and his deceased elder sister.

In the second study, we identified other variants that could account for the phenotypical differences observed between the *SCN5A* SNV carrier individuals. However, since these variants have not been studied, it remains to be elucidated their possible implication as sodium current modulators, and the mechanisms by which these regulatory effects would impact $I_{Na}$ in the context of the *SCN5A* SNV. It has been described in BrS cases that the function of the $Na_V1.5$ channel can potentially be affected by other variants that interact with the channel.[249] Accumulation of genetic variants may modulate disease susceptibility, suggesting that the currently accepted Mendelian inheritance for BrS should be replaced with a polygenic or oligogenic model.[253] The results presented in this thesis further support this oligogenic model of inheritance for BrS.

Therefore, future studies regarding channelopathies that display incomplete penetrance in a family with a known disease-causing mutation should further explore the presence of other variants that could be modulating its phenotypical expression.

# VII. Conclusions

1. The SNV *SCN1B*_c.308A>T located in the β1 and β1b subunits causes a loss of function of the cardiac-type sodium current, which could explain the clinical presentation of progressive atrial standstill, intra-atrial reentrant tachycardia, and cardiac conduction disorder in the proband of the first family studied.
2. The *SCN1B* SNV could contribute to the proband's brain phenotype at two different stages. The gain of function of the brain-type sodium channel caused by the mutant β1b could affect the brain during development and early life, when the β1b isoform is predominant. During adulthood, when the β1 subunit is predominantly expressed, the loss of function produced by the mutant β1 of the Na$_V$1.1 sodium current could lead to arrhythmogenic brain activity.
3. Loss and gain of function of Na$_V$1.1 caused by the β1 and β1b mutant subunits might aggravate a brain condition caused by the combination of the two *POLR1C* mutations that the patient inherited from his father and mother.
4. The heterologous expression of the SNV *SCN5A*_c.4573G>A in HEK-293T cells causes a loss of function of the Na$_V$1.5 channel. The children-derived iPS-CM, which carry the SNV, also showed a loss of function of the cardiac sodium channel, but the magnitude of the effect of the SNV was greater in this cellular model.
5. The differences observed between HEK-293T cells and patient-specific iPS-CM expressing the same SNV can be explained by the fact that iPS-CM provide cardiac tissue specificity. This implies that other molecules interacting with the α subunit can further modify the deleterious effect of the SNV.
6. The loss of function of Na$_V$1.5 observed in the iPS-CM obtained from both the girl and the boy of the second family studied was greater than 50% respect to their father's (non-carrier) derived cells. Since the SNV is carried in heterozygous form in the family, this larger than expected effect of the mutation could be interpreted as a dominant negative effect of the mutant channel over the WT Na$_V$1.5 α subunit.
7. Patient-specific genetic background modulates the effect of the SNV in iPS-CM:
    a. The mother carries the polymorphism Na$_V$1.5_p.H558R, that could be protecting the sodium channel from the deleterious effect of the mutation, explaining the lack of loss of function observed in her derived iPS-CM.

   b. To date, both children also remain clinically asymptomatic, although the boy tested positive to a flecainide test, which unmasked the BrS ECG. The differences observed in the flecainide test between the girl and the boy could be influenced by other variants identified in the genetic panel. Given that BrS symptoms appear in the adulthood, both children could develop clinical manifestations in the future.

8. Overall, we conclude that incomplete penetrance and variable expressivity observed within families carrying a disease-causing mutation are highly subject to modulation by patient-specific variants, other than the main identified SNV. Thus, the pathogenicity of a mutation in a family should be addressed by assessing the presence of other variants that could modulate its phenotypical expression.

# VIII. Bibliography

1. Kim, J.-B. Channelopathies. *Korean J Pediatr* **57**, 1–18 (2014).
2. Bartolini, E. *et al.* Epilepsy and brain channelopathies from infancy to adulthood. *Neurol. Sci.* **41**, 749–761 (2020).
3. Amin, A. S., Tan, H. L. & Wilde, A. A. M. Cardiac ion channels in health and disease. *Hear. Rhythm* **7**, 117–126 (2010).
4. Giudicessi, J. R. & Ackerman, M. J. Determinants of incomplete penetrance and variable expressivity in heritable cardiac arrhythmia syndromes. *Transl Res.* **161**, 1–14 (2013).
5. Giudicessi, J. R. & Ackerman, M. J. Genetic testing in heritable cardiac arrhythmia syndromes: differentiating pathogenic mutations from background genetic noise. *Curr. Opin. Cardiol.* **28**, 63–71 (2013).
6. Ackerman, M. J. *et al.* HRS/EHRA expert consensus statement on the state of genetic testing for the channelopathies and cardiomyopathies. *Europace* **13**, 1077–1109 (2011).
7. Jitpimolmard, N., Matthews, E. & Fialho, D. Treatment Updates for Neuromuscular Channelopathies. *Curr. Treat. Options Neurol.* **22**, 1–20 (2020).
8. Vivekanandam, V., Munot, P., Hanna, M. G. & Matthews, E. Skeletal Muscle Channelopathies. *Neurol. Clin.* **38**, 481–491 (2020).
9. Johnson, J. N. *et al.* Identification of a possible pathogenic link between congenital long QT syndrome and epilepsy. *Neurology* **72**, 224–231 (2009).
10. Bagnall, R. D. *et al.* Exome-based analysis of cardiac arrhythmia, respiratory control, and epilepsy genes in sudden unexpected death in epilepsy. *Ann. Neurol.* **79**, 522–534 (2016).
11. Tu, E., Bagnall, R. D., Duflou, J. & Semsarian, C. Post-mortem review and genetic analysis of sudden unexpected death in epilepsy (SUDEP) cases. *Brain Pathol.* **21**, 201–208 (2011).
12. Tiron, C. *et al.* Further evidence of the association between LQT syndrome and epilepsy in a family with KCNQ1 pathogenic variant. *Seizure* **25**, 65–67 (2015).
13. Haugaa, K. H. *et al.* Abnormal electroencephalograms in patients with long QT syndrome. *Hear. Rhythm* **10**, 1–25 (2013).
14. Fan, R. *et al.* Concomitant presentation of Anderson-Tawil syndrome and myasthenia gravis in an adult patient: A case report. *Exp. Ther. Med.* **12**, 2435–2438 (2016).
15. Parisi, P. *et al.* Coexistence of epilepsy and Brugada syndrome in a family with SCN5A mutation. *Epilepsy Res.* **105**, 415–418 (2013).
16. Ryan, D. P. & Ptáček, L. J. Episodic neurological channelopathies. *Neuron* **68**, 282–292 (2010).
17. Nappi, P. *et al.* Epileptic channelopathies caused by neuronal Kv7 (KCNQ) channel dysfunction. *Pflugers Arch. Eur. J. Physiol.* **472**, 881–898 (2020).
18. D'adamo, M. C., Liantonio, A., Rolland, J. F., Pessia, M. & Imbrici, P. Kv1.1 channelopathies: Pathophysiological mechanisms and therapeutic approaches. *Int. J.*

*Mol. Sci.* **21**, 1–21 (2020).

19. Bailey, C. S., Moldenhauer, H. J., Park, S. M., Keros, S. & Meredith, A. L. KCNMA1 - linked channelopathy. *J. Gen. Physiol.* **151**, 1173–1189 (2019).
20. Lory, P., Nicole, S. & Monteil, A. Neuronal Cav3 channelopathies: recent progress and perspectives. *Pflugers Arch. Eur. J. Physiol.* **472**, 831–844 (2020).
21. Marcantoni, A., Calorio, C., Hidisoglu, E., Chiantia, G. & Carbone, E. Cav1.2 channelopathies causing autism: new hallmarks on Timothy syndrome. *Pflugers Arch. Eur. J. Physiol.* **472**, 775–789 (2020).
22. Weiss, N. & Zamponi, G. W. Genetic T-type calcium channelopathies. *J. Med. Genet.* **57**, 1–10 (2020).
23. Menezes, L. F. S., Sabiá Júnior, E. F., Tibery, D. V., Carneiro, L. dos A. & Schwartz, E. F. Epilepsy-Related Voltage-Gated Sodium Channelopathies: A Review. *Front. Pharmacol.* **11**, 1–32 (2020).
24. Kruth, K. A., Grisolano, T. M., Ahern, C. A. & Williams, A. J. SCN2A channelopathies in the autism spectrum of neuropsychiatric disorders: A role for pluripotent stem cells? *Mol. Autism* **11**, 1–11 (2020).
25. Matthews, E., Balestrini, S., Sisodiya, S. M. & Hanna, M. G. Muscle and brain sodium channelopathies: genetic causes, clinical phenotypes, and management approaches. *Lancet Child Adolesc. Heal.* **4**, 1–12 (2020).
26. Scheffer, I. E. & Nabbout, R. SCN1A-related phenotypes: Epilepsy and beyond. *Epilepsia* **60**, S17–S24 (2019).
27. Kaplan, D. I., Isom, L. L. & Petrou, S. Role of sodium channels in epilepsy. *Cold Spring Harb. Perspect. Med.* **6**, 1–18 (2016).
28. Barela, A. J. *et al.* An epilepsy mutation in the sodium channel SCN1A that decreases channel excitability. *J. Neurosci.* **26**, 2714–2723 (2006).
29. Cossette, P. *et al.* Functional characterization of the D188V mutation in neuronal voltage-gated sodium channel causing generalized epilepsy with febrile seizures plus (GEFS). *Epilepsy Res.* **53**, 107–117 (2003).
30. Brunklaus, A. *et al.* SCN1A variants from bench to bedside—improved clinical prediction from functional characterization. *Hum. Mutat.* 1–12 (2019) doi:10.1002/humu.23943.
31. Meadows, L. S. *et al.* Functional and biochemical analysis of a sodium channel β1 subunit mutation responsible for generalized epilepsy with febrile seizures plus type 1. *J. Neurosci.* **22**, 10699–10709 (2002).
32. Tammaro, P., Conti, F. & Moran, O. Modulation of sodium current in mammalian cells by an epilepsy-correlated β1-subunit mutation. *Biochem. Biophys. Res. Commun.* **291**, 1095–1101 (2002).
33. Xu, R. *et al.* Generalized epilepsy with febrile seizures plus-associated sodium channel β1 subunit mutations severely reduce beta subunit-mediated modulation of sodium channel function. *Neuroscience* **148**, 164–174 (2007).
34. Patino, G. A. *et al.* A functional null mutation of SCN1B in a patient with Dravet

syndrome. *J. Neurosci.* **29**, 10764–10778 (2009).

35. Wallace, R. H. *et al.* Febrile seizures and generalized epilepsy associated with a mutation in the Na+-channel β1 subunit gene SCN1B. *Nat. Genet.* **19**, 366–370 (1998).
36. Gourraud, J. B. *et al.* The Brugada Syndrome: A Rare Arrhythmia Disorder with Complex Inheritance. *Front. Cardiovasc. Med.* **3**, 1–11 (2016).
37. Scicluna, B. P., Wilde, A. W. & Bezzina, C. R. The primary arrhythmia syndromes: Same mutation, different manifestations. Are we starting to understand why? *J. Cardiovasc. Electrophysiol.* **19**, 445–452 (2008).
38. Campuzano, O. *et al.* Genetics and cardiac channelopathies. *Genet. Med.* **12**, 260–267 (2010).
39. Van Den Boogaard, M. *et al.* Genetic variation in T-box binding element functionally affects SCN5A / SCN10A enhancer Find the latest version : Genetic variation in T-box binding element functionally affects SCN5A / SCN10A enhancer. *J. Clin. Invest.* **122**, 2519–2530 (2012).
40. Van Den Boogaard, M. *et al.* A common genetic variant within SCN10A modulates cardiac SCN5A expression. *J. Clin. Invest.* **124**, 1844–1852 (2014).
41. Bezzina, C. R. *et al.* Common sodium channel promoter haplotype in Asian subjects underlies variability in cardiac conduction. *Circulation* **113**, 338–344 (2006).
42. Fernández-Marmiesse, A. *et al.* Rare Variants in 48 Genes Account for 42% of Cases of Epilepsy With or Without Neurodevelopmental Delay in 246 Pediatric Patients. *Front. Neurosci.* **13**, 1–17 (2019).
43. Sarquella-Brugada, G., Campuzano, O., Arbelo, E., Brugada, J. & Brugada, R. Brugada syndrome: Clinical and genetic findings. *Genet. Med.* **18**, 3–12 (2016).
44. Probst, V. *et al.* Clinical aspects and prognosis of Brugada syndrome in children. *Circulation* **115**, 2042–2048 (2007).
45. Tran, C. H. *et al.* Interneuron desynchronization precedes seizures in a mouse model of Dravet syndrome. *J. Neurosci.* **40**, 2764–2775 (2020).
46. Mei, D., Cetica, V., Marini, C. & Guerrini, R. Dravet syndrome as part of the clinical and genetic spectrum of sodium channel epilepsies and encephalopathies. *Epilepsia* **60**, S2–S7 (2019).
47. Vernooy, K. *et al.* Genetic and biophysical basis for bupivacaine-induced ST segment elevation and VT/VF. Anesthesia unmasked Brugada syndrome. *Hear. Rhythm* **3**, 1074–1078 (2006).
48. Wood, J. N. & Iseppon, F. Sodium channels. *Brain Neurosci. Adv.* **2**, 239821281881068 (2018).
49. Hille, B. *Ion Channels of Excitable Membranes*. (Sinauer Associates, Inc., 2001).
50. Hodgkin, A. L. & Huxley, A. F. A QUANTITATIVE DESCRIPTION OF MEMBRANE CURRENT AND ITS APPLICATION TO CONDUCTION AND EXCITATION IN NERVE. *J. Physiol* **117**, 500–544 (1952).
51. Beneski, D. A. & Catterall, W. A. Covalent labeling of protein conponents of the

sodium channel with a photoactivable derivative of scorpion toxin. *Proc. Natl. Acad. Sci. U. S. A.* **77**, 639–643 (1980).

52. Catterall, W. A. Forty Years of Sodium Channels: Structure, Function, Pharmacology, and Epilepsy. *Neurochem. Res.* **42**, 2495–2504 (2017).
53. Hille, B. *Ion Channels of Excitable Membranes*. (Sinauer associates, Inc, 2001). doi:10.1007/3-540-29623-9_5640.
54. Bertrand, D. *et al.* Functional studies of sodium channels: From target to compound identification. *Curr. Protoc. Pharmacol.* **2016**, 9.21.1-9.21.35 (2016).
55. De Lera Ruiz, M. & Kraus, R. L. Voltage-Gated Sodium Channels: Structure, Function, Pharmacology, and Clinical Indications. *J. Med. Chem.* **58**, 7093–7118 (2015).
56. Amin, A. S., Verkerk, A. O., Bhuiyan, Z. A., Wilde, A. A. M. & Tan, H. L. Novel Brugada syndrome-causing mutation in ion-conducting pore of cardiac Na+ channel does not affect ion selectivity properties. *Acta Physiol. Scand.* **185**, 291–301 (2005).
57. Catterall, W. A. From ionic currents to molecular mechanisms: The structure and function of voltage-gated sodium channels. *Neuron* **26**, 13–25 (2000).
58. Heinemann, S. H., Terlau, H., Stuhmer, W., Imoto, K. & Numa, S. Calcium channel characteristics conferred on the sodium channel by single mutations. *Nature* **359**, 441–443 (1992).
59. Vetter, I. *et al.* NaV1.7 as a pain target – From gene to pharmacology. *Pharmacol. Ther.* **16**, 1–117 (2016).
60. Catterall, W. A. Structure and Function of Voltage-Gated Sodium Channels at Atomic Resolution. *Exp Physiol.* **99**, 1–26 (2014).
61. Kazen-Gillespie, K. A. *et al.* Cloning, localization, and functional expression of sodium channel β1A subunits. *J. Biol. Chem.* **275**, 1079–1088 (2000).
62. O'Malley, H. A. & Isom, L. L. Sodium channel β subunits: Emerging targets in channelopathies. *Annu. Rev. Physiol.* **77**, 481–504 (2015).
63. Patino, G. A. *et al.* Voltage-gated Na + channel β1B: A secreted cell adhesion molecule involved in human epilepsy. *J. Neurosci.* **31**, 14577–14591 (2011).
64. Patino, G. A. & Isom, L. L. Electrophysiology and beyond: Multiple roles of Na+ channel β subunits in development and disease. *Neurosci. Lett.* **486**, 53–59 (2010).
65. Boron, W. F. & Boulpaep, E. L. *Medical Physiology*. *A cellular and molecular approeach* (Saunders Elsevier, 2012). doi:10.1017/CBO9781107415324.004.
66. Ogden, D. *Microelectrode Techniques: The Plymouth Workshop Handbook*. (The Company of Biologists Limited, 1994).
67. Hamill, O. P., Marty, A., Neher, E., Sakmann, B. & Sigworth, F. J. Improved patch-clamp techniques for high-resolution current recording from cells and cell-free membrane patches. *Pflügers Arch. Eur. J. Physiol.* **391**, 85–100 (1981).
68. Neher, E. & Sakmann, B. Single-channel currents recorded from membrane of denervated frog muscle fibres. *Nature* **260**, 799–802 (1976).
69. Bezanilla, F. Gating currents. *J. Gen. Physiol.* **150**, 911–932 (2018).

70. Aldrich, R. W., Corey, D. P. & Stevens, C. F. A reinterpretation of mammalian sodium channel gating based on single channel recording. *Nature* **306**, 436–441 (1983).

71. Horn, R. & Vandenberg, C. A. Statistical properties of single sodium channels. *J. Gen. Physiol.* **84**, 505–534 (1984).

72. Bezanilla, F. & Armstrong, C. M. Inactivation of the sodium channel. I. Sodium Current Experiments. *J. Gen. Physiol.* **70**, 549–566 (1977).

73. Xu, L. *et al.* Voltage-gated sodium channels: structures, functions, and molecular modeling. *Drug Discov. Today* **24**, 1389–1397 (2019).

74. Papadatos, G. A. *et al.* Slowed conduction and ventricular tachycardia after targeted disruption of the cardiac sodium channel gene Scn5a. *Proc. Natl. Acad. Sci. U. S. A.* **99**, 6210–6215 (2002).

75. Remme, C. A. *et al.* Overlap syndrome of cardiac sodium channel disease in mice carrying the equivalent mutation of human SCN5A-1795insD. *Circulation* **114**, 2584–2594 (2006).

76. Mantegazza, M. & Broccoli, V. SCN1A/NaV1.1 channelopathies: Mechanisms in expression systems, animal models, and human iPSC models. *Epilepsia* **60**, S25–S38 (2019).

77. Sendfeld, F. *et al.* Experimental models of brugada syndrome. *Int. J. Mol. Sci.* **20**, (2019).

78. Park, D. S. *et al.* Genetically engineered SCN5A mutant pig hearts exhibit conduction defects and arrhythmias. *J. Clin. Invest.* **125**, 403–412 (2015).

79. Yan, G. X. & Antzelevitch, C. Cellular basis for the electrocardiographic J wave. *Circulation* **93**, 372–379 (1996).

80. Nishida, K. *et al.* Canine model of Brugada syndrome using regional epicardial cooling of the right ventricular outflow tract. *J. Cardiovasc. Electrophysiol.* **15**, 936–941 (2004).

81. Morita, H. *et al.* Repolarization heterogeneity in the right ventricular outflow tract: Correlation with ventricular arrhythmias in Brugada patients and in an in vitro canine Brugada model. *Hear. Rhythm* **5**, 725–733 (2008).

82. Schutte, S. S., Schutte, R. J., Barragan, E. V. & O'Dowd, D. K. Model systems for studying cellular mechanisms of SCN1A-related epilepsy. *J. Neurophysiol.* **115**, 1755–1766 (2016).

83. Griffin, A. *et al.* Preclinical animal models for Dravet syndrome: Seizure phenotypes, comorbidities and drug screening. *Front. Pharmacol.* **9**, 1–15 (2018).

84. Bezanilla, F. Ion Channels: From Conductance to Structure. *Neuron* **60**, 456–468 (2008).

85. de la Roche, J. *et al.* Comparing human iPSC-cardiomyocytes versus HEK293T cells unveils disease-causing effects of Brugada mutation A735V of NaV1.5 sodium channels. *Sci. Rep.* **9**, 1–14 (2019).

86. Deschênes, I. *et al.* Electrophysiological characterization of SCN5A mutations causing long QT (E1784K) and Brugada (R1512W and R1432G) syndromes. *Cardiovasc. Res.*

**46**, 55–65 (2000).

87. Goldberg-Stern, H. *et al.* Broad phenotypic heterogeneity due to a novel SCN1A mutation in a family with genetic epilepsy with febrile seizures plus. *J. Child Neurol.* **29**, 221–226 (2014).
88. Groenewegen, W. A. *et al.* A novel LQT3 mutation implicates the human cardiac sodium channel domain IVS6 in inactivation kinetics. *Cardiovasc. Res.* **57**, 1072–1078 (2003).
89. Makita, N. *et al.* The E1784K mutation in SCN5A is associated with mixed clinical phenotype of type 3 long QT syndrome. *J. Clin. Invest.* **118**, 2219–2229 (2008).
90. Ruan, Y. *et al.* Trafficking defects and gating abnormalities of a novel SCN5A mutation question gene-specific therapy in long QT syndrome type 3. *Circ. Res.* **106**, 1374–1383 (2010).
91. Selga, E. *et al.* Sodium channel current loss of function in induced pluripotent stem cell-derived cardiomyocytes from a Brugada syndrome patient. *J. Mol. Cell. Cardiol.* **114**, 10–19 (2018).
92. Tarradas, A. *et al.* A Novel Missense Mutation, I890T, in the Pore Region of Cardiac Sodium Channel Causes Brugada Syndrome. *PLoS One* **8**, 1–10 (2013).
93. Lossin, C. *et al.* Epilepsy-Associated Dysfunction in the Voltage-Gated Neuronal Sodium Channel SCN1A. *J. Neurosci.* **23**, 11289–11295 (2003).
94. Gurdon, J. B., Elsdale, T. R. & Fischberg, M. Sexually mature individuals of Xenopus laevis from the transplantation of single somatic nuclei. *Nature* **182**, 64–65 (1958).
95. GURDON, J. B. The developmental capacity of nuclei taken from intestinal epithelium cells of feeding tadpoles. *J. Embryol. Exp. Morphol.* **10**, 622–640 (1962).
96. Kaufman, M. H. & Evans, M. J. Establishment in culture of pluripotential cells from mouse embryos. *Nature* **292**, 154–156 (1981).
97. Martin, G. R. Isolation of a pluripotent cell line from early mouse embryos cultured in medium conditioned by teratocarcinoma stem cells. *Proc. Natl. Acad. Sci. U. S. A.* **78**, 7634–7638 (1981).
98. Tada, M., Takahama, Y., Abe, K., Nakatsuji, N. & Tada, T. Nuclear reprogramming of somatic cells by in vitro hybridization with ES cells. *Curr. Biol.* **11**, 1553–1558 (2001).
99. Cowan, C. A., Atienza, J., Melton, D. A. & Eggan, K. Nuclear reprogramming of somatic cells after fusion with human embryonic stem cells. *Science (80-. ).* **309**, 1369–1373 (2005).
100. Takahashi, K. & Yamanaka, S. Induction of Pluripotent Stem Cells from Mouse Embryonic and Adult Fibroblast Cultures by Defined Factors. *Cell* **126**, 663–676 (2006).
101. Takahashi, K. *et al.* Induction of Pluripotent Stem Cells from Adult Human Fibroblasts by Defined Factors. *Cell* **131**, 861–872 (2007).
102. Yu, J. *et al. Induced pluripotent stem cell lines derived from human somatic cells*. *Science* vol. 318 (2007).

103. Liu, Y. *et al.* Directed differentiation of forebrain GABA interneurons from human pluripotent stem cells. *Nat. Protoc.* **8**, 1670–1679 (2013).

104. Maroof, A. M. *et al.* Directed differentiation and functional maturation of cortical interneurons from human embryonic stem cells. *Cell Stem Cell* **12**, 559–572 (2013).

105. Nicholas, C. R. *et al.* Functional maturation of hPSC-derived forebrain interneurons requires an extended timeline and mimics human neural development. *Cell Stem Cell* **12**, 573–586 (2013).

106. Stover, A. E. *et al.* Process-Based Expansion and Neural Differentiation of Human Pluripotent Stem Cells for Transplantation and Disease Modeling. *J Neurosci Res* **91**, 1247–1262 (2013).

107. Zhang, Y. *et al.* Rapid Single-Step Induction of Functional Neurons from Human Pluripotent Stem Cells. *Neuron* **78**, 785–798 (2013).

108. Bossolasco, P. *et al.* Motor neuron differentiation of iPSCs obtained from peripheral blood of a mutant TARDBP ALS patient. *Stem Cell Res.* **30**, 61–68 (2018).

109. McKinney, C. E. Using induced pluripotent stem cells derived neurons to model brain diseases. *Neural Regen. Res.* **12**, 1062–1067 (2017).

110. Mertens, J., Marchetto, M. C., Bardy, C. & Gage, F. H. Evaluating cell reprogramming, differentiation and conversion technologies in neuroscience. *Nat. Rev. Neurosci.* **17**, 424–437 (2016).

111. Zhang, X., Li, Z., Liu, Y. & Gai, Z. Great expectations: Induced pluripotent stem cell technologies in neurodevelopmental impairments. *Int. J. Med. Sci.* **18**, 459–473 (2020).

112. Hirose, S. *et al.* Application of induced pluripotent stem cells in epilepsy. *Mol. Cell. Neurosci.* **108**, 1–32 (2020).

113. Higurashi, N. *et al.* A human Dravet syndrome model from patient induced pluripotent stem cells. *Mol. Brain* **6**, 1–12 (2013).

114. Liu, Y. *et al.* DRAVET SYNDROME PATIENT-DERIVED NEURONS SUGGEST A NOVEL EPILEPSY MECHANISM. *Ann. Neurol.* **74**, 128–139 (2013).

115. Jiao, J. *et al.* Modeling Dravet syndrome using induced pluripotent stem cells (iPSCs) and directly converted neurons. *Hum. Mol. Genet.* **22**, 4241–4252 (2013).

116. Scalise, S. *et al.* Generation of iPSC lines from two patients affected by febrile seizure due to inherited missense mutation in SCN1A gene. *Stem Cell Res.* **49**, 1–4 (2020).

117. Tidball, A. M. *et al.* Variant-specific changes in persistent or resurgent sodium current in SCN8A-related epilepsy patient-derived neurons. *Brain* **143**, 1–16 (2020).

118. Tidball, A. M. *et al.* Rapid Generation of Human Genetic Loss-of-Function iPSC Lines by Simultaneous Reprogramming and Gene Editing. *Stem Cell Reports* **9**, 725–731 (2017).

119. Maltsev, V. A., Rohwedel, J., Hescheler, J. & Wobus, A. M. Embryonic stem cells differentiate in vitro into cardiomyocytes representing sinusnodal, atrial and ventricular cell types. *Mech. Dev.* **44**, 41–50 (1993).

120. Yang, L. *et al.* Human cardiovascular progenitor cells develop from a KDR+ embryonic-stem-cell-derived population. *Nature* **453**, 524–528 (2008).

121. Kattman, S. J. *et al.* Stage-specific optimization of activin/nodal and BMP signaling promotes cardiac differentiation of mouse and human pluripotent stem cell lines. *Cell Stem Cell* **8**, 228–240 (2011).

122. Zhang, J. *et al.* Extracellular Matrix Promotes Highly Efficient Cardiac Differentiation of Human Pluripotent Stem Cells: The Matrix Sandwich Method. *Circ. Res.* **111**, 1125–1136 (2012).

123. Lian, X. *et al.* Directed cardiomyocyte differentiation from human pluripotent stem cells by modulating Wnt/β-catenin signaling under fully defined conditions. *Nat. Protoc.* **8**, 162–175 (2013).

124. Burridge, P. W. *et al.* Chemically defined generation of human cardiomyocytes. *Nat. Methods* **11**, 855–860 (2014).

125. Lian, X. *et al.* Chemically defined albumin-free human cardiomyocyte generation. *Nat. Methods* **12**, 595–596 (2015).

126. Liang, W., Gasparyan, L., AlQarawi, W. & Davis, D. R. Disease modeling of cardiac arrhythmias using human induced pluripotent stem cells. *Expert Opin. Biol. Ther.* **19**, 313–333 (2019).

127. Fatima, A. *et al.* The disease-specific phenotype in cardiomyocytes derived from induced pluripotent stem cells of two long qt syndrome type 3 patients. *PLoS One* **8**, 1–11 (2013).

128. Ma, D. *et al.* Modeling type 3 long QT syndrome with cardiomyocytes derived from patient-specific induced pluripotent stem cells. *Int. J. Cardiol.* **168**, 5277–5286 (2013).

129. Terrenoire, C. *et al.* Induced pluripotent stem cells used to reveal drug actions in a long QT syndrome family with complex genetics. *J. Gen. Physiol.* **141**, 61–72 (2013).

130. Malan, D. *et al.* Human iPS cell model of type 3 long QT syndrome recapitulates drug-based phenotype correction. *Basic Res. Cardiol.* **111**, 1–11 (2016).

131. Davis, R. P. *et al.* Cardiomyocytes derived from pluripotent stem cells recapitulate electrophysiological characteristics of an overlap syndrome of cardiac sodium channel disease. *Circulation* **125**, 3079–3091 (2012).

132. Veerman, C. C. *et al.* Immaturity of Human Stem-Cell-Derived Cardiomyocytes in Culture: Fatal Flaw or Soluble Problem? *Stem Cells Dev.* **24**, 1–57 (2015).

133. Yang, X., Pabon, L. & Murry, C. E. Engineering Adolescence: Maturation of Human Pluripotent Stem Cell-derived Cardiomyocytes. *Circ. Res.* **114**, 511–523 (2014).

134. Dubois, N. C. *et al.* SIRPA is a specific cell-surface marker for isolating cardiomyocytes derived from human pluripotent stem cells Nicole. *Nat. Biotechnol.* **29**, 1011–1018 (2011).

135. Tohyama, S. *et al.* Distinct metabolic flow enables large-scale purification of mouse and human pluripotent stem cell-derived cardiomyocytes. *Cell Stem Cell* **12**, 127–137 (2013).

136. Sharma, A. *et al.* Derivation of highly purified cardiomyocytes from human induced

pluripotent stem cells using small molecule-modulated differentiation and subsequent glucose starvation. *J. Vis. Exp.* **2015**, 3–10 (2015).

137. Marban, E., Yamagishi, T. & Tomaselli, G. F. Topical review: structure and function of voltage-gated sodium channel. *J. Physiol.* **508**, 647–657 (1998).

138. Nerbonne, J. M. & Kass, R. S. Molecular physiology of cardiac repolarization. *Physiol. Rev.* **85**, 1205–1253 (2005).

139. Marban, E. Cardiac channelopathies. *Nature* **415**, 213–218 (2002).

140. Keating, M. T.; Sanguinetti, M. C. Molecular and cellular mechanisms of cardiac arrhythmias. *Cell* **104**, 569–580 (2001).

141. Lane, J. D. & Tinker, A. Have the findings from clinical risk prediction and trials any key messages for safety pharmacology? *Front. Physiol.* **8**, 1–11 (2017).

142. Periasamy, M. & Kalyanasundaram, A. SERCA pump isoforms: Their role in calcium transport and disease. *Muscle and Nerve* **35**, 430–442 (2007).

143. Adabag, A. S., Luepker, R. V., Roger, V. L. & Gersh, B. J. Sudden cardiac death: Epidemiology and risk factors. *Nat. Rev. Cardiol.* **7**, 216–225 (2010).

144. Wong, C. X. *et al.* Epidemiology of Sudden Cardiac Death: Global and Regional Perspectives. *Hear. Lung Circ.* **28**, 6–14 (2019).

145. Paratz, E. D. *et al.* Cardiac arrest and sudden cardiac death registries: a systematic review of global coverage. *Open Hear.* **7**, 1–10 (2020).

146. Khan, H. M. & Leslie, S. J. Risk factors for sudden cardiac death to determine high risk patients in specific patient populations that may benefit from a wearable defibrillator. *World J. Cardiol.* **11**, 103–119 (2019).

147. Hayashi, M., Shimizu, W. & Albert, C. M. The Spectrum of Epidemiology Underlying Sudden Cardiac Death. *Circ. Res.* **116**, 1887–1906 (2015).

148. Chugh, S. S. *et al.* Epidemiology of Sudden Cardiac Death: Clinical and Research Implications. *Prog Cardiovasc Dis* **51**, 213–228 (2008).

149. Priori, S. G. *et al.* Task force on sudden cardiac death, European Society of Cardiology: Summary of recommendations. *Europace* **4**, 3–18 (2002).

150. Deo, R. & Albert, C. M. Epidemiology and genetics of sudden cardiac death. *Circulation* **125**, 620–637 (2012).

151. Friedlander, Y. *et al.* Family history as a risk factor for primary cardiac arrest. *Circulation* **97**, 155–160 (1998).

152. Albert, C. M. *et al.* Prospective study of sudden cardiac death among women in the United States. *Circulation* **107**, 2096–2101 (2003).

153. Zheng, Z. J., Croft, J. B., Giles, W. H. & Mensah, G. A. Sudden cardiac death in the United States, 1989 to 1998. *Circulation* **104**, 2158–2163 (2001).

154. Moon, R. Y., Horne, R. S. C. & Hauck, F. R. Sudden Infant Death Syndrome. *Lancet* **370**, 1578–1587 (2007).

155. Tfelt-Hansen, J., Winkel, B. G., Grunnet, M. & Jespersen, T. Cardiac channelopathies

and sudden infant death syndrome. *Cardiology* **119**, 21–33 (2011).

156. Wong, L. C. H. & Behr, E. R. Sudden unexplained death in infants and children: The role of undiagnosed inherited cardiac conditions. *Europace* **16**, 1706–1713 (2014).

157. Sarquella-Brugada, G. *et al.* Genetics of sudden cardiac death in children and young athletes. *Cardiol. Young* **23**, 159–173 (2013).

158. Zipes, D. P. *et al. ACC/AHA/ESC 2006 guidelines for management of patients with ventricular arrhythmias and the prevention of sudden cardiac death: A report of the American College of Cardiology/American Heart Association Task Force and the European Society of Cardiology Com*. *Circulation* vol. 114 (2006).

159. Gollob, M. H. *et al.* Recommendations for the use of genetic testing in the clinical evaluation of inherited cardiac arrhythmias associated with sudden cardiac death: Canadian cardiovascular society/Canadian heart rhythm society joint position paper. *Can. J. Cardiol.* **27**, 232–245 (2011).

160. Amin, A. S., Asghari-Roodsari, A. & Tan, H. L. Cardiac sodium channelopathies. *Pflugers Arch. Eur. J. Physiol.* **460**, 223–237 (2010).

161. Remme, C. A. Cardiac sodium channelopathy associated with SCN5A mutations: Electrophysiological, molecular and genetic aspects. *J. Physiol.* **591**, 4099–4116 (2013).

162. Hu, D. *et al.* A Mutation in the β3 Subunit of the Cardiac Sodium Channel Associated with Brugada ECG Phenotype. **2**, 270–278 (2009).

163. Brugada, J., Campuzano, O., Arbelo, E., Sarquella-Brugada, G. & Brugada, R. Present Status of Brugada Syndrome: JACC State-of-the-Art Review. *J. Am. Coll. Cardiol.* **72**, 1046–1059 (2018).

164. Antzelevitch, C. *et al.* Brugada syndrome: A decade of progress. *Circ. Res.* **91**, 1114–1118 (2002).

165. Brugada, P. & Brugada, J. Right Bundle Branch Block, Persistent ST Segment Elevation and Sudden Cardiac Death: A Distinct Clinical and Electrocardiographic Syndrome. *JACC* **20**, 1391–6 (1992).

166. Miyazaki, T. *et al.* Autonomic and Antiarrhythmic Drug Modulation of ST Segment Elevation in Patients with Brugada Syndrome. *JACC* **27**, 1061–1070 (1996).

167. Chen, Q. *et al.* Genetic basis and molecular mechanism for idiopathic ventricular fibrillation. *Nature* **392**, 293–296 (1998).

168. Kobayashi, T. *et al.* Familial Occurrence of Electrocardiographic Abnormalities of the Brugada-Type. *Intern. Med.* **35**, 637–640 (1996).

169. Peeters, U. *et al.* Contribution of Cardiac Sodium Channel β-Subunit Variants to Brugada Syndrome. *Circ. J.* **79**, 2118–2129 (2015).

170. Ma, D. *et al.* Identification of an I Na-dependent and I to-mediated proarrhythmic mechanism in cardiomyocytes derived from pluripotent stem cells of a Brugada syndrome patient. *Sci. Rep.* **8**, 1–11 (2018).

171. Meregalli, P. G., Wilde, A. A. M. & Tan, H. L. Pathophysiological mechanisms of Brugada syndrome: Depolarization disorder, repolarization disorder, or more?

*Cardiovasc. Res.* **67**, 367–378 (2005).

172. Probst, V. *et al.* Long-term prognosis of patients diagnosed with brugada syndrome: Results from the finger brugada syndrome registry. *Circulation* **121**, 635–643 (2010).

173. Antzelevitch, C. *et al.* Brugada syndrome: report of the second consensus conference. *Circulation* **2**, 429–440 (2005).

174. Frustaci, A., Russo, M. A. & Chimenti, C. Structural myocardial abnormalities in asymptomatic family members with Brugada syndrome and SCN5A gene mutation. *Eur. Heart J.* **30**, 1763 (2009).

175. Catalano, O. *et al.* Magnetic resonance investigations in Brugada syndrome reveal unexpectedly high rate of structural abnormalities. *Eur. Heart J.* **30**, 2241–2248 (2009).

176. Bayés De Luna, A. *et al.* Current electrocardiographic criteria for diagnosis of Brugada pattern: A consensus report. *J. Electrocardiol.* **45**, 433–442 (2012).

177. Dumaine, R. *et al.* Ionic mechanisms responsible for the electrocardiographic phenotype of the Brugada syndrome are temperature dependent. *Circ. Res.* **85**, 803–809 (1999).

178. Brugada, P., Benito, B., Brugada, R. & Brugada, J. Brugada syndrome: Update 2009. *Hell. J. Cardiol.* **50**, 352–372 (2009).

179. Sarkozy, A. *et al.* Long-term follow-up of primary prophylactic implantable cardioverter-defibrillator therapy in Brugada syndrome. *Eur. Heart J.* **28**, 334–344 (2007).

180. Nielsen, M. W., Holst, A. G., Olesen, S. P. & Olesen, M. S. The genetic component of brugada syndrome. *Front. Physiol.* **4 JUL**, 1–11 (2013).

181. Nademanee, K. *et al.* Prevention of ventricular fibrillation episodes in brugada syndrome by catheter ablation over the anterior right ventricular outflow tract epicardium. *Circulation* **123**, 1270–1279 (2011).

182. Selga, E. *et al.* Comprehensive genetic characterization of a Spanish Brugada syndrome cohort. *PLoS One* **10**, 1–15 (2015).

183. Tan, B. H., Valdivia, C. R., Song, C. & Makielski, J. C. Partial expression defect for the SCN5A missense mutation G1406R depends on splice variant background Q1077 and rescue by mexiletine. *Am. J. Physiol. - Hear. Circ. Physiol.* **291**, 1822–1828 (2006).

184. Kapplinger, J. D. *et al.* An international compendium of mutations in the SCN5A-encoded cardiac sodium channel in patients referred for Brugada syndrome genetic testing. *Hear. Rhythm* **7**, 33–46 (2010).

185. Delpón, E. *et al.* Functional Effects of KCNE3 Mutation and its Role in the Development of Brugada Syndrome. *Circ Arrhythm Electrophysiol.* **1**, 209–218 (2008).

186. Watanabe, H. *et al.* Sodium channel β1 subunit mutations associated with Brugada syndrome and cardiac conduction disease in humans. *J. Clin. Invest.* **118**, 2260–2268 (2008).

187. Hu, D. *et al.* A novel rare variant in SCN1Bb linked to Brugada syndrome and SIDS by combined modulation of Nav1.5 and Kv4.3 channel currents. *Hear. Rhythm* **9**, 760–

769 (2012).

188. Riuró, H. *et al.* A Missense Mutation in the Sodium Channel β2 Subunit Reveals SCN2B as a New Candidate Gene for Brugada Syndrome. *Hum. Mutat.* **34**, 961–966 (2013).

189. Wan, X., Wang, Q. & Kirsch, G. E. Functional suppression of sodium channels by β1-subunits as a molecular mechanism of idiopathic ventricular fibrillation. *J. Mol. Cell. Cardiol.* **32**, 1873–1884 (2000).

190. Hosseini, S. M. *et al.* Reappraisal of reported genes for sudden arrhythmic death: Evidence-based evaluation of gene validity for brugada syndrome. *Circulation* **138**, 1195–1205 (2018).

191. Di Diego, J. M., Sun, Z. Q. & Antzelevitch, C. I(to) and action potential notch are smaller in left vs. right canine ventricular epicardium. *Am. J. Physiol. - Hear. Circ. Physiol.* **271**, (1996).

192. Antzelevitch, C. The Brugada syndrome: Diagnostic criteria and cellular mechanisms. *Eur. Heart J.* **22**, 356–363 (2001).

193. Alings, M. & Wilde, A. "Brugada" Syndrome Clinical Data and Suggested Pathophysiological Mechanism. *Circulation* **99**, 666–673 (1999).

194. Benito, B., Brugada, J., Brugada, R. & Brugada, P. Brugada syndrome. *Rev Esp Cardiol.* **62**, 1297–1315 (2009).

195. Bezzina, C. *et al.* A single Na+ channel mutation causing both long-QT and Brugada syndromes. *Circ. Res.* **85**, 1206–1213 (1999).

196. Keller, D. I. *et al.* Brugada syndrome and fever: Genetic and molecular characterization of patients carrying SCN5A mutations. *Cardiovasc. Res.* **67**, 510–519 (2005).

197. Wan, X., Chen, S., Sadeghpour, A., Wang, Q. & Kirsch, G. E. Accelerated inactivation in a mutant Na+ channel associated with idiopathic ventricular fibrillation. *Am. J. Physiol. - Hear. Circ. Physiol.* **280**, 354–360 (2001).

198. Rook, M. B. *et al.* Human SCN5A gene mutations alter cardiac sodium channel kinetics and are associated with the Brugada syndrome. *Cardiovasc. Res.* **44**, 507–517 (1999).

199. Veldkamp, M. W. *et al.* Two distinct congenital arrhythmias evoked by a multidysfunctional Na(+) channel. *Circ. Res.* **86**, 1–7 (2000).

200. Riuró, H. *et al.* A Missense Mutation in the Sodium Channel β2 Subunit Reveals SCN2B as a New Candidate Gene for Brugada Syndrome. *Hum. Mutat.* **34**, 961–966 (2013).

201. London, B. *et al.* Mutation in glycerol-3-phosphate dehydrogenase 1-like gene (GPD1-L) decreases cardiac Na+ current and causes inherited arrhythmias. *Circulation* **116**, 2260–2268 (2007).

202. Liang, P. *et al.* Patient-specific and genome-edited induced pluripotent stem cell-derived cardiomyocytes elucidate single cell phenotype of Brugada Syndrome. *J. Am. Coll. Cardiol.* **68**, 1–22 (2016).

203. Li, W. *et al.* Disease Phenotypes and Mechanisms of iPSC-Derived Cardiomyocytes From Brugada Syndrome Patients With a Loss-of-Function SCN5A Mutation. *Front. Cell Dev. Biol.* **8**, 1–17 (2020).

204. Kosmidis, G. *et al.* Readthrough-promoting drugs gentamicin and PTC124 Fail to Rescue Nav1.5 function of human-induced pluripotent stem cell-derived cardiomyocytes carrying nonsense mutations in the sodium channel gene SCN5A. *Circ. Arrhythmia Electrophysiol.* **9**, 1–11 (2016).

205. Miller, D. C. *et al.* Ajmaline blocks INa and IKr without eliciting differences between Brugada syndrome patient and control human pluripotent stem cell-derived cardiac clusters. *Stem Cell Res.* **25**, 233–244 (2017).

206. Belbachir, N. *et al.* RRAD mutation causes electrical and cytoskeletal defects in cardiomyocytes derived from a familial case of Brugada syndrome. *Eur. Heart J.* **40**, 3081–3093 (2019).

207. Eldomery, M. K. *et al.* Lessons learned from additional research analyses of unsolved clinical exome cases. *Genome Med.* **9**, 1–15 (2017).

208. Kapplinger, J. D. *et al.* An international compendium of mutations in the SCN5A-encoded cardiac sodium channel in patients referred for Brugada syndrome genetic testing. *Heart Rhythm* **7**, 33–46 (2010).

209. Riuró, H. *et al.* A missense mutation in the sodium channel β1b subunit reveals SCN1B as a susceptibility gene underlying long QT syndrome. *Hear. Rhythm* **11**, 1202–1209 (2014).

210. Lin, Y. *et al.* Heparin Promotes Cardiac Differentiation of Human Pluripotent Stem Cells in Chemically Defined Albumin-Free Medium, Enabling Consistent Manufacture of Cardiomyocytes. *Stemcells Transl. Med.* **5**, 1–12 (2016).

211. Parikh, S. S. *et al.* Thyroid and Glucocorticoid Hormones Promote Functional T-Tubule Development in Human-Induced Pluripotent Stem Cell-Derived Cardiomyocytes. *Circ. Res.* **121**, 1323–1330 (2017).

212. Taylor, S. C., Berkelman, T., Yadav, G. & Hammond, M. A defined methodology for reliable quantification of western blot data. *Mol. Biotechnol.* **55**, 217–226 (2013).

213. Taylor, S. C. & Posch, A. The design of a quantitative western blot experiment. *Biomed Res. Int.* **2014**, (2014).

214. Xu, X. Q. *et al.* Chemically defined medium supporting cardiomyocyte differentiation of human embryonic stem cells. *Differentiation* **76**, 958–970 (2008).

215. Zanella, F. & Sheikh, F. Patient-specific induced pluripotent stem cell models: Generation and characterization of cardiac cells. *Methods Mol. Biol.* (2014) doi:10.1007/7651_2014_172.

216. Matsumura, H. *et al.* H558R, a common SCN5A polymorphism, modifies the clinical phenotype of Brugada syndrome by modulating DNA methylation of SCN5A promoters. *J. Biomed. Sci.* **24**, 1–10 (2017).

217. Martinez-Moreno, R. *et al.* An SCN1B Variant Affects Both Cardiac-Type (NaV1.5) and Brain-Type (NaV1.1) Sodium Currents and Contributes to Complex Concomitant Brain and Cardiac Disorders. *Front. Cell Dev. Biol.* **8**, (2020).

218. Qu, Y. *et al.* Modulation of cardiac Na+ channel expression in Xenopus oocytes by β1 subunits. *J. Biol. Chem.* **270**, 25696–25701 (1995).

219. Ko, S. H., Lenkowski, P. W., Lee, H. C., Mounsey, J. P. & Patel, M. K. Modulation of Nav1.5 by β1- and β3-subunit co-expression in mammalian cells. *Pflugers Arch. Eur. J. Physiol.* **449**, 403–412 (2005).

220. Yuan, L. *et al.* Investigations of the Navβ1b sodium channel subunit in human ventricle; functional characterization of the H162P Brugada syndrome mutant. *Am. J. Physiol. - Hear. Circ. Physiol.* **306**, 1204–1212 (2014).

221. Fahmi, A. I. *et al.* The sodium channel β-subunits SCN3b modulates the kinetics of SCN5a and is expressed heterogeneously in sheep heart. *J. Physiol.* **537**, 693–700 (2001).

222. Isom, L. L. *et al.* Primary structure and functional expression of the β1 subunit of the rat brain sodium channel. *Science (80-. ).* **256**, 839–842 (1992).

223. Aman, T. K. *et al.* Regulation of persistent na current by interactions between β subunits of voltage-gated na channels. *J. Neurosci.* **29**, 2027–2042 (2009).

224. Audenaert, D. *et al.* A deletion in SCN1B is associated with febrile seizures and early-onset abence epilepsy. *Neurology* **61**, 854–856 (2003).

225. Tan, B. H. *et al.* Sudden infant death syndrome-associated mutations in the sodium channel beta subunits. *Hear. Rhythm* **7**, 771–778 (2010).

226. Ricci, M. T. *et al.* SCN1B gene variants in Brugada syndrome: A study of 145 SCN5A-negative patients. *Sci. Rep.* **4**, 4–9 (2014).

227. Kruger, L. C. *et al.* β1-C121W is down but not out: Epilepsy-associated scn1b-C121W results in a deleterious gain-of-function. *J. Neurosci.* **36**, 6213–6224 (2016).

228. Symonds, J. D. & Zuberi, S. M. Genetics update: Monogenetics, polygene disorders and the quest for modifying genes. *Neuropharmacology* **132**, 3–19 (2018).

229. Thiffault, I. *et al.* Recessive mutations in POLR1C cause a leukodystrophy by impairing biogenesis of RNA polymerase III. *Nat. Commun.* **6**, 1–9 (2015).

230. Clatot, J. *et al.* Voltage-gated sodium channels assemble and gate as dimers. *Nat. Commun.* **8**, 1–14 (2017).

231. Herskowitz, I. Functional inactivation of genes by dominant negative mutations. *Nature* **329**, 219–222 (1987).

232. Sottas, V. & Abriel, H. Negative-dominance phenomenon with genetic variants of the cardiac sodium channel Nav1.5. *Biochim. Biophys. Acta - Mol. Cell Res.* **1863**, 1–22 (2016).

233. Clatot, J. *et al.* Dominant-negative effect of SCN5A N-terminal mutations through the interaction of Nav1.5 α-subunits. *Cardiovasc. Res.* **96**, 53–63 (2012).

234. Clatot, J. *et al.* Mutant voltage-gated Na+ channels can exert a dominant negative effect through coupled gating. *Am. J. Physiol. - Hear. Circ. Physiol.* **315**, H1250–H1257 (2018).

235. Mercier, A. *et al.* The β1-Subunit of Nav1.5 Cardiac Sodium Channel Is Required for a Dominant Negative Effect through α-α Interaction. *PLoS One* **7**, 5–12 (2012).

236. Núñez, L. *et al.* p.D1690N Nav1.5 rescues p.G1748D mutation gating defects in a

compound heterozygous Brugada syndrome patient. *Hear. Rhythm* **10**, 264–272 (2013).

237. Lizotte, E. *et al.* Genetic modulation of brugada syndrome by a common polymorphism. *J. Cardiovasc. Electrophysiol.* **20**, 1137–1141 (2009).

238. Viswanathan, P. C., Benson, D. W. & Balser, J. R. A common SCN5A polymorphism modulates the biophysical effects of an SCN5A mutation. *J. Clin. Invest.* **111**, 341–346 (2003).

239. Poelzing, S. *et al.* SCN5A polymorphism restores trafficking of a Brugada syndrome mutation on a separate gene. *Circulation* **114**, 368–376 (2006).

240. Shinlapawittayatorn, K. *et al.* A common SCN5A polymorphism modulates the biophysical defects of SCN5A mutations. *Hear. Rhythm* **8**, 455–462 (2011).

241. Marangoni, S. *et al.* A Brugada syndrome mutation (p.S216L) and its modulation by p.H558R polymorphism: Standard and dynamic characterization. *Cardiovasc. Res.* **91**, 606–616 (2011).

242. Antzelevitch, C. *et al.* Loss-of-Function Mutations in the Cardiac Calcium Channel Underlie a New Clinical Entity Characterized by ST-Segment Elevation, Short QT Intervals, and Sudden Cardiac Death. *Circulation* **115**, 442–449 (2007).

243. Hu, D. *et al.* Dual variation in SCN5A and CACNB2b underlies the development of cardiac conduction disease without Brugada syndrome. *Pacing Clin. Electrophysiol.* **33**, 274–285 (2010).

244. Antzelevitch, C. & Fish, J. M. Therapy for the brugada syndrome. *Handb. Exp. Pharmacol.* **171**, 305–330 (2006).

245. Garcia, S. *et al.* Hypertrophic Cardiomyopathy: A Review. *Soc. Bras. Cardiol.* 927–935 (2020).

246. Cirino, A. L. & Ho, C. Hypertrophic Cardiomyopathy Overview. *GeneReviews®* 1–16.

247. Campuzano, O., Fernández-Falgueras, A., Iglesias, A. & Brugada, R. Brugada Syndrome and PKP2: Evidences and uncertainties. *Int. J. Cardiol.* **214**, 1–9 (2016).

248. Corrado, D. *et al.* Right Bundle Branch Block, Right Precordial ST-Segment Elevation, and Sudden Death in Young People. *Circulation* **103**, 710–717 (2001).

249. Cerrone, M. *et al.* Missense Mutations in Plakophilin-2 Cause Sodium Current Deficit and Associate with a Brugada Syndrome Phenotype. *Circulation* **129**, 1092–1103 (2014).

250. Cerrone, M. *et al.* Sodium current deficit and arrhythmogenesis in a murine model of plakophilin-2 haploinsufficiency. *Cardiovasc. Res.* **95**, 460–468 (2012).

251. Lee, H.-C. H. & Ching, C.-K. Practical Aspects in Genetic Testing for Cardiomyopathies and Channelopathies. *Clin. Biochem. Rev.* **40**, 187–200 (2019).

252. Coll, M. *et al.* Incomplete penetrance and variable expressivity: Hallmarks in channelopathies associated with sudden cardiac death. *Biology (Basel).* **7**, 1–10 (2018).

253. Campuzano, O. *et al.* Update on genetic basis of Brugada syndrome: Monogenic,

polygenic or oligogenic? *Int. J. Mol. Sci.* **21**, 1–10 (2020).

# Annex

# Annex Contents

# Annex Figures

# Annex Tables

# 1. Cellular electricity

The cell membrane is a lipid bilayer formed by extracellular, intracellular and transcellular proteins associated. It is hydrophobic, impermeable to large molecules such as proteins and nucleic acids, and selectively permeable to ions. One of the ways ions can flow through the membrane is thanks to one kind of transmembrane proteins: the ion channels.[1–3]

The known functions of ion channels include establishing a resting membrane potential and shaping electrical signals, among several others. The importance of ions in cell excitability has been known since 1881. Sidney Ringer demonstrated that the perfusion solution for a frog heart must contain $Na^+$, $K^+$ and $Ca^{2+}$ ions, if the heart was to continue beating for long.[2] $K^+$ concentration is higher in the intracellular than in the extracellular compartment. On the contrary, $Na^+$ and $Ca^{2+}$ concentrations are higher in the extracellular than in the intracellular compartment (**Table 1**).[3] In 1902, Julius Bernstein proposed that the membrane of excitable cells is selectively permeable to $K^+$ ions at rest, and the permeability to other ions increases during excitation. He explained the resting potential of the membrane as a diffusion potential set up by the tendency of positively charged ions to diffuse from a high concentration in the cytoplasm to a low concentration in the extracellular solution. Upon excitation, the internal negativity is lost transiently as more ions diffuse across the membrane.[2]

**Table 1. Properties of the ions involved in cardiac electrophysiology at 37 °C and a $V_m$ of -80 mV.**

| Ion | Extracellular concentration $[X]_o$ (mM) | Intracellular concentration $[X]_i$ (mM) | $[X]_o/[X]_i$ | Equilibrium potential $E_X$ (mV) | Driving force ($V_m - E_X$) |
|---|---|---|---|---|---|
| $Na^+$ | 145 | 15 | 9.6667 | +61 | -141 |
| $K^+$ | 4.5 | 120 | 0.0375 | -88 | +8 |
| $Ca^{2+}$ | 1.2 | $10^{-4}$ | $12·10^3$ | +125 | -205 |
| $Cl^-$ | 116 | 20 | 5.8 | -47 | -33 |

## 1.1. Electrical properties of plasma membranes

### 1.1.1. Ohm's law

Most cellular plasma membranes are electrically polarized due to a transmembrane voltage, or membrane potential.[3] In 1827, Georg Ohm established the most important electrical law: Ohm's law. It describes a relation between current, voltage and conductance.[2] A few concepts are necessary to understand that law.

Atoms are made up of charged particles. Most bodies are neutral, because charged particles are normally present in equal quantities: one mole of hydrogen atom contains an Avogadro's number ($N = 6.02 \cdot 10^{23}$) of protons and the same number of electrons. The charge quantity is measured in coulombs (C), and the elementary charge of a proton is $q_e = 1.6 \cdot 10^{-19}$ C.[2]

The charge on a mole of protons is named the Faraday constant:[2]

$$F = N \cdot q_e = 6.02 \cdot 10^{23} \text{ x } 1.6 \cdot 10^{-19} \approx 10^5 \text{ C/mol}$$

The flow of charges is called a current (I), and arise when charges of opposite sign are separated or can move independently.[2] Current is measured in amperes (A), and corresponds to a steady flow of 1 C/s. Benjamin Franklin established that positive current flows in the movement direction of positive charges.[2] Michael Faraday proposed the terminology of ions, anions and cations. When anions flow towards the positive pole and cations to the negative, both carry electric current towards the negative pole.[2] The size of the current can be determined by two factors[2]:

- The **potential difference (V)** between the electrodes: Is measured in volts (V). The work needed to move 1 C of charge between two points is 1 V.
- The **electrical conductance (G)**: Is measured in siemens (S) and is defined as the ease of flow of current between two points.

Ohm's law states that current I equals the product of the conductance G and voltage V difference across the conductor:

$$I = G \cdot V$$

Ion channels can be seen as ion conductors, while the membrane bilayer is a poor conductor with a high resistance (R, measured in ohms (Ω)) to electrical current, reciprocal to G. According to Ohm's law, V and I are related by R:[2,3]

$$R = \frac{V}{I}$$

Biological membranes can be seen as electrical capacitors, as the insulating lipid bilayer separates internal and external conducting solutions and charges. In a charged capacitor, one of the sides bears a charge of +Q and the other side -Q. Said capacitor maintains a potential difference between both sides. The capacitance (C) is measured in farad (F = coulomb/volt), and it is defined as how much charge needs to be transferred between two conductors to set up a potential difference[2]:

$$C = \frac{Q}{V}$$

Membranes and ion channels can be represented as an electrical RC circuit (**Figure 1**). If the switch of said circuit remains open, the capacitor maintains the charge. When the switch is closed, the capacitor is discharged through a resistor and the voltage difference in the circuit between the points "in" and "out" decays from $V_0$ to 0.[3]

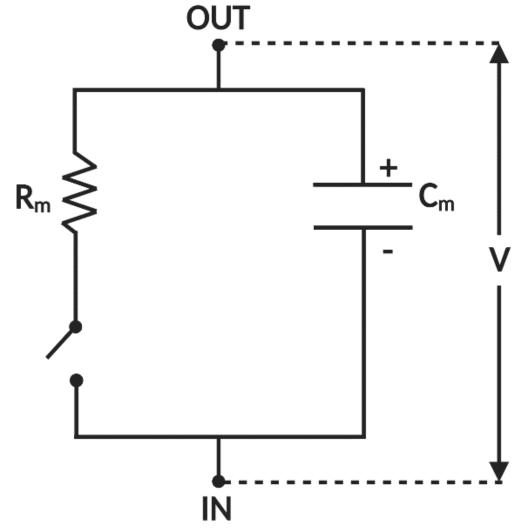

**Figure 1. Schematic representation of an electrical RC circuit.**

The decay time for the voltage to fall to 37% of the initial value is known as the time constant (τ):[3]

$$\tau = R_m \cdot C_m$$

And the time constant in voltage units is:

$$V = V_0 \cdot e^{-t/R \cdot C}$$

Although electrical circuits are well suited to represent the properties of membranes and ion channels, a modification in Ohm´s law must be included as the current through the ion channels (or conductors) do not reach a value of 0 mV.[2]

### 1.1.2. The Nernst equation

Walther Nernst worked in 1888 on electrical potentials arising from the diffusion of electrolytes in solution.[2] The driving force of an ion is defined as the electrochemical potential energy difference across the membrane, and determines the flow of ions. This electrochemical potential energy includes a contribution of the concentration gradient of the solute, and any difference in voltage between the two cellular compartments (inside (i) and outside (o)). For an ion X, it is defined as:[3]

$$\Delta\mu_X = RT\ln\frac{[X]_i}{[X]_o} + z_X F(\Psi_i - \Psi_o)$$

Where $\Delta\mu_X$ is the net driving force of X, R is the gas constant, T is absolute temperature, $[X]_i$ and $[X]_o$ is the ion concentration inside and outside the cell, $z_X$ is the valence and F the Faraday's constant. $\Psi_i$ - $\Psi_o$ is the voltage difference across the membrane, known as membrane potential ($V_m$). The first term on the right side of the equation is the difference in chemical potential energy, and describes the energy change in J/mole as X moves across the membrane. The second term is the electrical potential energy difference, and describes the energy change of a mole of charged particles when it moves across the membrane. [3]

If no net driving force is acting on an ion, that ion is said to be at equilibrium across the membrane ($\Delta\mu_X$ = 0), also known as steady state. The net driving force of an ion $\Delta\mu_X$ (J/mole) is more commonly defined in voltage (mV) as ($V_m$ – $E_X$).[3] All systems are moving towards equilibrium, and the previous equation can be rearranged in the following way:

$$V_m = E_X = -\frac{RT}{z_X F}\ln\frac{[X]_i}{[X]_o}$$

This is the Nernst equation, and describes the conditions when an ion is in equilibrium across the membrane. $E_X$ is the equilibrium potential of ion X, also known as Nernst potential. It can be considered as the membrane voltage needed for an ion X to be in equilibrium.[3] Ionic equilibrium potentials vary linearly with the absolute temperature, and logarithmically with the ion concentration ratio. The sign of the equilibrium potential will be determined by the charge of the ion and the driving force. When $V_m$ is more negative than $E_X$, the current is negative or inward; when $V_m$ is more positive than $E_X$, the current is positive or outwards.[2,3]

The equilibrium potential follows two principles. Taking $Na^+$ ions as an example:[2]

- If the membrane pores are only permeable to $Na^+$ ions, these ions will move towards its equilibrium potential and the membrane potential will change to $E_{Na}$.
- If the membrane potential is held at $E_{Na}$, there will not be a flux of $Na^+$ ions.

Going back to the $Na^+$ example, the current will be inward if $V_m$ is more negative than $E_{Na}$. If the voltages are more positive than $E_{Na}$, the current will then go in an outward direction (**Figure 2**).

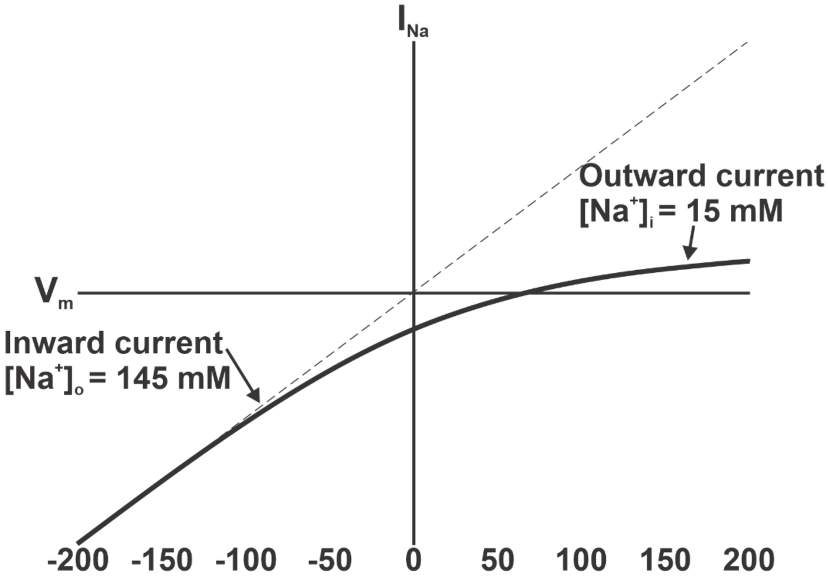

**Figure 2. $Na^+$ predicted current voltage relationship.**

### 1.1.3. Membrane potential

The equilibrium potential of an ion also predicts the reversal potential ($V_{rev}$) for that ion, that is the voltage where the direction of the current reverses.[3] The Goldman-Hodgkin-Katz (GHK) voltage equation calculates $V_{rev}$. It is a modified Nernst equation which includes ion permeability ratios (P):

$$V_{rev} = \frac{RT}{F} \ln \frac{P_A[A]_o + P_B[B]_o}{P_A[A]_i + P_B[B]_i}$$

Equilibrium potentials and other properties of the ions in normal physiological conditions involved in cardiac electrophysiology are listed in **Table 2**:[3]

- The driving force for **$Na^+$** ($V_m$ - $E_{Na}$) at normal membrane resting potential is strongly negative, thus it favors the passive movement of $Na^+$ ions into every cell of the body. Voltage-gated $Na^+$ channels ($Na_V$) are responsible for starting the action potential in many excitable cells.
- The driving force for **$K^+$** ($V_m$ – $E_K$) at normal membrane resting potential is close to 0 or positive, thus $K^+$ ions are either at equilibrium or tends to move outward the cell. $K^+$ channels play a major role in generating a resting membrane voltage that is

inside-negative. These channels also participate in the cell membrane repolarization, which terminates the action potential.

- The driving force for **$Ca^{2+}$** ($V_m - E_{Ca}$) at normal membrane resting potential is strongly negative, thus $Ca^{2+}$ ions tend to move inward the cell. $Ca^{2+}$ channels play a vital role in transmembrane signaling in both nonexcitable and excitable cells, and in generating action potentials.[3]

With Walther Nernst findings, Hodgkin and Huxley modified the Ohm's law including the driving force of ion X as the term $V_m - E_X$:[2,3]

$$I_X = G_X \cdot (V_m - E_X)$$

## 1.2. Cellular current recordings

The ionic theory of membrane excitation explained throughout this chapter was proved by Alan Hodgkin, Andrew Huxley and Bernard Katz between 1935 and 1952. They studied the passive membrane properties and the AP propagation in the squid giant axon.[2] Hodgkin and Huxley recognized three different components of current in their work with the squid giant axon in 1952, which they called: sodium, potassium and leakage. This leakage current, was defined as a small and voltage-independent background conductance.[2]

Hodgkin and Huxley used a modified version of Ohm's law to explain the electrical model of the membrane, by introducing ionic conductances. They also modified the circuit representation to include their recently discovered current components (**Figure 3**).[2]

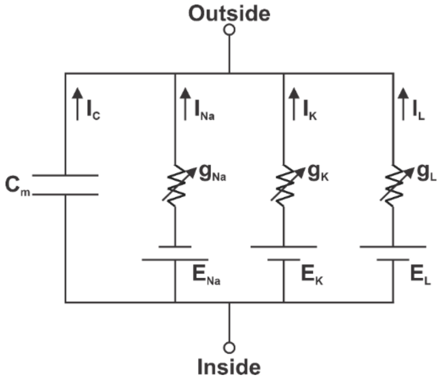

**Figure 3. Schematic representation of an electrical circuit of an axon membrane, presented by Hodgkin and Huxley.** $C_m$ represents the capacitive dielectric properties of the cell membrane. g refers to the ions (Na, K) and leak (L) conductances, I to their currents, and E to their electromotive forces. The resistors with arrows through them denote time- and voltage-varying conductances. Adapted from Hille.[2]

The membrane potential $E_M$, is defined as the inside potential minus the outside. Usually the outside medium is considered to be at ground potential of 0 mV, and thus $E_M$ is simply the intracellular potential.[2] $E_M$ is measured with glass micropipette electrodes (or microelectrodes) made with capillary tubing, and filled with a salt solution whose composition depends on the experimental protocol. The capillary containing a silver chloride wire electrode was connected to an amplifier. This system allowed to measure potentials in the region outside the electrode tip.[2,4] The microelectrode has to be mechanically stable to avoid drift with respect to the cell that could damage the membrane and produce leak. This drift can arise from the cell moving in the preparation, or the microelectrode moving in its holder.[4]

Ion channel properties can be studied in the laboratory with different techniques. The current or the voltage of a cell can be changed to a fixed value (clamped) for a constant time, to be returned to the original value again. This is known as a square pulse:[3,4]

- **Current clamp:** If the current is clamped injecting a current pulse, the voltage will change in response with a time constant τ as previously seen in section 6.1.1.
- **Voltage clamp:** To voltage clamp means to control the voltage across the cell membrane as a means to measure the electrical current that results from the flow of ions.[2,4] If the voltage is clamped injecting a voltage pulse, the current will change. A transient capacitive current $I_C$ appears (Figure) as charge flows onto the capacitor, being maximal at the beginning of the pulse. This current then falls exponentially with a time constant τ. When voltage reaches its original value, $I_C$ flows in the opposite direction: $I_C$ is represented as brief spikes at the beginning and end of the pulse. When the voltage applied is constant, this $I_C$ is zero.

### 1.2.1. Voltage clamp

To control the voltage across the cell membrane, the current needed to keep a constant potential is supplied even when the membrane permeability changes. To readjust the current, a feedback amplifier with a good high-frequency response is used.[2] A schematic voltage clamp circuit is represented in **Figure 4**. In this circuit, $V_m$ is the membrane potential measured by the voltage follower. The clamping amplifier with a gain A, compares $V_m$ with the command potential E to pass current through the access resistance $R_a$ (given by the cytoplasmic resistance) to control $V_m$. $R_s$ represents a resistance in series with the membrane and the electrodes. This resistance leads to a discrepancy between the clamping amplifier membrane potential $V_m$ and the true potential across the membrane. This $R_s$ can be compensated by adding a voltage signal proportional to the membrane current.[4]

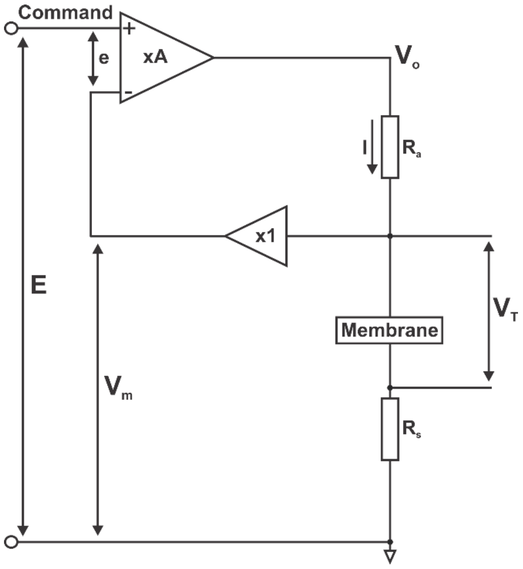

**Figure 4. Simplified schematic voltage clamp circuit.** Adapted from Ogden.[4]

Much of what we know about ion channel properties in cell membranes comes from experiments using voltage clamp. This method was developed by Cole in 1949, and Hodgkin and Huxley in 1952 using the squid giant axon as a model.[4] Another big step in electrophysiology came with the development of the gigaseal and patch clamp methods.[2] In 1976, Neher and Sakmann reported the first record from a tiny area (or patch) of the membrane obtained by pressing a fire-polished pipette.[5] Five years later, Hamill *et al.* showed that clean glass pipettes could fuse with cell membranes to form a high resistance seal with mechanical stability. This seal was called a gigaseal because it could have an electrical resistance of tens of gigaohms.[6]

This gigaseal is needed for two reasons. First, the higher the resistance, the more electrical isolation of the membrane patch. And second, a high seal resistance reduces the current noise of the recording.[4]

The discovery of the gigaseal permitted four new electrical recording configurations (**Figure 5**):[2,4]

- **On-cell or cell-attached patch:** As soon as the pipette is sealed to the membrane, single channels can be recorded.
- **Inside-out or excised patch:** If the seal is stable, the patch can be pulled off the cell by being still sealed to the pipette and single channels can be recorded.
- **Outside-out patch:** It results from pulling the pipette away from the cell in the whole-cell configuration, allowing the recording of single channels.
- **Whole-cell:** In the on-cell configuration, the patch can be suctioned and thus ruptured with the pipette still sealed to the cell. The contents of the pipette solution alter the composition of the cytoplasm, and thus is a valuable tool for cell biological and biochemical studies.

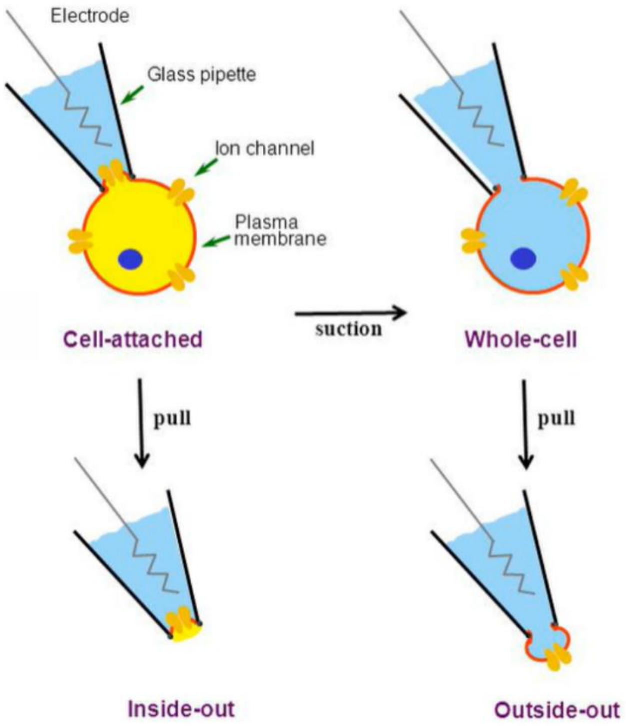

**Figure 5. Patch clamp recording configurations.** Adapted from Biophysics 702 Patch Clamp Techniques, by Stuart Mangel (https://slideplayer.com/slide/3334202/).

When a whole-cell experiment involves a change in membrane potential, the macroscopic currents recorded represent the sum of the ions flowing through many channels and of different types. To study a particular ion channel, this macroscopic current has to be separated into its constituent components. For that, several methods (alone or in combination) are used:[4]

- **Time of measurement:** The currents can be separated if their kinetics are sufficiently different, by using a suitable time during a voltage clamp pulse.
- **Ionic substitution:** If it is possible to perfuse the inside of the cell, it can be applied to intracellular and extracellular substitutions. In the whole cell patch clamp technique, this method is widely used.
- **Pharmacological separation:** Different substances that block ion channels are used. These blockers can range from simple inorganic ions to synthetic drugs, to complex natural toxins. They can act from the inside as well the outside of the cell. Sometimes this method is used in combination with ionic substitution.
- **Voltage pulse protocol:** This method is suitable when the activation and inactivation of different channels occurs over different membrane potential ranges.
- **Channel expression:** In cell types that have little or no intrinsic ion conductance like *Xenopus* oocytes and HEK cells, a particular channel can be cloned and expressed. The main disadvantage of this method is that the cloned channel may not exactly reflect its behavior in the native cell, due to the lack of certain regulatory proteins.

## 2. Primers and probes used in the qPCR experiments

**Table 2. Sequence, amplicon length and efficiency of the primers for the qPCR experiments using the KAPA SYBR FAST qPCR Kit.**

| Gene | Sequence | Amplicon (bp) | Efficiency (%) |
|---|---|---|---|
| ***GAPDH*** | FW: CTGCACCACCAACTGCTTAG<br>RV: GAGGCAGGGATGATGTTCTGG | 177 | 99.1 |
| **Nanog** | FW: GACAAGGTCCCGGTCAAGAA<br>RV: CTGAGGTTCAGGATGTTGGA | 140 | 103.1 |
| **Sox-2** | FW: AGTCCGAGGCCAGCTCCA<br>RV: TAGTGCTGGGACATGTGAAGTC | 160 | 98.7 |
| **Oct-4** | FW: CCCGCCGTATGAGTTCTGTG<br>RV: CATCGGAGTTGCTCTCCACC | 134 | 96.3 |
| ***MYBPC3*** | FW: CCATCTGAGTACGAGCGCAT<br>RV: GCCCTTGAGCCTCTTTAGCA | 75 | 106.98 |
| ***TNNI3*** | FW: CCTCCAACTACCGCGCTTAT<br>RV: CTGCAATTTTCTCGAGGCGG | 77 | 108.57 |
| ***SCN5A*** | FW: CGAGGCCAGTGCATCTCAGG<br>RV: GTATCACCTTCCACTCTGTCCA | 125 | 101.2 |

**Table 3. Probe code, amplicon length and exon boundary of the probes used for the qPCR experiments using the TaqMan® Gene Expression Assays.**

| Gene | Probe code | Amplicon (bp) | Exon boundary |
|---|---|---|---|
| ***PPIA*** | Hs04194521_s1 | 97 | 6 |
| **18S** | Hs99999901_s1 | 187 | 1 |
| ***MYL2*** | Hs00166405_m1 | 98 | 6 - 7 |
| ***MYL7*** | Hs01085598_g1 | 74 | 4 - 5 |
| ***HCN4*** | Hs04982536_s1 | 96 | 1 |

## 3. Generation of iPS cell lines

**Table 4. Expression levels of the pluripotency transcription factors obtained by relative quantification (Rq) of the GPG1 iPSc, compared with the GPG1 fibroblasts.**

| GPG1 | | | | | | | | | |
|---|---|---|---|---|---|---|---|---|---|
| Sample | Nanog | | | Sox-2 | | | Oct-4 | | |
| | Rq | Rq min | Rq max | Rq | Rq min | Rq max | Rq | Rq min | Rq max |
| **Fibroblasts** | 1 | 0.64 | 1.57 | 1 | 0.87 | 1.15 | 1 | 0.93 | 1.08 |
| **iPSc** | 652.68 | 632.85 | 673.14 | 19335.55 | 18965.88 | 19721.78 | 1953.92 | 1899.32 | 2010.09 |

**Table 5. Expression levels of the pluripotency transcription factors obtained by relative quantification (Rq) of the discarded clones for the individual Rb20234, compared with the non-related control GPG1 iPSc.**

| Rb20234 iPSc | | | | | | | | | |
|---|---|---|---|---|---|---|---|---|---|
| Clones | Nanog | | | Sox-2 | | | Oct-4 | | |
| | Rq | Rq min | Rq max | Rq | Rq min | Rq max | Rq | Rq min | Rq max |
| **C16** | 3.913 | 3.747 | 4.091 | 4.710 | 4.569 | 8.857 | 1.014 | 0.980 | 1.048 |
| **C18** | 3.713 | 3.416 | 4.038 | 2.747 | 2.541 | 2.971 | 1.393 | 1.284 | 1.511 |
| **C22** | 3.233 | 2.937 | 3.595 | 4.491 | 3.672 | 5.534 | 0.853 | 0.802 | 0.917 |
| **C26** | 3.164 | 1.972 | 5.576 | 4.760 | 3.214 | 7.373 | 0.593 | 0.488 | 0.795 |
| **C30** | 1.891 | 1.796 | 1.991 | 1.604 | 1.401 | 1.862 | 1.465 | 1.391 | 1.545 |
| **C31** | 1.070 | 0.991 | 1.157 | 1.129 | 1.039 | 1.229 | 0.728 | 0.686 | 0.775 |
| **C34** | 1.804 | 1.717 | 1.895 | 1.520 | 1.453 | 1.592 | 0.757 | 0.719 | 0.797 |
| **C41** | 3.193 | 3.051 | 3.343 | 1.925 | 1.840 | 2.014 | 0.893 | 0.863 | 0.925 |
| **C46** | 1.717 | 1.633 | 1.806 | 2.159 | 2.092 | 2.228 | 0.657 | 0.631 | 0.684 |
| **C49** | 1.158 | 1.095 | 1.227 | 2.277 | 2.186 | 2.374 | 0.487 | 0.450 | 0.528 |
| **C54** | 1.573 | 1.475 | 1.679 | 1.860 | 1.795 | 1.927 | 0.611 | 0.566 | 0.661 |

**Table 6. Expression levels of the pluripotency transcription factors obtained by relative quantification (Rq) of the discarded clones for the individual Rb20235, compared with the non-related control GPG1 iPSc.**

| Rb20235 iPSc | | | | | | | | | |
|---|---|---|---|---|---|---|---|---|---|
| Clones | Nanog | | | Sox-2 | | | Oct-4 | | |
| | Rq | Rq min | Rq max | Rq | Rq min | Rq max | Rq | Rq min | Rq max |
| C1 | 6.278 | 3.722 | 11.258 | 7.762 | 6.639 | 9.156 | 1.268 | 1.102 | 1.461 |
| C26 | 1.023 | 0.981 | 1.066 | 2.257 | 2.135 | 2.386 | 0.344 | 0.326 | 0.363 |
| C40 | 0.357 | 0.339 | 0.377 | 0.962 | 0.928 | 0.997 | 0.255 | 0.239 | 0.272 |

**Table 7. Expression levels of the pluripotency transcription factors obtained by relative quantification (Rq) of the discarded clones for the individual Rb20236, compared with the non-related control GPG1 iPSc.**

| Rb20236 iPSc | | | | | | | | | |
|---|---|---|---|---|---|---|---|---|---|
| Clones | Nanog | | | Sox-2 | | | Oct-4 | | |
| | Rq | Rq min | Rq max | Rq | Rq min | Rq max | Rq | Rq min | Rq max |
| C8 | 0.983 | 0.937 | 1.032 | 1.043 | 1.003 | 1.084 | 1.142 | 1.023 | 1.279 |
| C9 | 1.505 | 1.449 | 1.562 | 1.008 | 0.955 | 1.065 | 0.655 | 0.634 | 0.677 |
| C25 | 12.485 | 10.438 | 14.982 | 2.032 | 1.846 | 2.241 | 4.289 | 3.981 | 4.622 |
| C29 | 2.605 | 2.497 | 2.717 | 0.609 | 0.588 | 0.631 | 1.122 | 1.069 | 1.178 |
| C32 | 1.908 | 1.787 | 2.039 | 0.686 | 0.672 | 0.700 | 0.914 | 0.879 | 0.951 |

**Table 8. Expression levels of the pluripotency transcription factors obtained by relative quantification (Rq) of the discarded clones for the individual Rb20237, compared with the non-related control GPG1 iPSc.**

| Rb20237 iPSc | | | | | | | | | |
|---|---|---|---|---|---|---|---|---|---|
| Clones | Nanog | | | Sox-2 | | | Oct-4 | | |
| | Rq | Rq min | Rq max | Rq | Rq min | Rq max | Rq | Rq min | Rq max |
| C1 | 0.820 | 0.751 | 0.908 | 0.511 | 0.454 | 0.582 | 0.222 | 0.197 | 0.257 |
| C3 | 1.118 | 0.817 | 1.673 | 0.604 | 0.552 | 0.662 | 0.236 | 0.172 | 0.376 |
| C4 | 1.790 | 1.562 | 2.093 | 0.535 | 0.452 | 0.633 | 0.253 | 0.253 | 0.253 |
| C6 | 1.113 | 0.973 | 1.279 | 0.869 | 0.763 | 0.991 | 0.199 | 0.169 | 0.237 |

## 4. Clone characterization

Rb20234 C17 iPSc

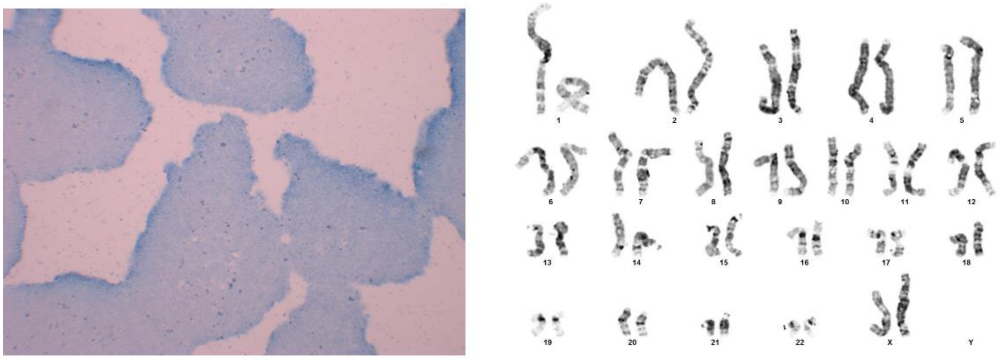

Rb20236 C21 iPSc

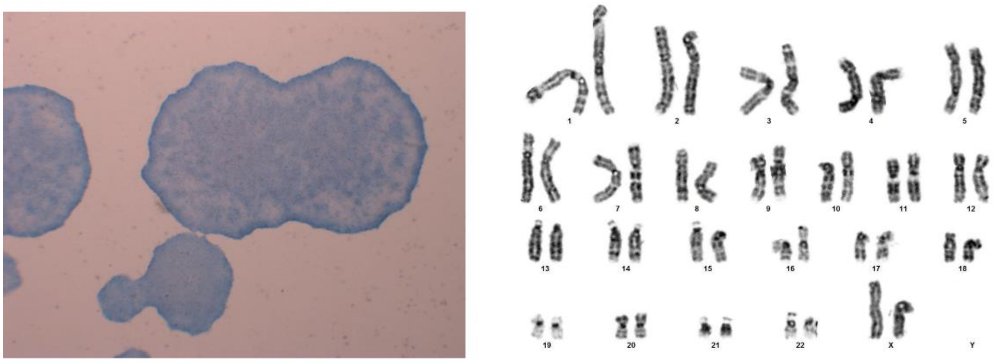

Rb20237 C5 iPSc

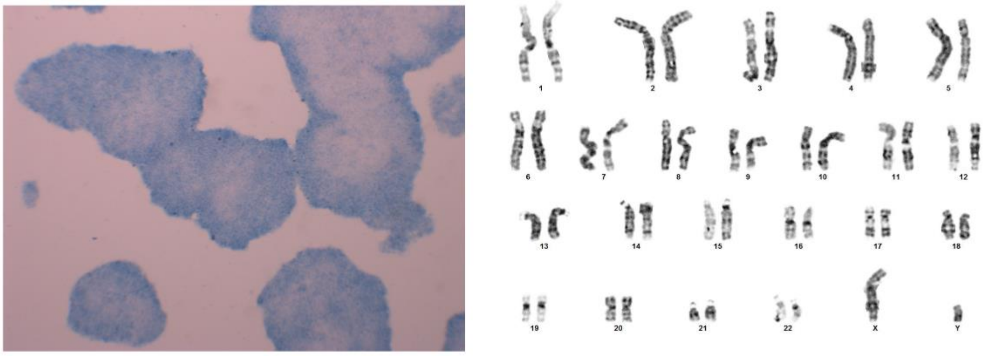

**Figure 6. iPSc colonies showing Alkaline phosphatase staining (left) and karyotype (right) of Rb20234 C17 iPSc (top), Rb202236 C21 iPSc (middle) and Rb20237 C5 iPSc (bottom).**

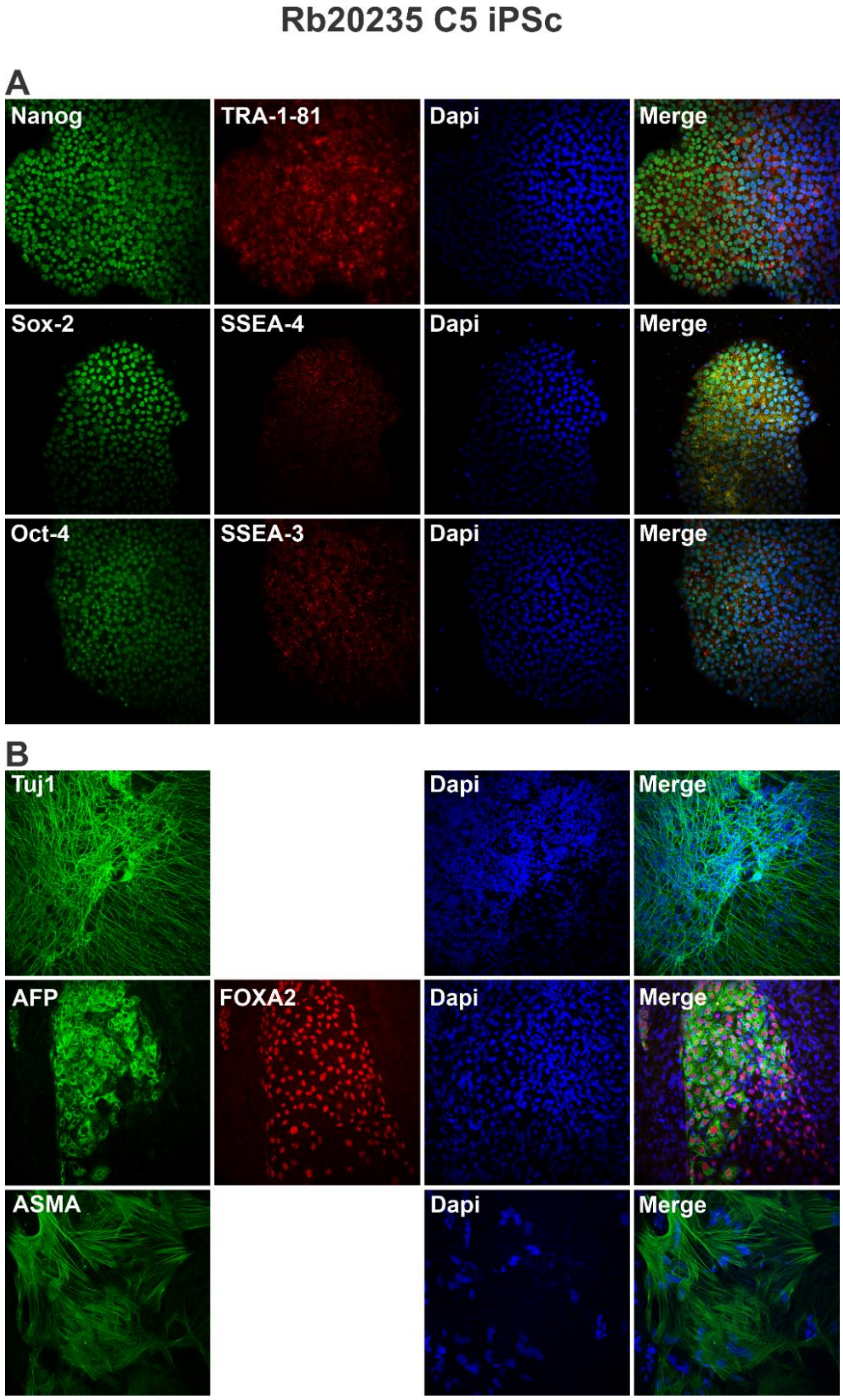

**Figure 7. Pluripotency characterization of Rb20235 C5 iPSc clone. (A)** iPSc clone Rb20235 C5 tested positive for pluripotency markers Nanog and TRA-1-81 (upper panel), Sox-2 and SSEA-4 (middle panel), and Oct-4 and SSEA-3 (bottom panel). **(B)** Studies of in vitro differentiation to cells of the 3 germ layers showed the capacity of the studied iPSc to differentiate into cells of the ectoderm (positive staining for Tuj1, upper panel), endoderm (positive staining for AFP and FOXA2, middle panel), and mesoderm (positive staining for ASMA, bottom panel).

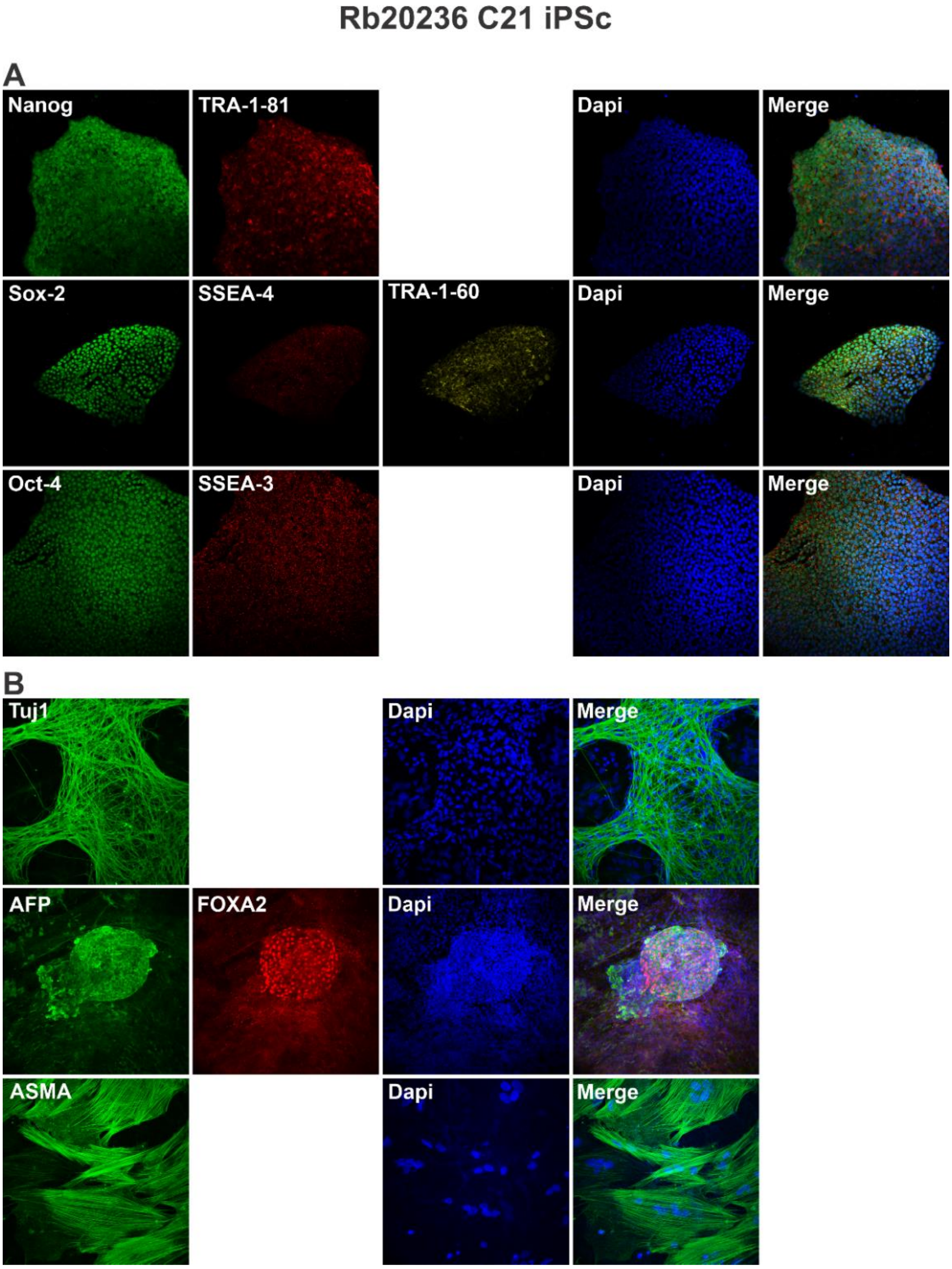

**Figure 8. Pluripotency characterization of Rb20236 C21 iPSc clone. (A)** iPSc clone Rb20236 C21 tested positive for pluripotency markers Nanog and TRA-1-81 (upper panel), Sox-2, SSEA-4 and TRA-1-60 (middle panel), and Oct-4 and SSEA-3 (bottom panel). **(B)** Studies of in vitro differentiation to cells of the 3 germ layers showed the capacity of the studied iPSc to differentiate into cells of the ectoderm (positive staining for Tuj1, upper panel), endoderm (positive staining for AFP and FOXA2, middle panel), and mesoderm (positive staining for ASMA, bottom panel).

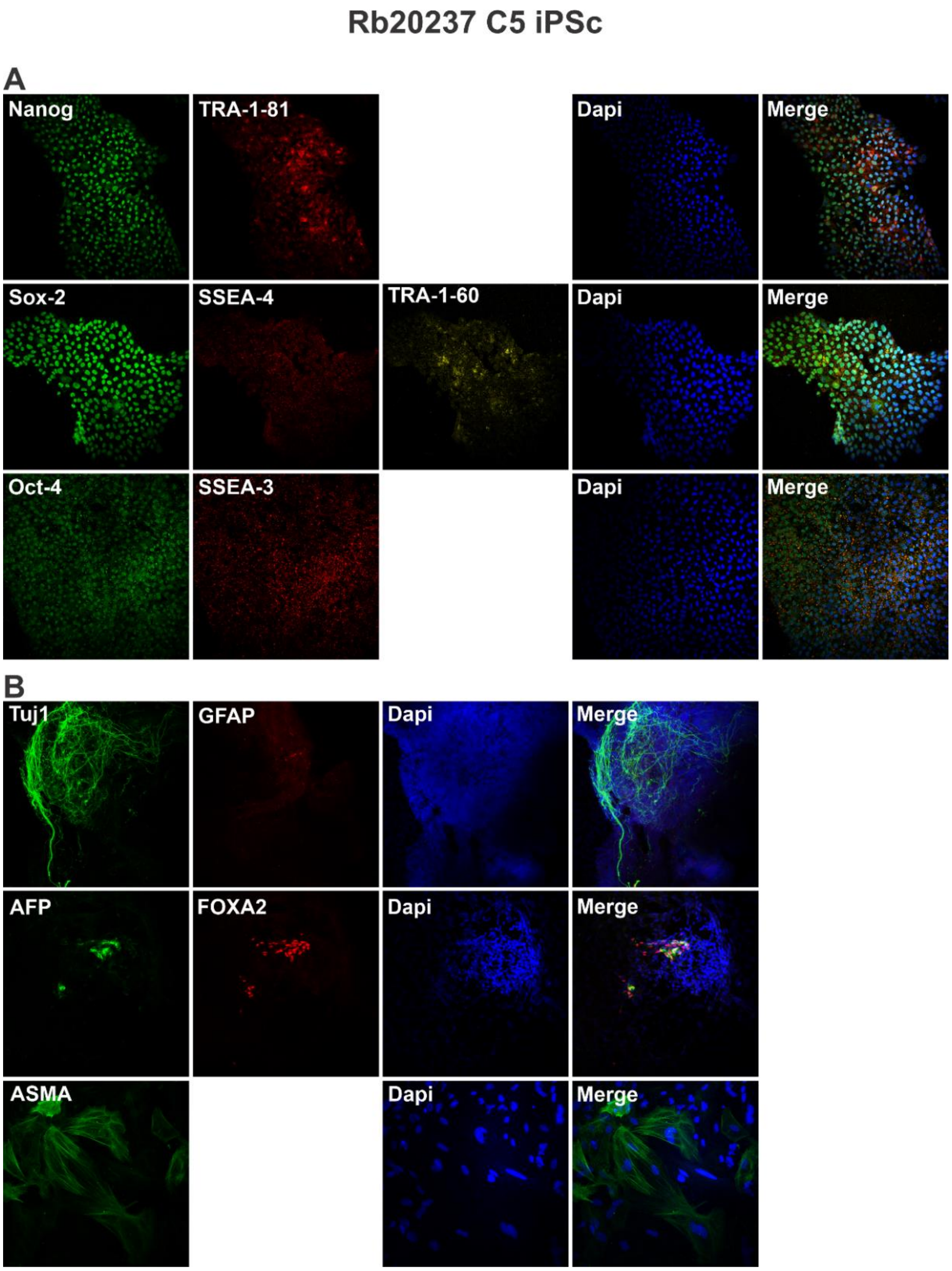

**Figure 9. Pluripotency characterization of Rb20236 C21 iPSc clone. (A)** iPSc clone Rb20236 C21 tested positive for pluripotency markers Nanog and TRA-1-81 (upper panel), Sox-2, SSEA-4 and TRA-1-60 (middle panel), and Oct-4 and SSEA-3 (bottom panel). **(B)** Studies of in vitro differentiation to cells of the 3 germ layers showed the capacity of the studied iPSc to differentiate into cells of the ectoderm (positive staining for Tuj1 and GFAP, upper panel), endoderm (positive staining for AFP and FOXA2, middle panel), and mesoderm (positive staining for ASMA, bottom panel).

## 5. Cardiomyocyte characterization

**Table 9. Expression levels of the pluripotency transcription factors obtained by relative quantification (Rq) of three iPS-CM differentiation rounds for the two selected clones from individual Rb20234, compared with their respective iPSc.**

| Rb20234 iPS-CM | | | | | | | | | | |
|---|---|---|---|---|---|---|---|---|---|---|
| Clone | Round | Nanog | | | Sox-2 | | | Oct-4 | | |
| | | Rq | Rq min | Rq max | Rq | Rq min | Rq max | Rq | Rq min | Rq max |
| C5 | R15 | 0.013 | 0.011 | 0.014 | 0.013 | 0.012 | 0.015 | 0.009 | 0.008 | 0.009 |
| | R18 | 0.017 | 0.016 | 0.019 | 0.003 | 0.003 | 0.004 | 0.005 | 0.005 | 0.005 |
| | R20 | 0.035 | 0.031 | 0.04 | 0.003 | 0.002 | 0.003 | 0.004 | 0.003 | 0.004 |
| C17 | R7 | 0.172 | 0.162 | 0.182 | 0.016 | 0.014 | 0.018 | 0.030 | 0.028 | 0.033 |
| | R10 | 0.156 | 0.146 | 0.167 | 0.024 | 0.023 | 0.026 | 0.037 | 0.030 | 0.046 |
| | R12 | 0.005 | 0.003 | 0.008 | 0.001 | 0.000 | 0.001 | 0.001 | 0.001 | 0.002 |

**Table 10. Expression levels of the pluripotency transcription factors obtained by relative quantification (Rq) of three iPS-CM differentiation rounds for the two selected clones from individual Rb20235, compared with their respective iPSc.**

| Rb20235 iPS-CM | | | | | | | | | | |
|---|---|---|---|---|---|---|---|---|---|---|
| Clone | Round | Nanog | | | Sox-2 | | | Oct-4 | | |
| | | Rq | Rq min | Rq max | Rq | Rq min | Rq max | Rq | Rq min | Rq max |
| C5 | R7 | 0.001 | 0.001 | 0.002 | 0.000 | 0.000 | 0.000 | 0.000 | 0.000 | 0.000 |
| | R8 | 0.022 | 0.020 | 0.023 | 0.004 | 0.004 | 0.004 | 0.003 | 0.003 | 0.004 |
| | R11 | 0.021 | 0.017 | 0.025 | 0.002 | 0.002 | 0.002 | 0.002 | 0.002 | 0.003 |
| C39 | R6 | 0.016 | 0.014 | 0.018 | 0.001 | 0.001 | 0.002 | 0.003 | 0.003 | 0.004 |
| | R8 | 0.010 | 0.008 | 0.013 | 0.001 | 0.001 | 0.002 | 0.002 | 0.002 | 0.002 |
| | R9 | 0.006 | 0.004 | 0.008 | 0.000 | 0.000 | 0.000 | 0.001 | 0.001 | 0.002 |

**Table 11. Expression levels of the pluripotency transcription factors obtained by relative quantification (Rq) of three iPS-CM differentiation rounds for the two selected clones from individual Rb20236, compared with their respective iPSc.**

| Rb20236 iPS-CM | | | | | | | | | | |
|---|---|---|---|---|---|---|---|---|---|---|
| Clone | Round | Nanog | | | Sox-2 | | | Oct-4 | | |
| | | Rq | Rq min | Rq max | Rq | Rq min | Rq max | Rq | Rq min | Rq max |
| C21 | R1 | 0.005 | 0.004 | 0.006 | 0.003 | 0.003 | 0.003 | 0.002 | 0.002 | 0.003 |
| | R2 | 0.005 | 0.005 | 0.006 | 0.003 | 0.002 | 0.003 | 0.004 | 0.004 | 0.004 |
| | R5 | 0.016 | 0.015 | 0.017 | 0.002 | 0.002 | 0.002 | 0.003 | 0.003 | 0.003 |
| C24 | R3 | 0.006 | 0.005 | 0.007 | 0.002 | 0.001 | 0.002 | 0.003 | 0.003 | 0.003 |
| | R4 | 0.011 | 0.011 | 0.012 | 0.005 | 0.004 | 0.006 | 0.006 | 0.005 | 0.006 |
| | R12 | 0.006 | 0.004 | 0.009 | 0.002 | 0.001 | 0.002 | 0.003 | 0.002 | 0.004 |

**Table 12. Expression levels of the pluripotency transcription factors obtained by relative quantification (Rq) of three iPS-CM differentiation rounds for the two selected clones from individual Rb20237, compared with their respective iPSc.**

| Rb20237 iPS-CM | | | | | | | | | | |
|---|---|---|---|---|---|---|---|---|---|---|
| Clone | Round | Nanog | | | Sox-2 | | | Oct-4 | | |
| | | Rq | Rq min | Rq max | Rq | Rq min | Rq max | Rq | Rq min | Rq max |
| **C2** | **R1** | 0.006 | 0.006 | 0.007 | 0.002 | 0.002 | 0.002 | 0.002 | 0.002 | 0.002 |
| | **R2** | 0.008 | 0.006 | 0.011 | 0.001 | 0.001 | 0.002 | 0.003 | 0.002 | 0.003 |
| | **R4** | 0.010 | 0.009 | 0.011 | 0.004 | 0.004 | 0.004 | 0.002 | 0.002 | 0.003 |
| **C5** | **R4** | 0.010 | 0.010 | 0.011 | 0.001 | 0.001 | 0.001 | 0.008 | 0.007 | 0.008 |
| | **R6** | 0.013 | 0.012 | 0.015 | 0.002 | 0.002 | 0.002 | 0.013 | 0.011 | 0.014 |
| | **R8** | 0.051 | 0.045 | 0.057 | 0.007 | 0.007 | 0.008 | 0.010 | 0.010 | 0.011 |

**Table 13. Expression levels of the cardiac markers obtained by relative quantification (Rq) of three iPS-CM differentiation rounds for the two selected clones from individual Rb20234, compared with their respective iPSc.**

| Rb20234 iPS-CM | | | | | | | | | | |
|---|---|---|---|---|---|---|---|---|---|---|
| Clone | Round | *MYBPC3* | | | *TNNI3* | | | *SCN5A* | | |
| | | Rq | Rq min | Rq max | Rq | Rq min | Rq max | Rq | Rq min | Rq max |
| **C5** | **R15** | 217578.7 | 199624.8 | 237147.2 | 3233.4 | 2965.6 | 3525.5 | 301.7 | 279.1 | 326.1 |
| | **R18** | 392975.5 | 373007.8 | 414012.1 | 1898.8 | 1801.0 | 2001.9 | 363.0 | 345.1 | 381.8 |
| | **R20** | 47325.8 | 42136.3 | 53154.3 | 1503.1 | 1376.4 | 1641.3 | 53.1 | 40.9 | 68.9 |
| **C17** | **R7** | 1502394.4 | 1413491.2 | 1596889.2 | 1139.6 | 1076.3 | 1206.6 | 1768.1 | 1662.4 | 1880.7 |
| | **R10** | 334468.7 | 312329.7 | 358176.9 | 3777.3 | 3519.4 | 4054.0 | 105.4 | 93.7 | 119.7 |
| | **R12** | 42897.9 | 39121.6 | 470038.7 | 457.9 | 408.5 | 513.3 | 19.3 | 17.1 | 21.8 |

**Table 14. Expression levels of the cardiac markers obtained by relative quantification (Rq) of three iPS-CM differentiation rounds for the two selected clones from individual Rb20235, compared with their respective iPSc.**

| Rb20235 iPS-CM | | | | | | | | | | |
|---|---|---|---|---|---|---|---|---|---|---|
| Clone | Round | *MYBPC3* | | | *TNNI3* | | | *SCN5A* | | |
| | | Rq | Rq min | Rq max | Rq | Rq min | Rq max | Rq | Rq min | Rq max |
| **C5** | **R7** | 2154.5 | 1937.6 | 2375.6 | 3160.5 | 2850.9 | 3503.7 | 47.2 | 42.4 | 52.6 |
| | **R8** | 6915.5 | 6693.2 | 7145.3 | 928.5 | 890.3 | 968.4 | 5.1 | 4.9 | 5.3 |
| | **R11** | 25148.9 | 23904.1 | 26458.5 | 3627.5 | 3424.2 | 3842.8 | 50.7 | 48.2 | 53.3 |
| **C39** | **R6** | 57276.2 | 55176.3 | 59456 | 1225.7 | 1176.2 | 1277.4 | 38.3 | 36.8 | 39.8 |
| | **R8** | 66876.4 | 63054.9 | 70929.5 | 13603.5 | 12833.2 | 14419.9 | 93.1 | 87.4 | 99.2 |
| | **R9** | 43392.7 | 41569.9 | 45295.5 | 594.5 | 573.7 | 616.1 | 33.4 | 32.2 | 34.6 |

**Table 15. Expression levels of the cardiac markers obtained by relative quantification (Rq) of three iPS-CM differentiation rounds for the two selected clones from individual Rb20236, compared with their respective iPSc.**

| Rb20236 iPS-CM | | | | | | | | | | |
|---|---|---|---|---|---|---|---|---|---|---|
| **Clone** | **Round** | ***MYBPC3*** | | | ***TNNI3*** | | | ***SCN5A*** | | |
| | | **Rq** | **Rq min** | **Rq max** | **Rq** | **Rq min** | **Rq max** | **Rq** | **Rq min** | **Rq max** |
| **C21** | **R1** | 157631.9 | 149.940.2 | 165718.1 | 3549.5 | 3331.4 | 3781.9 | 61.9 | 59 | 64.9 |
| | **R2** | 220772.6 | 218617.7 | 222948.8 | 5105.7 | 4999.4 | 5214.2 | 12.5 | 12.3 | 12.8 |
| | **R5** | 48714.3 | 47179.4 | 50299.2 | 2060.6 | 2019.1 | 2103 | 11.2 | 10.8 | 11.7 |
| **C24** | **R3** | 10429.4 | 9971.6 | 10908.2 | 803.4 | 768.2 | 840.2 | 19.3 | 18.6 | 20.1 |
| | **R4** | 53341.9 | 51547.7 | 55198.7 | 3915.4 | 3757.4 | 4080.1 | 123.5 | 119.2 | 127.9 |
| | **R12** | 32845.3 | 26467.7 | 40759.7 | 2684.7 | 2135.4 | 3375.2 | 116.9 | 84.5 | 161.8 |

**Table 16. Expression levels of the cardiac markers obtained by relative quantification (Rq) of three iPS-CM differentiation rounds for the two selected clones from individual Rb20237, compared with their respective iPSc.**

| Rb20237 iPS-CM | | | | | | | | | | |
|---|---|---|---|---|---|---|---|---|---|---|
| **Clone** | **Round** | ***MYBPC3*** | | | ***TNNI3*** | | | ***SCN5A*** | | |
| | | **Rq** | **Rq min** | **Rq max** | **Rq** | **Rq min** | **Rq max** | **Rq** | **Rq min** | **Rq max** |
| **C2** | **R1** | 1248.9 | 1193.9 | 1306.5 | 100.1 | 96.0 | 104.4 | 8.5 | 7.8 | 9.2 |
| | **R2** | 4149.5 | 3961.8 | 4345.9 | 232.5 | 222.7 | 242.7 | 32.1 | 30.1 | 34.1 |
| | **R4** | 7427.0 | 7044.6 | 7830.2 | 1404.0 | 1327.9 | 1484.5 | 42.6 | 40.1 | 45.2 |
| **C5** | **R4** | 14867.2 | 13169.2 | 16784.2 | 352.2 | 330.6 | 375.2 | 7.6 | 6.9 | 8.4 |
| | **R6** | 24849.2 | 22458.3 | 27494.6 | 318.1 | 287.9 | 351.5 | 13.9 | 12.5 | 15.4 |
| | **R8** | 3225.5 | 3013.5 | 3452.5 | 178.2 | 166.1 | 191.1 | 2.3 | 2.1 | 2.5 |

## 6. Electrophysiological characterization of iPS-CM

**Table 17. Expression levels of the ventricular and auricular markers obtained by relative quantification (Rq) of five iPS-CM differentiation rounds for each individual and the individual Rq mean, normalized by the nodal marker HCN4 and compared with Rb20237.**

| Individual | Clone | Round | *MYL2* | *MYL2* mean | *MYL7* | *MYL7* mean |
|---|---|---|---|---|---|---|
| | | | Rq±SEM | Rq±SEM | Rq±SEM | Rq±SEM |
| **Rb20234** | **C5** | **R18** | 2.84±1.20 | 2.41±0.41 | 2.75±1.08 | 2.20±0.39 |
| | | **R20** | 1.95±0.69 | | 1.74±0.69 | |
| | **C17** | **R7** | 3.66±1.17 | | 3.09±1.22 | |
| | | **R10** | 1.51±0.52 | | 1.33±0.52 | |
| | | **R12** | 2.12±0.93 | | 2.08±0.82 | |
| **Rb20235** | **C5** | **R8** | 1.39±0.46 | 3.32±0.76 | 1.20±0.47 | 2.63±0.67 |
| | | **R11** | 2.52±0.97 | | 2.11±0.97 | |
| | **C39** | **R6** | 3.48±1.14 | | 2.98±1.17 | |
| | | **R8** | 8.42±2.38 | | 6.22±2.45 | |
| | | **R9** | 0.79±0.24 | | 0.64±0.25 | |
| **Rb20236** | **C21** | **R1** | 2.01±0.65 | 3.15±0.51 | 1.71±0.68 | 2.51±0.46 |
| | | **R2** | 2.84±1.04 | | 2.57±1.01 | |
| | | **R5** | 5.65±1.61 | | 3.94±1.56 | |
| | **C24** | **R3** | 1.89±0.56 | | 1.52±0.60 | |
| | | **R12** | 3.38±1.06 | | 2.82±1.11 | |

**Table 18. Biophysical parameters of Rb20234 C5 and Rb20234 C17 iPS-CM and pooled data.**

| Parameter | Rb20234 C5 | Rb20234 C17 | Pooled Rb20234 |
|---|---|---|---|
| **Peak $I_{Na}$ density** | | | |
| **pA/pF** | -19.72±2.63 | -26.52±5.29 | -22.96±2.90 |
| **n** | 11 | 10 | 21 |
| **Activation** | | | |
| **$V_{1/2}$ (mV)** | -33.16±1.75 | -35.19±1.76 | -34.09±1.23 |
| **k** | 5.25±0.31 | 4.29±0.35 | 4.81±0.25 |
| **n** | 12 | 10 | 22 |
| **Steady-state inactivation** | | | |
| **$V_{1/2}$ (mV)** | -53.89±1.40 | -54.73±1.43 | -54.66±0.99 |
| **k** | 7.70±0.32 | 8.07±0.64 | 7.46±0.29 |
| **n** | 10 | 8 | 18 |
| **Recovery from inactivation** | | | |
| **τ (ms)** | 6.29±1.32 | 7.12±1.24 | 6.68±0.88 |
| **n** | 7 | 6 | 13 |

**Table 19. Biophysical parameters of Rb20235 C5 and Rb20235 C39 iPS-CM and pooled data.**

| Parameter | Rb20235 C5 | Rb20235 C39 | Pooled Rb20235 |
|---|---|---|---|
| **Peak $I_{Na}$ density** | | | |
| **pA/pF** | -21.46±5.48 | -26.82±9.85 | -22.53±4.72 |
| **n** | 16 | 4 | 20 |
| **Activation** | | | |
| **$V_{1/2}$ (mV)** | -29.71±1.51 | -32.12±1.97 | -30.33±1.23 |
| **k** | 5.27±0.41 | 3.92±0.35 | 4.92±0.34 |
| **n** | 15 | 4 | 19 |
| **Steady-state inactivation** | | | |
| **$V_{1/2}$ (mV)** | -56.45±1.67 | -51.52±2.40 | -55.14±1.46 |
| **k** | 6.59±0.81 | 5.32±0.75 | 6.25±0.65 |
| **n** | 11 | 4 | 15 |
| **Recovery from inactivation** | | | |
| **τ (ms)** | 4.44±0.71 | 5.76±1.68 | 4.79±0.67 |
| **n** | 11 | 4 | 15 |

**Table 20. Biophysical parameters of Rb20236 C21 and Rb20236 C24 iPS-CM and pooled data.**

| Parameter | Rb20236 C21 | Rb20236 C24 | Pooled Rb20236 |
|---|---|---|---|
| **Peak $I_{Na}$ density** | | | |
| **pA/pF** | -176.98±20.28 | -170.64±30.81 | -173.55±18.73 |
| **n** | 11 | 13 | 24 |
| **Activation** | | | |
| **$V_{1/2}$ (mV)** | -38.23±1.87 | -41.35±1.57 | -40.10±1.22 |
| **k** | 3.48±0.45 | 4.42±0.56 | 4.04±0.39 |
| **n** | 8 | 12 | 20 |
| **Steady-state inactivation** | | | |
| **$V_{1/2}$ (mV)** | -60.09±1.32 | -60.86±2.44 | -60.34±1.16 |
| **k** | 6.98±0.62 | 7.58±0.88 | 7.18±0.50 |
| **n** | 12 | 6 | 18 |
| **Recovery from inactivation** | | | |
| **τ (ms)** | 4.58±0.62 | 3.98±0.75 | 4.37±0.47 |
| **n** | 11 | 6 | 17 |

**Table 21. Expression levels of *SCN5A* obtained by relative quantification (Rq) of five iPS-CM differentiation rounds for each individual and the individual Rq mean, compared with Rb20237.**

| Individual | Clone | Round | *SCN5A* | *SCN5A* mean |
|---|---|---|---|---|
| | | | Rq±SEM | Rq±SEM |
| **Rb20234** | **C5** | **R18** | 0.16±0.05 | 2.15±0.60 |
| | | **R20** | 2.28±0.68 | |
| | **C17** | **R7** | 6.45±1.92 | |
| | | **R10** | 0.48±0.14 | |
| | | **R12** | 1.38±0.41 | |
| **Rb20235** | **C5** | **R8** | 0.61±0.18 | 1.60±0.30 |
| | | **R11** | 2.09±0.62 | |
| | **C39** | **R6** | 1.49±0.44 | |
| | | **R8** | 3.19±0.95 | |
| | | **R9** | 0.63±0.19 | |
| **Rb20236** | **C21** | **R1** | 1.25±0.37 | 2.26±0.50 |
| | | **R2** | 1.32±0.40 | |
| | | **R5** | 0.35±0.10 | |
| | **C24** | **R3** | 3.34±0.99 | |
| | | **R12** | 5.12±1.53 | |

## 7. Study of the genetic background with a panel of genes related to cardiac arrhythmias

**Table 22. Common variants in structural genes identified in the four members of the family.**

| Gene | Variant |
|---|---|
| *ACTN2* | c.877-8C>G |
| *AKAP9* | c.1389G>T |
| | c.4004_4006dup |
| | c.6945+8C>T |
| | c.8375A>G |
| | c.8935C>T |
| *CRYAB* | c.324+4T>G |
| *DMD* | c.8810G>A |
| | c.2645A>G |
| *DSP* | c.2631G>A |
| *JUP* | c.2089A>T |
| *NEBL* | c.1671+9T>C |
| | c.1008+5A>G |
| *NEXN* | c.733G>A |
| *PDLIM3* | c.906C>T |
| *RBM20* | c.2303G>C |
| | c.3452-9G>C |
| | c.3667G>C |
| *TNNI3* | c.373-10T>G |
| *TNNT2* | c.53-11_53-7del |
| *TRDN* | c.1313T>G |
| | c.1188A>G |
| | c.601C>G |
| | c.383C>G |
| *TTN* | c.93062-10del |
| | c.59542G>C |
| | c.10256G>A |
| | c.9781G>A |
| | c.4480+6C>T |
| | c.3884C>T |
| | c.3601A>G |

**Table 23. Common variants in non-structural genes identified in the four members of the family.**

| Gene | Variant |
|---|---|
| *ABCC9* | c.1165-6del |
| *BAG3* | c.451T>C |
| *CASQ2* | c.420+6T>C |
|  | c.738-5del |
| *KCNE1* | c.112A>G |
| *KCNJ5* | c.844C>G |
| *RYR2* | c.13783-6A>G |
| *SCN10A* | c.5137A>G |
| *TGFBR2* | c.263+7A>G |

Table 24. Common variants in structural genes identified in the four members of the family. Green filled cells indicate the individual as carrier of the SNV.

| Gene | Variant | Rb20234 | Rb20235 | Rb20236 | Rb20237 |
|---|---|---|---|---|---|
| *DMPK* | c.611+6T>C | 🟩 |  |  | 🟩 |
| *DSC2* | c.2393G>A |  |  |  | 🟩 |
| *DSG2* | c.2137G>A | 🟩 | 🟩 |  | 🟩 |
|  | c.2318G>A | 🟩 | 🟩 |  | 🟩 |
|  | c.523+24del | 🟩 | 🟩 | 🟩 |  |
|  | c.877A>G | 🟩 | 🟩 | 🟩 |  |
| *DSP* | c.5213G>A |  |  | 🟩 |  |
| *FBN1* | c.3464-5G>A | 🟩 | 🟩 | 🟩 |  |
|  | c.1415G>A |  |  |  | 🟩 |
| *JPH2* | c.1186G>A | 🟩 | 🟩 |  | 🟩 |
| *LMNA* | c.1698C>T | 🟩 | 🟩 |  | 🟩 |
| *MYBPC3* | c.472G>A |  | 🟩 |  | 🟩 |
|  | c.706A>G | 🟩 | 🟩 | 🟩 |  |
| *MYH6* | c.3979-8del | 🟩 | 🟩 |  | 🟩 |
|  | c.3302T>C | 🟩 | 🟩 |  | 🟩 |
|  | c.3979-7_3979-5dup |  | 🟩 | 🟩 |  |
| *MYH7* | c.3337-3_3337-1dup |  | 🟩 |  | 🟩 |
|  | c.732C>T |  | 🟩 |  | 🟩 |
| *MYPN* | c.1884C>G |  | 🟩 | 🟩 | 🟩 |
|  | c.2072G>A |  | 🟩 | 🟩 | 🟩 |
|  | c.2120G>A |  | 🟩 | 🟩 | 🟩 |
|  | c.2409C>G |  | 🟩 | 🟩 | 🟩 |
|  | c.3403C>A |  | 🟩 | 🟩 | 🟩 |
| *PKP2* | c.1097T>C |  | 🟩 |  | 🟩 |
| *RBM20* | c.1527+8C>T |  | 🟩 |  | 🟩 |
| *TMPO* | c.1079+5dup | 🟩 |  | 🟩 |  |
| *TNNI3* | c.25-8T>A |  | 🟩 | 🟩 | 🟩 |
| *TRDN* | c.1805-7del | 🟩 |  |  |  |
|  | c.1805-7_1805-5dup |  | 🟩 | 🟩 |  |
|  | c.1105+5G>A |  | 🟩 | 🟩 |  |
| *TRIM63* | c.709A>G | 🟩 | 🟩 |  | 🟩 |
| *TTN* | c.55319C>T | 🟩 |  | 🟩 |  |
|  | c.35254A>G | 🟩 | 🟩 |  | 🟩 |
|  | c.26951-3del | 🟩 |  | 🟩 | 🟩 |
|  | c.19054G>C | 🟩 | 🟩 |  | 🟩 |
|  | c.2432C>T |  |  |  | 🟩 |

**Table 25. Common variants in non-structural genes identified in the four members of the family. Green filled cells indicate the individual as carrier of the SNV.**

| Gene | Variant | Rb20234 | Rb20235 | Rb20236 | Rb20237 |
|---|---|---|---|---|---|
| *ABCC9* | c.4450-5del | 🟩 | | | 🟩 |
| | c.574-5C>A | 🟩 | | 🟩 | 🟩 |
| *BAG3* | c.1220C>T | | | | 🟩 |
| *CACNA2D1* | c.1516-10del | 🟩 | 🟩 | | |
| | c.659-3del | 🟩 | 🟩 | 🟩 | |
| | c.355-5_355-3dup | 🟩 | 🟩 | 🟩 | |
| *CACNB2* | c.1803T>G | 🟩 | 🟩 | 🟩 | |
| *FKTN* | c.608G>A | 🟩 | 🟩 | | 🟩 |
| | c.166C>T | | | | 🟩 |
| *KCNH2* | c.2690A>C | 🟩 | 🟩 | 🟩 | |
| *KCNJ5* | c.938-10G>A | 🟩 | 🟩 | | 🟩 |
| *RYR2* | c.849-8T>C | 🟩 | | 🟩 | |
| *SCN10A* | c.3275T>C | | | 🟩 | |
| | c.3218T>C | | | 🟩 | |
| | c.2884A>G | | | 🟩 | |
| | c.1868-9A>G | | | 🟩 | |
| *SCN1B* | c.629T>C | | | | 🟩 |
| *SCN5A* | c.1673A>G | | | 🟩 | |
| | c.1141-3C>A | | | 🟩 | |
| *SLMAP* | c.1341C>T | | 🟩 | | 🟩 |
| *TGFBR2* | c.455-4T>A | | 🟩 | | 🟩 |

# Annex Bibliography

1. Bezanilla, F. Ion Channels: From Conductance to Structure. *Neuron* **60**, 456–468 (2008).
2. Hille, B. *Ion Channels of Excitable Membranes*. (Sinauer associates, Inc, 2001). doi:10.1007/3-540-29623-9_5640.
3. Boron, W. F. & Boulpaep, E. L. *Medical Physiology*. *A cellular and molecular approeach* (Saunders Elsevier, 2012). doi:10.1017/CBO9781107415324.004.
4. Ogden, D. *Microelectrode Techniques: The Plymouth Workshop Handbook*. (The Company of Biologists Limited, 1994).
5. Neher, E. & Sakmann, B. Single-channel currents recorded from membrane of denervated frog muscle fibres. *Nature* **260**, 799–802 (1976).
6. Hamill, O. P., Marty, A., Neher, E., Sakmann, B. & Sigworth, F. J. Improved patch-clamp techniques for high-resolution current recording from cells and cell-free membrane patches. *Pflügers Arch. Eur. J. Physiol.* **391**, 85–100 (1981).